SAPIENZA
UNIVERSITÀ DI ROMA

Validation of RELAP5-3D© for liquid metal reactor technologies

Facoltà di Ingegneria Civile e Industriale
Dipartimento di Ingegneria Astronautica, Elettrica ed Energetica
Corso di Dottorato di Ricerca in Energia e Ambiente – Scuola di Dottorato in Scienze e Tecnologie per l'Innovazione Industriale – XXXII Ciclo

Candidate
Vincenzo Narcisi
Matricola 1394736

Thesis Advisor
Prof. Gianfranco Caruso

Co-Supervisor
Dott. Ing. Fabio Giannetti

January 2020

Summary

LIST OF FIGURES

LIST OF TABLES

ABSTRACT

The present research work set in an international and national context that includes the efforts of several universities and research centers in a strict collaboration. Within the international framework, the Department of Astronautical, Electrical and Energy Engineering (DIAEE) of "Sapienza" University of Rome (UNIROMA1) has been recently involved in the Horizon 2020 (H2020) SESAME (thermal-hydraulic Simulations and Experiments for the Safety Assessment of MEtal-cooled reactors) project. The project aims to contribute to the liquid metal-cooled fast reactors (LMFRs) development, including the advanced numerical approaches for the design and safety evaluation of the technologies. Regarding the national context, R&D efforts are mainly dedicated on the development of the lead-cooled fast reactor (LFR) technologies, involving three main partners: ENEA (Italian National Agency for New Technologies, Energy and Sustainable Economic Development), CIRTEN (Interuniversity Consortium for Technological Nuclear Research) and the industrial partner ANSALDO NUCLEARE. Strong collaboration and comparing among the three partners are devoted to the development of the reference LFR project: the Advanced Lead Fast Reactor European Demonstrator (ALFRED).

In this framework, the purpose of the present research activity has been to contribute to the understanding of relevant thermal-hydraulic phenomena that characterize the operations of the LMFR, and to the fundamental validation process of the innovative numerical tools, adopted for safety analysis and licensing of new Generation IV (GEN IV) technologies. The research activity has dealt with the validation of RELAP5-3D© (R5-3D) for applications on liquid metal-cooled pool-type fast reactors.

The thesis is divided in seven chapters. The first one is dedicated to the definition of the general background of the research activity. Chapters 2, 3 and 4 are focused on the validation of R5-3D for application on LMFRs. The merits of the simulations are evaluated comparing the results with experimental data from CIRCE (CIRColazione Eutettico) facility, Phénix reactor and PERSEO (in-Pool Energy Removal System for Emergency Operation) facility. The numerical activities have been used to explore and validate different modelling approaches and the acquired know-how has been used to support the design of ALFRED reactor. This topic is examined in chapter 5 that is basically divided in two subsections: the first one analyzes the reference configuration of ALFRED and the second one deals with the revised configuration of the reactor. Chapter 6 presents a methodology for the uncertainty quantification, based on the coupling approach between RELAP5-3D and RAVEN codes. Experimental data from the loop-type facility, called NACIE (NAtural CIrculation Experiment), have been used for the qualification of the methodology. Finally, the main results and guidelines, as well as the weaknesses and the future perspective coming out during the present research activity, are pointed out in chapter 7.

CIRCE is a multipurpose pool-type facility aimed to investigate thermal-hydraulics of innovative heavy liquid metal (HLM) cooled pool-type systems. Two experimental campaigns have been considered in the present work, related to two different configurations of the facility: ICE (Integral Circulation Experiment) and HERO (Heavy liquid mEtal pRessurized water cOoled tubes).

The experimental campaign promoted in CIRCE-ICE test facility was aimed to investigate the thermal-hydraulics of a complex HLM system and to provide data for validation of computational tools. Two experimental tests have been analyzed in this activity: Test A, consisting in a transition from no-power to full power steady-state conditions, and Test I, consisting in a transition from gas-enhanced circulation (GEC) to natural circulation (NC), simulating a protected loss of heat sink plus loss of flow accident. The computational activity has been addressed to investigate the capability of RELAP5-3D© to predict thermal stratification phenomenon in an HLM pool. Several examples were found in literature concerning the simulation of large tanks with RELAP5. The state of art on the simulation of the thermal stratification in large pool has been confirmed by the calculations performed

on CIRCE-ICE. The mono-dimensional approach, using a single channel for pool modelling, highlights discrepancies with the experimental data, failing on the prediction of the axial temperature profile. A high peak temperature in the middle of the tank, which is not observed by the experiment, is caused by a total absence of the natural flow within the pool. In order to verify how the axial conduction within the fluid can improve the computational results, a thermal conduction model has been implemented in the nodalization, using several heat structures that couple adjacent meshes. As expected, the axial conduction reduces the peak but not enough to match the experimental temperature profile. To reproduce buoyancy within the LM tank, the pool has been divided in three vertical channels, connected with cross junctions. This approach (model #1) has shown good capabilities on the thermal stratification evaluation. The qualitative trend is well reproduced, predicting two relevant stratifications in the upper and in the middle volumes of the pool. In the lower part of the tank, the LBE temperature is very well simulated but, at 4 m, the plateau temperature is under-predicted of about 15 K and this discrepancy is maintained up to the cover gas. R5-3D was improved with a fully integrated multi-dimensional (MULTID) modelling scheme, mainly developed for volumes where the movement of the fluid is preferably 1D. The MULTID component has been used for the simulation of CIRCE pool. In addition, the fuel pin simulator (FPS) modelling has been improved for the subchannel analysis (model #2). Several figures of merit have been selected, assessing the capabilities of the two models to reproduce thermal-hydraulics of an HLM cooled pool-type system in safety-relevant operations. The comparison with experimental data has highlighted excellent capabilities of the two models to predict thermal-hydraulics of the main flow path, managing to evaluate the most important features: LBE mass flow rate in both GEC and NC conditions, heat exchange within FPS, heat exchanger (HX) and decay heat removal system (DHR), and heat losses. In addition, model #2 assesses RELAP5-3D abilities as a subchannel analysis code, in both GEC and NC operations. The effect of the radial conduction has been evaluated: specific heat structures have been implemented to reproduce thermal conduction through adjacent subchannels. This analysis has shown small effects of the radial conduction, even if, in low flow rate regimes, such as NC operation, it provides not negligible improvement on the prediction of the temperature profile. In this case, the simulation is in good agreement with experimental data; the highest discrepancies are observed in the edge of the bundle (4 degrees) where the errors can be justified by the uncertainties related to the thermocouples positions. Focusing on the pool simulation, the MULTID component has introduced relevant improvements on the prediction of the thermal stratification phenomenon. The two relevant stratifications have been observed by the calculation. The temperature in the lower part matches very well the experimental measurements. The lower stratification level is well predicted and the temperature hot plateau underestimation has been reduced to 5 K. After the transition from GEC to NC, both the models are able to predict the upper stratification attenuation and the movement of the lower one below the DHR outlet. In the long term, the two calculations provide the same temperature profile that matches well the experimental trend, limiting the discrepancies below 4 degrees. Evaluation of the axial conduction within the pool has been performed, highlighting limited effects, especially when the natural circulation (NC) inside the pool is considered.

HERO test section was employed in CIRCE facility to investigate thermal-hydraulics of a double wall bayonet tube (DWBT) steam generator (SG), in a relevant configuration for ALFRED SG. Moreover, a validation benchmark was proposed within the H2020 SESAME project to asses the capabilities of different computational tools to predict the main thermal-hydraulic phenomena in an HLM-cooled pool-type facility. UNIROMA1 supported the definition and the realization of the experimental campaign, developing a nodalization scheme, based on the validated CIRCE-ICE model, for the pre-test analysis. The calculations have investigated different transient scenarios, highlighting the capabilities of HERO test section to guarantee sufficient NC to remove the decay heat in the short term. Based on these results, a set of three experimental tests has been performed, consisting in three protected loss of flow accidents (PLOFAs), occurred during the normal operation of the facility. The numerical activity has concerned two of the three tests, adopting an improved nodalization scheme. Regarding post-test

analysis of Test 3, simulation of the full power conditions is globally in agreement with experimental data for all the primary circuit physical quantities monitored, including the thermal stratification phenomenon; some discrepancies are highlighted on the secondary side, mainly due to the lack of some information which determines large uncertainties on the boundary conditions related to the operation of the secondary loop. Starting from the full power steady-state conditions, two transient calculations have been performed, assuming the same boundary conditions, except for the feedwater (FW) mass flow rate after the transition event. Case 1 assumes the reference value of the secondary flow rate (0.078 kg/s), obtained with the energy balance equation applied to the FW pre-heater. This calculation highlights an overestimation of the power removed by the SG. A second calculation has been performed adjusting the total secondary flow rate to 0.047 kg/s; that value guarantees the correct SG power. Both the simulations are in good agreement with experimental data in the first 200 s, reproducing very well the first minutes after the transition event. After the Ar injection cut off, the first calculation provides a good estimation of the minimum value of the LBE MFR, underpredicted by the second calculation of about 2 kg/s. The long term behavior strongly depends on the feedwater mass flow rate. Case 1 shows an overestimation of the whole system energy unbalance, leading to the overprediction of the natural circulation contribution and of the cooling trend. The SG power balance analysis has highlighted an overestimation of the power removed of about 30% of the experimental value. The large uncertainties related to the measurement of the secondary system quantities have suggested the calibration of the secondary flow rate to obtain the correct SG power removed. This assumption has been justified comparing the experimental flow rate, acquired at the inlet of the tubes 0 and 4, with the simulation results: the experimental data are underestimated but the calculation results remain within the experimental uncertainty bands. Looking at the primary system, the assumption of a lower FW flow rate leads to a better agreement with experimental data, providing a good estimation of the long term behavior. Some discrepancies are still maintained on the secondary side, where the steam outlet temperature is overpredicted by the code. The differences could be due to a not perfect agreement of the powder thermal conductivity, which represents a large source of uncertainties. This opens the possibility to continue the post-test analysis for the secondary side, leading an improved experimental results analysis, despite the good global results obtained. Similar conclusions are obtained from the post-test analysis of Test 1, confirming good capabilities of R5-3D to reproduce thermal-hydraulics of HLM-cooled systems in safety-relevant operations. In addition, the subchannel analysis performed has highlighted a good prediction of the subchannel thermal-hydraulics within the FPS bundle in the postulated transient accident.

The Phénix Dissymmetric End-of-Life test, proposed for a benchmark exercise within the H2020 SESAME project, offered useful data for the analysis of more complex systems where asymmetrical effects could play a relevant role in the system thermal-hydraulics. As a participant to the validation benchmark, in collaboration with ENEA, UNIROMA1 has developed a detailed nodalization of the reactor, including a three-dimensional modelling of the pools and an assembly per assembly core modelling in the active region, suitable for a neutron kinetic and thermal-hydraulic (NK-TH) coupling calculation. The full power calculation has highlighted a good capability of the code to reproduce the normal operation of the reactor. Starting from the steady-state results, the transient calculation has been performed assuming the dissymmetric test boundary conditions provided by CEA. The asymmetric distribution of the flow rate through the secondary loops leads to an asymmetric operation within the primary system, which is well predicted by R5-3D. The asymmetrical operation of the two secondary systems leads to a dissymmetric evolution of the thermal-hydraulics within the cold pool. Good agreements have been observed between experiment and simulation. In particular, the movement of the hot sodium within the cold pool is well predicted by the code, which is able to predict the local peak temperature at the PP1 inlet. At this regard, the three-dimensional momentum equation adopted in the MULTID modelling seems to provide a good instrument for the evaluation of the temperature and flow distribution within large volumes.

Safety and reliability are relevant aspects of the development of GEN IV reactors. In this framework, LMFRs present peculiar characteristics related to the thermophysical properties of the coolant, basically regarding the possibility of coolant freezing, that can occur in long term DHR operation if the thermal power removed by the DHR system exceeds the decay residual power. For this reason, in LMFRs, the DHR system must ensure an efficient power removal, avoiding to overcome technological limits in terms of maximum temperatures, and must prevent coolant freezing in the grace time period. In addition, according to GIF guidelines, passive DHR systems are needed to prevent unexpected evolution of accidental scenarios following a total loss of the continuous electrical power supply. The solution consisting of an isolation condenser (IC) immersed in a water tank, acting as a final heat sink, could meet the above-mentioned characteristics. The operation of such a system, is based on in-tube condensation under NC condition and pool boiling. For this reason, a validation process is required for STH codes, such as R5-3D. In this framework, PERSEO facility provided useful experimental data. UNIROMA1 developed a 1D model of the facility. In order to reduce the computational cost, a mono-dimensional model of the pools (three parallel pipes with cross junctions) has been included. This modelling choice is justified by the negligible effect of the thermal stratification on the system thermal-hydraulics. The numerical activity has shown satisfactory capabilities of the code to reproduce the safety performance of the passive system. The main limitation observed in R5-3D calculations, and in almost all the STH codes adopted in the benchmark exercise, is the significant underestimation of the power exchanged between the HX and the HX pool. This can be attributed to the underprediction of the heat transfer coefficient (HTC) in both the tube-side and pool-side, where the condensation under natural circulation conditions and the pool boiling are outside of the validity ranges of the correlation fully integrated into the code. For this reason, the main improvement adopted in the nodalization has been the application of a constant multiplicative factor (2.4) to the HTC on both the sides.

The main target of the validation activity was to qualify R5-3D STH code to support the design of the GEN IV nuclear power plants. The numerical activity was used to explore and validate different modelling approaches and the acquired know-how has been used to support the design of ALFRED reactor, investigating the reference and the improved configurations of the LFR concept. The first numerical activity has concerned the reference concept of the reactor, developed within the LEADER project. Based on the experience learned during the analysis of the experimental campaign performed in CIRCE and on the references found in literature, a thermal stratification phenomenon was expected into the main pool of the reactor. For this reason, a detailed three-dimensional model of the pool has been developed. In addition, an assembly per assembly core modelling, assuming the approach adopted for Phénix simulations, has been developed, allowing the calculation of the power distribution at the beginning of life (BOL) of the reactor using the NK-TH methodology. It is based on the RELAP5-3D/PHISICS coupling calculation. The full power calculation has highlighted a relevant thermal stratification, of about 70 K, in the upper part of the pool, that is not been involved in the primary flow path. Thermal stratification represents a significant technological issue. This was one of the reasons that encourages the designers to develop a revised concept of ALFRED reactor. In this frame, the solution was to include an internal structure, within the Reactor Vessel, that forces the cold lead, exiting the SG, to move upward and then, passing through specific holes in the upper part of the IS, to move downward towards the core inlet. In this way, zones not involved in the flow path are avoided. A thermal-hydraulic model of the new configuration was developed in order to verify, among other issues, the absence of relevant thermal stratifications in both normal and accidental operations. For this purpose, a detailed MULTID component was developed to reproduce the pools of the reactor. The numerical activity has demonstrated the improved pool thermal-hydraulics: significant thermal stratifications are avoided in both full-power operation and SBO scenario. Another issue is related to the possibility of coolant freezing in all the operative conditions, including accidental scenarios. A solution that limits the maximum temperatures in the first instants after the transition event and modulates the power removed from the primary coolant in the long term, has been proposed, adopting an IC, immersed in water pool, equipped

with non-condensable (nitrogen) tank. The non-condensable tank allows to passively modulate the power removed by the DHR system, by injecting nitrogen within the IC bundle. The non-condensable flow rate is passively controlled by the pressure difference between the gas tank and the water system. The numerical activity has been aimed to verify the revised concept of the DHR system under a postulated protected loss of offsite power (PLOOP). The simulation shows the capability of the safety system to restrict the maximum temperatures in the first phases of the transient within the technological limits. In the long term, as the depressurization of the secondary system occurs, nitrogen is injected within the IC bundle, degrading the heat exchange. This is enough to limit the power removed by the DHR system to the decay heat value, limiting the Pb minimum temperature to 630 K, about 30 K higher the Pb freezing point.

Finally, the last chapter of the thesis has proposed a best estimate plus uncertainty (BEPU) methodology, based on a statistical exploration of the input space considering the associated uncertainties altogether and the analyses of the responses with several validation metrics. The methodology consists in the RELAP5-3D/RAVEN coupled calculation. The objective has been to verify the coupled methodology for the uncertainty quantification of LM-cooled systems. For this purpose, the experimental campaign performed on NACIE facility and the thermal-hydraulic model developed by UNIROMA1 has been considered. The UQ has been based on the perturbation of the input space following a Monte Carlo sampling, propagating the input uncertainties. The analysis of the main outcomes related to selected FOMs, has been performed with three comparison metrics, fully integrated into RAVEN tool. The application of the comparison metrics has shown the capabilities of the methodology, highlighting the merits and the weaknesses of the thermal-hydraulic model. The future perspectives could be the application of the model to more complex models to increase the validation process of the methodology and to apply it to the verification process of the new NPP concepts.

The main outcomes and guidelines coming out during the research activity are summarized in four main sections:

1. Pool modelling:
    - Several modelling approaches have been explored;
    - Mono-dimensional approach based on a single equivalent channel fails to reproduce large pool thermal-hydraulics;
    - Mono-dimensional modelling approach, consisting in more parallel channels connected with cross junction, is preferable when satisfactory prediction of pool thermal-hydraulics are required, even if phenomena such as thermal stratification do not assume relevant role in the behavior of the whole system. This modelling approach allow to reduce computational cost;
    - MUILTID modelling approach is preferable if relevant thermal stratification phenomena are expected, justifying the computational cost increase;
    - Calculations have highlighted the importance of specific heat transfer correlations applicable for large pool geometries, that are not implemented in the actual version of RELAP5-3D. In this framework, UNIROMA1 is actually working on a modified version of RELAP5 mod. 3.3 that, among other implementations, will include specific correlation for heat transfer in large pools.
2. Liquid metal system operation:
    - Calculations have shown satisfactory capabilities of R5-3D to reproduce primary system if LMFR under safety-relevant conditions;
    - Simulation performed in the frame of ALFRED have highlighted the importance of STH codes in the verification and licensing process of an innovative NPP;
    - R5-3D has shown satisfactory capabilities as subchannel codes; Several modelling choices are explored.

3. Passive safety system:
    - Good capabilities of R5-3D to reproduce safety performances of a passive DHR system based on an IC immersed in a water tank;
    - Main limitations related to the prediction of the power removed by the IC, due to the lack of a specific heat transfer correlation for pool boiling and in-tube condensation under NC;
    - Simulation performed in the frame of the revised ALFRED concept demonstrates the safety capabilities of the DHR system designed for the reactor. Maximum temperatures are restricted within the technological limits and lead freezing is prevented in the grace time period.
4. BEPU methodology:
    - Methodology based on a statistical exploration of the input space considering the associated uncertainties altogether;
    - Three comparison metrics have been used for the analysis of the main outcomes, highlighting the merits and the weakness of the thermal-hydraulic model;
    - The future perspectives could be the application of the model to more complex models to increase the validation process of the methodology and to apply it to the verification process of the new NPP concepts.

1 INTRODUCTION

1.1 General background

The expected increase of world's population, combining with the necessity to move towards a sustainable and low-carbon energy mix and to improve the actual access to energy, leads nuclear energy to a key role in the near future energy landscape. Nowadays, nuclear energy represents 40% of the low-carbon generation worldwide and, according to the International Energy Agency (IEA), in order to achieve the objective to limit the global temperature increase to 2°C in this century, nuclear energy must increase from 10% to 15% of worldwide electricity production by 2060 [1].

Further developments in nuclear technologies are needed to meet this goal. For this purpose, in January 2000, nine countries, including the European Atomic Energy Community (EURATOM), founded the Generation IV International Forum (GIF), individuating the main goals for the development of the next generation of nuclear power plants (NPPs), the so-called Generation IV (GEN IV) [2]. The four macro-areas are summarized below:

- sustainability;
- safety and reliability;
- economic competitiveness;
- proliferation resistance and physical protection.

Several innovative concepts were investigated by experts and six nuclear power systems were identifies as GEN IV technologies:

- Gas-cooled Fast Reactor (GFR);
- Lead-cooled Fast Reactor (LFR);
- Molten Salt Reactor (MSR);
- Sodium-cooled Fast Reactor (SFR);
- SuperCritical-Water-cooled Reactor (SCWR);
- Very-High-Temperature Reactor (VHTR).

The six concepts were confirmed in the Technology Roadmap Update [2], that revised the timelines of each technology. As presented in Figure 1, that compares the original roadmap (left) with the updated timelines (right), SFR and LFR systems are the most advanced technologies.

The 2014 update of the Technology Roadmap fixed the achievements of the first ten years and it defined the key objectives and the research and development (R&D) steps for each technology in the present decades. Verification & Validation (VV) and Uncertainty Quantification (UQ) of the advanced modelling tools was considered one of the most relevant aspects for the development of the Liquid Metal (LM) cooled reactors.

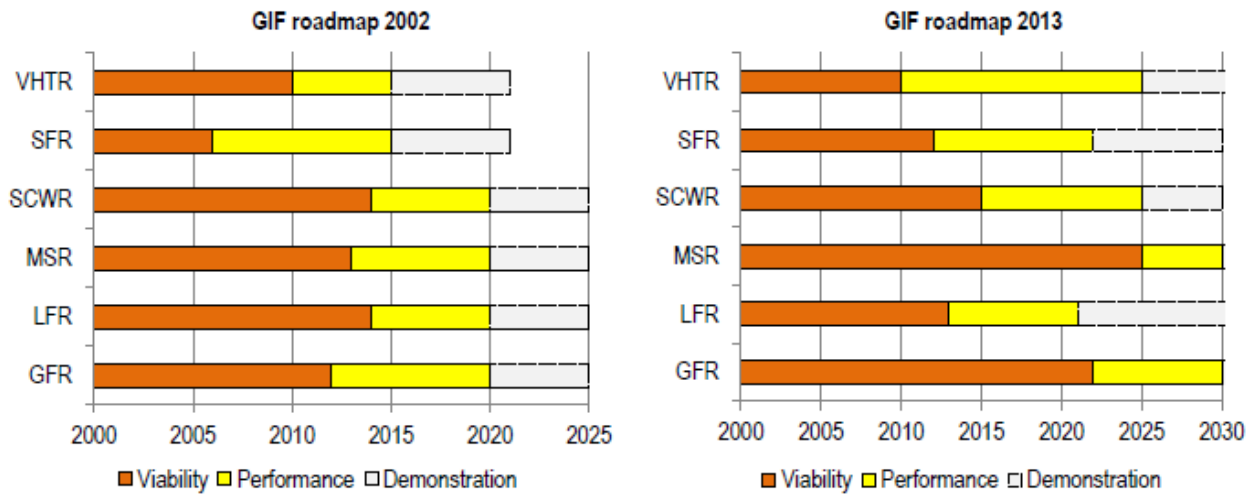

Figure 1. System development timelines: 2002 Roadmap (left) and 2013 Roadmap Update (right)

1.2 Why liquid metals? Advantages and drawbacks of liquid metals as coolants

Nowadays, the efficiency of Generation III (GEN III) and Generation III+ (GEN III+) reactors, in terms of uranium consumption, is low. In the current structure of the NPPs, the Light Water-cooled Reactors (LWRs) are predominant; their operation is based on the irradiation of enriched uranium with thermalized neutrons, produced within the reactor core and moderated by the water. In the so-called thermal reactors, only low portions of uranium are split in fission products and energy.

The efficiency of uranium consumption could be improved by switching to fast reactors. The unique characteristics of the Fast Breeder Reactors (FBRs) could be summarized in the capability of nuclear fuel breeding, involving ^{238}U in the fuel cycle, and the flexibility of the NPP, that can be used as plutonium incinerators or to transmute the long-lived radioactive elements by changing the design of the reactor core [3][4].

The possibility to use fast spectrum for fission reactions is strictly related to the fluid used as coolant; water can not be used to cool the reactor core, due to its moderation capabilities. The GIF identified three concepts of FBR: the GFR, consisting of a high-temperature helium-cooled fast-spectrum reactor, the LFR, which includes lead and lead-bismuth alloy technologies, and the SFR. Even if, in the earlier phase of the FBR development, the possibility to use high pressure gases to cool the reactor core was studied, liquid metals offer several benefits making their choice the most promising one.

As presented in the previous section, LM systems, especially SFR, represent the most advanced FBR technologies, due to the considerable experience gained in the first phase of fast breeder reactor development [5][6]. The choice of liquid metal as coolant for FBRs is mostly related to the neutronic characteristics, for which the fast neutrons produced by fission reactions are not slowed down and a large amount of these remains within the reactor core to feed the nuclear chain reaction, and to the advantageous thermophysical properties [4]. In the typical operating conditions of a liquid metal-cooled fast reactor (LMFR), sodium, lead and lead-bismuth alloy are liquid, and they present a large margin to the evaporation point. This feature makes possible to operate the reactor at low pressure, in contrast to typical LWRs which need pressurization for working conditions. LMs are characterized by excellent heat transfer capabilities and by high heat capacity that allow efficient heat removal from the reactor core and offer large grace time in case of accidents occurrence, providing the opportunity to

achieve high specific power densities within the core. Safety aspect represents a key point for the GEN IV reactors; in this regard, the high density (especially for lead and lead alloy) and the large coefficient of thermal expansion (mainly for sodium) promote the establishing of the natural circulation in case of accident situations. In this frame, the excellent heat transport characteristics of lead and lead alloys allow large rod pitches within the fuel assemblies (FAs), reducing the pressure drops across the reactor core. The natural circulation represents a crucial safety aspect, allowing a reliable residual heat removal during accidental scenarios that imply the total loss of electrical supplies. The high density of lead provides another relevant safety aspect related to the capability to scatter the molten fuel in case of a severe accident, preventing the formation of critical masses. LMs are also characterized by high boiling point (1156 K for sodium, 2018 K for lead and 1943 K for lead-bismuth alloy) that mitigates the issues with core voiding, especially for LFR systems, in which the voiding within the reactor core is prevented because the clad failure would occur before the lead boiling. The advantages of the high boiling point are not only related to safety aspects but also to economic features, because the high operative temperature, typical of the liquid metal fast reactors, allows high efficiency for electricity production [4]. In addition to the above mentioned common benefits, lead presents another advantage: it is chemically inert with air and water and this feature allows to integrate the steam generators (SGs) within the main vessel, in the so-called pool-type reactor, eliminating the issues related to the out-of vessel primary system and providing a high self-shielding capacity [4].

However, LM systems present significant drawbacks that must be taken into account during the development and the operation of these innovative nuclear reactors. The high mass of liquid metals, especially for lead and lead alloys, represents a typical issue for this technology, requiring special measures for seismic events. Two other features of LMs are the high melting point (371 K for sodium, 600 K for lead and 398 K for lead-bismuth alloy) and the opacity. Regarding the first one, it requires a pre-heating system and special measures to prevent the solidification of the coolant in both normal and accidental conditions. In addition, the in-service inspection in opaque coolants is more difficult; for this reason, R&D activities are needed for ad-hoc monitoring systems [4]. Furthermore, other specific issues related to sodium and lead are added to the common drawback above-mentioned. Regarding the SFRs, the main issue related to the coolant is the chemical reactivity of sodium with air and water, resulting in explosion potential. Typically, this issue determines multiple barriers between sodium and the environment. In addition, an intermediate sodium system is required to avoid the activated sodium-water reaction in case of steam generator tube rupture (SGTR). Another solution is to replace the secondary water system with a gas-cooled system, feeding a Brayton cycle. Regarding the LFRs, the main issues are related to corrosion and erosion. Especially at temperatures above 870 K, corrosion is a crucial aspect and innovative materials need to be developed to withstand the corrosion issues. Erosion issues are due to the high mass of lead or lead-bismuth alloy, that limits the coolant velocity below 2 m/s. In addition, in lead-bismuth systems, the production of highly radiotoxic polonium must be taken into account [4].

The comparison of the basic characteristics of the two liquid metals is summarized in Table 1 [3].

Table 1. Coolant comparison

Coolant	Advantages	Drawbacks
Sodium	Best thermal-hydraulic features Low operative pressure Good neutronic characteristics Non-corrosive to stainless steel and any fuel compositions Decay heat removal by passive features Relatively low density, allowing passive safety rod injection by gravity force and preventing the FA from floating up Retention of cesium, strontium, iodine and tritium Neutrons do not generate radionuclides with a half-life more than 2.6 years (^{23}Na)	Chemical activity with oxygen and water High γ-activity of ^{24}Na Need intermediate circuit High melting temperature; heaters are required for maintaining liquid phase Problems related to sodium removal and disposal during reactor plant operation and decommissioning
Lead and lead alloys	Lack of the high γ-activity Chemically inert Good neutronic characteristics Good reflecting properties Decay heat removal by passive features High boiling temperature; coolant void reactivity is negative	A-radioactive (lead-bismuth alloy) Highly corrosive to steels and some fuel compositions High density; probability of core pollution by suspensions High freezing temperature High residual activity of coolant Formation of the products of water and heavy metal interaction; possibility of blockage A leak-before-break argument in safety analysis is questionable because of a risk of corrosion damage Problems with radioactive waste management and coolant disposal during decommissioning

1.3 Verification and Validation

The Technology Roadmap Update for GEN IV [2], issued by the Organization for Economic Co-operation and Development – Nuclear Energy Agency (OECD NEA), aimed to summarize achievements of the first ten years of the GIF schedule and to define the challenges and the development needs for the present decade. One of the main issues, individuated for both the SFR and the LFR concepts, was the verification and validation (V&V) of the advanced modelling tools [2]. Nowadays, the System Thermal-Hydraulic (STH) codes are the reference tool for

the reactor transient analysis. The most of them, such as RELAP (Reactor Excursion and Leak Analysis Program), CATHARE (Code for Analysis of THermalhydraulics during an Accident of Reactor and safety Evaluation) or TRACE (TRAC/RELAP Advanced Computational Engine), were developed and validated for the best-estimate transient simulation of LWRs. Liquid metals application requires several enhancements of the STH codes, focused on the introduction of new working fluids and correlations related to LM thermal-hydraulics, and new modelling capabilities, taking into account the innovative configurations of the GEN IV reactors (three-dimensional modelling capabilities and neutronic point kinetics models). Validation process of these enhancements represents a milestone of actual R&D activity.

As suggested in Ref. [9], any computational tools or calculation methods used in the safety analysis shall undergo VV to a sufficient agree. The verification process is the review of source coding, done by the code developers. The system code verification is needed to ensure the quality of the models and methods implemented, and to verify the accuracy of the descriptions provided in the system code documentation.

The validation process aims to determine if the analitichal models, implemented in the code, are adequate to reproduce the real system that is investigated. The validation process implies the comparison of the code predictions with experimental data and observations of the actual system. Code validation is done by independent users of the tool. The validation procedure aims to assess the accuracy of values predicted by the code, comparing the simulation results with relevant experimental data for the important phenomena expected to occur (see section 1.5).

The main target of code validation is the assessment of the qualitative and quantitative accuracy. The qualitative analysis is mainly based on a visual comparison between experimental and calculated trends. For this purpose, after identifying the thermal-hydraulic phenomenon to be analyzed, the test case must be divided in relevant phenomenological windows in which this phenomenon is predominant. The evaluation of the qualitative code accuracy will be based on a comprehensive comparison between the computational results and the experimental data. After a positive results of the qualitative assessment, the quantitive accuracy evaluation, taking into account the uncertainties related to the experimental measurements, represents the second step.

The present research activity has been devoted to the validation of RELAP5-3D system thermal-hydraulic code for liquid metal-cooled fast reactors applications. The validation process mainly consists in a qualitative evaluation of the code accuracy. Moreover, a methodology for the quantitave evaluation of the code accuracy is presented in section 6.

1.4 Description of the code: RELAP5-3D©

RELAP5-3D© (R5-3D) is the latest in the RELAP5 code series, developed at Idaho National Laboratory. It is a highly generic system code mainly used for the best-estimate transient simulation of light water reactors, but also for simulations concerning a wide variety of thermal-hydraulic transients in non-nuclear systems. R5-3D includes several improvements that can be summarized in the fully integrated multi-dimensional thermal-hydraulic and kinetic modelling capabilities. The multi-dimensional (MULTID) component has been conceived to allow the user to model more accurately multi-dimensional flow behavior that can occur in typical components of the reactor, such as core, downcomer or steam generators. The enhancements of the latest version also include new thermodynamic properties for water and all the features and models available in ATHENA configuration of the code: addition of new working fluids (i.e. sodium, lead, lead bismuth and lithium lead alloy molten salt) and a magneto-hydrodynamic model [15].

It is a Eulerian code with a finite difference approach, basically one-dimensional (1D), with the recent addition of the multi-dimensional modelling capabilities, defining a one-, two- or three-dimensional array (Cartesian or

cylindrical geometry) of volumes connected with internal junctions. The code adopts a semi implicit numerical solving scheme and it is based on a non-homogeneous and non-equilibrium model for the two phases; it is based on 6 equations: the mass, energy and momentum conservation equations for the liquid and vapor phases. The MULTID component allows the user to select a mono-dimensional or a three-dimensional (3D) matrix solver for the momentum equations.

The closure laws used for the heat transfer are the interphase mass and energy transfer. For the momentum transfer, the interphase drag, wall friction and eventual source terms (for pumps or turbines) are used. Special models for relevant physical phenomena are also added: Critical Heat Flux (CHF), Chocked Flow, countercurrent flow limitation, tracking of non-condensable gases and boron.

R5-3D is validated for a wide variety of thermal-hydraulic problems concerning water systems. Regarding the correlations used by the code, in boling regime, R5-3D adopts Chen correlation for nucleate and transition boiling, and Bromley correlation for film boiling. For the condensation, the code uses correlations derived by the Nusselt for laminar regime, Chato-Shah for turbulent regime, and Colburn-Hougen for the diffusion of non-condensable gases. Concerning the pressure drops, the two-phase friction multiplier approach, in accordance with Lockhart-Martinelli model, is used in two-phase problems. For liquid metal applications, two correlations are implemented for the evaluation of the heat transfer coefficient (HTC): Seban & Shimazaki correlation for non-bundle geometries and Westinghouse correlation for bundle geometries. Regarding the pressure drop in LM systems, the laminar friction factor model is based on the exact solution for the fully developed flow and constant fluid properties, for $0 \leq Re \leq 2200$. The turbulent friction factor is calculated from Zigrang & Sylvester approximation to the Colebrook & White correlation [41].

1.5 State of art and main challenges

The application of liquid metals as coolant for FBRs, combined with innovative safety aspects, leads to the identification of typical thermal-hydraulic challenges, that characterize the operation of these innovative systems. In this section, an overview of the main challenges will be presented, focusing on the pool-type configuration.

Pool thermal-hydraulics is one of the main challenges. It includes several phenomena, such as thermal stratification, thermal striping or mixing convection, that require to be investigated. Thermal stratification is a crucial issue in a quasi-stagnant liquid metal pool, where the inertial and buoyancy forces assume a similar order of magnitude, resulting in the separation of the hot and cold liquid layers in the vertical direction. Thermal stratification depends on the heat losses from internal components and towards the external environment. The hot fluid, heated by the hotter walls, moves upward producing the hot layer in the upper volume of the pool, while the cold liquid metal is confined in the lower plenum. This phenomenon depends on the flow conditions and the temperature difference at the thermal front is higher as the coolant flow rates decreases. This is a typical condition of a quasi-stagnant LM pool. The interface between two layers is subject to large temperature differences that can expose surrounding structures to low-cycle thermal fatigue. For this reason, mitigation of the thermal front is an important objective in reactor design [4].

Thermal stratification phenomenon has been already studied in the past, related to the light water-cooled reactors, where thermal stratification can occur in the piping system [10][11][12] and inside the pressurizer, or to the thermal-hydraulics of passive safety systems, where large tank at low pressure operates as heat sink [13].

Different modelling approaches are available in the literature for the evaluation of the thermal stratification in large pools. They are related to the numerical tools adopted: STH or Computational Fluid Dynamics (CFD) codes. RELAP5, specifically the RELAP5-3D code, has been developed at Idaho National Laboratory (INL) for the thermal-

hydraulic analyses of nuclear systems. RELAP5 uses a first-order semi-implicit upwind differencing scheme which leads to an axial artificial mixing of the hot and cold fluids that does not allow an accurate evaluation of a sharp thermal front. For this reason, a thermal stratification model was implemented in RELAP5. This model is based on HARTEN's subcell resolution scheme [14], tracking the thermal front in the interior of the control volume instead at the edge of the cell as in system codes [15]. This approach allows a good evaluation of the thermal stratification when a relatively coarse nodalization is applicable, such as the pressurizer modelling case. Based on experimental investigation [16][17], simulation activities presented in Ref. [18] and [19] assessed the capability of RELAP5 to reproduce thermal stratification phenomenon in the pressurizer, modelling the component with a single vertical pipe and adopting the stratification model. The computational activity has been repeated investigating the influence of the number of nodes on the evaluation of the thermal stratification [20]. Simulations highlighted good agreement with experiment when the nodalization scheme is sufficiently fine, 10 nodes in this case. When the number of nodes is increased to 20, the calculation observed negligible improvements in the results.

When multi-dimensional effects are relevant, such as in large tanks, the modelling approach described above shows limitations on the evaluation of thermal stratification. This result is reported in Ref. [21], comparing simulations, performed with RELAP5/MOD3.2, with the experimental campaign conducted on an isolation condenser immersed in a gravity driven water tank. A different approach was applied in Ref. [22], modelling the large tank with three parallel pipes and cross junctions to simulate buoyancy inside the pool. Due to the cross junctions, the thermal stratification model could not be activated, so a detailed nodalization (more than 50 volumes per each pipe) of the tank was necessary to predict the thermal front. This modification led to a better estimation of the experimental results. A similar approach was used in Ref. [23], using RELAP5/MOD3.3 to reproduce a passive containment cooling system (PCCS) with open natural circulation. The pool was reproduced with four parallel pipes (20 control volumes per each pipe) with cross junction highlighting the goodness of this modelling approach on the evaluation of the thermal stratification in large volumes.

The modelling guidelines obtained for the simulation of large volume in LWR system, were used to assess the capability of RELAP5/MOD3.3, modified with the implementation of lead alloy thermophysical properties by ENEA (Italian National Agency for New Technologies, Energy and Sustainable Economic Development) and ANSALDO NUCLEARE, to reproduce the thermal-hydraulics of an LBE-cooled pool-type facility, called CIRCE [24]. The modelling approach was to divide the upper part of the pool, where relevant stratification was expected, in three parallel vertical pipes with cross junctions; the lower part was modelled with a single vertical channel. The results showed a good qualitative temperature trend inside the pool, even if some discrepancies were observed in the middle of the pool.

Part of the present work has been focused on the investigation of RELAP5-3D capabilities on the evaluation of the thermal stratification within liquid metal pools. For this purpose, different modelling approaches have been considered and simulations results have been compared with experimental data concerning sodium and lead bismuth eutectic (LBE) alloy systems to evaluate guidelines to reproduce large volumes of quasi-stagnant liquid metal. Knowledge acquired from this research work has been applied for the analysis of new conceptual designs of the Advanced Lead Fast Reactor European Demonstrator (ALFRED).

Among the main targets for the LM-cooled reactors development, core thermal-hydraulics is one of the main challenges. This topic includes the complete core modelling and the fuel assembly analysis. The first one aims to study the overall cooling of the reactor core, considering each phenomenon that contributes in both normal and abnormal conditions. Especially in natural circulation regimes, complex flows, occurring between a warmer and a cooler zone, characterize the core cooling in liquid metal reactors: recirculation within each fuel assembly,

between adjacent subassemblies and inside the core bypass [4]. The fuel assembly analysis is focused on the thermal-hydraulic (TH) characterization of the subassembly, aiming to study complex phenomena occurring within each FA. This is an important topic for the SFR and LFR development, investigating the maximum fuel cladding temperature in each operational condition. The analysis must consider to different geometrical configurations: FA employing wire wraps and FA employing grid spacers [4].

Currently, the complete core analysis is carried out with STH code [25] and the FA modelling with subchannel codes [26]. However, capabilities of RELAP5 as subchannel analysis code were assessed in Ref. [27]; the influence of heat conduction on axial and radial directions was investigated. Calculations showed that axial conduction had not effects on the temperature distribution through the fuel bundle and radial heat conduction presented negligible effects assuming high mass flow rate (MFR) but significant improvement for low coolant mass flow rate. Peclet number represents the ratio between the magnitude of heat convection and radial heat conduction; radial conduction assumes relevant effect when Pe < 1. For the evaluation of the axial conduction influence, Ref. [28] proposed a modified expression of Peclet number $Pe^* = Re\ Pr\ L/D_h$; axial conduction must be accounted when Pe* < 100.

In order to increase knowledge on the use of RELAP5-3D as a subchannel code, part of this research activity has been dedicated to the investigation of different modelling approaches able to reproduce thermal-hydraulics of FA. Simulations results have been compared with experimental data to assess the capabilities of the code. In addition, considering complex systems, such as the sodium-cooled reactor Phénix, a detailed nodalization scheme of the complete core has been developed, suitable for coupling the STH code with neutronics tools. Indeed, the possibility to couple thermal-hydraulics and neutronics is considered an important challenge for the next future. The transport of neutrons depends on several parameters, including temperature of fuel, cladding and coolant. The aim of this approach is to calculate temperatures with thermal-hydraulic code and to use them as input for neutronic code, that evaluates the power generated within the reactor core and returns this parameter to the thermal-hydraulic code as an input. Nowadays, STH code has been used as thermal-hydraulic one. For example, RELAP5-3D has been coupled with the neutronic code PHISICS (Parallel and Highly Innovative Simulation for INL Code System), developed at INL, to reproduce transients of VVER-440 Russian pressurized water reactors [29], and High Temperature Gas-cooled Reactors (HTGR) [30][31]. In this research activity, the coupling method is applied to ALFRED, in the design developed within the EURATOM FP7 LEADER project (Lead-cooled European Advanced DEmonstration Reactor), to evaluate the capability of the methodology and the evolution of the reactor thermal-hydraulics in transition events typical of LFR systems.

Other challenges for the development of the LMFRs are related to the development and the verification of specific systems, such as primary pumps and heat exchangers (HXs) (for the application in both fission and fusion technologies [32][33]). These components imply innovative design, in order to allow the installation within the reactor primary pool [4]. For this reason, HX must be tested and capabilities of the computational tools to reproduce thermal-hydraulics of the component must to be assessed. In this framework, an experimental and computational campaign has been promoted at ENEA Brasimone Research Center (RC), to investigate the performance of a double-wall bayonet tube (DWBT) steam generator in a relevant configuration for ALFRED SG. The whole experimental campaign has been supported in this research activity performing, at first, pre-test calculations, that have provided useful information to the experimentalists for the realization of the experiment, and then the post-test simulations that, on one hand have helped the understanding of the experiment, and on the other hand, have investigated the capabilities of RELAP5-3D to reproduce the thermal-hydraulics of the whole systems, including the SG performance.

With respect to the important topics above-mentioned for the development of innovative LMFRs, the quality control of the numerical simulations must be assessed. The validation of simulation codes (e.g. RELAP5-3D) is always a fundamental process in the development and assessment of the accuracy of the employed physical models. The state-of-art methodology is well described in Ref. [34]. Such approach treats uncertainties individually (i.e. each uncertain parameter is considered distinctly from one another). In this research work a new methodology has been evaluated, using a coupling approach between RAVEN (Risk Analysis and Virtual ENviroment) and RELAP5-3D codes. This methodology performs the exploration of the input space considering the associated uncertainties altogether and analyzes the responses with several validation metrics. Uncertainties in the input space are considered separately from ones in the output space. Such distinction is performed employing sampling of the input space. Such capability, available in the RAVEN code, permits to compare a larger sample of data [35].

1.6 International and national framework of the research activity

The present research work set in an international and national context that includes the efforts of several universities and research centers in a strict collaboration.

Within the international framework, the Department of Astronautical, Electrical and Energy Engineering (DIAEE) of "Sapienza" University of Rome (UNIROMA1) has been recently involved in the Horizon 2020 (H2020) SESAME (thermal-hydraulic Simulations and Experiments for the Safety Assessment of MEtal-cooled reactors) project. The project was cofounded in 2015 by the EURATOM and other 23 partners from 9 European countries (The Netherlands, Belgium, France, Germany, Italy, Slovenia, Czech Republic, Sweden and Switzerland); it gathers also benefits from international cooperation with US DoE laboratories: Argonne National Laboratory (ANL) and Oak Ridge National Laboratory (ORNL) [4][36]. SESAME project supports the development of the LMFR technologies identified within the European Sustainable Nuclear Industrial Initiative (ESNII):

- ASTRID (Advanced Sodium Technological Reactor for Industrial Demonstration): the sodium-cooled fast neutron industrial demonstrator [37];
- ALFRED: the European scaled demonstrator of the LFR technology [38];
- MYRRHA (Multi-purpose hYbrid Research Reactor for Hightech Applications): the flexible experimental accelerator driven system (ADS), developed at SCK-CEN (Research Centre for the Applications of Nuclear Energy), Belgium [39].

In this framework, SESAME project addresses the pre-normative, fundamental and safety-related challenges of these reactors, mainly focusing on the thermal-hydraulic issues and the advanced modelling capabilities to predict such phenomena. The main objectives of the project are listed below[4]:

- development and validation of advanced numerical approaches for the design and safety evaluation of advanced reactors;
- achievement of a new or extended validation base by creating new reference data;
- establishment of best practice guidelines, verification and validation methodologies and uncertainty quantification methods for LMFR thermal-hydraulics.

In the national context, the R&D efforts are mainly dedicated on the development of the LFR technologies. Three main partners are involved in this challenge: ENEA, CIRTEN (Interuniversity Consortium for Technological Nuclear Research) and the industrial partner ANSALDO NUCLEARE. Strong collaboration and comparing among the three partners are devoted to the development of the reference LFR project: ALFRED reactor. In this framework, ENEA acquired an extended knowledge base, developing, designing and building a large experimental complex dedicated to the investigation of LFR typical issues. Strong collaboration has been established in these years

between ENEA Brasimone RC and DIAEE of “Sapienza” University of Rome. Form 2015, UNIROMA1 is involved in the definition, operation and understanding of the experimental campaign performed in CIRCE (CIRColazione Eutettico) facility. Moreover, ENEA, in collaboration with CIRTEN and ANSALDO NUCLEARE, establishes the Programmatic Agreement with the Italian Ministry of the Economic Development to promote research activities for the improvement of the reliability and the quality of the Italian electrical system. DIAEE of “Sapienza” University of Rome was involved in different topics, including the development of LFR technology [40].

1.7 Structure of the document

The present document is divided in seven chapters, basically individuating five macro-sections.

The first one, identified by chapter 1, is dedicated to the definition of the general background of the research activity. The role of the liquid metal technologies in the nuclear engineering is presented and the main challenges related to the innovative system developments are introduced. After that, the chapter provides an overview of the outcomes available in literature, regarding the modelling guidelines for the simulation of innovative nuclear systems, and of the international and national framework in which the present research activity is focused.

The second section includes chapter 2, 3 and 4. It is basically focused on the validation of RELAP5-3D© STH code for the applications on innovative LM-cooled fast reactors and related safety systems, comparing simulation results with available experimental data. The three chapters have similar structure: at first, the facility and the experimental campaign are presented, then the modelling solutions and the simulation results are analyzed, and finally the main outcomes of the validation activity are summarized.

The know-how acquired in the validation activity, has been applied to support the design of the LFR demonstrator. This topic is examined in the third section (chapter 5). This chapter is basically divided in two subsections: the first one analyzes the reference configuration of ALFRED and the second one deals with the revised configuration of the reactor.

Chapter 6, the fourth section, presents a methodology for the uncertainty quantification, based on the coupling approach between RELAP5-3D and RAVEN codes. The qualification of the methodology has been performed using experimental data from a loop-type LM facility. At first, the experimental section is presented. After that the modelling approach is introduced and the main outcomes of the activity are summarized.

Finally, the main results and guidelines, as well as the weaknesses and the future perspective coming out during the present research activity, are pointed in chapter 7.

2 COMPUTATIONAL ACTIVITY ON CIRCE POOL FACILTY

2.1 CIRCE-ICE computational activity

The numerical activity has aimed to evaluate the capability of RELAP5-3D© to reproduce the main thermal-hydraulic phenomena in a heavy liquid metal (HLM) pool-type facility, in different operative conditions. For this purpose, the experimental campaign performed in CIRCE-ICE (Integral Circulation Experiment) test facility has been selected for the code assessment. Two experimental tests have been analyzed: TEST A consisting in a transition from no-power to full power steady-state conditions, and TEST I, consisting in a transition from gas-enhanced circulation to natural circulation, simulating a protected loss of heat sink plus a loss of flow accident. Three different pool modelling approaches are assessed: single vertical pipe, parallel pipes with cross junctions and multi-dimensional component. The comparison with experimental data has highlighted the need to divide the large pool in several sections to reproduce the natural convection, strictly correlated with thermal stratification. Multi-dimensional component seems to be the best practice for the evaluation of this phenomenon even if the lack of specific correlation for heat transfer coefficient in quasi-stagnant conditions in large tanks is a limit for the accuracy of the results. In addition, the research work presents a detailed nodalization of the fuel pin bundle, highlighting quite good capabilities of RELAP5-3D as a subchannel analysis code [42].

2.1.1 Description of the test facility

CIRCE is a multifunctional pool-type facility aimed to investigate innovative HLM systems. The facility consists of three tanks: the main vessel and two auxiliary tanks (respectively S100, S200 and S300 in Figure 2). The main vessel, filled with about 70 tons of molten LBE, has been designed to host different test sections (TSs), welded to and hung from the bolted heads. It is characterized by the outer diameter of 1200 mm and the height of 8500 mm and the whole surface is thermally insulated, except for the cover head. The auxiliary tanks are needed to store LBE during the maintenance phases and to provide an expansion volume during the loading and the drainage phases [43].

Figure 3 depicts ICE test section, installed within the main vessel of CIRCE facility to reproduce the primary system of an HLM-cooled pool-type reactor. The main components are identified in Figure 3 where the primary main flow path is represented by the arrows (hot LBE in red and cold LBE in blue). Cold LBE enters the test section through the feeding conduit, at the bottom of the facility. The feeding conduit is equipped with a Venturi-nozzle flow meter to measure the LBE mass flow rate entering the heat source (HS). The LBE moves inside the fuel pin simulator (FPS) crossing the lower grid (see Figure 4). The FPS is composed of 37 electrically heated pins. It is divided into three axial regions (see Figure 5), individuated by three spacer grids positioned between the bottom mixing zone and the active length inlet (in red in Fig. 1), at the middle of the HS and between the active length outlet and the upper mixing zone. The heat source consists of an electrical pin bundle characterized by a nominal thermal power of 800 kW and an active length of 1000 mm. Each pin, characterized by the outer diameter of 8.2 mm, supplies a thermal power of 25 kW and a heat flux at the pin wall of 1 MW/m2. Rods are arranged in a wrapped hexagonal lattice with a pitch to diameter ratio (*p/d*) equal to 1.8 and they are kept in positions with the lower grid, three spacer grids and an upper grid, that operates as the FPS cap. The upper grid forces liquid metal to exit the FPS through six lateral holes, moving inside the fitting volume, a large component which collects the hot LBE and guarantees the connection between the HS and the riser. The riser is a double wall pipe insulated with air gap in order to reduce the heat losses towards the pool. A nozzle is installed at the riser inlet to inject argon (Ar) inside the molten metal, enhancing the circulation of the primary coolant. The argon pipe line descends through the LBE pool, passing through the facility cover head. The mixture Ar-LBE flows upward and it is collected inside the separator, which is the upper component of the test section. The separator operates as a hot pool and it has two main functions: to allow the separation of the mixture and to provide the expansion

volume. Argon moves upward towards the gas plenum and the molten LBE enters the heat exchanger (HX). Figure 7 shows the radial and azimuthal disposition of the primary main components. The riser outlet and the HX inlet are included inside the separator. The FPS is positioned below the dead volume allowing the passage of the power supply rods which feed the HS. The dead volume consists of two concentric pipes thermally insulated with a non-conductive material which partially fills the annular volume between the two pipes. Because of the power dissipated by Joule effect, a dedicated air-cooling system is adopted and included inside the inner pipe [44].

The heat exchanger is composed of 91 water-cooled bayonet tubes, arranged in a triangular bundle (*p/d* equal to 1.22) and characterized by an active length of 3462 mm. LBE flows downward through the free volume between the cylindrical shroud and the tubes, decreasing the temperature. Figure 8 shows a schematic view of the bayonet tube, composed of three concentric tubes; feedwater (FW) enters the unit at the inner tube top edge, it flows downward reaching the lower plenum of the bayonet element and then it flows upward through the annular riser. The volume between second and third tube is filled with pressurized helium to detect any leakage or rupture.

The decay heat removal (DHR) system is submerged in the pool, as shown in Figure 3 and Figure 7. The DHR is composed of one air-cooled bayonet tube included inside a double wall insulated shell with a thin air insulation gap to reduce heat losses towards the pool. LBE enters the unit through six inlet holes obtained at the upper zone of the shell and then it flows downward.

The test facility is monitored with several thermocouples (TCs) to investigate the thermal behavior of the LBE loop. For this purpose, the FPS is equipped with 36 TCs arranged at seven axial levels. Two series of penetration are obtained at both inlet and outlet levels of the HS active length to measure the temperature difference across three subchannels; in addition, four different sections are monitored: 60 mm downward the lower spacer grid, 20 mm upward the middle spacer grid, on the mid plane of the middle spacer grid and 60 mm upward the upper spacer grid. In each section, the temperature of three different subchannels is acquired. The temperature of the pin outer wall is also monitored in different axial levels (18 TCs). Flowing through the primary flow path, the LBE temperature is measured at inlet and outlet of the riser and the HX [45].

One of the main tasks of the experiment was to study mixing convection and thermal stratification inside the pool. For this purpose, 119 TCs are installed on 9 vertical rods arranged inside the pool (from A to I in Figure 7), measuring LBE temperature in 17 axial levels along the pool. The axial positions of the thermocouples installed in the B rod are individuated in Figure 3 by red points. As shown, the TCs disposition is intensified between the HX and DHR outlets, where a relevant thermal stratification was expected to occur. In addition, LBE temperature at the inlet and outlet sections of the DHR is acquired with 12 TCs [45].

The evaluation of the thermocouple measurement uncertainties is presented in Ref. [46], where the global uncertainty is considered composed of the instrument uncertainty and the standard deviation of the temperature measurement. The same approach has been adopted in this research work. In addition, calibration and accuracy estimation of the Venturi flow meter were analyzed in a previous experimental campaign, described in Ref. [47] and [48]. For LBE mass flow rate around 50 kg/s, a relative error of about 25% was evaluated.

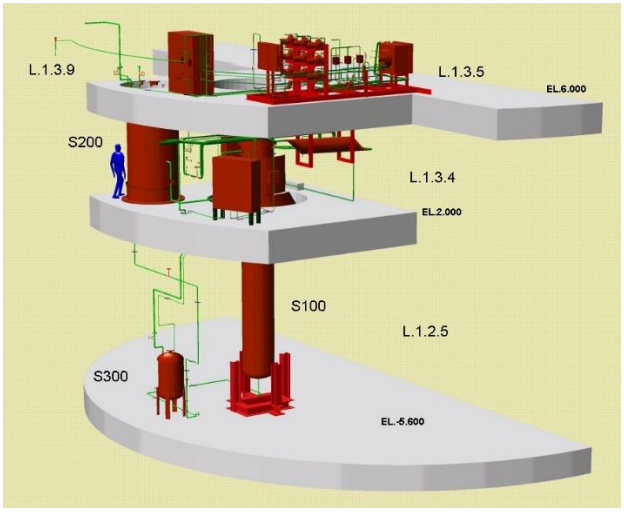

Figure 2. CIRCE facility

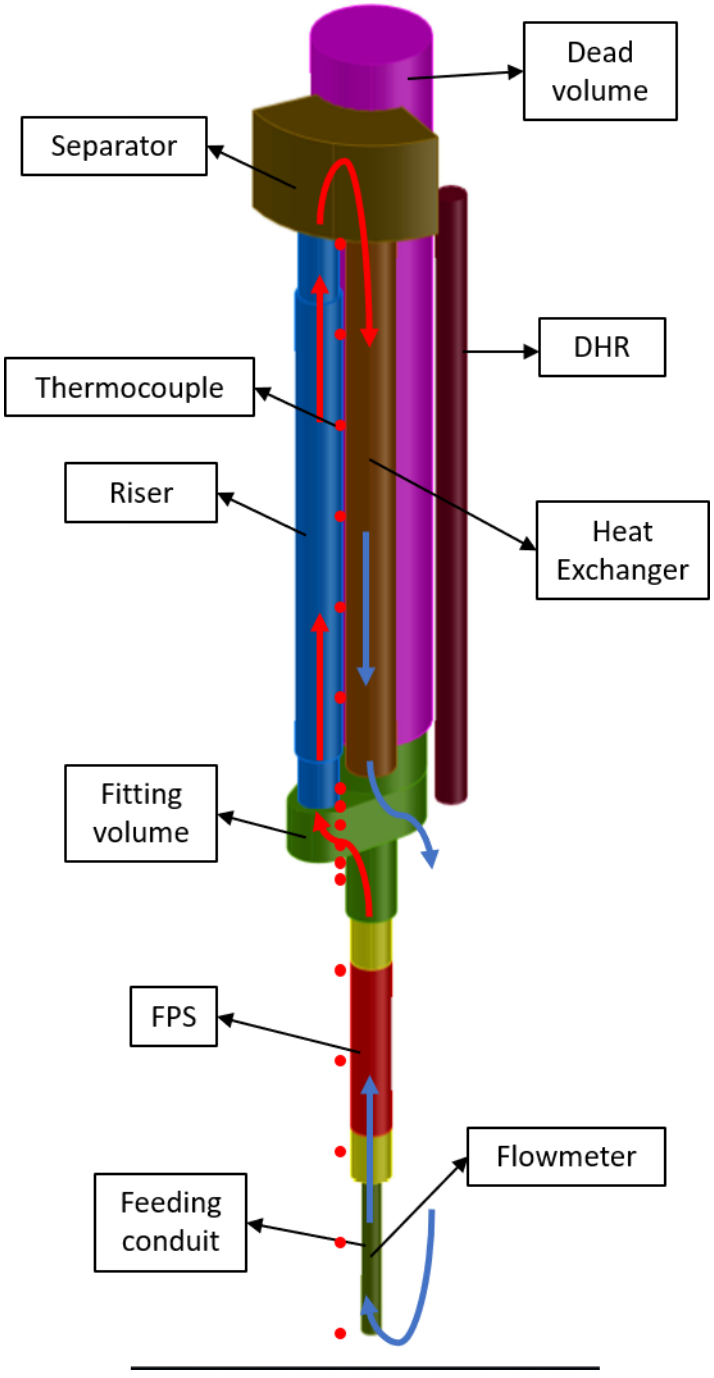

Figure 3. CIRCE-ICE test section

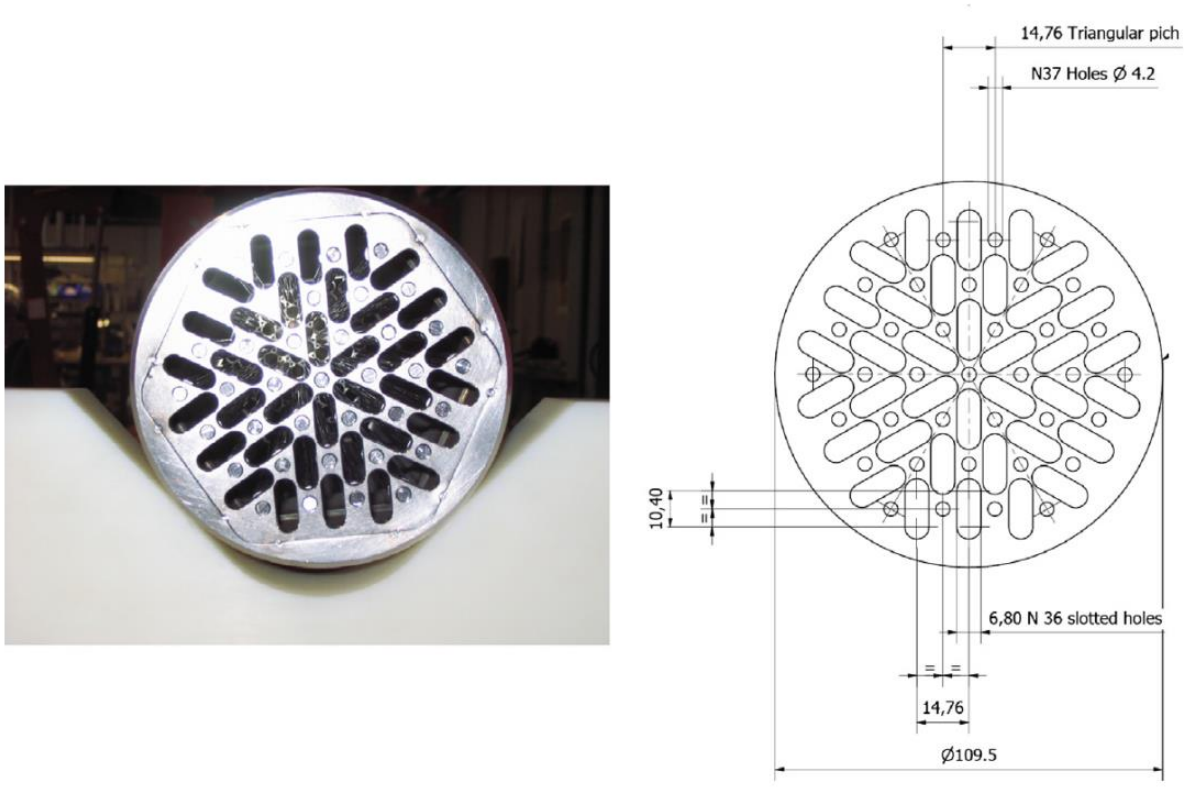

Figure 4. Lower grid

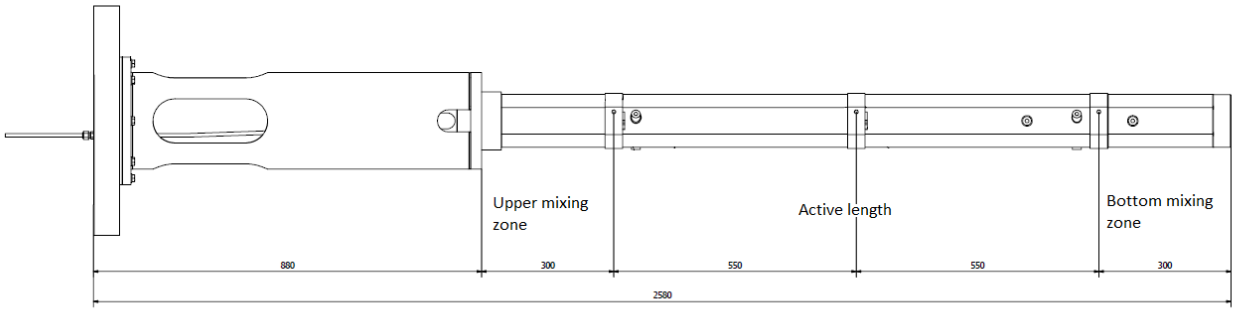

Figure 5. Fuel Pin Simulator: axial division

Figure 6. Spacer grid

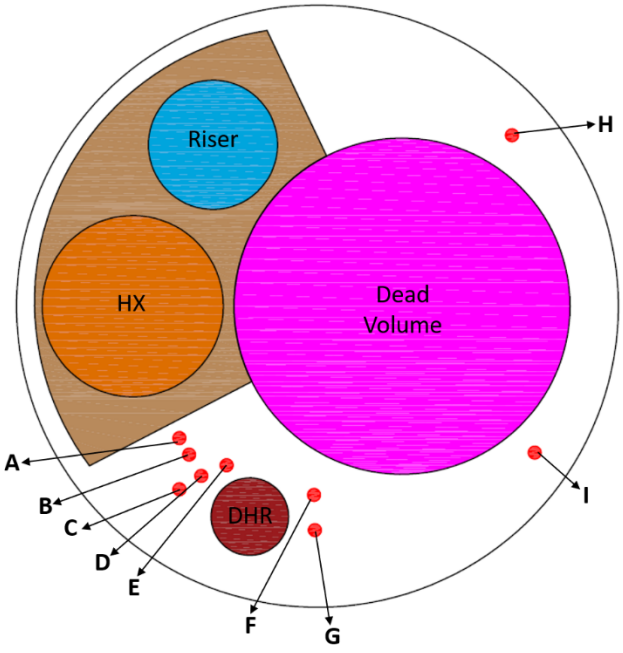

Figure 7. Disposition of the main components

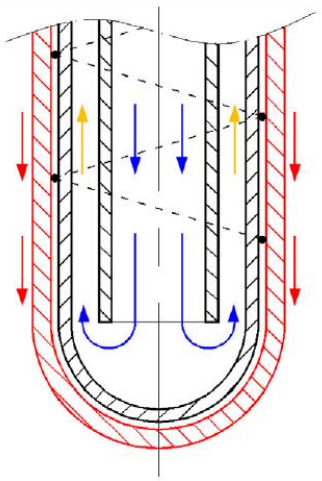

Figure 8. HX bayonet tube

2.1.2 Overview of the experimental campaign

The objective of the experimental campaign was to investigate the main phenomena occurring in an HLM pool. Two tests have been considered in this research activity: TEST A [49] and TEST I [45].

TEST A starts in steady-state conditions, with the FPS turned-off and injection of Ar and feedwater disabled. After about 600 s, argon is injected inside the test section and, after a delay time of about 500 s, the FPS starts to supply thermal power reaching the nominal value of 800 kW in 180 s. After the achievement of the full power, feedwater starts to flow into the secondary loop, reaching a mass flow rate of 0.6 kg/s. The boundary conditions are maintained constant for the duration of the test.

TEST I consists in a protected loss of heat sink (PLOHS) plus loss of flow (LOF) simulating the total loss of primary flow, the loss of secondary circuit, the consequent SCRAM of the reactor and the activation of the DHR system. It aims to analyze the transition of thermal stratification inside the pool, passing from gas-enhanced circulation (GEC) to natural circulation (NC) conditions. The test starts in no-power steady-state conditions; after 450 s, argon is injected to obtain a “forced” circulation condition and the FPS is activated after a delay time of about 470 s. Full power of 730 kW is obtained at 1100 s and, at this time, FW starts to circulate inside the secondary loop. These conditions are maintained for 25000 s, when the transition from GEC to NC occurs. The accident is reproduced reducing to zero argon injection and feedwater circulation. The HS thermal power decreases to 7% of the nominal value, following a typical decay heat curve for an HLM-cooled fast reactor and the DHR secondary side is fed by 0.223 kg/s of air.

The chronology of the two tests is summarized in Table 2.

Table 2. Experimental tests: time events

Full power calculation		
Test	**Event**	**Time (s)**
A	Ar injection	600 → END
	FPS power ramp	1100 → 1280
	FPS full power	1280 → END
	FW injection	1280 → END
I	Ar injection	450 → 25400
	FPS power ramp	920 → 1100
	FPS full power	1100 → 25300
	FW injection	1100 → 25400
Transient calculation		
Test	**Event**	**Time (s)**
I	Ar injection disabled	25400 → END
	FW disabled	25400 → END
	FPS power ramp	25300 → 25430
	FPS decay heat value	25430 → END
	Air Injection	25440 → END

2.1.3 Description of the thermal-hydraulic model

The activity aims to investigate the capability RELAP5-3D© to reproduce the main thermal-hydraulic phenomena occurring in an HLM pool-type facility. To assess R5-3D ability, a mesh sensitivity analysis was carried out, including both the main flow path and the pool of the facility. The mesh influence on the calculations is presented in section 2.1.5.1. In the present section, two basic nodalization approaches are presented and the main results are discussed in section 2.1.4.

The first geometrical scheme (model #1) consists of a mono-dimensional model of the whole facility. The nodalization is shown in Figure 9. The model includes each component described in section 2.1.1 and they are reported with different colors in Figure 9. The feeding conduit (in green) is simulated using a pipe component, in which the Venturi flow meter is reproduced with a local pressure drop coefficient, dependent on the flow conditions [41] and validated in previous computational activity [50]:

$$K_{Venturi} = 10.5\, Re^{-0.016} \tag{1}$$

where *Re* is the Reynolds number evaluated in the feeding conduit. The grids installed in the test section are also simulated with local pressure drops coefficients, evaluated with the Rehme correlation [51]:

$$\Delta p_{grid} = C_v \cdot \varepsilon^2 \cdot 0.5 \cdot \rho \cdot v^2 \tag{2}$$

where *ρ* and *v* are respectively fluid density and velocity and ε represents the grid flow blockage factor, calculated as:

$$\varepsilon = \frac{A_{grid}}{A_{flow}} \tag{3}$$

The C_v parameter is a modified drag coefficient, calculated as:

$$C_v = MIN\left[3.5 + \frac{73.14}{Re^{0.264}} + \frac{2.79 \cdot 10^{10}}{Re^{279}}, \frac{2.6}{\varepsilon^2}\right] \tag{4}$$

The fuel pin simulator is reproduced with a single equivalent channel, axially divided into an appropriate number of volumes to individuate the FPS main regions and to compare the calculated LBE temperature in the correct TCs axial positions: 3 volumes for the bottom mixing zone (in yellow), 8 for the active length (in red) and 5 for the top mixing zone (in yellow). The active region is thermally coupled with 8 heat structures reproducing the thermal power supplied by the 37 pins (in total 80 active nodes). The HS thermal power is fixed with a general table as boundary condition. In addition, 6 heat structures simulate the heat losses through the FPS hexagonal shell, considering an equivalent cylindrical geometry in which inner and outer diameters are calculated to preserve the thermal inertia of the hexagonal duct, and the active length of each heat structure is evaluated to obtain the correct heat exchange area. The default correlation for the evaluation of the HTC coefficient in bundle geometries is the Westinghouse correlation [41]:

$$Nu = 4.0 + 0.33\left(\frac{p}{d}\right)^{3.8}\left(\frac{Pe}{100}\right)^{0.86} + 0.16\left(\frac{p}{d}\right)^{5} \tag{5}$$

where *Nu* represents the Nusselt number. The correlation was obtained in the ranges of 1.1<*p/d*<1.4 and 10<*Pe*<5000; this means that FPS *p/d* is out of validity range. In addition, Westinghouse correlation underestimates the HTC for *p/d* higher than 1.2 [52]. According to the state of art, a better estimation of the HTC was found with Ushakov correlation [53]:

$$Nu = 7.55\frac{p}{d} - 20\left(\frac{p}{d}\right)^{-13} + \frac{3.67}{\left(90\frac{p}{d}\right)^{2}} Pe^{\left(0.56+0.19\frac{p}{d}\right)} \tag{6}$$

In CIRCE-ICE operational temperature and velocity, the two correlations show a similar gradient of *Nu* versus *Pe*; for this reason, it is possible to calculate a constant value of the ratio between Ushakov and Westinghouse correlations, equal to 1.2. This multiplicative factor has been applied to the HTC evaluated by the code on the LBE side of the FPS active length, as described in [54].

For non-bundle geometry, Seban & Shimazaki correlation is applied [41]:

$$Nu = 5.0 + 0.025Pe^{0.8} \quad (7)$$

A vertical pipe is used to model the connection between the HS and the fitting volume. This latter component plays a relevant role for the pool thermal stratification. In fact, the fitting volume provides a large not insulated heat transfer area between the inner hot region and the cold pool, allowing a large amount of heat losses. A sensitivity study was carried out modelling the fitting volume with a single volume and with a horizontal pipe with variable flow area (in green in Figure 9). The analysis highlighted that the second approach allows a better simulation of the flow path inside the component, providing an improved evaluation of the heat transfer coefficient. As presented in Ref. [50], a single volume cannot reproduce the LBE flow condition within the fitting volume, underestimating the HTC inside the component. This causes a large underprediction of the temperature in the middle of the pool, failing to reproduce the qualitative temperature profile. The riser (in blue) is modelled with a vertical pipe composed of 26 control volumes. The gas lift system is simulated with a time-dependent junction, connected with the bottom of the riser, which sets the argon flow rate injected inside the test section; the gas conditions are defined with a time-dependent volume. In the upper part, the separator operates as a hot pool, allowing the separation of the two fluids. Due to the large difference in density between molten LBE and argon, the fluctuation of the free surface produces oscillations in the LBE mass flow rate calculated by R5-3D. A sensitivity study was performed regarding the modelling approach applied to the separator, in order to reduce the mass flow spikes. Different methods were investigated: a single vertical pipe, two, three and four parallel vertical pipes with cross junctions, and a MULTID component. The analysis highlighted that a single pipe allows to damp the large oscillations of the primary mass flow rate, but this approach cannot reproduce the fast free level decrease occurring in the first seconds after the transition from GEC to NC. Using multiple parallel pipes and cross junctions, the buoyancy inside the large component is better simulated, allowing the free surface movement. However, this solution causes mass flow fluctuations when the free level passes through two contiguous volumes; the oscillations increase with the number of parallel pipes and adopting the MULTID component. For this reason, two parallel pipes, connected with cross junctions, were adopted and the effect of the axial meshing was assessed, highlighting that a coarse vertical division reduces the mass flow spikes, limiting the number of free level passage between contiguous volumes. The separator is connected upward with the gas plenum, composed of a vertical pipe where the cover gas pressure is fixed by a time-dependent volume above the pipe, and downward with the HX. Primary side of the heat exchanger is modelled with a single equivalent pipe composed of 22 control volumes (in orange), reproducing the HX subchannels. On the secondary side, the 91 bayonet tubes are represented with two equivalent tubes, modelling the descending and the ascending side of the bayonet element (in yellow). Two time-dependent volumes impose the FW inlet temperature and the mixture outlet pressure, and the secondary mass flow rate is set by a time-dependent junction. The HX primary and secondary sides are thermally coupled with 24 heat structures (744 heat transfer nodes). As described for the HS bundle, for the evaluation of the LBE side HTC, a multiplicative factor, equal to 1.02, is applied. In addition, 31 heat structures (310 thermal nodes) simulate the heat exchange between the descending and the ascending secondary side and other 46 heat structures (460 nodes) the heat losses between the HX and the LBE pool.

The DHR is immersed inside the pool; its modelling (in red) consists of a single pipe for the LBE side and two pipes for the secondary side. Two time-dependent volumes set air inlet temperature and outlet pressure, and a time-dependent junction imposes the air mass flow rate. An overall number of 174 heat structures reproduce the heat removed by the system, the heat losses towards the pool and the heat exchange between the descending and the ascending secondary side.

As presented in section 1.3, multiple channels with crossflow junctions are needed to reproduce multi-dimensional flow effects in large pools. The presence of the cross junction in each volume does not allow the application of the R5-3D thermal stratification model and a detailed axial discretization is required for the evaluation of phenomena such as thermal stratification. For this purpose, CIRCE pool is modelled with three parallel pipes, dividing the tank into three sections as shown in Figure 10. Each pipe is divided in 52 control volumes. The axial mesh sizing follows the flow path nodalization, in accordance with the sliced modelling approach and the vertical stratification model is applied in all the vertically oriented volumes. Furthermore, this geometrical scheme allows the comparison of the calculated LBE temperature in the correct axial positions of the TCs installed inside the pool.

In a large pool, the liquid is free to flow in all directions, depending on the pressure gradient. In order to reproduce the horizontal flow, 156 cross junctions connect adjacent volumes at same axial levels. The junction area is equal to the flow area in the cross direction per each level. The pressure gradient between adjacent pipes is calculated by R5-3D; no form loss coefficients are included in the cross junctions modelling.

The heat losses from the primary flow path towards the pool are completely simulated. Moreover, the heat dissipations through the vessel walls are considered assuming a constant temperature of the external environment and imposing a constant HTC on the outer wall of the insulator.

Mesh and time step sensitivities were carried out. The mesh sensitivity analyzed the effect of FPS, riser and HX axial discretization on the accuracy of the solution. Three calculations were performed, assuming control volumes mean length equal to 100, 150 and 200 mm, highlighting negligible differences. The results of the study will be presented in section 2.1.5.1. Regarding the pool, Ref. [20] highlighted that the effect of the axial discretization on the accuracy of solution is minimal and a sufficiently fine meshing permits a good evaluation of the thermal stratification. For this purpose, CIRCE-ICE model presents a very fine nodalization along the axial coordinate, following the primary flow path discretization, in accordance with the sliced modelling approach.

The time step sensitivity study was carried out assuming three different values of the maximum time step size: 0.005, 0.002 and 0.001 s. Negligible effects were highlighted proving that this parameter does not affect the accuracy of the results. The analysis will be presented in section 2.1.5.1.

The second geometrical scheme (model #2) aims to investigate more accurately the fuel pin simulator and the pool. The main primary flow path is the same as the previous nodalization, except for the FPS, that is reproduced with all the actual subchannels, and the pool, in which a multi-dimensional component substitutes for the three parallel pipes.

Figure 11 shows the scheme of the HS modelling. The whole model consists of 72 parallel channels reproduced with pipe components. Three different channel types are defined: inner subchannels (54), edge subchannels (6) and corner subchannels (12). Each subchannel maintains the axial division presented in model #1 but the flow area and the equivalent diameter has been evaluated considering the geometry presented in Figure 11. As described in Ref. [27], cross-flow represents a crucial aspect for the correct evaluation of the coolant temperature. Cross-flow depends on the pressure gradients between adjacent subchannels, and on the hydraulic resistance. In order to evaluate the mass transfer between subchannels, 1536 cross junctions are included in the FPS modelling, connecting adjacent subchannels for each axial level. Junction area is calculated as the lateral flow area between two adjacent pins for each level. The pressure gradient is evaluated by RELAP5-3D, while the hydraulic resistance is introduced as a local pressure loss coefficient depending on flow regimes. Equation proposed in Ref. [55] for the calculation of the form loss coefficient for bundle of staggered rods was used:

$$K_{CF} = \left(z_p + 1\right) \cdot [3.2 + 0.66 \cdot (1.7 - \bar{s})^{1.5}] \cdot \varphi \cdot Re^{-0.27} \quad (8)$$

where z_p is the number of ranks, φ is the flow direction coefficient defined as:

$$\varphi = \frac{\theta}{90°} \quad (9)$$

where θ is the angle between the cross-flow direction and the inclination of the rods. The parameter $\bar{s}$, introduced in Eq. 8, is the pitch ratio, equal to 1 in the FPS geometrical configuration. In accordance with Eq. 8, the form loss coefficients, dependent on flow conditions, are introduced in the model as:

$$K_{CF} = 7.17 \cdot Re^{-0.27} \quad (10)$$

The thermal power, provided by the electrically heated pins, is reproduced with 576 heat structures (5760 heat transfer active nodes), supplying the power proportional to the heat transfer area of the control volumes that compose the active zone. As for model #1, the multiplicative factor is applied to the HTC within the HS. In accordance with the experiment, the power distribution is considered flat. In addition, 432 passive heat structures (1728 thermal nodes) reproduce the heat dissipation through the hexagonal shell, coupling edge and corner subchannels with the volume between the hexagonal and the cylindrical shells.

In section 2.1.5.2, thermal conduction effect between adjacent subchannels is analyzed. At full power operation, conduction effect is negligible but, at low mass flow rate (typically in natural circulation condition), thermal conduction must be considered. For this purpose, 1152 heat structures (3456 nodes) simulate the heat transfer between adjacent subchannels, assuming a dummy material with negligible heat capacity and LBE thermal conductivity. A high HTC multiplicative factor is applied to practically exclude the convective resistance on the evaluation of the heat transfer.

The second improvement, introduced into the model #2, is the MULTID component, which simulates the pool of the facility (see Figure 12). The model consists of 4 radial meshes (r- coordinate), 8 azimuthal intervals (theta-coordinate) and 51 axial levels (z- coordinate). Nodalization scheme in r- and theta- directions is highly dependent on the positions of the thermocouples (see Figure 7) and on the test section asymmetry, as shown in Figure 12, where cross section at 7 relevant axial levels are reported showing the volume occupied by the internals. In accordance with the sliced approach, that should be applied in the modelling of parallel channels to reduce unphysical oscillations, the nodalization along the z-direction follows the mono-dimensional mesh of the primary flow path, in order to place the center of the corresponding volumes at the same height. The meshing along z-coordinate allows the acquisition of the LBE temperature in the “real” position of the thermocouples. Volume factors, defined as the ratio between the real free volume and the mesh original volume, are introduced to consider the volume occupied by the test section. In the same way, junction area factors are calculated for the flow area evaluation in three directions. In order to limit the wall friction in free volumes inside the MULTID component, a high equivalent diameter is introduced when fluid is free to move without interaction with walls.

The whole heat losses between test section and LBE pool are considered. Several heat structures are introduced, coupling each component of the 1D model with the corresponding pool zone. In addition, the heat losses towards the external environment are considered, applying the same boundary conditions of model #1.

Models dimensions and relative calculation times are summarized in Table 3. Models #1 and #2: main parameters. The calculation time is related to a single core of an Intel® Xeon® E5-2690 v4 @3.22 GHz used in both calculations, adopting a time step equal to 0.005 s for the calculations.

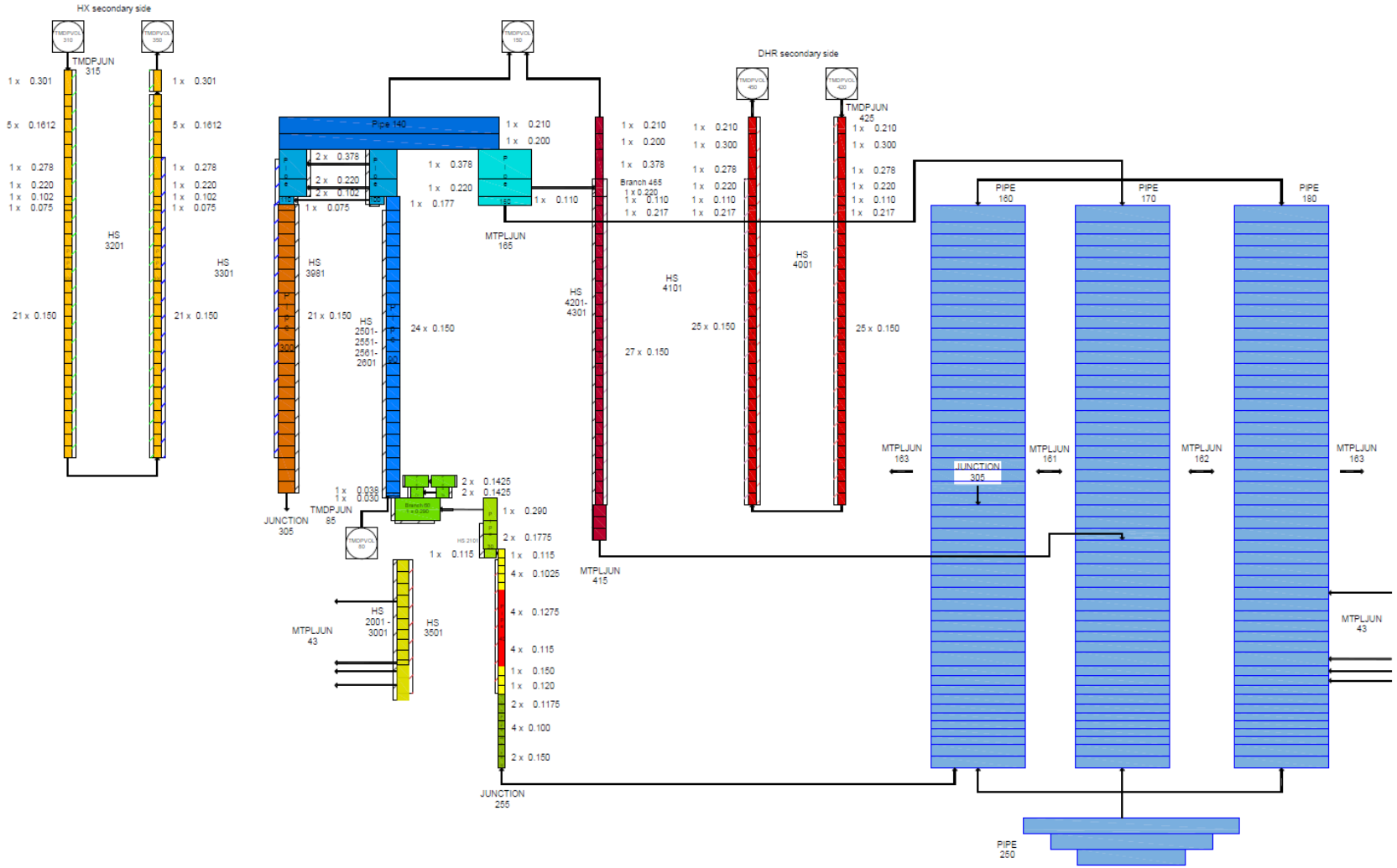

Figure 9. CIRCE-ICE nodalization scheme: model #1

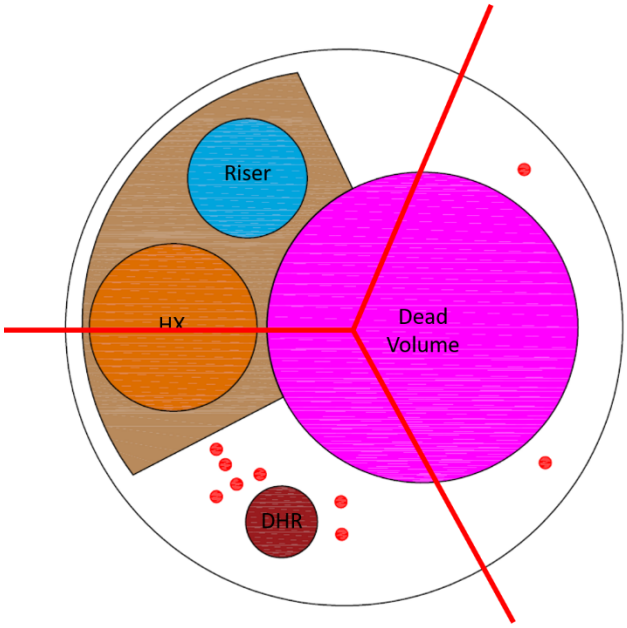

Figure 10. Pool modelling approach: model #1

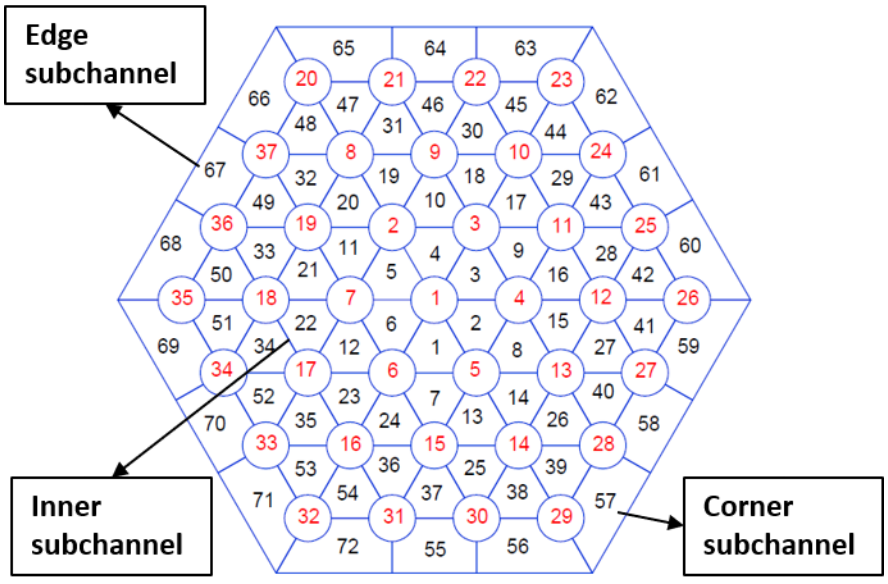

Figure 11. FPS nodalization scheme: model #2

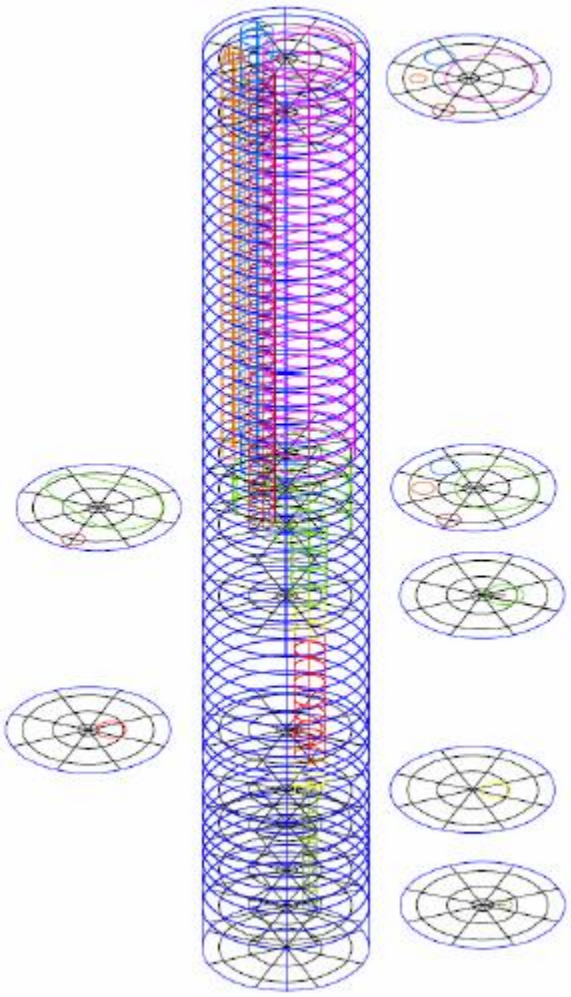

Figure 12. MULTID component: model #2

Table 3. Models #1 and #2: main parameters

Parameters	Model #1	Model #2
Number of hydrodynamic volumes	355	1929
Number of hydrodynamic junctions	409	4856
Number of heat structure mesh points	3828	15353
Mean calculation time (CPU time / problem time)	8.5	60

2.1.4 Simulations results

The calculations analyzed in this section have been performed using the most recent LBE thermophysical properties correlations, recommended by NEA [56] and implemented in R5-3D during a research activity performed at DIAEE and described in Ref. [57]. Concerning the MULTID component, the three-dimensional momentum equations are used.

2.1.4.1 Test A

Boundary conditions, described in section 2.1.2, are shown in Figure 13, where the reproduced values (black lines) have been compared with the experimental data (red dotted lines). Test A starts at no-power steady-state conditions. Figure 13 (a) and (c) show that, at the beginning, the experimental measurement system acquires no-zero values for argon and feedwater flow rate (0.35 Nl/s and 0.1 kg/s respectively), due to instruments signals, which are at digital full scale. For this reason, the simulated inlet flows are set to zero. When Ar injection system is activated, the reproduced value increases to the nominal flow rate, neglecting the peak during the first minutes of the transient.

Figure 13 (b) compares the experimental electrical power supplied to the FPS with the simulated HS thermal power. As presented in Ref. [24], the simulated value has been reduced to 95% of the nominal power, taking into account the dissipations which occur in the cables and connectors of the outer circuits, that do not contribute to the thermal power supplied to the primary coolant. The thermal power supplied to LBE is equal to Joule heat production along the nickel-chrome wires that compose the FPS active length [45]. The amount of the dissipations in the cables of the outer circuits has been estimated from the circuit length and electrical resistivity.

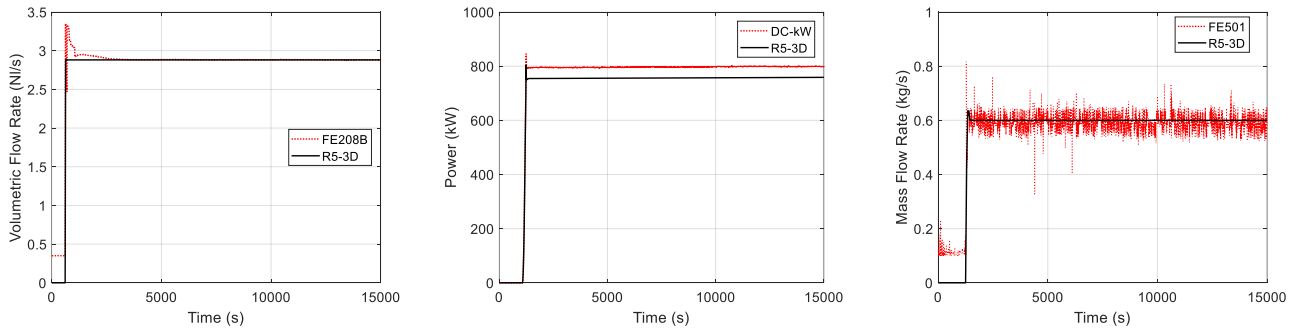

(a) Ar injection (b) FPS Power (c) FW mass flow rate

Figure 13. Test A: boundary conditions

In next figures, simulation results are compared with experimental data, which are reported with their uncertainties bands (dotted line). The experimental data have been smoothed with Savitzky-Golay filter [58]. The standard deviation of the measurements has been included in the global uncertainties, as proposed in Ref. [46].

In Figure 14, the LBE mass flow rate acquired by the flow meter (FM), reported in red line, is compared with the flow rate predicted by the two models in the actual position of the instrument. After the activation of Ar injection system, the primary mass flow rate reaches a value of 62 kg/s, maintained until the heater activation, which occurs at 1100 s. At this point, the mass flow increases up to 65 kg/s, due to the natural circulation contribution. As shown in Figure 14, the models provide a good estimation of the LBE flow rate, in both gas enhanced and gas enhanced plus natural circulation, proving the capability of the two geometrical schemes to reproduce the argon-induced natural circulation and the pressure drops of the whole primary system at high values of Re. After the FPS activation, adopting the model #1, oscillations of the LBE mass flow are highlighted, due to the instantaneous NC contribution, that is damped down in 2000 seconds. This phenomenon is not predicted by the model #2, which allows the mass transfer between the HS subchannels, providing an instantaneous attenuation of the effect.

Figure 15 compares the LBE temperature measured by the TCs at the HS inlet and outlet with the simulated values. At the FPS inlet, liquid metal temperature is uniform; for this reason, the calculated values are compared with a single experimental data. At the active length outlet, experiment highlights significant no-uniform distribution of the temperature due to the larger LBE mass flow in the edge and corner subchannels, because of a larger flow area. In addition, heat losses through the hexagonal shell enhance this difference.

Temperatures acquired by two thermocouples at the HS outlet (T-FPS 34 and T-FPS-36) are reported. As exposed in section 2.1.3, the FPS nodalization scheme in model #1 consists in a single equivalent channel providing an estimation of the mean temperature at the HS outlet. Model #2 has been developed to carry out a subchannel analysis, so in Figure 15, the experimental data are compared with the calculated temperature in the exact subchannels (number 12 and 67 in Figure 11). Both models provide a good prediction of the qualitative temperature trends. In particular, model #2 reproduces very well the radial temperature distribution at the active length outlet, proving good capabilities of R5-3D to perform a subchannel analysis in LBE systems. The influence of the thermal conductivity will be presented in section 2.1.5.2.

Figure 16 shows the comparison of the inlet and outlet HX primary side temperature. The temperature difference between HX inlet and FPS outlet provides an evaluation of the heat losses towards the pool. The higher heat dissipations occur inside the fitting volume and the separator, characterized by a large heat transfer area without insulations. The qualitative trend of the HX inlet temperature is well reproduced by the two nodalization schemes, even if model #1 provides a larger estimation of the heat losses through the main flow path walls, underestimating of 5 K the HX inlet temperature, outside the lower limit of the error band. This can be explained by the underestimation of the pool temperature. A comprehensive analysis of the pool thermal-hydraulics will be presented in the following. The temperature drop along the HX is well reproduced by both the models; Figure 16 shows a lower value of the outlet temperature from the experiment but the discrepancy is justified by a not perfect positioning of the outlet control volume, which provides temperature calculation slightly upstream the TCs. The thermal power removed by the HX is compared in Figure 17 and it highlights the good agreement of both simulations.

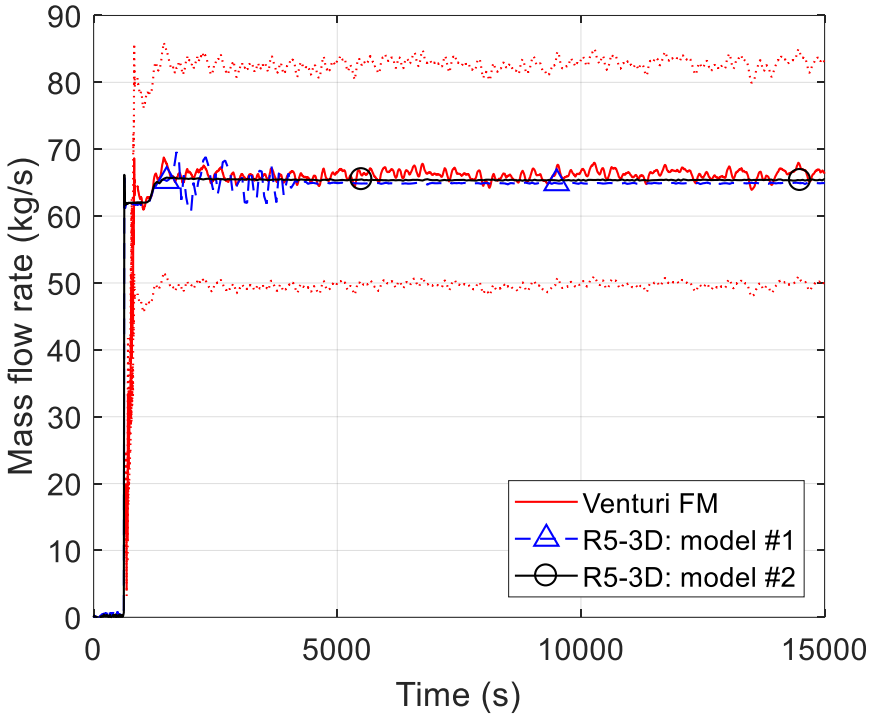

Figure 14. Test A: LBE mass flow rate

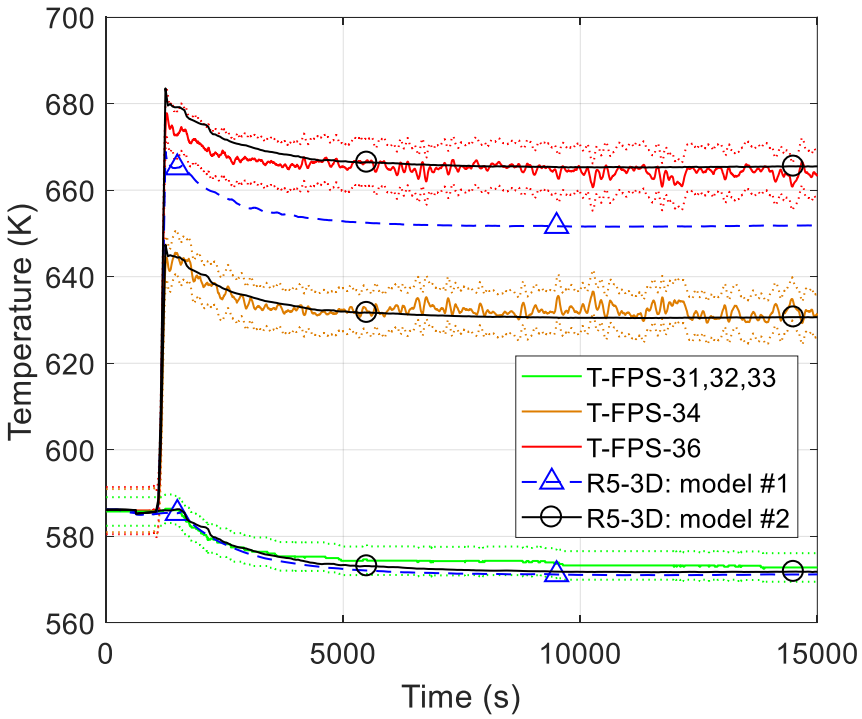

Figure 15. Test A: LBE FPS inlet/outlet temperature

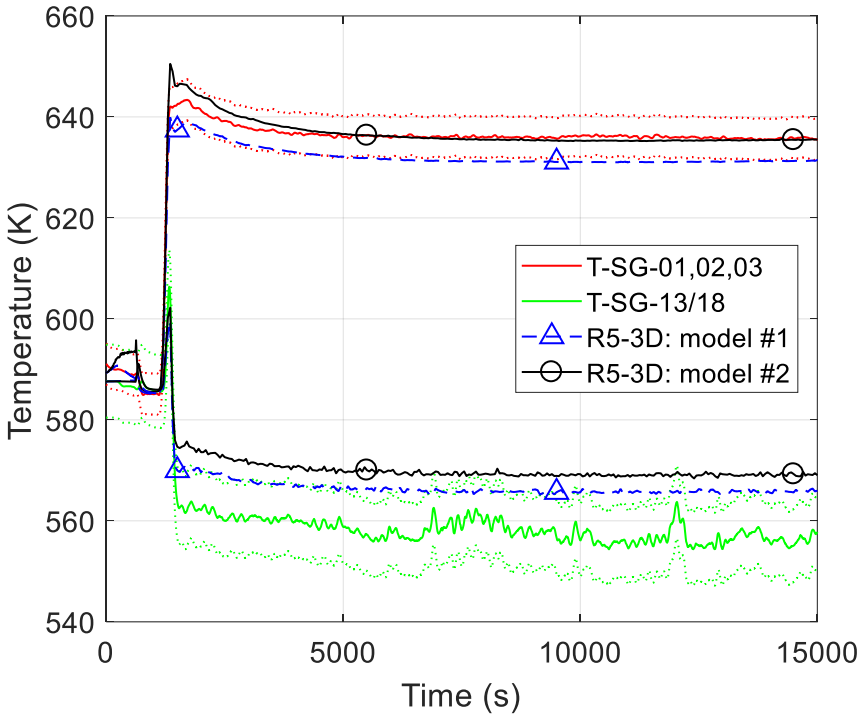

Figure 16. Test A: LBE HX inlet/outlet temperature

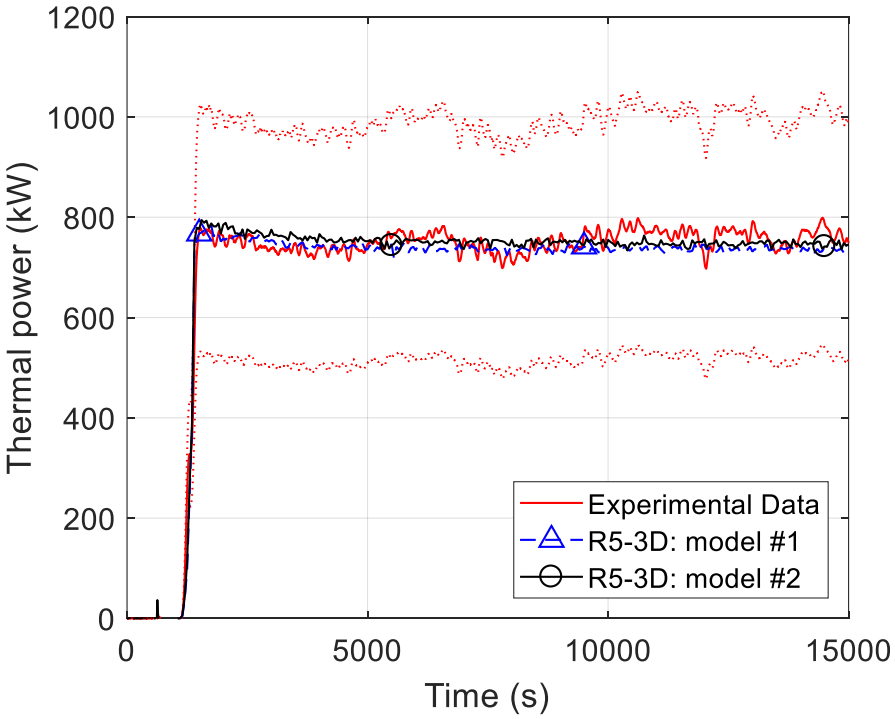

Figure 17. Test A: HX power removed

Next figures aim to evaluate the capability of R5-3D to reproduce the thermal-hydraulics of an HLM pool, adopting two different modelling approaches: a mono-dimensional model, consisting of three parallel pipes and several cross junctions, and a three-dimensional model, using a MULTID component to reproduce the large volumes and adopting three-dimensional momentum equations.

The vertical profile of the LBE temperature is analyzed in four relevant regions: Figure 18 (a) shows the mean value of the measurement in A, B, C, D and E positions, Figure 18 (b) represents the mean temperature acquired by TCs in F and G positions covering the upper part of the pool only and Figure 18 (c) and (d) show the LBE temperature along the H and I supports. In each figure, the error bar is associated to the experimental temperature.

Due to the pool modelling approach in model #1, the temperature trend is the same from Figure 18 (a) to (d), whereas MULTID component in model #2 compares the effective temperature in the four relevant positions.

Experimental data show that at the same axial level LBE temperature is quite uniform while, in the vertical trend, two main stratification phenomena occur at the level of the HX, between 7 to 5.2 m, and of the fitting volume, between 3.5 and 4 m. The heat exchanger is not insulated and the external shell provides a large heat transfer area, cooling the LBE inside the pool. This vertical trend is interrupted at the fitting volume level, where LBE temperature assumes a rather constant value of 592 K. The LBE inside the fitting volume, at about 660 K, warms the liquid metal in the pool, causing this temperature profile. Below the fitting volume, a steep stratification of 20 K occurs and, from 3 m to the lower plenum, the LBE assumes a uniform temperature of 570 K. Figure 18 shows good capability of the two models to reproduce the qualitative temperature trend. Both models are able to predict the two relevant thermal stratifications which occur inside the pool, even if some discrepancies are highlighted. The mono-dimensional modelling approach evaluates well the temperature in the lower part of the pool. Here the LBE temperature is a bit underestimated but discrepancy with experiment is limited within the error band (lower than 3 K). Thanks to the detailed nodalization along the vertical coordinate, the level of the middle stratification is well reproduced (4 m), even if a sharper temperature decrease is predicted. The maximum discrepancy with experimental data is observed between 4 and 6 m. In this zone, the magnitude of the temperature plateau is underestimated of about 15 degrees. The difference between experiment and calculations is reduced with the increase in the level, due to an over prediction of the upper stratification slope.

The three-dimensional modelling approach highlights some improvements in the pool thermal-hydraulics evaluation. In accordance with the experimental data, the MULTID component predicts a uniform temperature at the same level of the pool. The temperature in the lower volumes perfectly matches the measured values. Even if the magnitude of the temperature plateau between 3.5 to 5.5 m is underpredicted, the 3D nodalization, in comparison with model #1, provides a better estimation of the stratification slope between 3.5 and 4 m. The stratification level of 4 m is very well reproduced and the discrepancies with experimental data are reduced to about 12 K, although they are still higher than the upper limit of the error bands. The over prediction of the heat losses along the hot leg, previously discussed, could be explained by the higher discrepancies observed within the pool by model #1.

Figure 19 (a) shows the LBE temperature obtained in the MULTID component, observing the most representative section that includes the FPS and the HX. To provide useful qualitative information, the DHR element is also included in the section. The temperature map shows that the upper stratification occurs in the first half of the HX, following the temperature drop along this component. Between 5.5 to 4 m, the temperature is quite uniform and then the second stratification occurs at the fitting volume level. Figure 19 (b) shows the error distribution map in the same section. The TCs cover only 9 positions in the r-theta plane so, to obtain the experimental data map, uniform temperature is considered at the same levels (the experimental results justified this assumption)

and along the z- coordinate, the LBE temperature is obtained with linear interpolation between two consecutive measurement points, in order to cover the whole axial length. The picture highlights that the three-dimensional model provides a perfect matching in the lower half pool. The error sharply increases at 4 m and it is maintained higher than 10 degrees up to the gas plenum (the maximum discrepancy of 13 K occurs at about 6 m). The large discrepancy at the HX outlet is not representative because it is expected that in this point the temperature is lower due to the cold LBE exiting the HX and uniform temperature in this region is not expected.

These results highlight the limits of RELAP5-3D to reproduce the exact temperature trend in a large HLM volume. In fact, R5-3D provides only one HTC correlation for HLM in a no-bundle geometry, mainly developed for liquid metal flowing in a duct. A situation where the liquid metal is in quasi-stagnant condition within a large volume, is out of the applicable range of the Seban & Shimazaki correlation, and the constant term included in this correlation could underestimate the heat transfer. In addition, R5-3D have not a fully integrated heat conduction model for the working fluid and this term could assume a relevant role in HLM systems (the effect of liquid thermal conduction is evaluated in section 2.1.5.3).

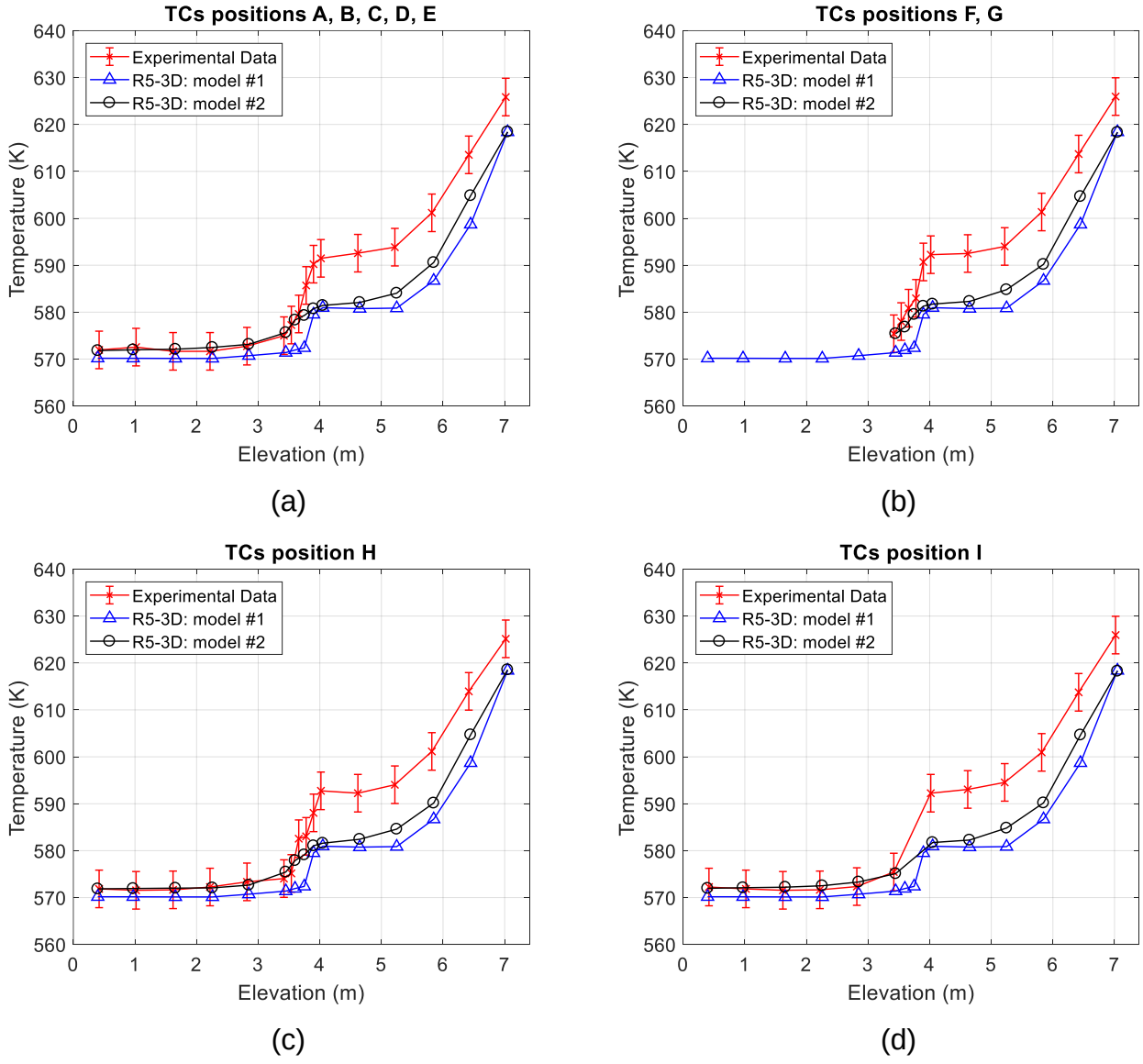

Figure 18.Test A: pool thermal stratification

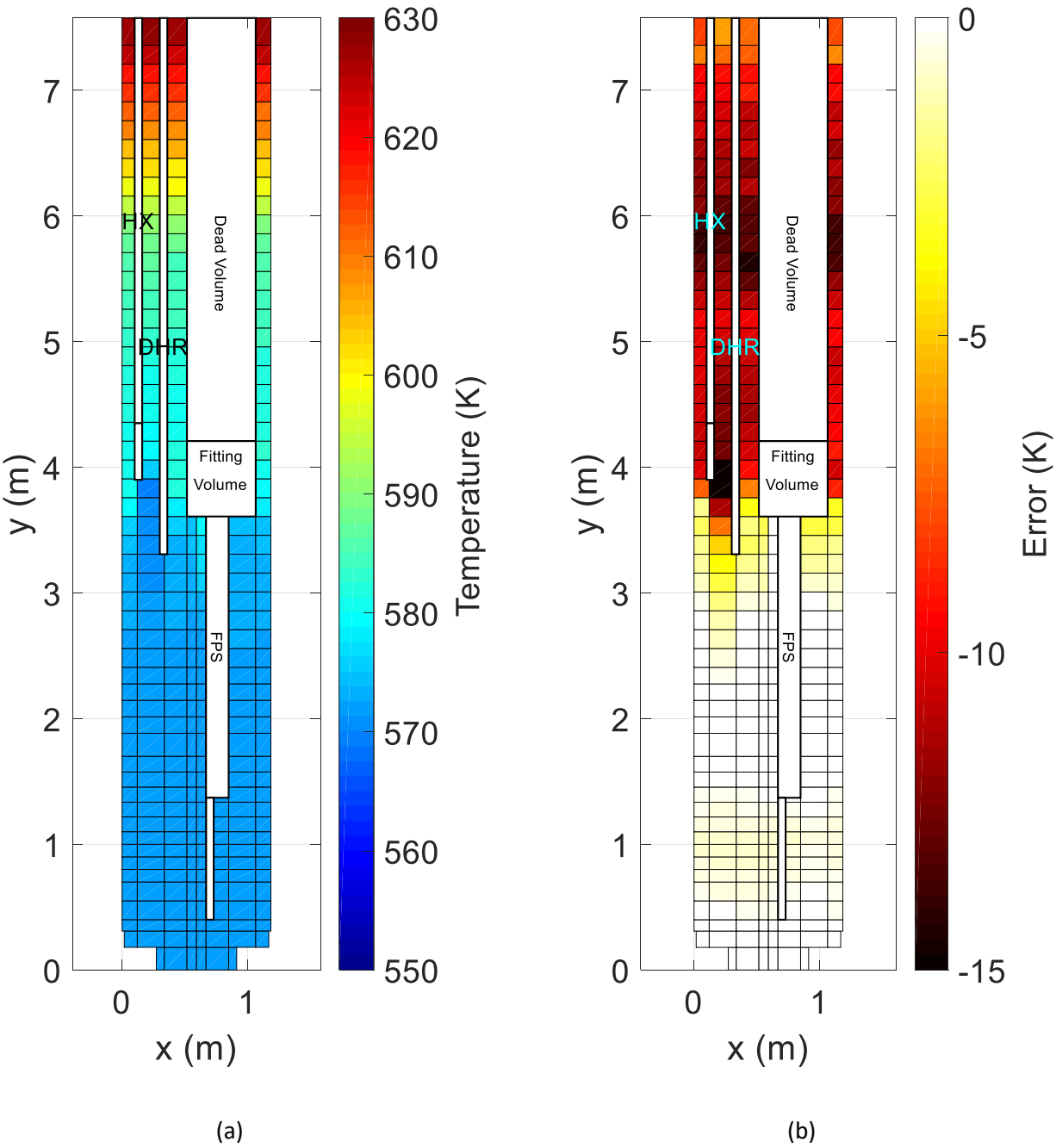

Figure 19. Test A: pool temperature, model #2

2.1.4.2 Test I

Test I has been reproduced to verify R5-3D capability to simulate a transition from GEC to NC with activation of DHR system. The boundary conditions assumed for the calculation are presented in Figure 20. The test starts at zero-power steady-state conditions, with each control system turned off. After 450 s, argon is injected inside the test section with a volumetric flow rate of 1.7 Nl/s, increasing to 1.78 at 8600 s. At 25400 s the gas injection is

disabled, decreasing to zero in 1 second (the instruments signal reaches the digital full scale at 0.35 Nl/s in Figure 20 (a)). The FPS power ramp (see Figure 20 (b)) starts at 920 s, reaching the nominal value after 180 seconds; full power conditions are assumed with a 5% reduction of the electrical signal to consider dissipations. At 25300 the transient event starts and the power is reduced to 7% in 130 s. Feedwater injection is depicted in Figure 20 (c) and it is replaced in R5-3D, unless the fluctuation due to measurement chain. Figure 20 (d) shows the air mass flow rate that feeds the DHR system; at the beginning, measurement of the air flow rate is disabled, giving a value of zero but the control system sets the air mass flow in order to remove about 3 kW. For this reason, a mass flow rate of about 21 g/s is considered in the calculation, for the first part of the test. After the transition from GEC to NC, air flow rate is increased following the experimental curve and setting a constant value of 226.7 g/s.

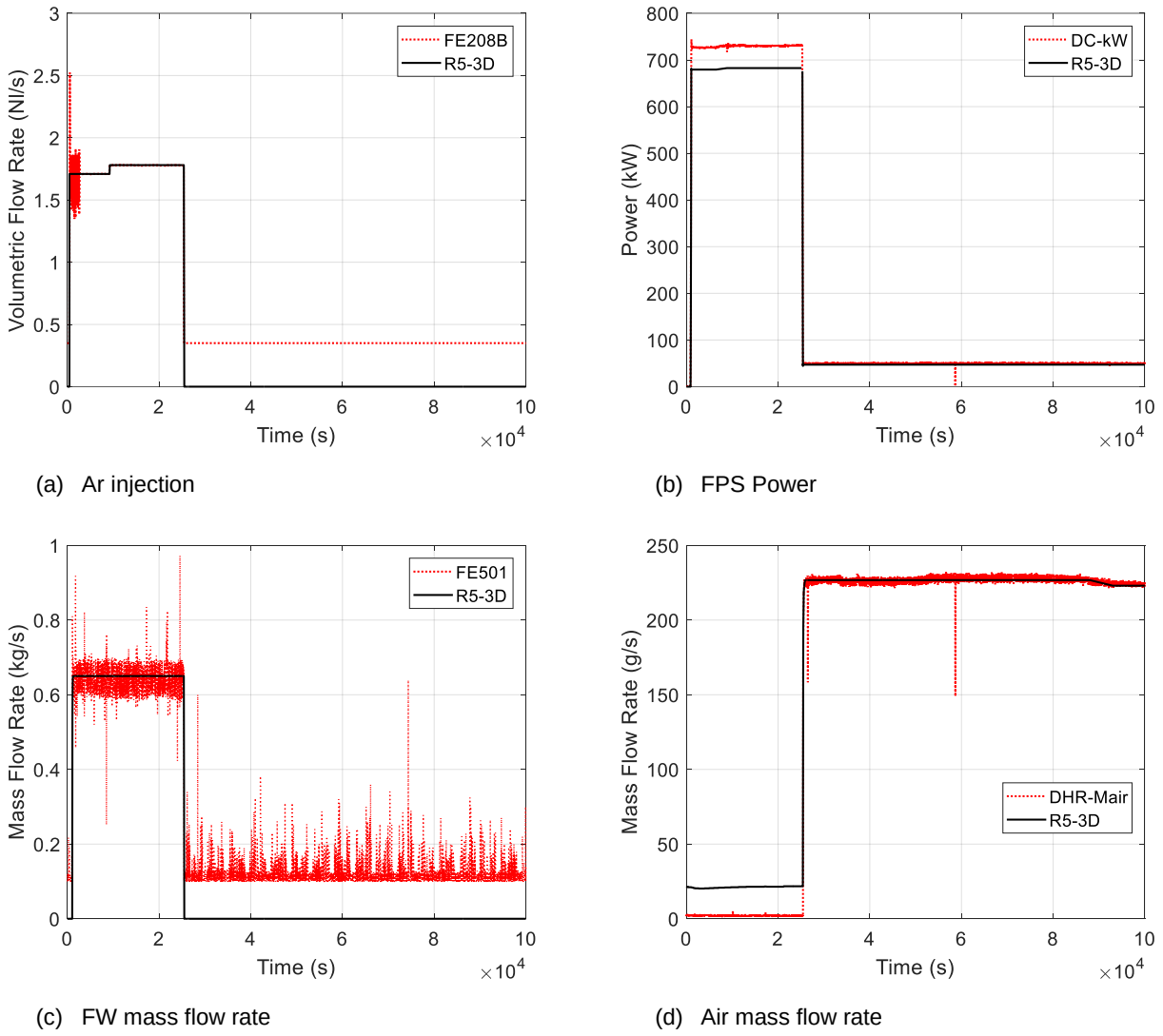

Figure 20.Test I: boundary conditions

Figure 21 compares LBE mass flow rate acquired by Venturi FM with the values obtained by calculations. At full power conditions, the acquisition system observes a constant LBE flow rate of 56 kg/s; after the transition, natural circulation is established to 7.3 kg/s. Both the calculations highlight a good prediction of the primary mass flow rate in GEC conditions. After the transition, both the simulations show a slight overestimation of the

flow rate acquired by Venturi FM. At low values, the measurement system is affected by large uncertainties, that could explain these discrepancies: mass flow rates evaluated by R5-3D (8.4 kg/s with model #1 and 8.6 kg/s with model #2) are included within the error bands. Natural circulation is mainly due to the thermal power supplied by the FPS and the heat losses towards the pool and the calculations demonstrate the R5-3D capabilities on the prediction of macroscopic phenomena during a postulated accident in an HLM system.

Figure 22 shows the LBE temperature trend at inlet and outlet of the FPS active length. During the full power operation, LBE temperature at the FPS inlet is uniform. The two models provide a good estimation of the temporal trend, highlighting a slight underprediction of the temperature, even if the discrepancies are contained within the error band. At the HS outlet, model #1 evaluates a good qualitative trend of the mean temperature. The subchannel analysis carried out with model #2, highlights code capability on the evaluation of the inner subchannel temperature, acquired by the thermocouple T-FPS-36. However, the temperature on the edge subchannel is underestimated of about 6 degrees (T-FPS-34). The lack of information about the exact position of the thermocouple T-FPS-34 could explain this discrepancy. In fact, it is expected a quite uniform temperature in the inner subchannels, due to the uniform distribution of the thermal power, and a sharp decrease at the lateral edge. For this reason, the value of the temperature is strongly influenced by the exact position of the instrumentation. Unless this discrepancy, R5-3D shows enough capabilities on the utilization as a subchannel analysis code, providing an estimation of the temperature difference between the center and the edge of the bundle.

During the first hour after the transition, both the models well reproduce the low peak at the HS inlet. Up to the end of the test, the models are able to simulate temperature evolution at the FPS inlet due to the global thermal power imbalance, limiting the discrepancies with experimental data within the error bands (lower than 3.6 degrees). At the HS outlet, the prompt temperature decrease is well predicted by R5-3D. Model #1 calculates a qualitative trend in good agreement with experimental data. After the transition from GEC to NC, the temperature difference between inner and edge subchannels is reduced, due to the low primary mass flow rate. The transition is well reproduced by model #2 that is able to predict the temperature distribution inside the bundle. The discrepancies with experimental data are limited to a maximum value of 3.5 K at the end of the test.

Figure 23 shows the comparison of LBE temperature through the HX. The two models well reproduce the qualitative trend of the temperature over the whole test. As for Test A, model #1 highlights higher heat losses through the hot leg, calculating a lower HX inlet temperature during the GEC operation (about 3 K). The peak temperature at 650 s is under-predicted by the calculations, even if the discrepancies with experimental data are contained within error bands. Some differences are observed in the first hour of the transition, when the prompt temperature decrease at the HX inlet is underestimated by the simulations. After that, the qualitative trend is well reproduced by the code, even if the two calculations provide slightly different results: the inlet temperature is over-predicted by model #1 of about 1 degree. After the loss of heat sink, the temperature drop provides information about the heat losses through the HX shell. The two simulations agree but, in comparison with experimental data, the temperature drop is under-predicted of about 1.8 K, proving the underestimation of the heat losses towards the pool. This sentence is confirmed by the power removed by HX, shown in Figure 24. The experimental power is obtained applying the energy balance (EB) equation, considering the LBE temperature acquired by the TCs at HX inlet and outlet section and the LBE mass flow rate measured by the Venturi flow meter. For this purpose, some assumptions are considered: the whole mass flow rate flowing through the hot leg is led into the HX and steady-state conditions are supposed. The propagation errors have been calculated and reported in the figure as a dotted line. Figure 24 shows the overprediction of the power removed by the HX but the large uncertainty bands make difficult the assessment of the calculation goodness.

The temperature evolution at the DHR inlet and outlet primary side is presented in Figure 25. The large error band (+/- 17 K) at the DHR outlet is due to the high fluctuations observed by the acquisitions of the TCs at the outlet section. During GEC operation, the DHR system is turned off and the temperature difference between inlet and outlet is mainly due to the thermal stratification inside the pool, explaining the discrepancy of the outlet temperature calculated with model #1. After the simulated accident, the DHR is fed with air mass flow rate (see Figure 20 (d)) and both the models provide a good estimation of the DHR behavior. The simulations highlight an overestimation of the intel temperature of about 3 degrees, remaining within the error bands. This behavior will be explained in the thermal stratification analysis. Unless this difference, the temperature drop across the DHR is well reproduced by the two models, matching very well the LBE outlet temperature in NC operation. This is confirmed in Figure 26, where the experimental power removed by the DHR is compared with R5-3D results. The prompt power increase is well predicted by the calculations that match well the experimental data until 80000 s. After that, experimental data assumes a lower gradient and the discrepancy with computational results increases up to 4% at the end of the test.

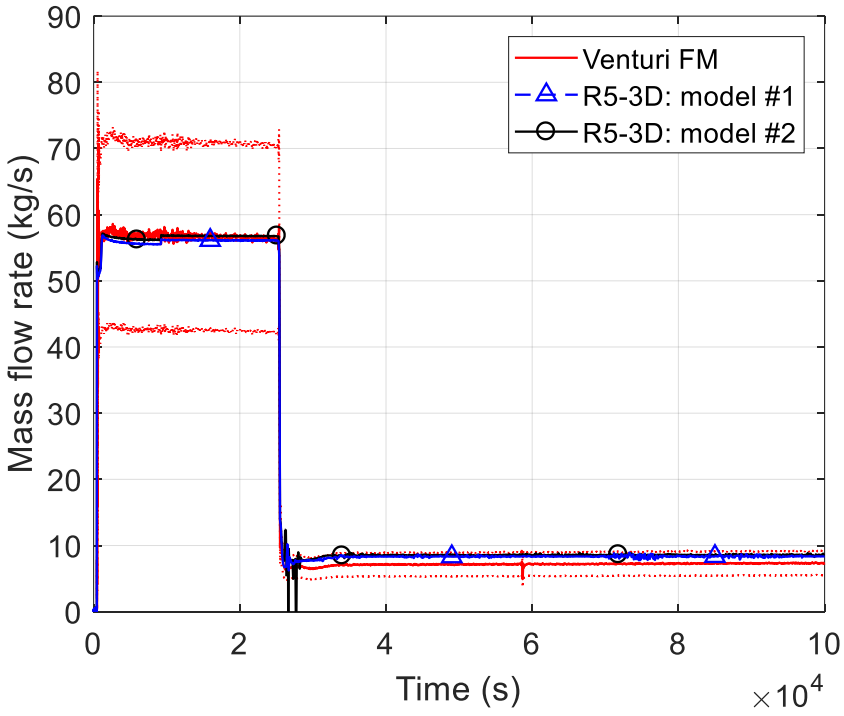

Figure 21. Test I: LBE mass flow rate

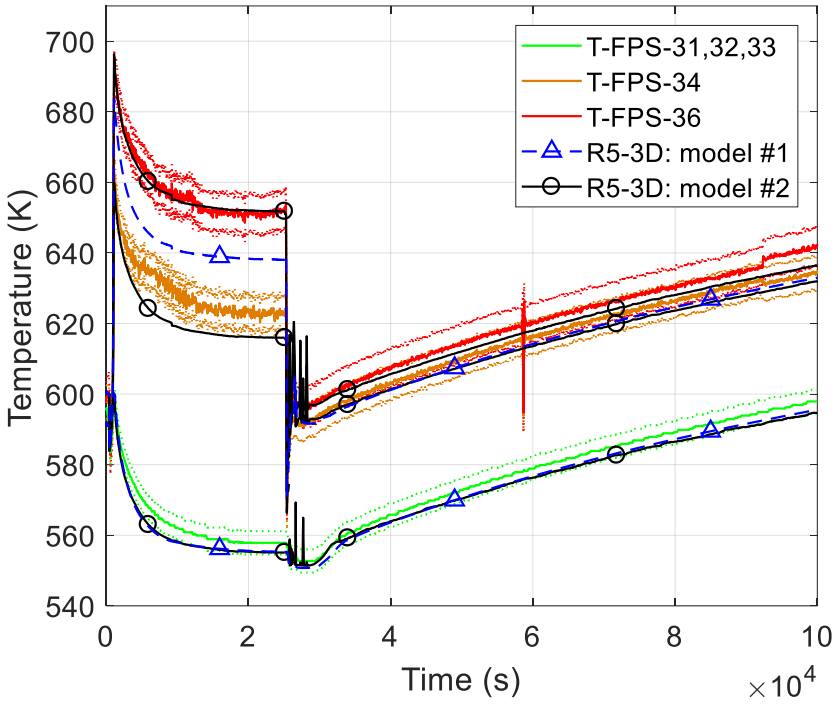

Figure 22. Test I: LBE FPS inlet/outlet temperature

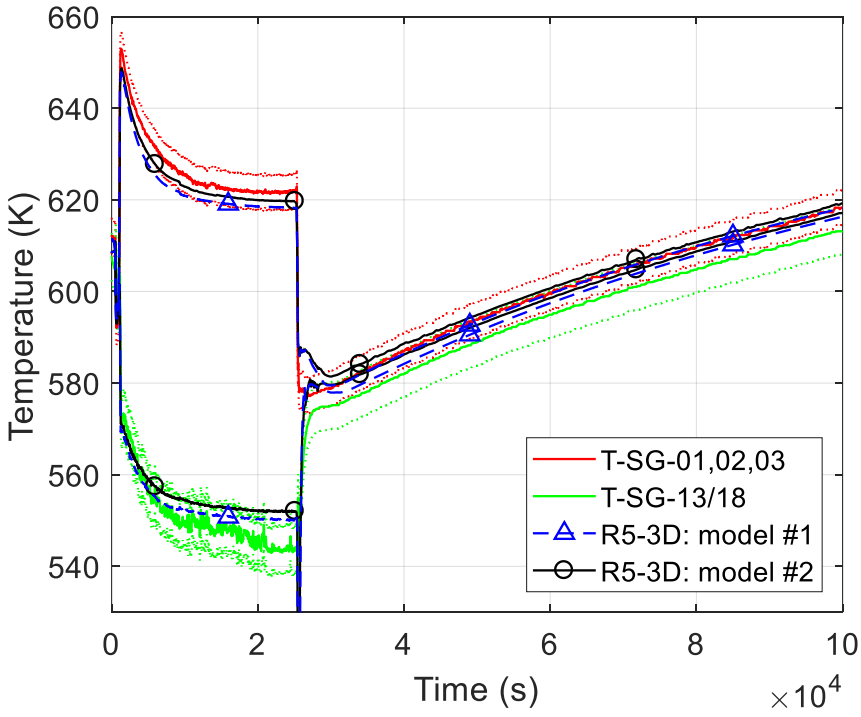

Figure 23. Test I: LBE HX inlet/outlet temperature

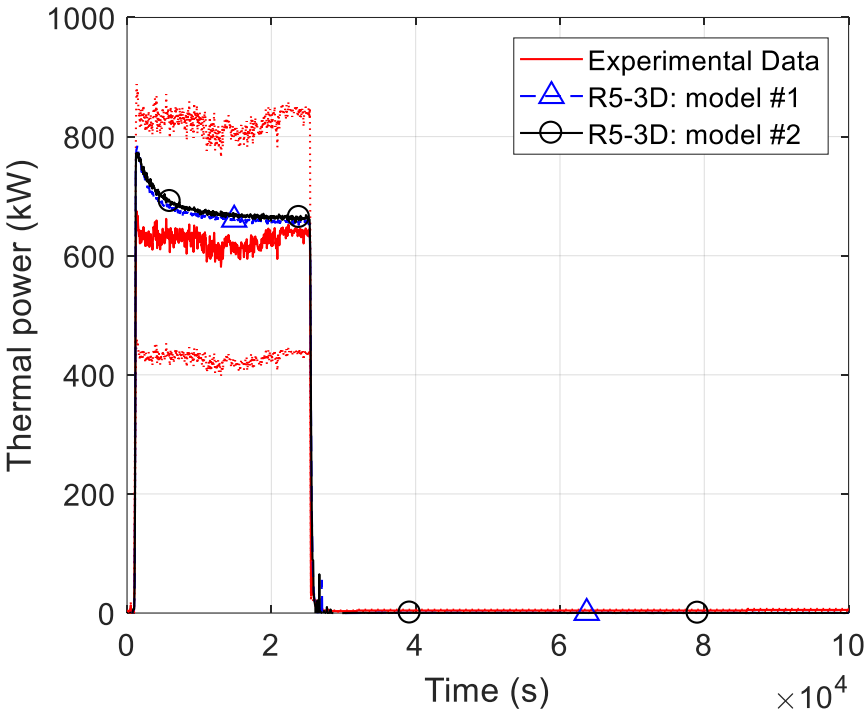

Figure 24. Test I: HX power removed

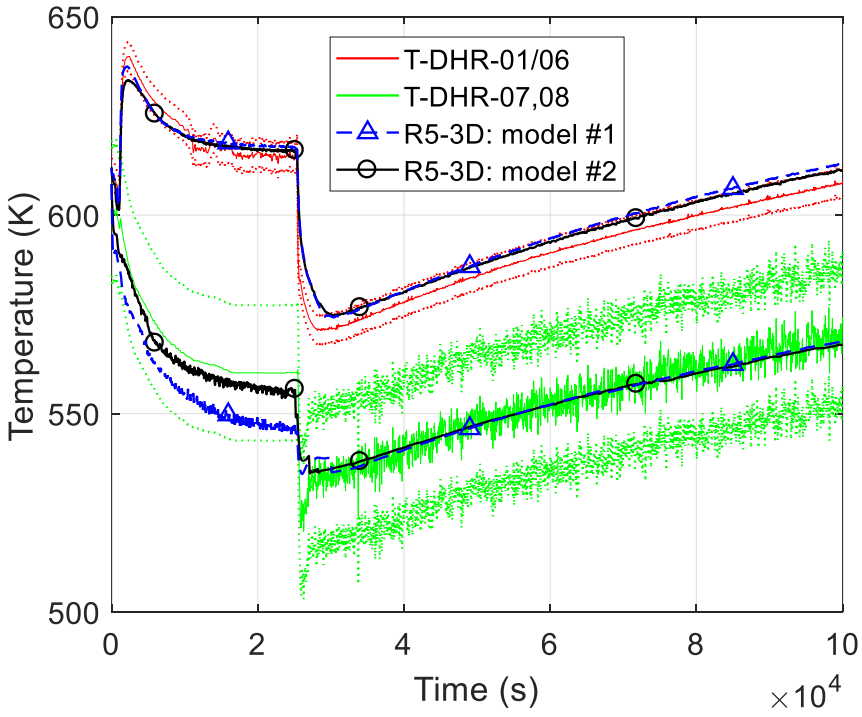

Figure 25. Test I: LBE DHR inlet/outlet temperature

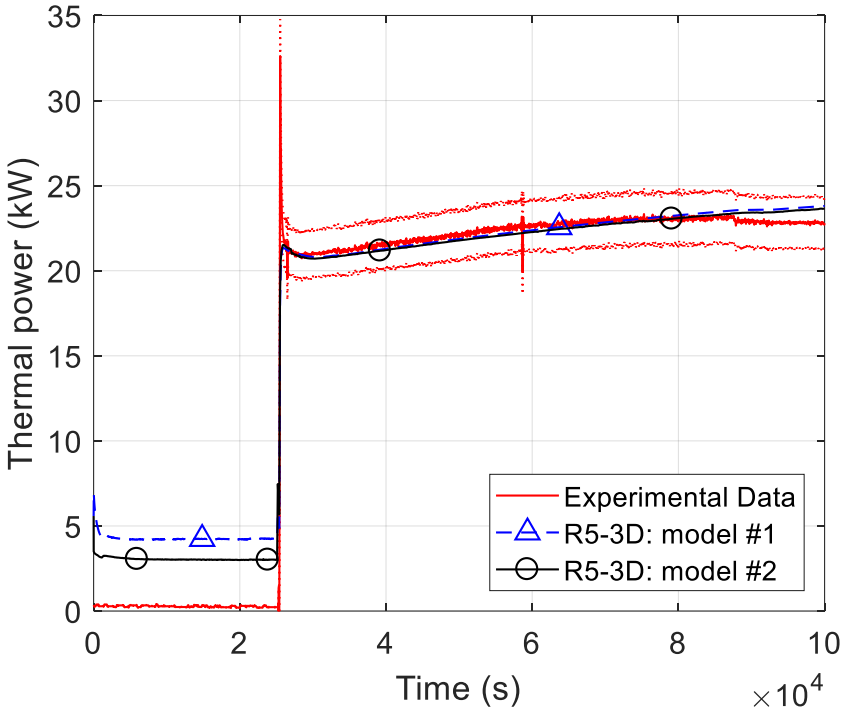

Figure 26. Test I: DHR power removed

In next figures the pool thermal stratification phenomenon is analyzed. Figure 27 shows the full power steady-state conditions obtained at 25000 s. The experimental trend is similar to the one observed in Test A. Two relevant vertical stratifications occur along the HX shell (between 7 and 5 m) and at the HX outlet level (4 m from the pool bottom). The models provide results consistent with Test A conclusions. Model #1 matches very well temperature in the lower half part of the pool, where discrepancies with experimental data are lower than 1 K. The middle stratification is obtained in the exact position (4 m) but the magnitude of the temperature plateau is under-predicted of about 15 K. In the upper part of the pool, model #1 provides a good estimation of the qualitative trend, but the difference with experimental temperature remains higher than 4 degrees up to the top. The MULTID component introduces improvements in the evaluation of the middle stratification. As shown in Figure 31 (a), in the lower part of the pool discrepancies with experimental data are lower than 1 degree. The calculated profile matches very well the measured temperatures up to 3.8 m, where the temperature plateau remains lower than experimental one of about 5 K. In the upper part, the multi-dimensional simulation matches the mono-dimensional one, under predicting the experimental temperature of about 10 degrees up to the top of the pool (see also Figure 31 (a)).

After the transition, because of the loss of heat sink, LBE along the HX assumes quite uniform temperature that increases from 580 to 620 K along the transient test. The temperature inside the HX is comparable with the pool temperature and the decrease of heat losses leads to the attenuation of the upper thermal stratification. Figure 28 shows the vertical temperature trend at 28000 s, after 3000 s from the transition event. The upper stratification disappears (uniform temperature of 573 K is observed between 3.5 and 7 m) and the middle stratification moves downward to the DHR outlet level. The transition is very well predicted by the two models. The mono-dimensional scheme obtains the maximum discrepancies at 3 m, where the LBE temperature is underestimated of about 4 K (within the error bands). In the upper part, a slight stratification effect is still

observed between 6.5 and 7 m. The MULTID component provides a perfect agreement with experimental data. Figure 30 (b) shows a useful representation of the temperature inside the pool, highlighting the absence of the upper stratification and the movement of the middle one downstream of the DHR outlet. In the upper part, a slight stratification is also observed between 6.5 and 7 m, where the maximum discrepancy with the experiment occurs (see Figure 31 (b)).

In NC operation the power removed by DHR plus the heat losses towards the environment are lower than FPS supplied power. The energy imbalance causes the temperature increase in the whole test facility, as shown in the previous figures. This evolution is also observed inside the pool, where the qualitative temperature profile is maintained over the whole transient, but the mean temperature increases. Figure 29 shows the final conditions: the thermal stratification still occurs at 3.3 m from the bottom and the mean temperature increases to about 610 K. Both models are able to reproduce the evolution inside the pool. At the end of the test a perfect agreement between the two calculations is observed. The stratification level is well defined in Figure 30 (c) which shows the temperature representation in a relevant 2D section of the multi-dimensional component. The final conditions are well predicted by the code, limiting the discrepancies to a maximum value of 4 degrees (within the error bars), underestimated and overestimated respectively in the bottom and upper half part of the pool, as shown in Figure 31 (c).

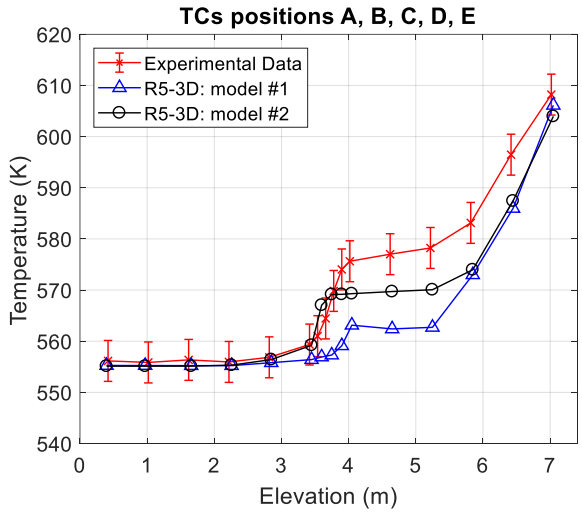

(a)

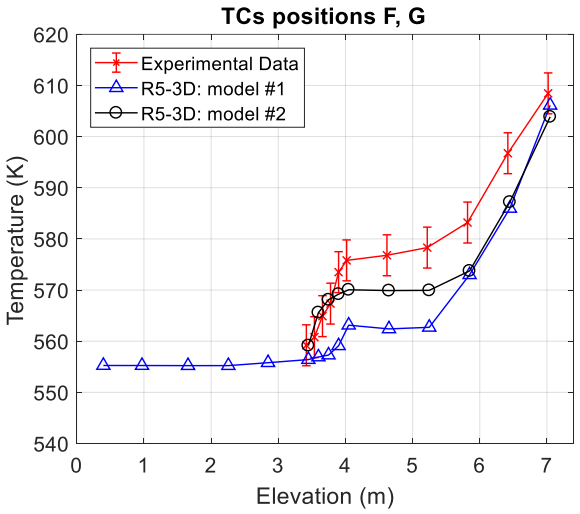

(b)

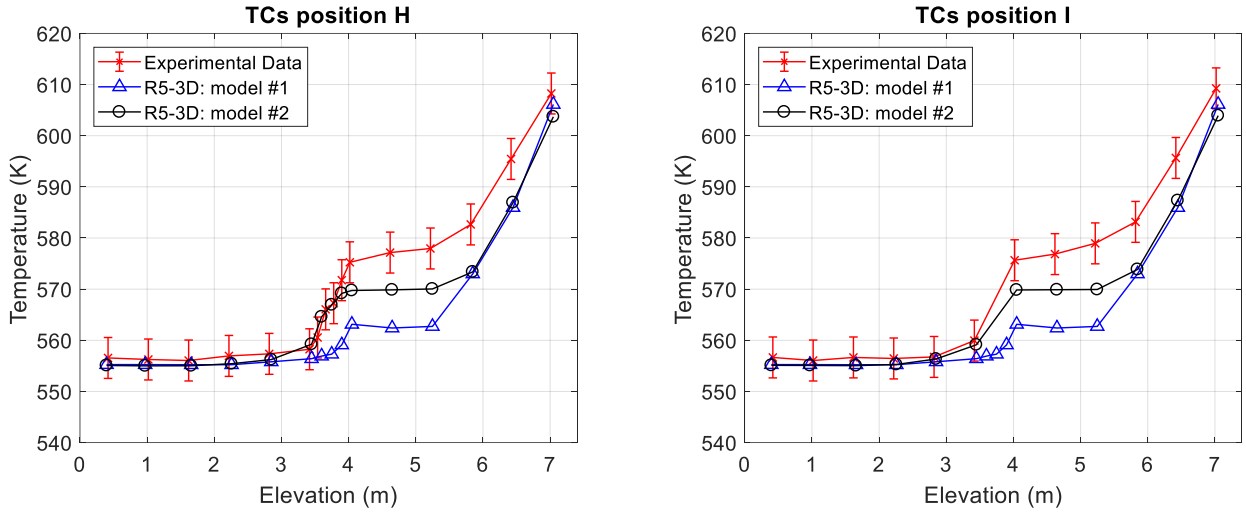

Figure 27. Test I: pool thermal stratification (25000 s)

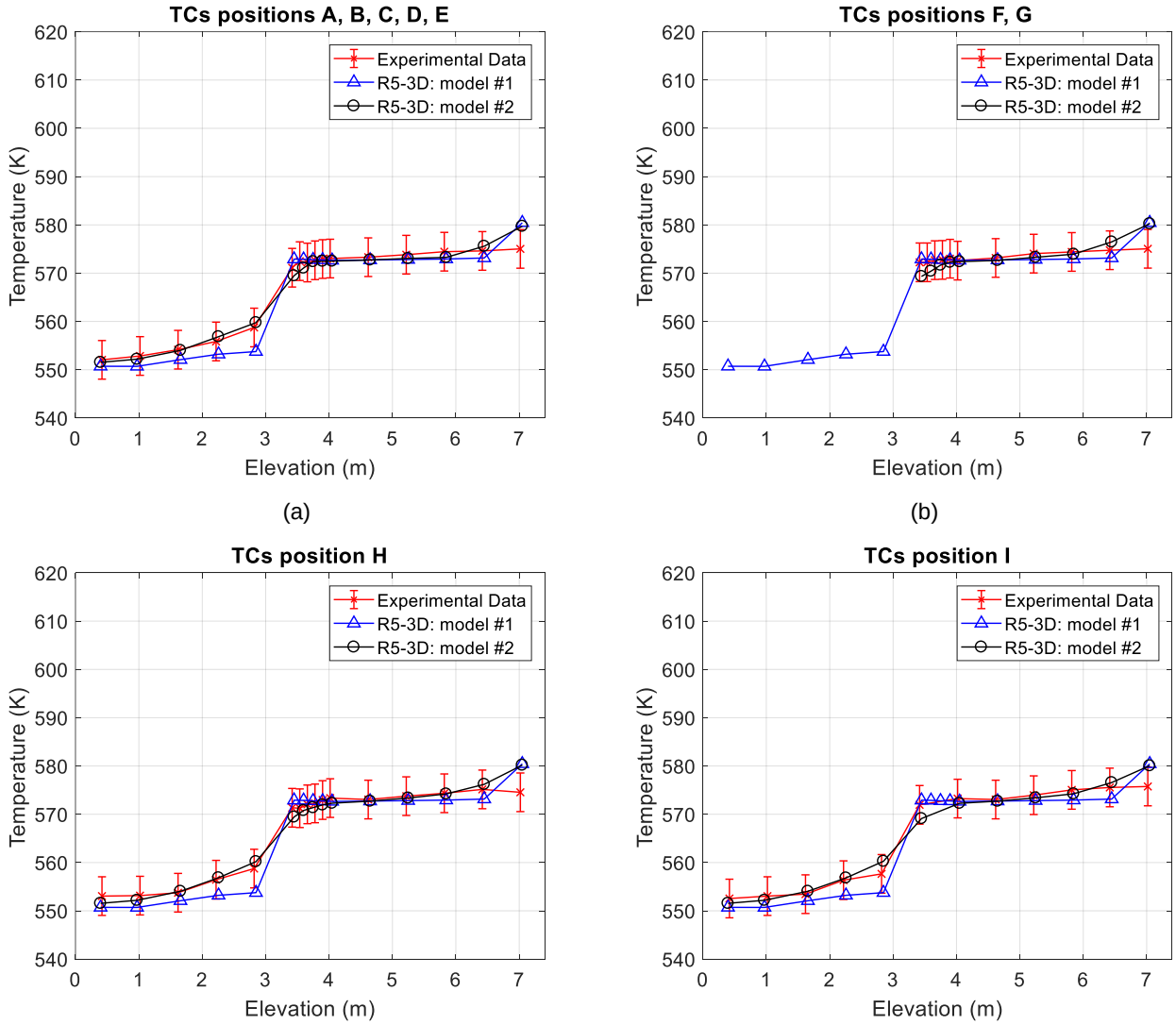

(c) (d)

Figure 28. Test I: pool thermal stratification (28000 s)

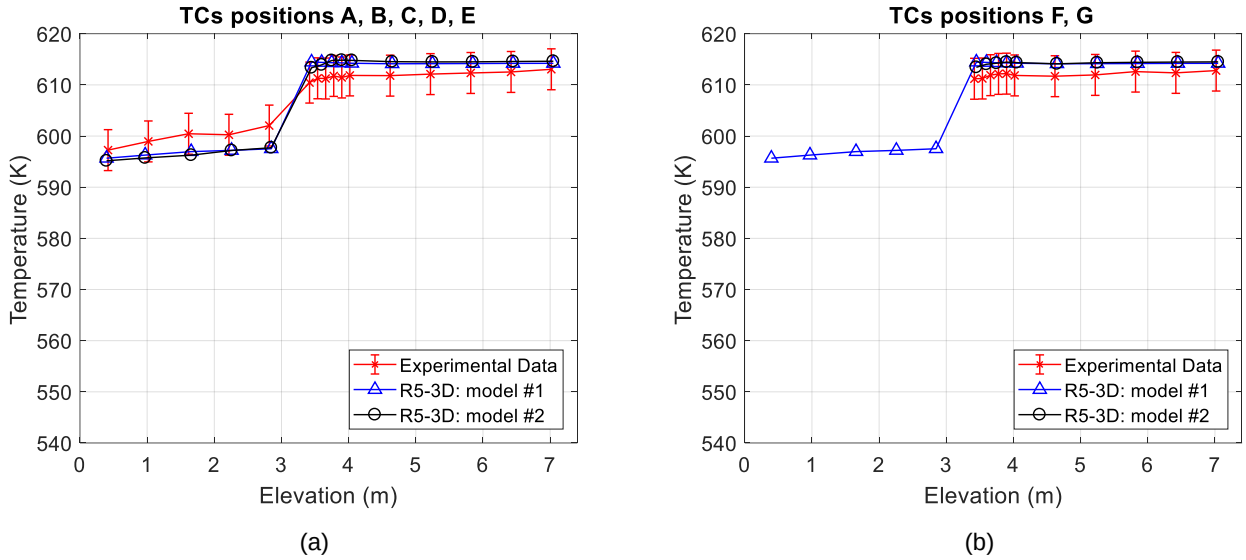

(a) (b)

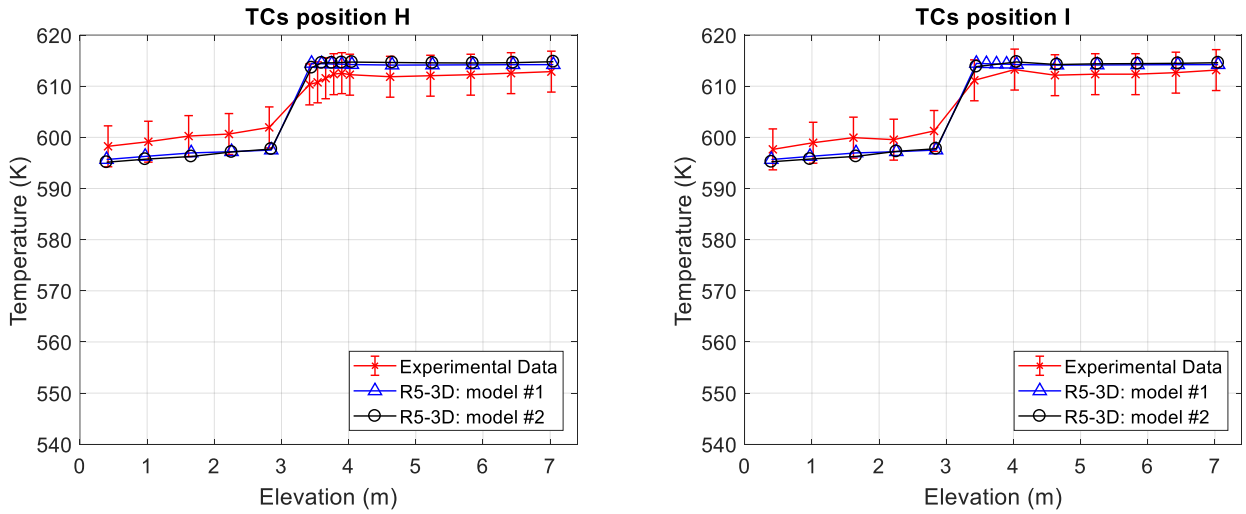

(c) (d)

Figure 29. Test I: pool thermal stratification (100000 s)

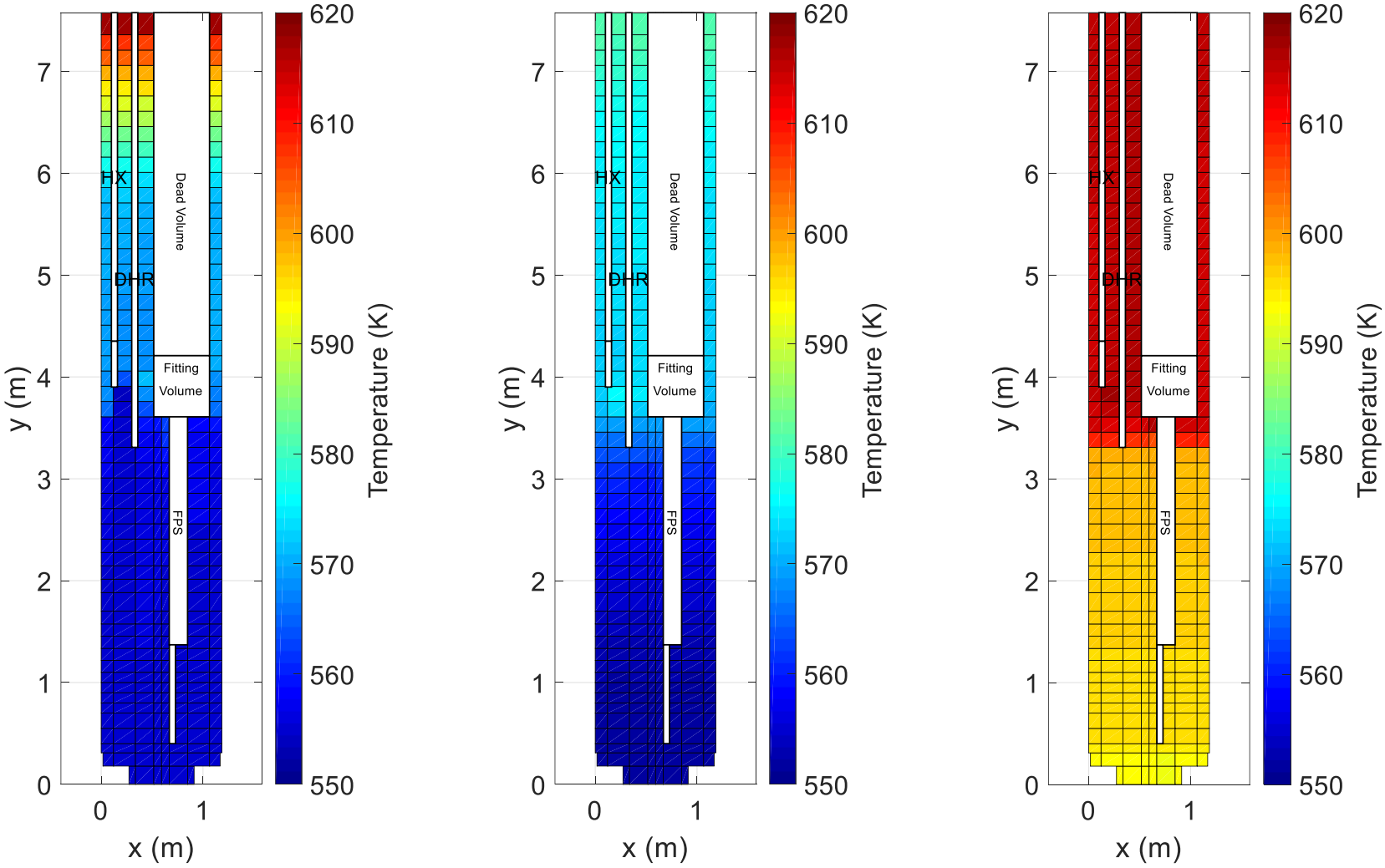

(a) 25000 s

(b) 28000 s

(c) 100000 s

Figure 30. Test I: pool temperature, model #2

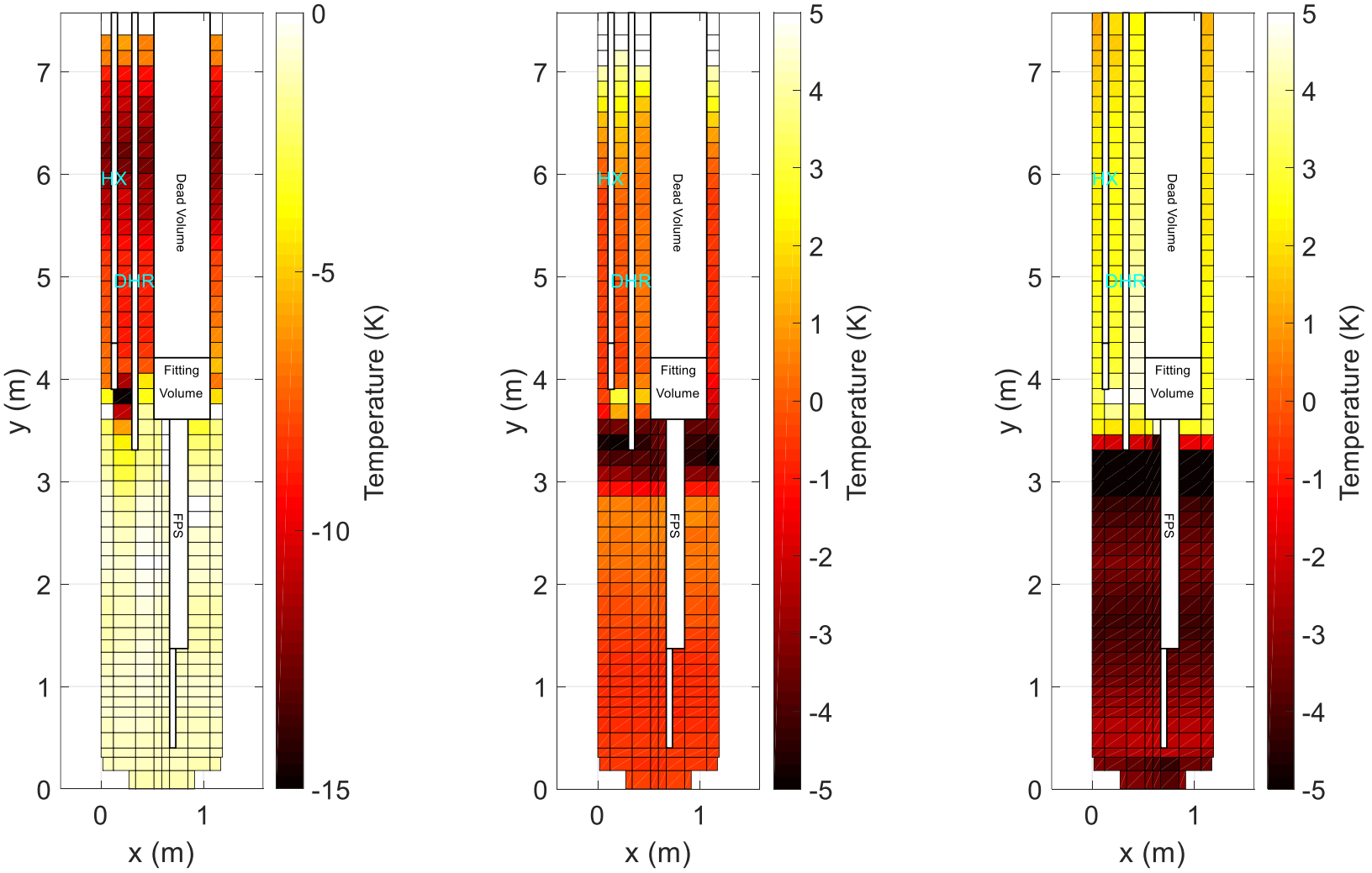

(a) 25000 s (b) 28000 s (c) 100000 s

Figure 31. Test I: error distribution map, model #2

2.1.5 Modelling analysis

2.1.5.1 Time step and mesh sensitivities

Figure 32 shows the time step sensitivity performed with model #1; time step has been set to 0.005, 0.002 and 0.001 s. Six relevant parameters have been considered to verify time step effect on the accuracy of the simulations: LBE mass flow rate (Figure 32 (a)), FPS inlet and outlet temperature (Figure 32 (b)), HX inlet and outlet temperature (Figure 32 (c)) and thermal stratification profile within the pool (Figure 32 (d)). The calculations reproduce the full power operation of Test I and the comparison with experimental data is shown. The three calculations highlight a perfect matching, proving that the accuracy of the results is not affected by the time step.

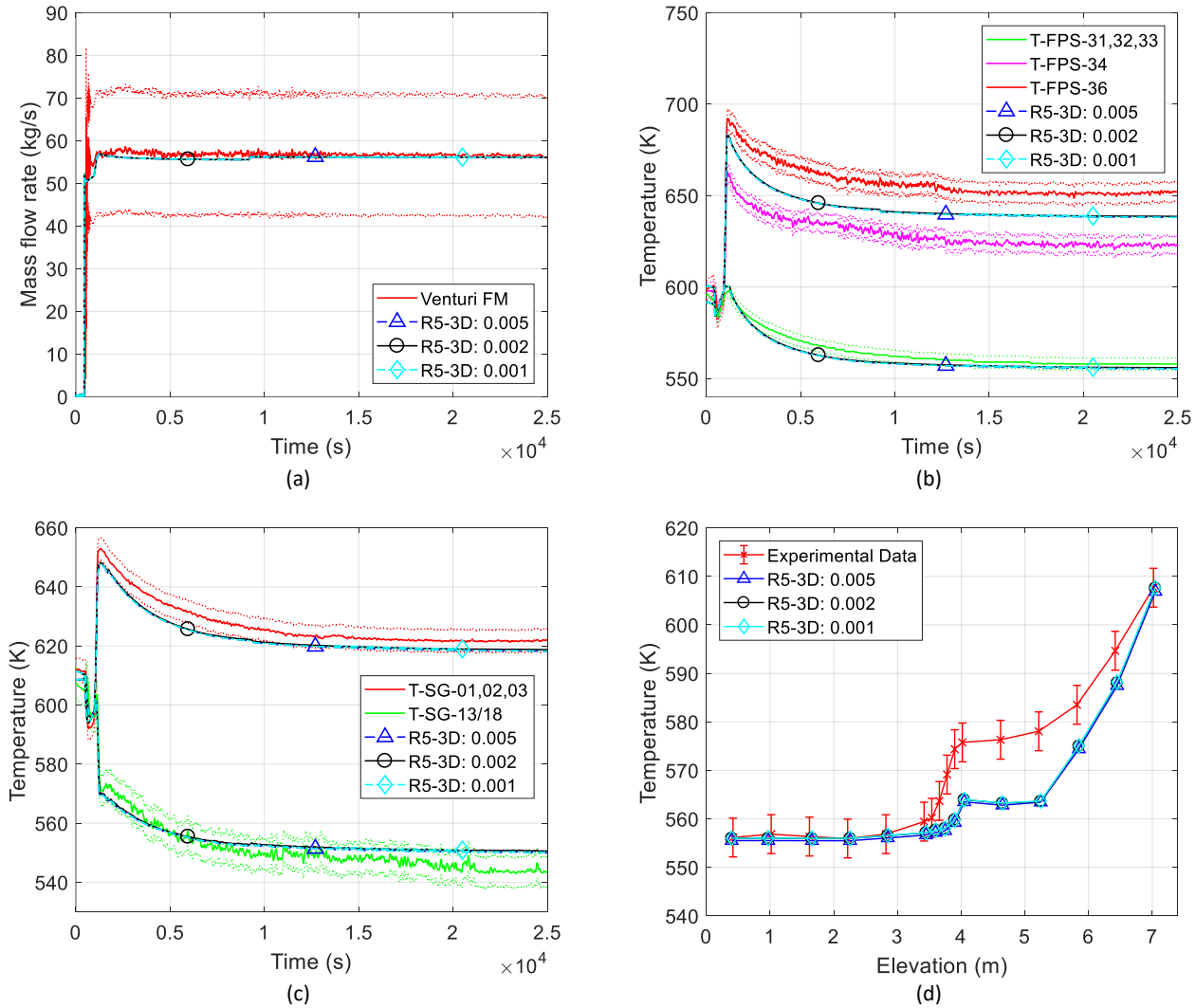

Figure 32. Time step sensitivity

The same figures of merit have been considered to assess the effect of the mesh discretization on the accuracy of the results. The mesh sensitivity concerns the FPS, riser and HX modelling, as described in section 2.1.3. Figure

33 shows the comparison of the calculations with experimental data. In the plots, the mesh resolution is specified in the legend. The study highlights the negligible effect of the mesh on the accuracy of the calculations.

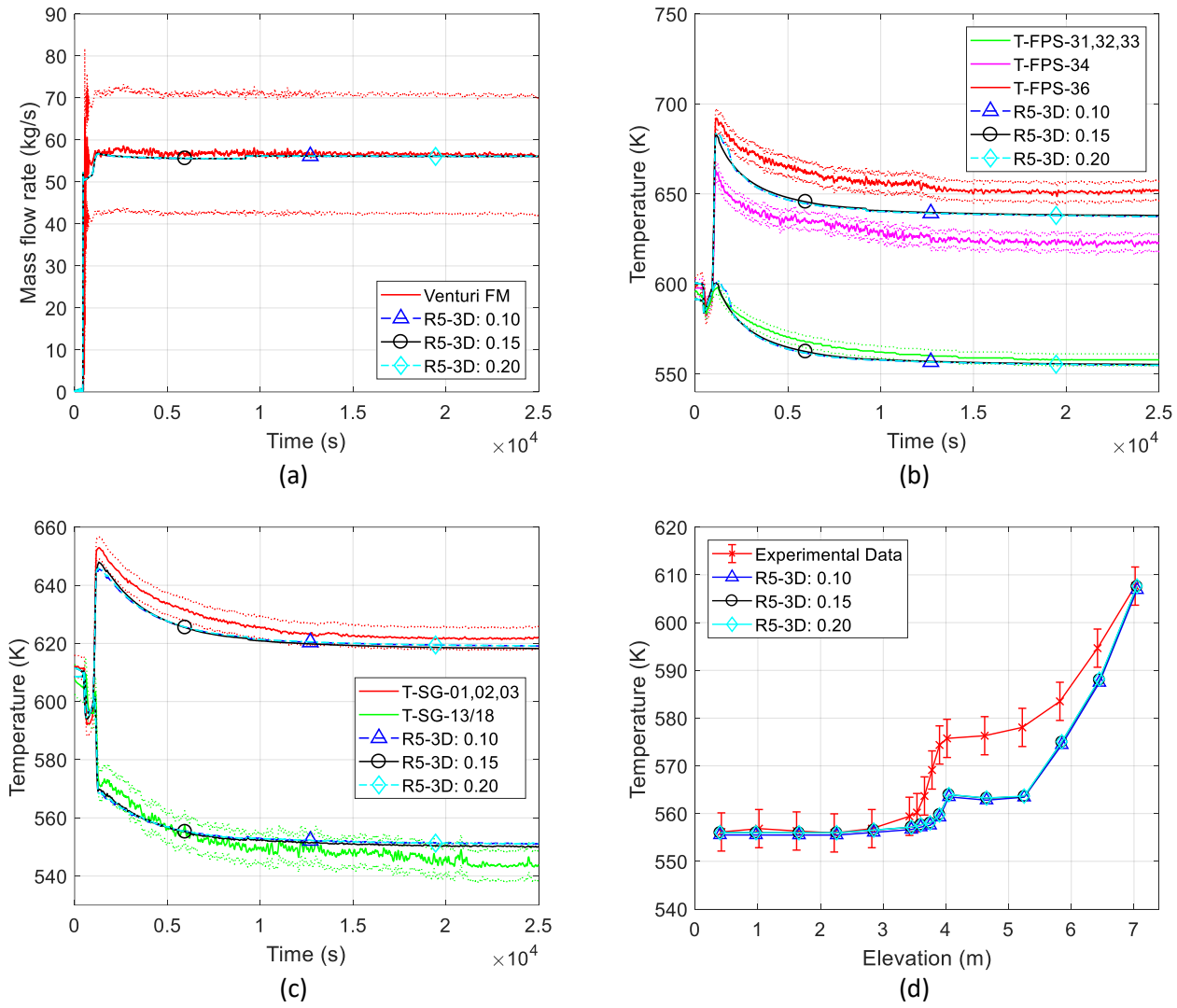

Figure 33. Mesh sensitivity

2.1.5.2 FPS radial conduction

In model #2 the FPS subchannel modelling has been introduced. As presented in section 2.1.3, calibrated heat structures have been implemented to consider radial conduction that could play a crucial role in the evaluation of temperature distribution through the FPS.

In CIRCE-ICE experiment, Pe and Pe* (see section 1.3) assume values equal to 2005 and 106940 in GEC operation and 300 and 16043 in NC condition. Pe* is significantly higher than 100 in both GEC and NC operations and the axial contribution has not been considered in the analysis. Radial heat conduction also should not have relevant effects on the calculations; this aspect has been assessed.

Figure 34 (a) shows the temperature distribution calculated by R5-3D with radial conduction at the end of the HS active length, in GEC operation. As expected, due to the uniform supply of the thermal power, a flat temperature distribution is obtained in the inner zone of the bundle but a sharp temperature decrease (30 K) is observed approaching the hexagonal shell. Figure 34 (b) depicts the temperature difference between the case with radial conduction and the case without heat conduction. At full power operation, when the LBE mass flow rate is 56 kg/s, discrepancies between the calculations are negligible, limiting the maximum difference to 1.2 K (in the corner and edge subchannels). Figure 35 compares the temperature profile in the radial direction obtained by the two calculations. In the same plot, temperatures measured by TCs and the error bars, representing the uncertainties on the temperature acquisitions and the instrument positions are reported. A good agreement with experimental data is observed with both the calculations. Radial conduction tends to smooth the temperature profile, but this effect is practically negligible.

The same analysis is carried out in NC operation, when the LBE mass flow rate is about 7 kg/s. Due to the low value of power, the temperature difference between the inner and edge subchannels is reduced to about 5 degrees (see Figure 36 (a) representing the calculation assuming radial conduction). In this case, the effect of the radial conduction is slightly higher than the GEC condition. Figure 36 (b) shows that the maximum discrepancy between two calculations increases to about 2.5 K in the edge subchannels. In Figure 37 the effect of the thermal conductivity is visible, flattening the temperature profile at the HS exit. Some discrepancies are observed with the experimental data, but the radial heat conduction provides a better estimation of the qualitative profile and it reduces the discrepancies on the bundle edge.

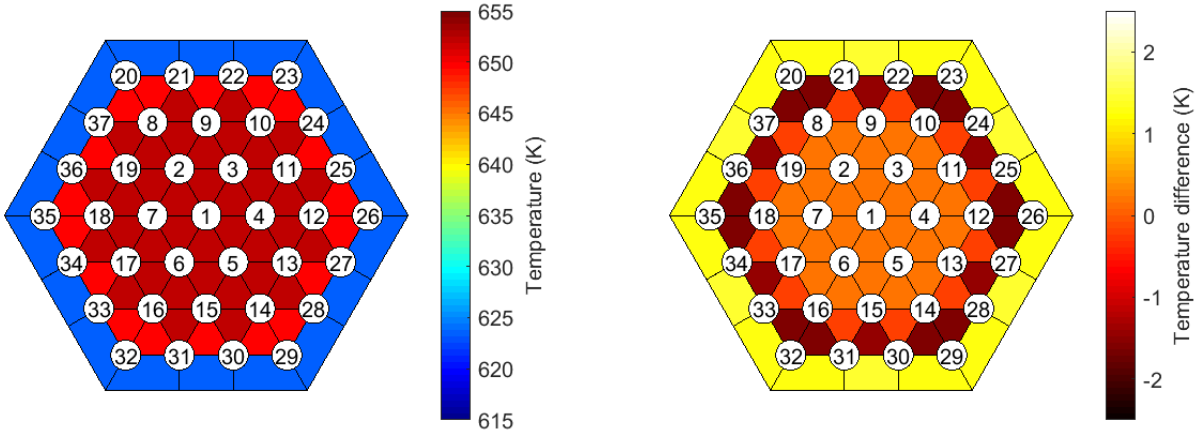

(a) (b)

Figure 34. FPS outlet temperature: radial conduction effect (20000 s).

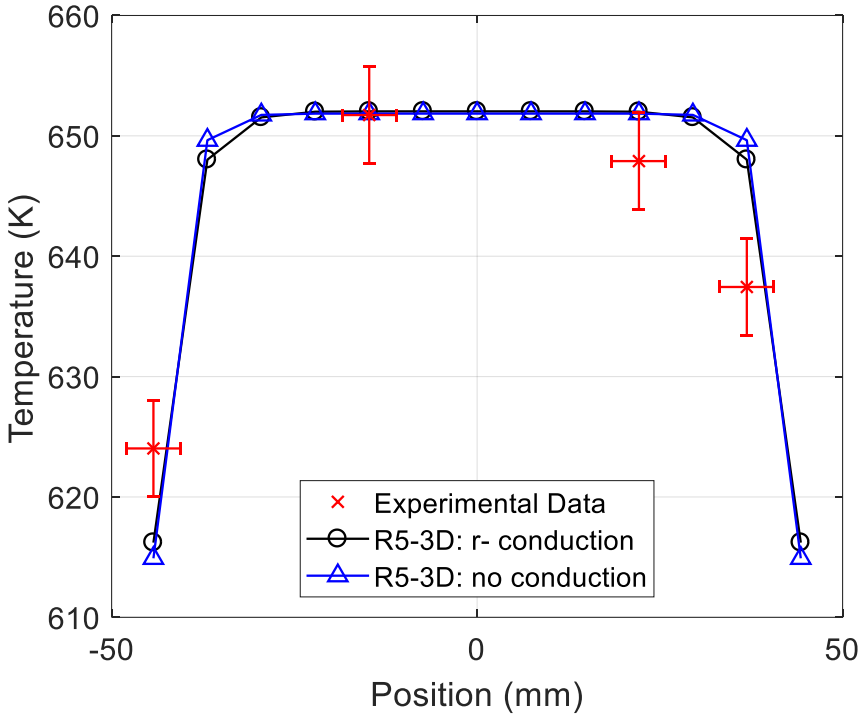

Figure 35. FPS outlet temperature: comparison with experimental measurements (20000 s)

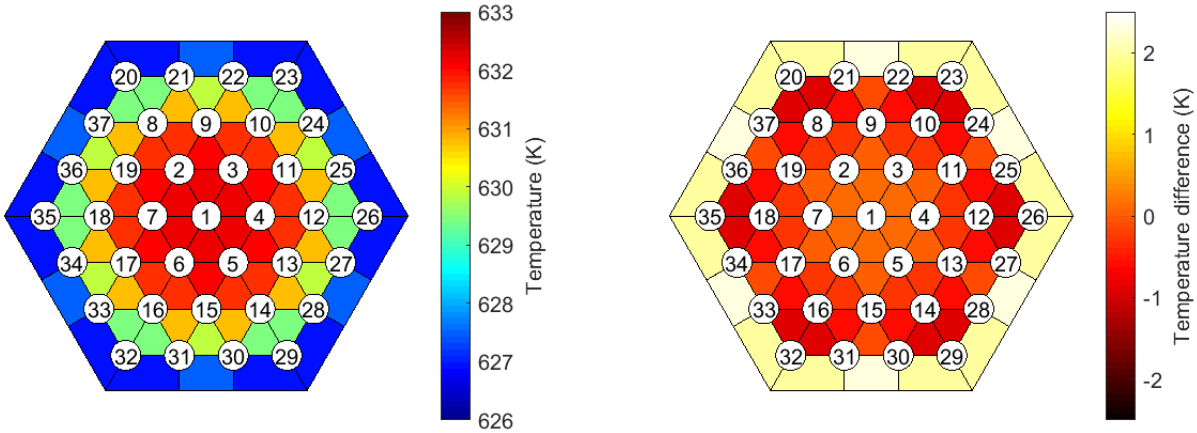

Figure 36. FPS outlet temperature: radial conduction effect (89000 s)

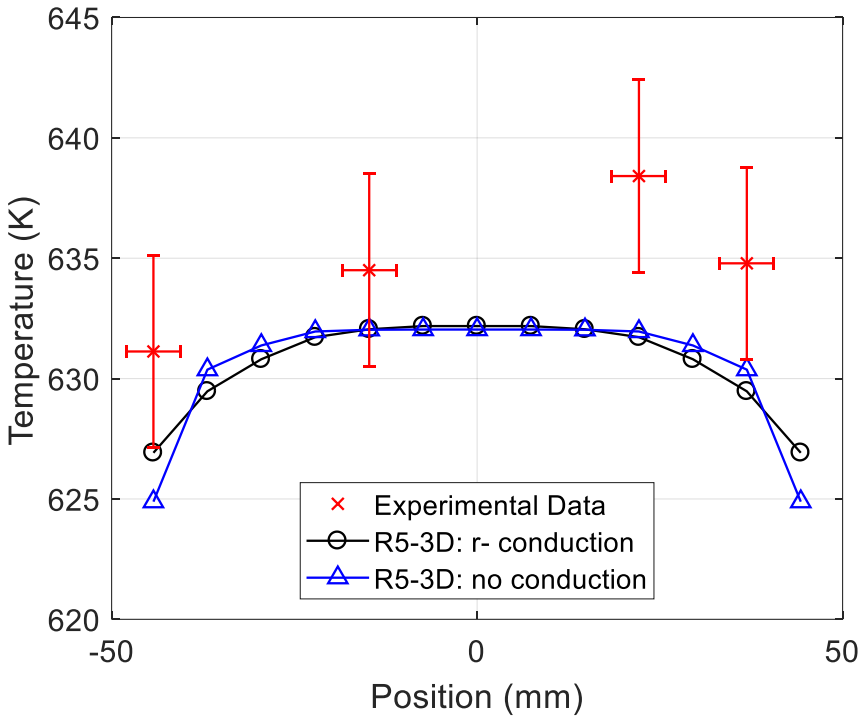

Figure 37. FPS temperature: comparison with experimental measurements (89000 s)

2.1.5.3 Pool modelling

RELAP5-3D capabilities on the prediction of relevant phenomena into large pool have been investigated, evaluating the best practice for the pool simulation. The simplest approach is to reproduce LBE pool with a single vertical pipe. As mentioned in section 1.3, a thermal stratification model was introduced in RELAP5-3D to improve the solutions when a separation of hot and cold liquid layers appears in a vertical stack of cells [15]. In Figure 38 this option is investigated, comparing two calculations: disabled model (R5-3D in Figure 38) and thermal stratification model (R5-3D: t). In addition, due to the quasi-stagnant conditions within the pool, thermal conduction could play a crucial role. For this purpose, the effect of the vertical conduction is assessed by introducing heat structures between each pool cell, assuming a dummy material with negligible heat capacity and LBE thermal conductivity, the LBE volume of the nodalization and a high HTC multiplicative factor to reduce the convective resistance. Figure 38 shows good prediction in the lower part (between 0 and 2.5 m), where the difference with experimental data are limited to 1 degree, and in the upper part (between 5.5 and 7 m), where the error is higher (about 6 K) but the qualitative trend is well reproduced. Relevant discrepancies are observed in the middle zone. In this region, the large amount of the heat losses from the hot leg causes a prompt temperature increase at 3.8 m. A single pipe is not able to simulate buoyancy and mixing convection, resulting in a stagnant LBE inside the pool, where the upward flow of the hot liquid is not allowed. The activation of thermal stratification model does not produce improvements on the accuracy of the simulations while the implementation of the vertical conduction reduces the thermal peak at 3.8 m but a large discrepancy with the experiment is still observed.

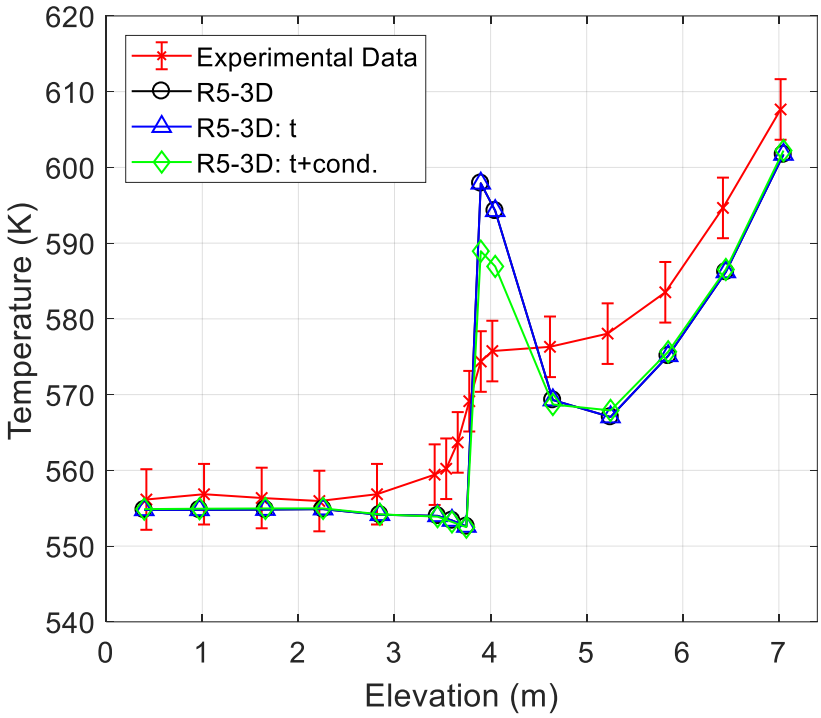

Figure 38. Pool modelling: single pipe

Examples of RELAP5 applications on the thermal stratification simulation in large tanks were found in literature, highlighting capabilities of the code to reproduce this phenomenon with multiple channels and several cross junctions. This approach has been applied in CIRCE-ICE modelling, considering two different nodalization schemes. Model #1.0 consists of 3 parallel pipes and 156 cross junctions. The axial discretization is the same presented in section 2.1.3 but, in this case, one vertical channel includes the central part of the pool, in contact with the whole test section, and the other two simulate the pool edge, thermally connected with the external environment. The second modelling approach, model #1, has been presented in section 2.1.3. The results of simulations are presented in Figure 39. In addition, the vertical conduction model is implemented in model #1 to assess the magnitude of this effect (radial conduction has not been considered because it is expected to be not relevant due to the temperature distribution uniformity at the same axial level). Figure 39 shows good agreement between the calculations in the lower and upper part of the pool. In the middle zone, model #1.0 does not predict the temperature plateau because the cold LBE exiting the HX is mixed with LBE inside the pool, decreasing the temperature and causing a low peak at 3.8 m. On model #1, thermal conduction does not affect the computational results because mixing phenomena induce to larger order of magnitude thermal effects. On the other hand, the implementation of the conduction model increases the model run time of 7.5%.

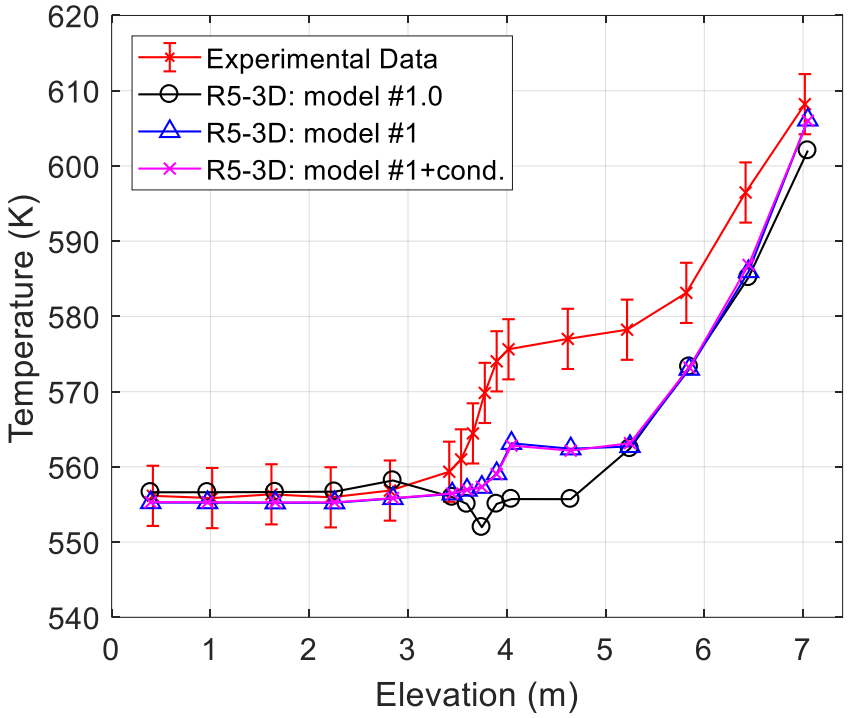

Figure 39. Pool modelling: three parallel pipes with cross junctions

In model #2, a multi-dimensional component has been introduced to reproduce CIRCE pool. RELAP-3D allows to use two sets of momentum equations within MULTID component: three-dimensional momentum equations or mono-dimensional momentum equations (in this case they are applied on each of the coordinate directions) [41]. In Figure 40 the influence of the momentum equations set is assessed. Discrepancies between the calculations are limited in the middle zone of the pool and the magnitude of the differences is about 1 degree. In particular, the use of 1D momentum equations (R5-3D: 1D in Figure 40) led to an under prediction of the temperature plateau during the GEC operation (see Figure 40 (a)). After the transition, two simulations highlight good agreement; low differences are observed between 0 and 3 m from the bottom of the pool (Figure 40 (b)).

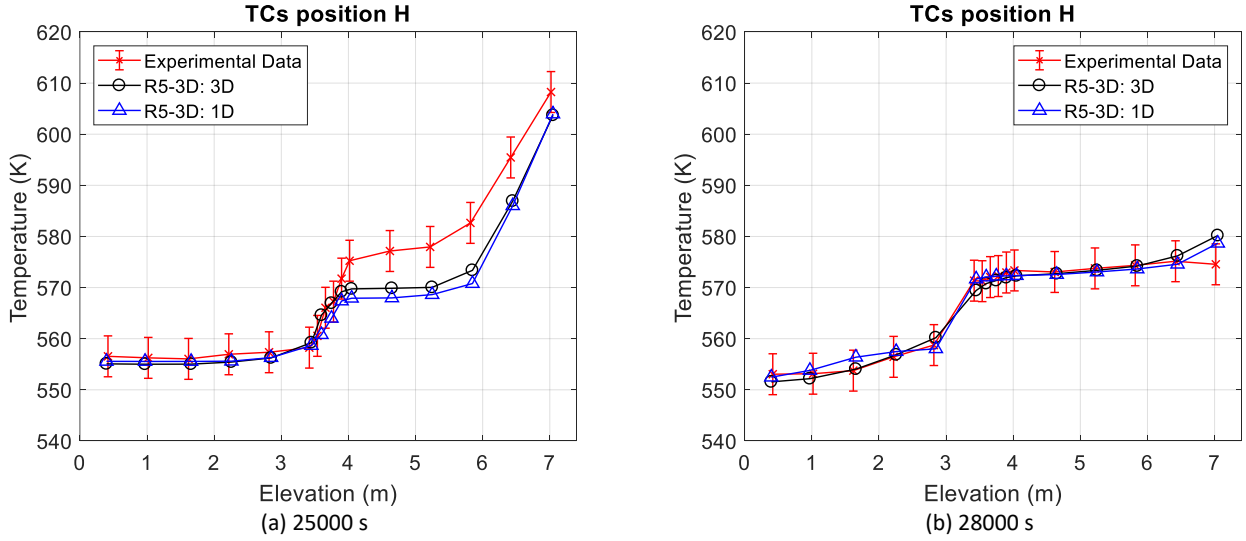

Figure 40. Influence of the momentum equations

2.1.6 Conclusive remarks

The experimental campaign promoted in CIRCE-ICE test facility was aimed to investigate the thermal-hydraulics of a complex HLM system and to provide data for validation of computational tools. Two experimental tests have been analyzed in this activity: Test A, consisting in a transition from no-power to full power steady-state conditions, and Test I, consisting in a transition from GEC to NC, simulating a protected loss of heat sink plus loss of flow accident. The aim of the computational activity has been to investigate the capability of RELAP5-3D© to predict thermal stratification phenomenon in an HLM pool.

Several examples were found in literature concerning the simulation of large tanks with RELAP5. A thermal stratification model was implemented in RELAP5, trying to achieve an accurate evaluation of the phenomenon in a tank. This model can be only applied to vertically oriented components without cross junctions. Even if this approach provided good results on the simulation of tanks with limited volume, such as a pressurizer, it highlighted some limits on the simulation of large pools. In this case, a better evaluation of the thermal stratification was found simulating the pool with multiple vertical channels with cross junctions, not allowing the application of thermal stratification model. In this research activity, the two modelling methods are applied and compared with an additional approach consisting in the application of the multi-dimensional component for the simulation of the pool.

The state of art on the simulation of the thermal stratification in a large pool has been confirmed by the calculation performed on CIRCE-ICE. The mono-dimensional approach, using a single channel for pool modelling, highlights discrepancies with the experimental data, failing on the prediction of the axial temperature profile. A high peak temperature in the middle of the tank, which is not observed by the experiment, is caused by a total absence of the natural flow within the pool. In order to verify how the axial conduction within the fluid can improve the computational results, a thermal conduction model has been implemented in the nodalization, using several heat structures that couple adjacent meshes. As expected, the axial conduction reduces the peak but not enough to match the experimental temperature profile.

In order to allow natural circulation inside the pool, the second approach has been applied, dividing the pool in three vertical channels connected with cross junctions. Two nodalization schemes have been presented for the discretization of the pool. This approach has shown good capabilities on the thermal stratification evaluation. The qualitative trend is well reproduced, predicting two relevant stratification in the upper and in the middle volumes of the pool. In the lower part of the tank, the LBE temperature is very well simulated but, at 4 m, the plateau temperature is under-predicted of about 15 K and this discrepancy is maintained up to the cover gas.

RELAP5-3D capabilities were improved with a fully integrated multi-dimensional modelling scheme, mainly developed for volumes where the movement of the fluid is preferably 1D. In this activity the MULTID component has been used for the simulation of CIRCE pool. The nodalization scheme is the same of model #1 except for the pool, simulated with a detailed three-dimensional component, and the FPS, where subchannel division has been performed.

The same boundary conditions have been applied to model #1 and #2, reproducing the two experimental transient tests. Several figures of merit have been selected, assessing the capabilities of the two models to reproduce thermal-hydraulics of an HLM cooled pool-type system in safety-relevant operations. The comparison with experimental data has highlighted excellent capabilities of the two models to predict thermal-hydraulics of the main flow path, managing to evaluate the most important features: LBE mass flow rate in both GEC and NC conditions, heat exchange within FPS, HX and DHR, and heat losses. In each condition, the computational results are included within the experimental error band. In addition, model #2 assesses RELAP5-3D abilities as a subchannel analysis code, in both GEC and NC operations. The effect of the radial conduction has been evaluated:

specific heat structures has been implemented to reproduce thermal conduction through adjacent subchannels. This analysis has shown small effects of the radial conduction, even if, in low flow rate regimes, such as NC operation, it provides not negligible improvement on the prediction of the temperature profile. In this case the simulation is in good agreement with experimental data; the highest discrepancies are observed in the edge of the bundle (4 degrees) where the errors can be justified by the uncertainties related to the TCs positions.

Focusing on the pool simulation, the MULTID component has introduced relevant improvements on the prediction of the thermal stratification phenomenon. The two relevant stratifications have been observed by the calculation. The temperature in the lower part matches very well the experimental measurements. The lower stratification level is well predicted and the temperature hot plateau underestimation has been reduced to 5 K. After the transition from GEC to NC, both the models are able to predict the upper stratification attenuation and the movement of the lower one below the DHR outlet. In the long term, the two calculations provide the same temperature profile that matches well the experimental trend, limiting the discrepancies below 4 degrees. Evaluation of the axial conduction within the pool has been performed, highlighting limited effects, especially when the natural circulation inside the pool is considered.

In conclusion, RELAP5-3D shows good capabilities on the prediction of the thermal stratification by modelling the pool with multiple channels with cross junctions or with a multi-dimensional component. The natural circulation within the pool seems to play a crucial role for the thermal stratification instauration. The qualitative temperature profile is well reproduced by the two approaches but the multi-dimensional nodalization reduces discrepancies with the experimental data. The discrepancies seem due to a not perfect evaluation of the heat losses through the wall of the internal component. In this frame, the implementation of a specific correlation for the heat transfer coefficient evaluation in large volumes could play a crucial role in the accuracy of the results.

2.2 CIRCE-HERO computational activity

In the framework of the H2020 SESAME project, a validation benchmark has been proposed to investigate capabilities of different computational codes to predict the main thermal-hydraulic phenomena in a heavy liquid metal-cooled pool-type fast reactor. Four participants were involved in the benchmark exercise: ENEA, SCK-CEN and “Sapienza” University of Rome, using different versions of RELAP5, and NRG (Nuclear Research and consultancy Group), using a coupled approach between the system thermal-hydraulic code SPECTRA (Sophisticated Plant Evaluation Code for Thermal-hydraulic Response Assessment) and the commercial code ANSYS CFX [36]. The validation benchmark has concerned the experimental campaign performed in CIRCE facility, that was refurbished to host a new test section, called HERO (Heavy liquid mEtal pRessurized water cOoled tubes), consisting in a double-wall bayonet tubes steam generator. The main purposes of the experimental campaign were to prove feasibility and performance of a DWBT SG in a relevant configuration for ALFRED SG [38], and to provide experimental data suitable for code validation [59].

DIAEE of “Sapienza” University of Rome supports the definition and the realization of the experimental campaign. The nodalization scheme, presented in section 2.1.3, has been improved with the modelling of the new test section and it has been applied for the pre-test simulations. Section 2.2.2 will present the main outcomes of the pre-test activity that has been focused on the identification of the initial steady-state conditions and of the transient boundary conditions for the realization of the test matrix. The pre-test analysis has highlighted the excellent thermal-hydraulic capability of HERO, ensuring enough NC conditions to remove the decay heat in short term [60].

The results of the pre-test calculations have been used by the experimentalist to carry out the experimental campaign. The CIRCE-HERO nodalization scheme, developed for the pre-test calculations, has been improved

starting from the information obtained by the experiment analysis and during the blind phase of the benchmark exercise [61]. The results of the post-test calculations, performed by UNIROMA1 within the validation benchmark promoted in H2020 SESAME project, are presented in section 2.2.3.3 [62][63]. The analysis has been focused on the relevant phenomena occurring in the experimental test:

- the transition from gas-enhanced circulation (GEC) to natural circulation (NC);
- the heat transfer within the fuel pin simulator (FPS);
- the steam generator (SG) heat transfer;
- the heat losses;
- the pressure drops;
- the pool thermal stratification.

2.2.1 Description of the test facility

CIRCE test facility, introduced in section 2.1.1, was refurbished to host HERO test section, depicted in Figure 41. The primary flow path is the same of ICE configuration, except for the HX, which is replaced with the DWBT SG, and for the DHR system, that is extracted from the pool and its function is performed by the SG, moderating the secondary flow rate. Furthermore, in order to reduce heat losses between the FPS and the cold pool, the holes obtained on the HS cylindrical shroud for the penetration of the TCs, have been closed with metal sheets, obtaining an insulator gap between the FPS hexagonal and cylindrical wrappers, filled by stagnant LBE.

The steam generator consists of a bundle of seven DWBTs, arranged in a hexagonal lattice, characterized by a p/d of 1.42 (see Figure 42). Five spacer grids limit the vibration of the bayonet tubes, ensuring their correct position within the hexagonal shell (Figure 42). Thermal insulation between the component and the pool is obtained adopting a double-wall shell with air gap. The tubes are characterized by an active length of 6 m. Primary coolant flows downward through the free volume between the DWBTs and the hexagonal shell, and then it is released into the main pool. Figure 43 shows a schematic view of the DWBT, consisting in four concentric tubes. Feedwater enters the unit at the top edge of the inner tube, moving downward to the lower plenum, where flow is inverted. Then, secondary coolant moves upward across the annular riser between second and third tube, where the boiling occurs. The steam, exiting the seven DWBTs, is collected inside the steam chamber and then it is released into the steam discharge line. The volume between inner and second tube is filled with an insulator, to prevent the steam condensation on the outside wall of the second tube; the gap between third and fourth tube is filled with pressurized helium and high thermal conductivity powder. The helium pressure is monitored to detect any possible leakages and the heat exchange performance is guaranteed by the high conductivity powder. Secondary loop is completed with the feeding line, equipped with a demineralizer, a volumetric piston pump, a helical pre-heating system, a manifold, which distributes the feedwater to the seven bayonet tubes, and a bypass line used for the start-up phases [64].

The monitoring system of ICE configuration has been improved with an overall number of 42 TCs, installed in the primary and secondary side of the SG, several pressure transducers, to characterize the pressure distribution through the secondary loop, a Coriolis FM, measuring the total FW mass flow rate downstream the secondary pump, and six mini turbine flow meters (TFMs), installed at the inlet section of six bayonet tubes [59]. In addition, the acquisition points of the LBE temperature within the pool are intensified at the level of the HS top edge, where pre-test calculations predicted a relevant thermal stratification phenomenon [60].

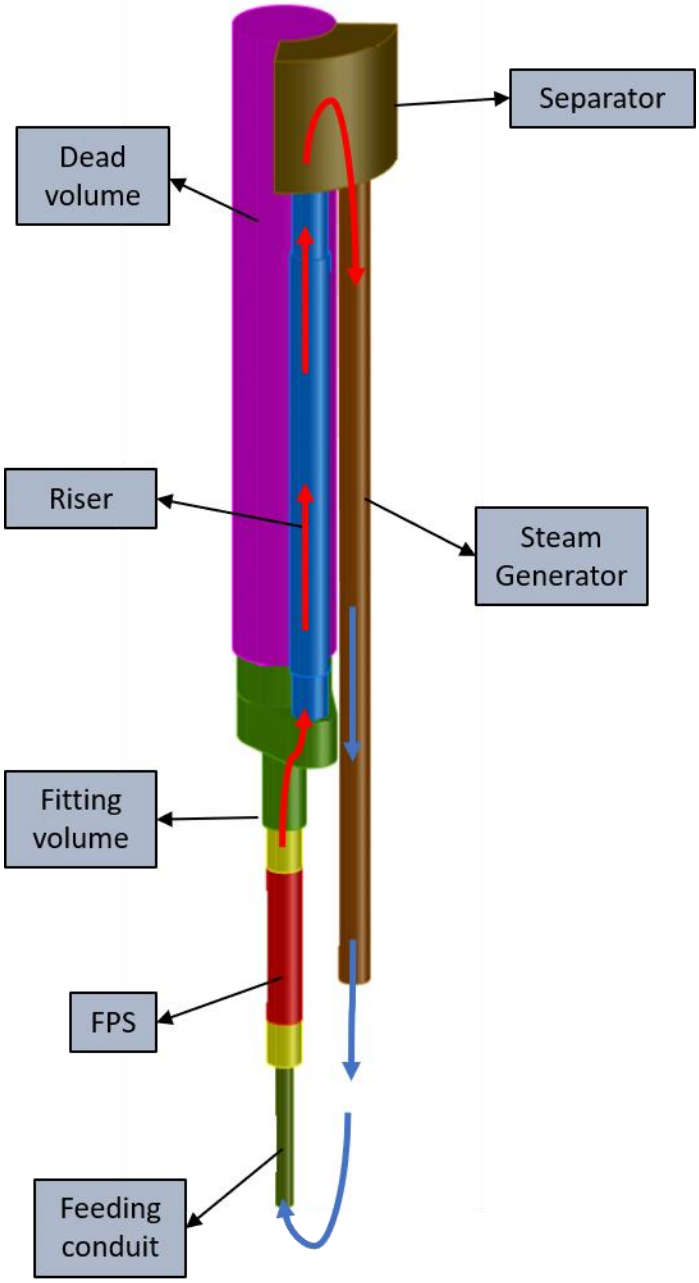

Figure 41. HERO test section

Figure 42. DWBT SG bundle

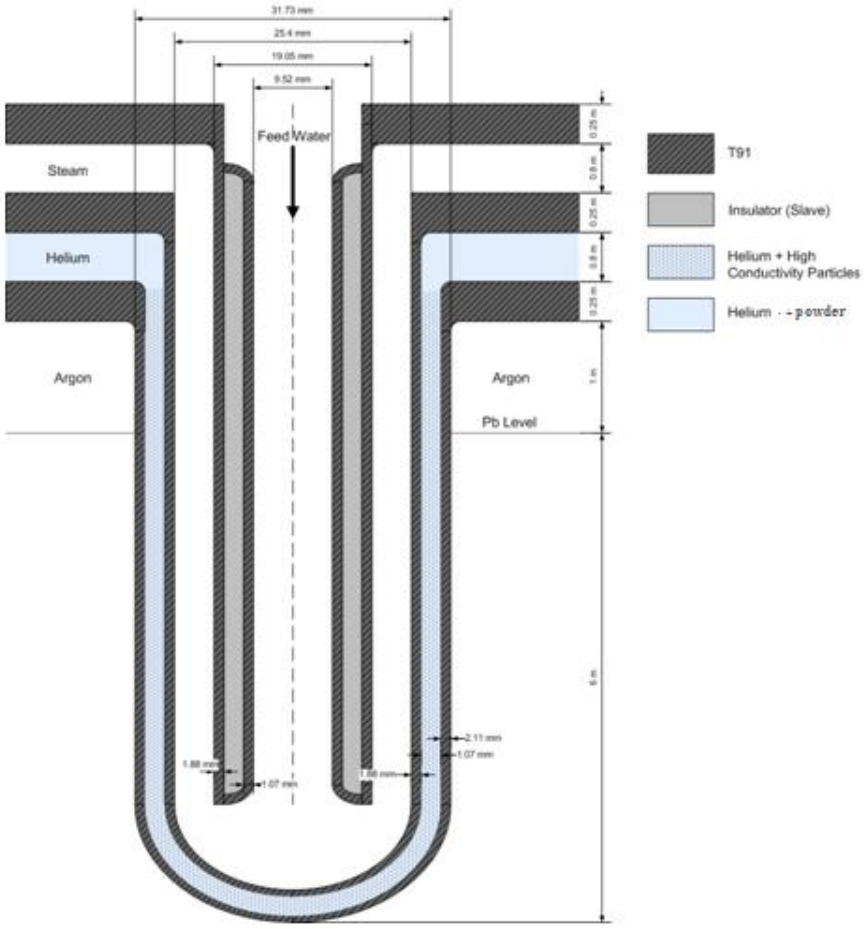

Figure 43. Double wall bayonet tube

2.2.2 Pre-test activity

2.2.2.1 Description of the thermal-hydraulic model

CIRCE-HERO nodalization scheme, adopted for pre-test calculations, is based on the model #2 presented in section 2.1.3. The model has been upgraded to reproduce the new test section. It maintains the division in two macro-regions: a mono-dimensional scheme of the primary system and of the DWBTs secondary side, and a multi-dimensional model of the pool. Figure 44 shows the 1D nodalization. It is the same presented in section 2.1.3 for model #2 of CIRCE-ICE test facility, except for the SG, the DHR system and the FPS external shroud.

SG primary side is simulated with a single equivalent pipe, composed of 43 control volumes and hydraulically coupled with the separator on the top, and the 3D component on the bottom. The pressure drops related to the spacer grids are evaluated with Eq. 2, based on the flow area occupied by the grids (see Figure 43). The secondary side of the steam generator bayonet tubes (SGBTs) is collapsed in two equivalent pipes: the first one for the descending side and the second one for the annular riser. Feedwater inlet conditions are set with a time-dependent volume, connected with the inlet section of the descending pipe using a time-dependent junction which imposes the inlet mass flow rate. Another time-dependent volume fixes steam pressure at the outlet of the DWBTs outlet [65]. An overall number of 129 heat structures reproduces the thermal behavior of the unit: 48 heat structures (960 nodes) couple descending and ascending side of the DWBT modelling, 42 heat structures (1302 nodes) reproduce the heat transfer between SG primary and secondary sides (a multiplicative factor of 1.02 is applied on the primary side to correct the HTC according to Ushakov correlation) and 39 heat structures (1354 nodes) simulates heat losses toward the pool.

In CIRCE-ICE configuration, the TCs penetrations through the FPS cylindrical shroud realize a bypass loop within the pool, increasing the heat losses. The bypass loop has been included in model #1 and #2 presented in section 2.1.3. To reduce heat losses between FPS and cold pool, the penetrations have been closed, realizing a thermal insulation with stagnant LBE gap. In CIRCE-HERO modelling, the bypass loop has been deleted and stagnant LBE is included in the heat structures.

MULTID component is the same presented in section 2.1.3, except for the volume factors that are reassessed taking into account the absence of the DHR and the volume occupied by the DWBT SG.

The main dimensions of the model are summarized in Table 4

Table 4. CIRCE-HERO modelling dimensions

Parameters	**Value**
Number of hydrodynamic volumes	2942
Number of hydrodynamic junctions	7565
Number of heat structure mesh points	21153

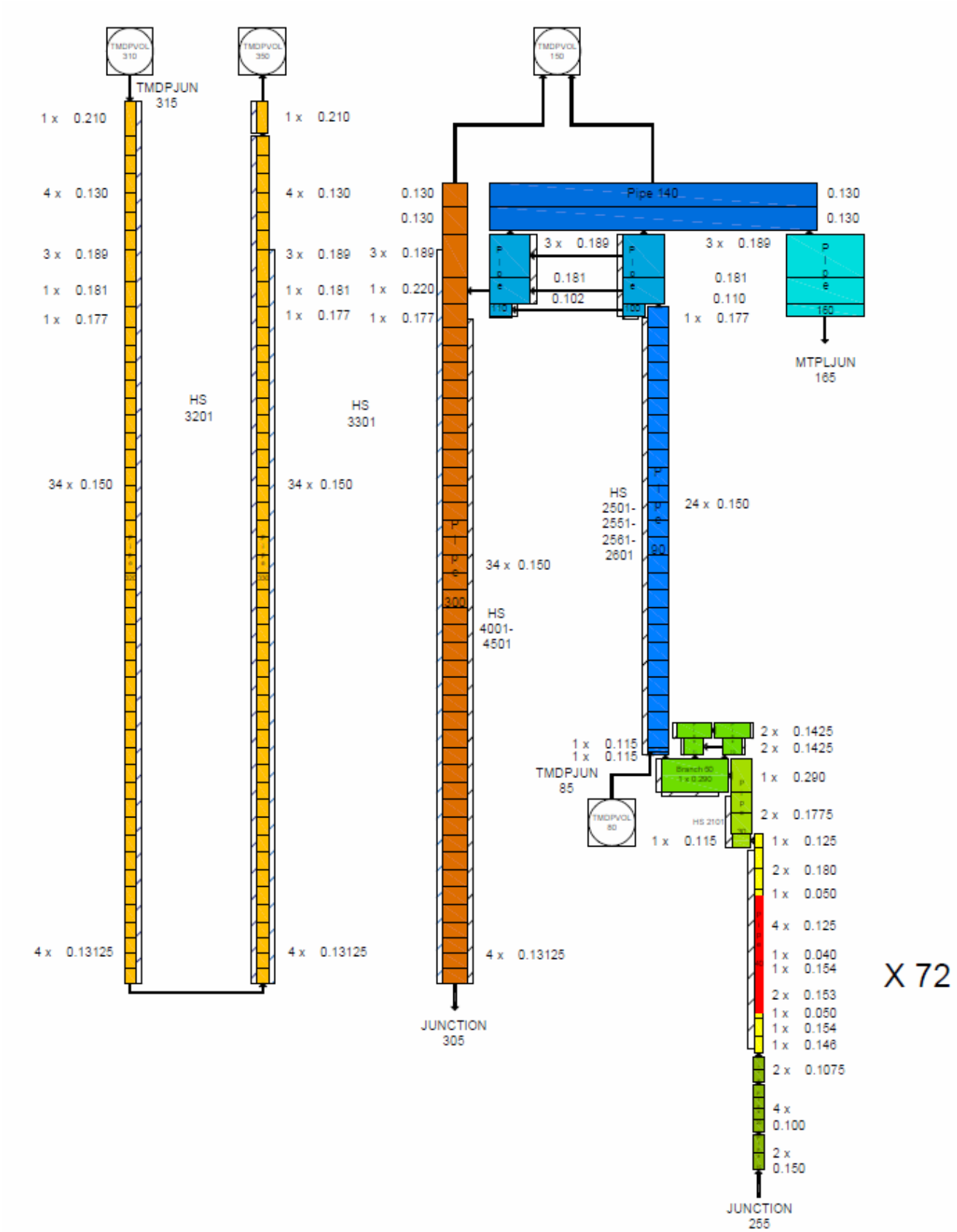

Figure 44. CIRCE-HERO nodalization scheme: 1D region

2.2.2.2 Identification of full power steady-state conditions

The experiment consists in the transition from forced to natural circulation occurring in a loss of flow accidental scenario. To identify initial conditions of the transient tests, several full power conditions are analyzed. The initial and boundary conditions of each case are summarized in Table 5. Case 1 is carried out to achieve a constant temperature drop across the FPS equal to 80 K in the range 673-753 K, which is representative of the temperature increase across the core of ALFRED. Case 2 aims to obtain the LBE mass flow rate across the SG equal to 44.7 kg/s, representative of the scaled down ALFRED SG. From case 1 to 6 the boundary conditions are the same, except for the Ar mass flow rate injected inside test section, as shown in Table 5.

Table 5. Full power calculations: boundary conditions

Parameter	Unit	Case 1	Case 2	Case 3	Case 4	Case 5	Case 6
FPS thermal power	kW	450.0					
LBE pool average temperature	K	669.0					
Ar flow rate	Nl/s	1.290	2.354	2.242	2.130	1.850	1.790
Steam pressure	Bar	172.0					
Feedwater inlet temperature	K	608.0					
Feedwater mass flow rate	kg/s	0.331					

The problem time of the full power calculations is set to 30000 s, in order to obtain steady-state conditions. The main results are summarized in Table 6. The full power steady-state, selected as the initial conditions for the transient simulations, is case 1. Figure 45 shows the zoom of the boundary conditions in the first 3000 seconds, which remain constant up to the end of the calculation. Simulation begins in steady-state conditions with the HS turned off and the injection of the argon and the feedwater disabled. At 50 s, the injection of Ar starts and the LBE mass flow rate reaches the value of 36.5 kg/s (see Figure 46). After 220 s, the HS increases the thermal power supplied up to the nominal value, reached at 390 s, and primary mass flow rises to the value of 38 kg/s. The temperature of the whole system increases (see Figure 47) and, at 2000 seconds, the secondary system is activated. The power removed by the SG contributes to the NC of the LBE, that reaches the nominal value of 39.2 kg/s.

After the activation of the FPS, LBE temperature at the outlet section of the heat source increases. The effect of the heat losses, combined with boundary effects, determines the relevant temperature drop between internal and external subchannels (respectively IC and EC), as shown in Figure 48, that depicts LBE temperature in five relevant sections of the FPS. During the first 2000 seconds, there is no temperature drop through the SG primary side and LBE temperature follows the same trend observed at FPS outlet section. When feedwater is injected, the HS outlet temperature and at the SG inlet temperature reaches the maximum values. SG starts to remove thermal power and LBE temperature at the SG outlet rapidly decreases to the value of 690 K. After reaching nominal boundary conditions, the temperature of the main flow path decreases to the nominal value. Figure 49 represents LBE temperature in the most representative section of the pool, which includes FPS and HERO SG. It shows the temperature difference between the internal components and the cold pool, where the temperature is uniform at the same vertical level and a thermal stratification phenomenon occurs at about 2.8 m from the bottom of the vessel. The level of the thermal stratification is deeply related to the heat losses from the internal component, occurring at the same level of the HS hottest zone.

LBE free level, initially set to 7.986 m from the bottom of the main vessel (0.33 m from the bottom wall of the separator), moves due to the overall pressure drops and to the thermal expansion of LBE. The free level

difference between pool and separator (about 200 mm at full power steady-state conditions, see Figure 50) provides an estimation of the overall irreversible pressure drop of the main flow path.

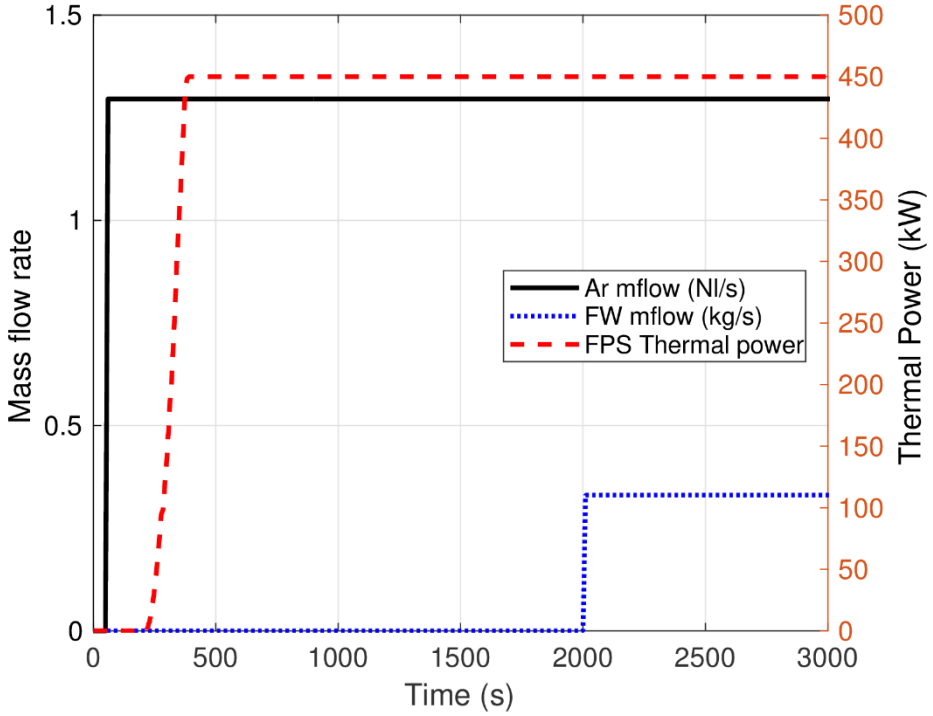

Figure 45. Full power calculations: boundary conditions

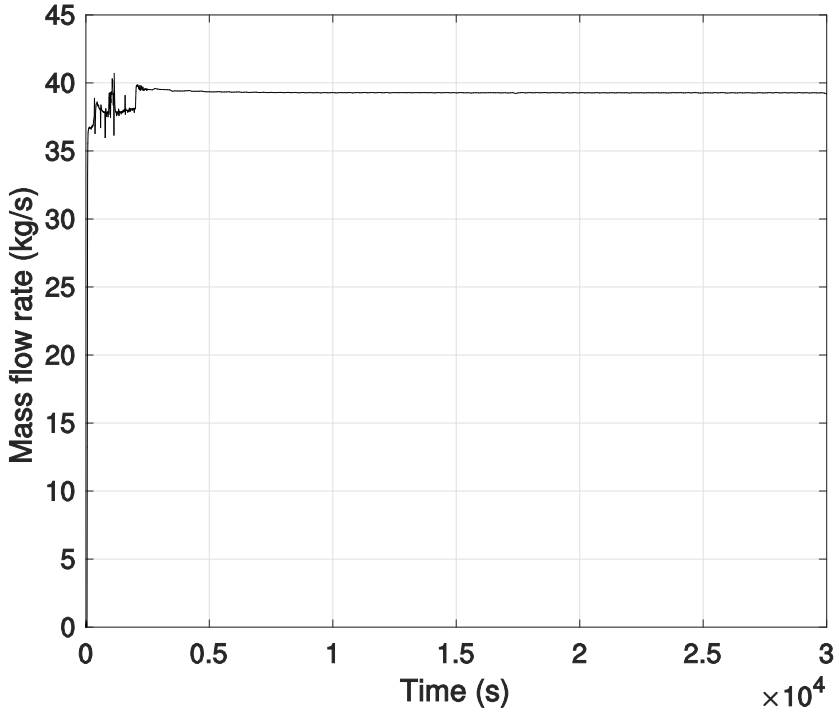

Figure 46. Case 1: LBE mass flow rate

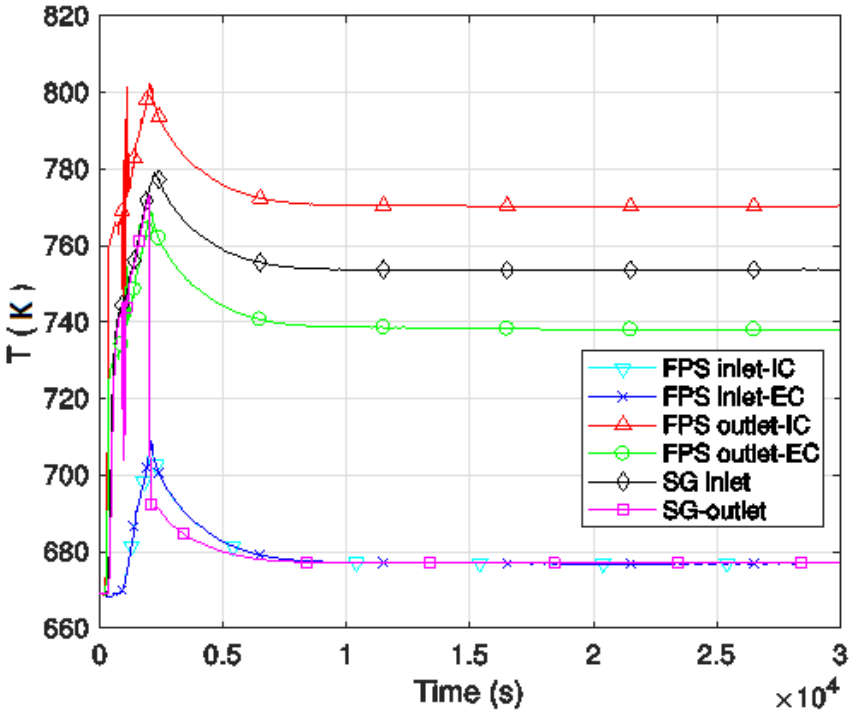

Figure 47. Case 1: LBE temperatures

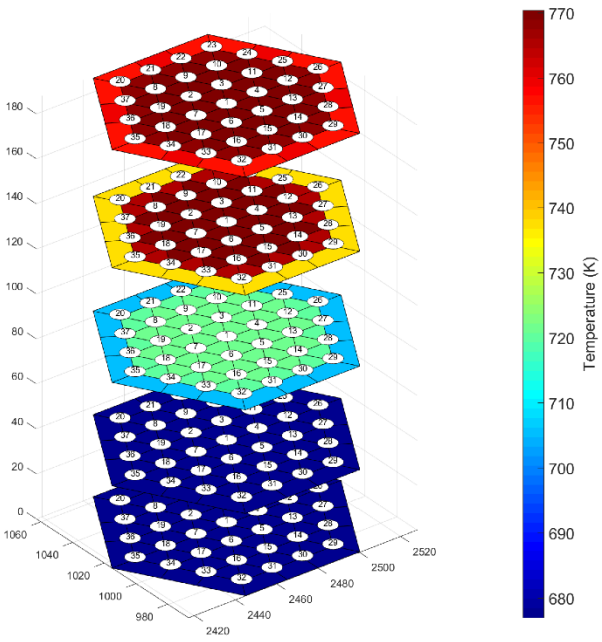

Figure 48. Case 1: FPS temperatures

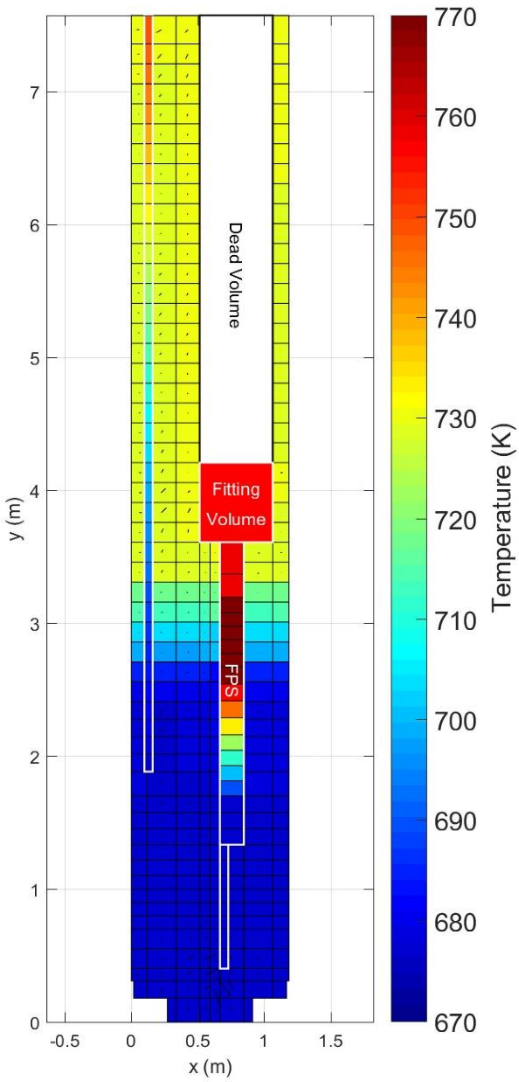

Figure 49. Case 1: pool temperatures

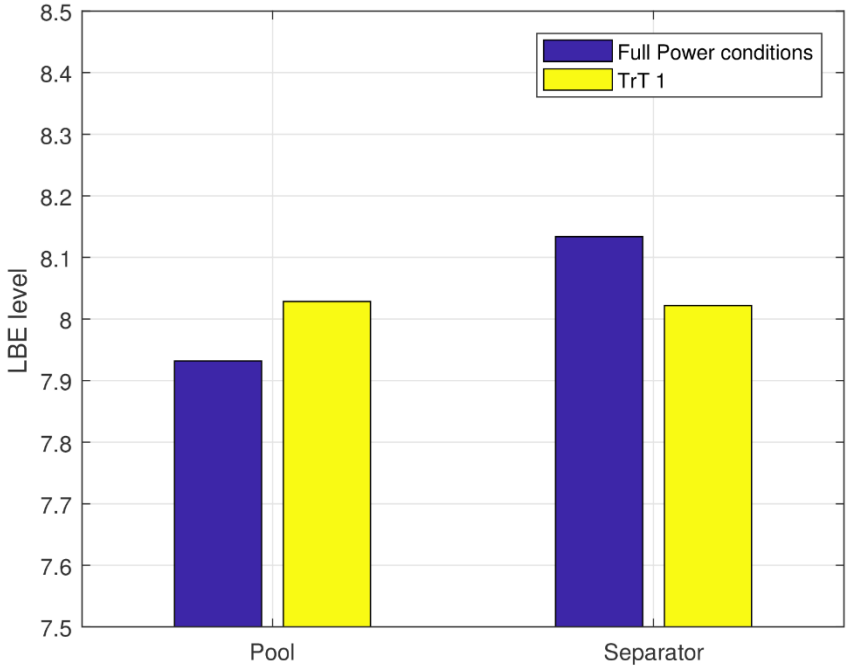

Figure 50. LBE free levels

Table 6. Full power calculations: main results

Parameter	Unit	Case 1	Case 2	Case 3	Case 4	Case 5	Case 6
FPS LBE inlet T	K	677.0	672.5	672.3	672.1	671.5	671.2
FPS LBE average outlet T	K	760	740.9	741.4	742.0	743.8	744.3
HERO LBE inlet T	K	753.8	732.3	733.2	733.6	734.7	734.9
HERO LBE outlet T	K	677.1	672.5	672.2	672.2	671.5	671.1
LBE mass flow rate at inlet section of HERO	kg/s	39.2	44.5	43.9	43.4	42.1	41.7
Power removed by HERO	kW	438.0	440.0	439.0	439.0	438.0	440.0
Steam max T	K	672.1	659.2	659.1	659.1	659.1	658.8
Heat losses	kW	12.0	10.0	11.0	11.0	12.0	10.0

2.2.2.3 Transient analysis

Starting from the full power steady-state conditions of case 1, five transient tests have been evaluated.

Transient test 1 (TrT 1) consists in a protected loss of primary pump, characterized by the following boundary conditions:

- argon injection decreases to 0 following a calibrated curve, simulating the presence of a pump flywheel;
- thermal power supplied by the HS reproduces a decay heat curve, scaled down from a reference curve for fast reactor and compensated with heat losses towards the environment;
- feedwater mass flow rate decreases to 10% of the nominal value, simulating the DHR activation.

Transient test 2 investigates the effect of higher secondary flow rate during the DHR operation; boundary conditions are the same of the TrT 1, except for the FW mass flow rate, set to 20% of the nominal value. Transient test three consists in a loss of primary pump plus loss of DHR function in hot condition, maintaining the same boundary conditions of TrT 1, except for FW injection which decreases to zero. Transients 4 and 5 investigate the effect of the heat losses compensation; boundary conditions are the same of TrT 1 and 3, except for the decay curve that is not compensated.

The transient analysis aims to investigate the short-term operation after the postulated accidents. For this purpose, the problem time is limited to 1000 s. Figure 51 shows a zoom of the first 300 s of the boundary conditions:

- FW mass flow rate instantly decreases to the final value;
- HS thermal power rapidly decreases below 100 kW; the compensated decay power is reached at about 150 s;
- Ar injection system enhances LBE circulation during the transient beginning; at about 25 seconds, Ar flow rate is still 50 % of the nominal value and, at 300 s, it becomes zero.

Comparison between the compensated and no-compensated decay curve is depicted in Figure 52.

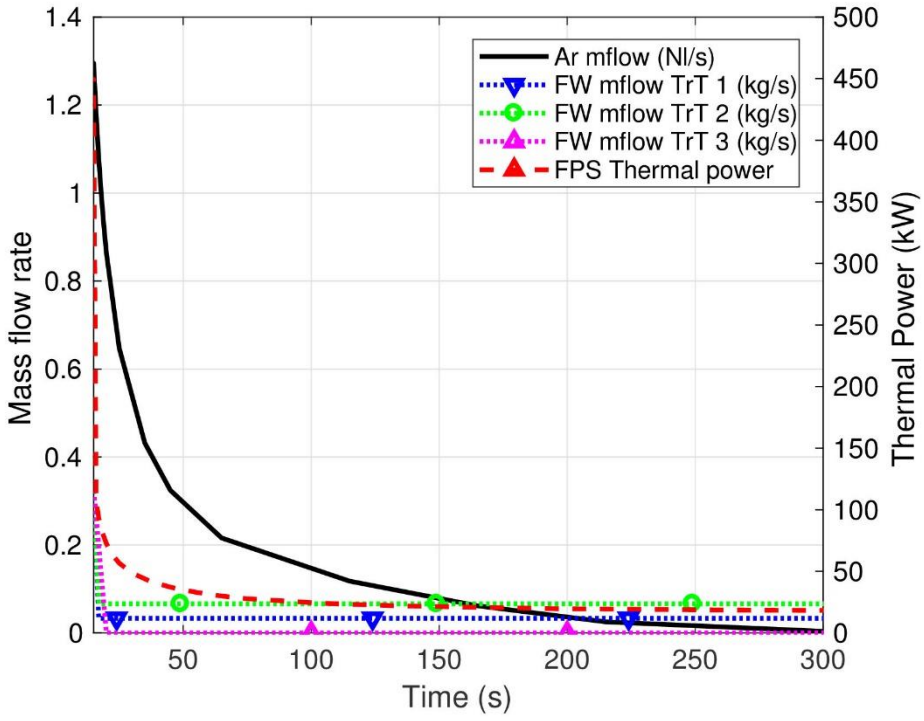

Figure 51. Transient test: boundary conditions

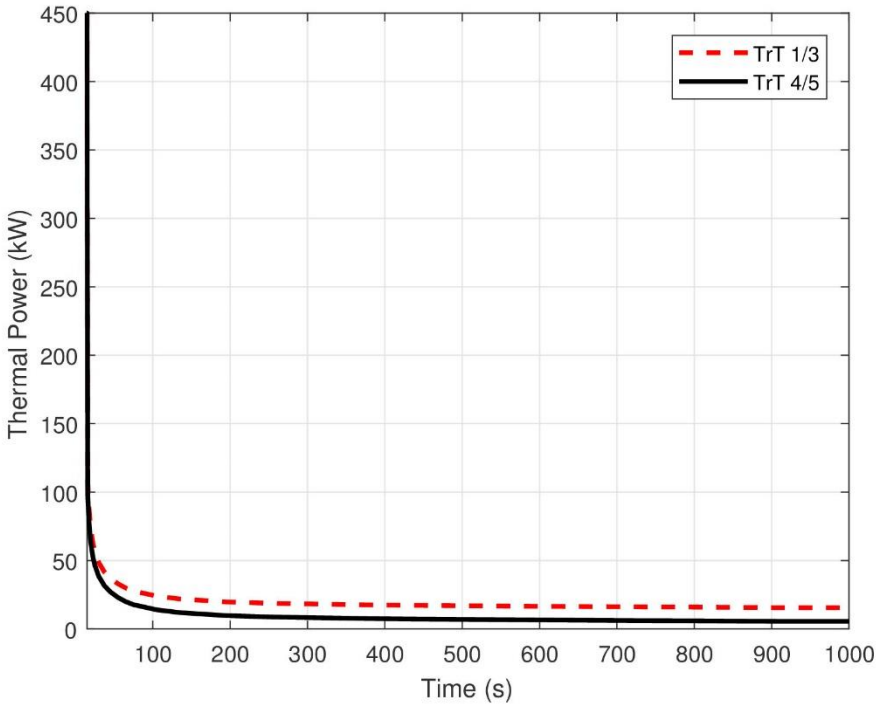

Figure 52. Transient test: decay heat curve

The main events of the TrT 1 are summarized in Table 7. Figure 53 and Figure 54 depict the evolution of LBE mass flow rate at the SG inlet section and of the inlet and outlet temperatures of FPS and SG. LBE temperature at the outlet section of the HS rapidly decreases to the minimum value of 690 K. At this time, LBE mass flow rate is close to 50% of the nominal value and FPS thermal power approaches the compensated decay power; it causes the minimum value of the temperature increase across FPS and, after a delay time of about 30 s, the minimum value of the temperature drop across the SG (outlet LBE temperature reaches the peak value of 715 K, see Figure 54). LBE temperature at the inlet section of SG is not significantly influenced by the temperature trend at the HS outlet. This is due to the thermal inertia of the large volume of liquid metal contained within the separator and to the low value of the primary mass flow; therefore, LBE temperature inside the separator decreases slower than in the components upstream.

At about 25 seconds, the oscillations observed in the LBE mass flow rate are caused by fluctuation of the free level, that passes through two contiguous control volumes inside the separator. When the argon injection is disabled, primary mass flow rate reaches the minimum value of 1.4 kg/s and FPS outlet temperature amounts to the peak value of 745 K, remaining lower than the nominal value observed at full power operation. At the same time, temperature drop across the steam generator increases and LBE outlet temperature reaches the minimum value of 630 K, lower than LBE temperature inside the pool, as shown in Figure 55 (c). LBE mass flow rate increases to the value of 3.7 kg/s and the average temperature of the whole system decreases. Figure 55 shows evolution of LBE temperature inside the main vessel during the transient test, highlighting that, at the thermal stratification level, the vertical gradient of the temperature is reduced in respect to steady-state conditions, as shown in Figure 56, where LBE temperature within the pool is plotted versus the elevation from the bottom of the vessel. This phenomenon is due to the hot LBE exiting the SG during the first instants of the transient test. After 350 s, LBE exiting the SG is cooler than liquid metal inside the pool, which starts to decrease its temperature

and causes the vertical trend at the end of the test. Figure 57 summarizes evolution of the LBE temperature inside the FPS.

The lower value of LBE mass flow rate causes the reduction of the irreversible pressure drops across the whole system. As a consequence, the free level inside the separator and the pool moves, respectively, downstream and upstream of about 100 mm, as shown in Figure 50, where the positions of the free levels are compared with the position at the beginning of the test.

Table 7. TrT 1: main events

Time (s)	Main events
0	Start of the transient sequence
80	Minimum value of the LBE temperature at the outlet section of the FPS
110	Peak temperature at SG outlet section
340	Minimum value of the LBE mass flow rate
350	Peak temperature at the outlet section of the FPS and minimum temperature at the outlet of HERO
1000	End of the transient test

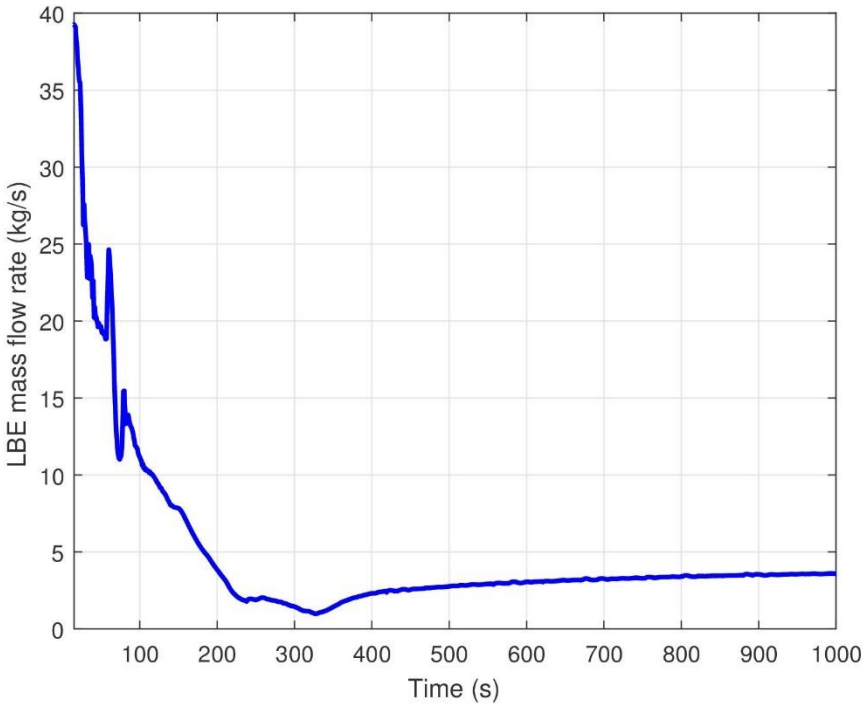

Figure 53. TrT 1: LBE mass flow rate

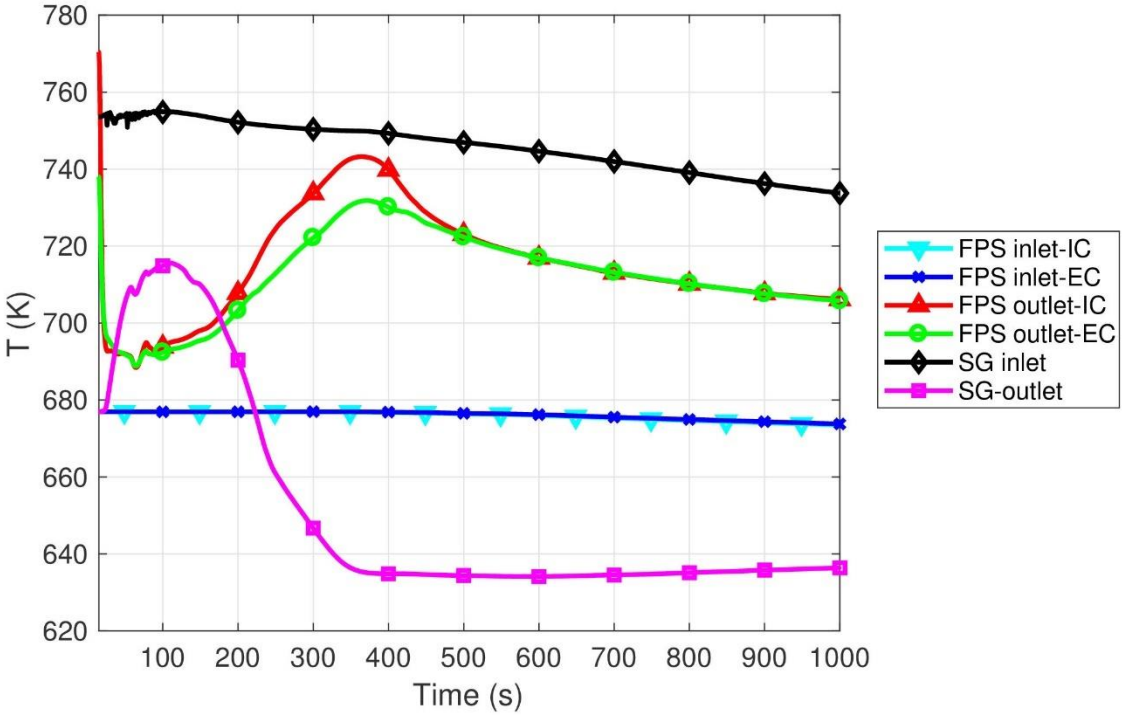

Figure 54. TrT 1: LBE temperatures

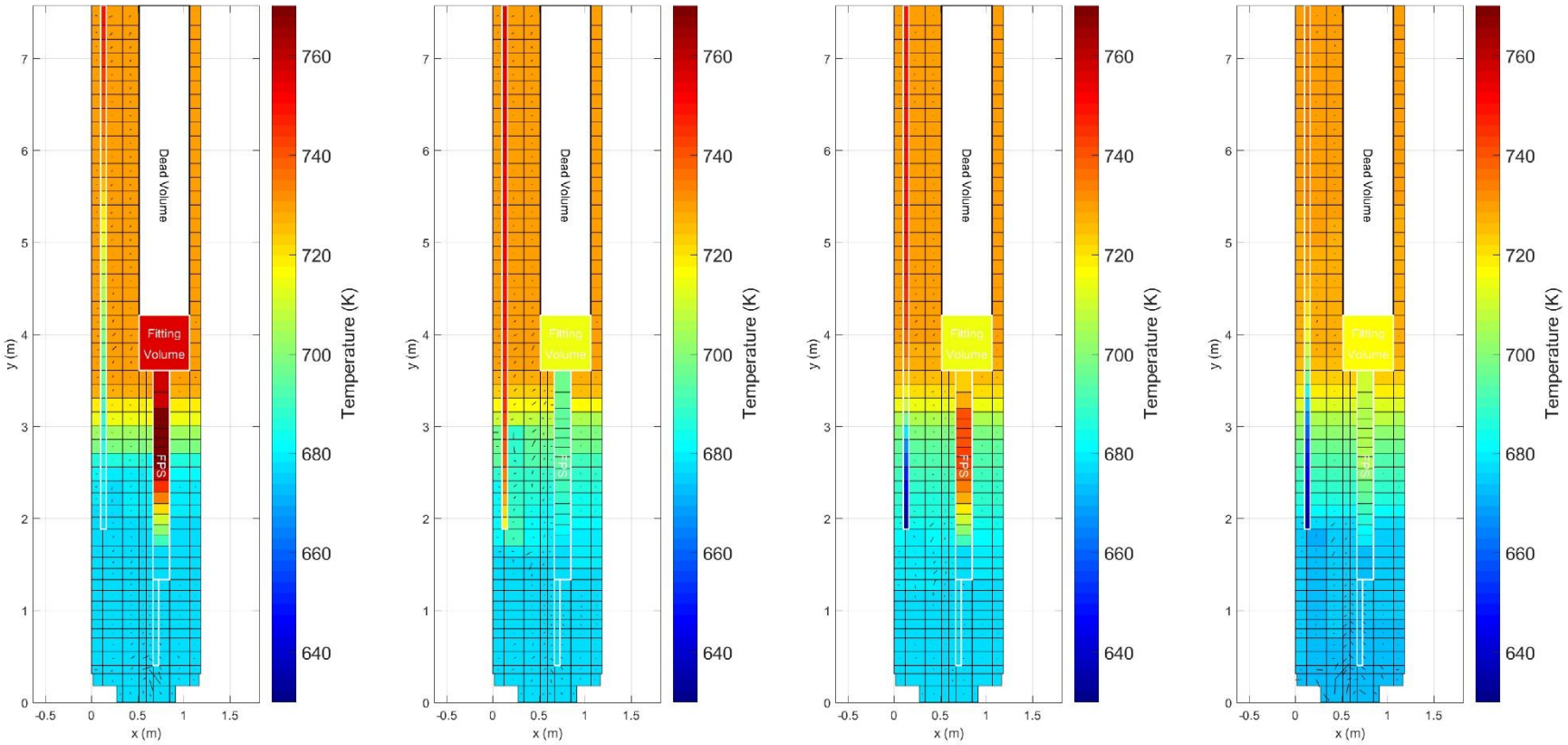

(a) 0 s (b) 110 s (c) 350 s (d) 1000 s

Figure 55. pool temperature evolution

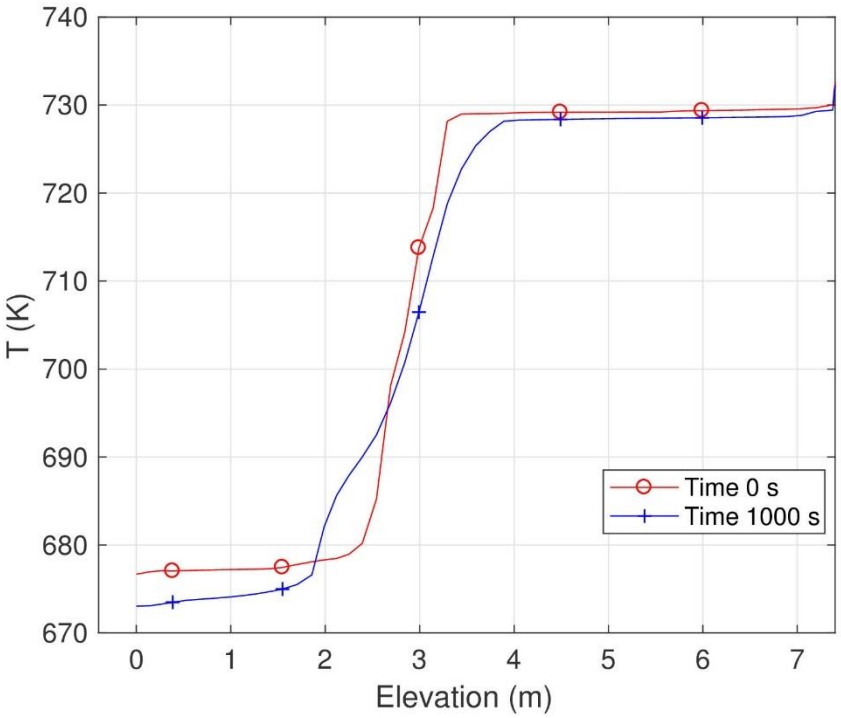

Figure 56. TrT 1: thermal stratification

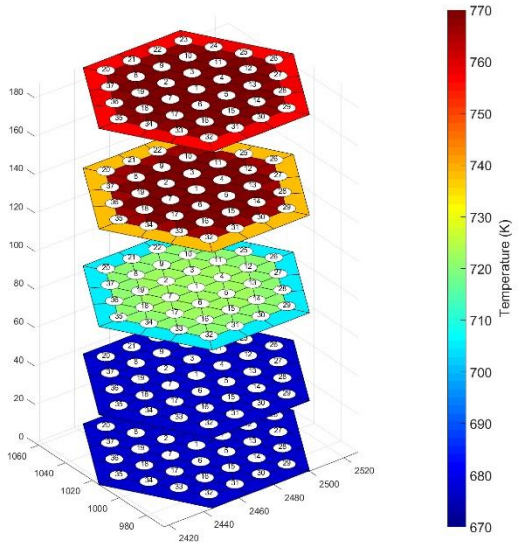

(a) 0 s

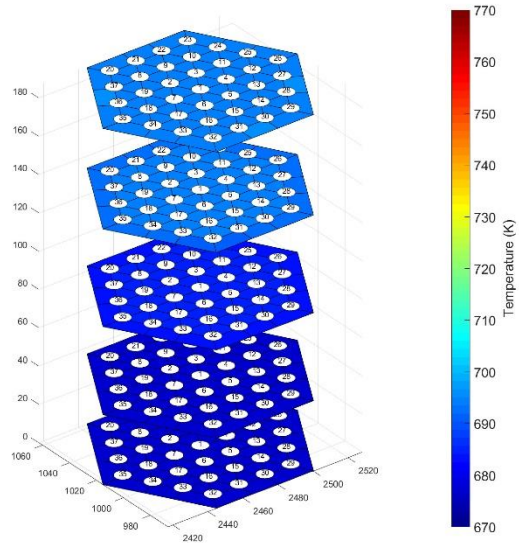

(b) 80 s

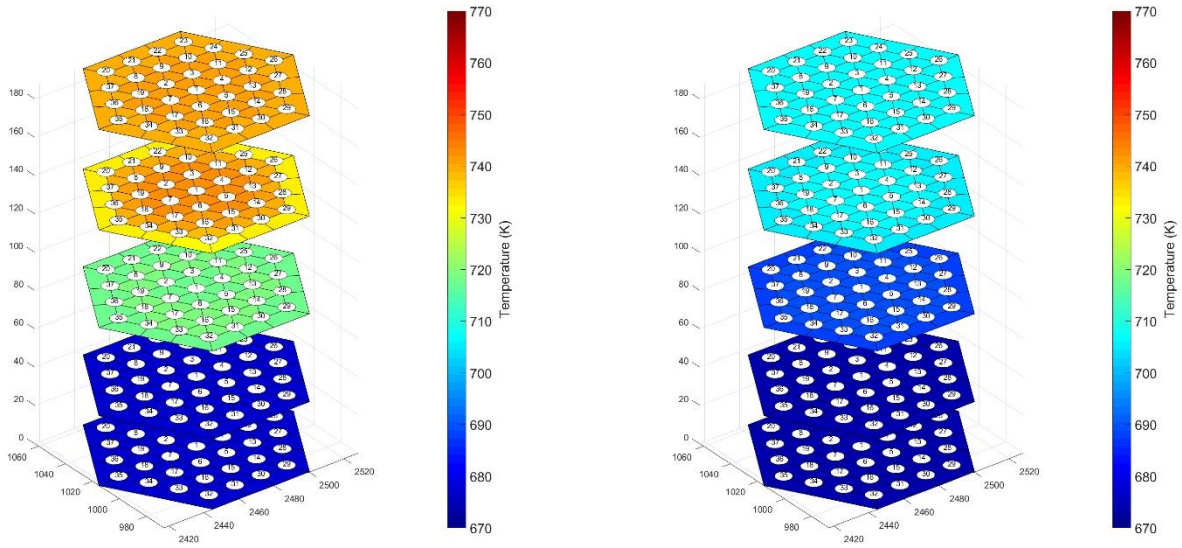

(c) 350 s (d) 1000 s

Figure 57. TrT1: FPS temperature evolution

The following analysis concerns the comparison of the results of TrT1, 2 and 3. Figure 58 shows LBE mass flow rate at the SG inlet section; during the first 50 seconds, primary flow is still enhanced by argon injected into the riser (see Figure 51) and the trend of the three simulations is similar, as the LBE temperature at the inlet and outlet section of the FPS and SG (see Figure 59 and Figure 60). After 150 s, gas injection is decreased enough to observe differences between the three calculations: the most important contribution to the driving force is the natural circulation, promoted by the thermal power removed by the SG, and LBE mass flow in test 2 is constantly higher than MFR calculated in TrT 1 and 3. In particular, during the TrT 3, the driving force only depends on the heat losses through the main vessel, since feedwater injection is halted. In this case, LBE temperature at the SG outlet reaches the maximum value of 738 K, at about 110 s, remaining higher than 730 K up to 200 s (see Figure 60); at the same time FPS outlet temperature is close to the minimum value of about 690 K. Due to this thermal configuration, a natural circulation cell arises, opposing itself to the residual lift force exerted by the driving gas. This gas flow, in the absence of the feedwater contribution, it is no longer sufficient to push LBE inside the FPS, causing the temperature peak of 738 K at the HS inlet (see Figure 59). The liquid metal reverse flow is maintained between 220 and 370 s, as shown in Figure 58; afterward, the gradual heating of the FPS, due to the decay heat, weakens the temperature gradient responsible for the opposing circulation and the forward flow are restored, assuming the value of 0.5 kg/s. Due to the compensation of the heat losses, the temperature of the whole system increases reaching, at the HS outlet, the maximum value of 820 K, close to the maximum temperature experimentally allowed.

Figure 61shows LBE temperature inside the pool, comparing final conditions of each calculation. The expansion of the thermal stratification zone, highlighted at the end of the TrT 1, also occurs during TrT 2 and 3. At the end of test 2, the vertical trend of the temperature is similar to the final conditions of the TrT 1, assuming lower temperature in the bottom volume of the pool. Due to the higher temperature at the outlet section of the SG, in the TrT 3 the stratification zone is wider than in TrT 1 and 2, arriving at 1 m from the bottom of the pool (see also Figure 62).

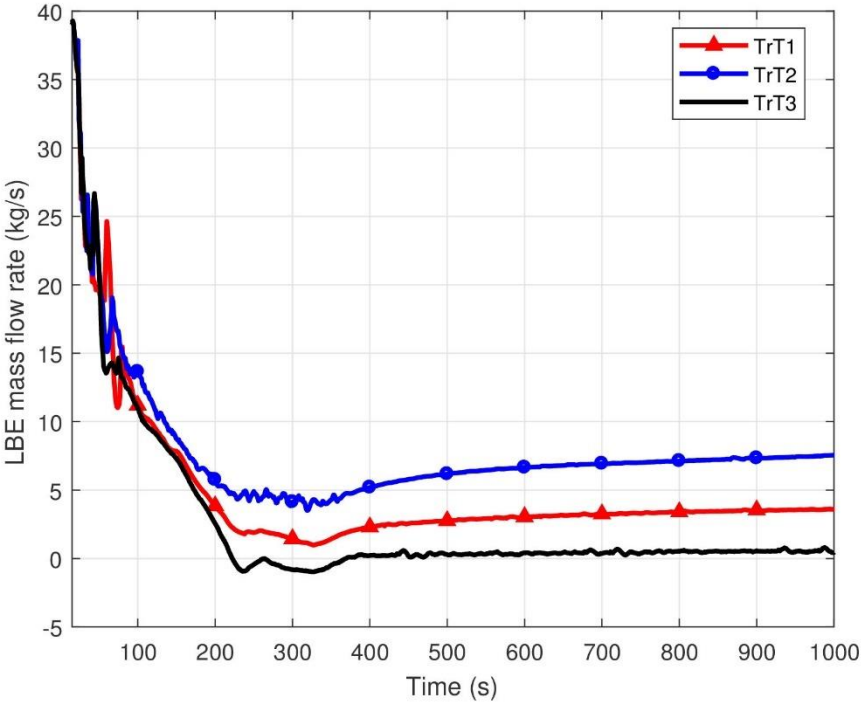

Figure 58. First comparison: LBE mass flow rate

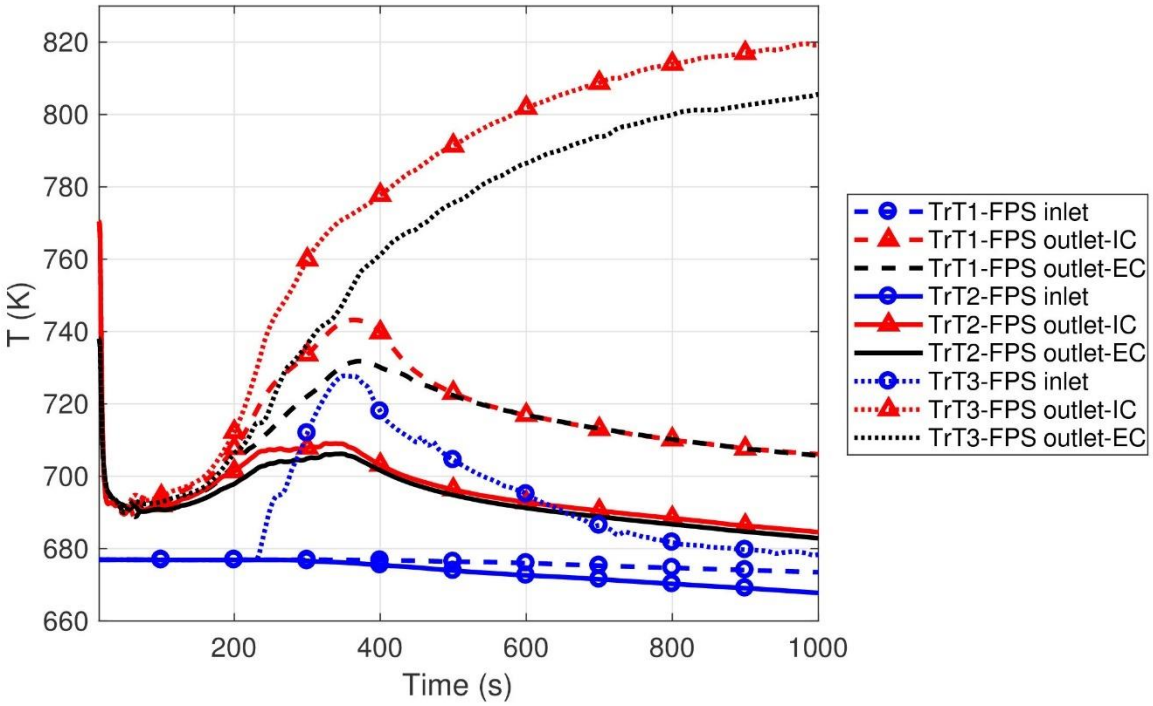

Figure 59.First comparison: FPS temperatures

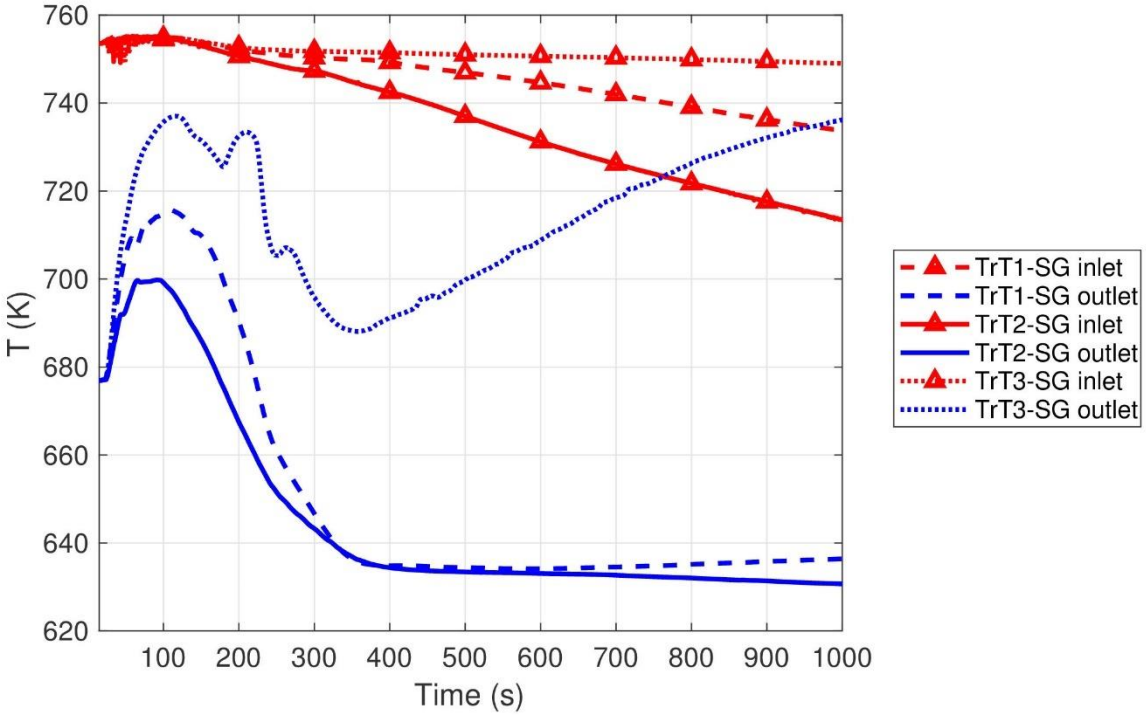

Figure 60. First comparison: SG temperatures

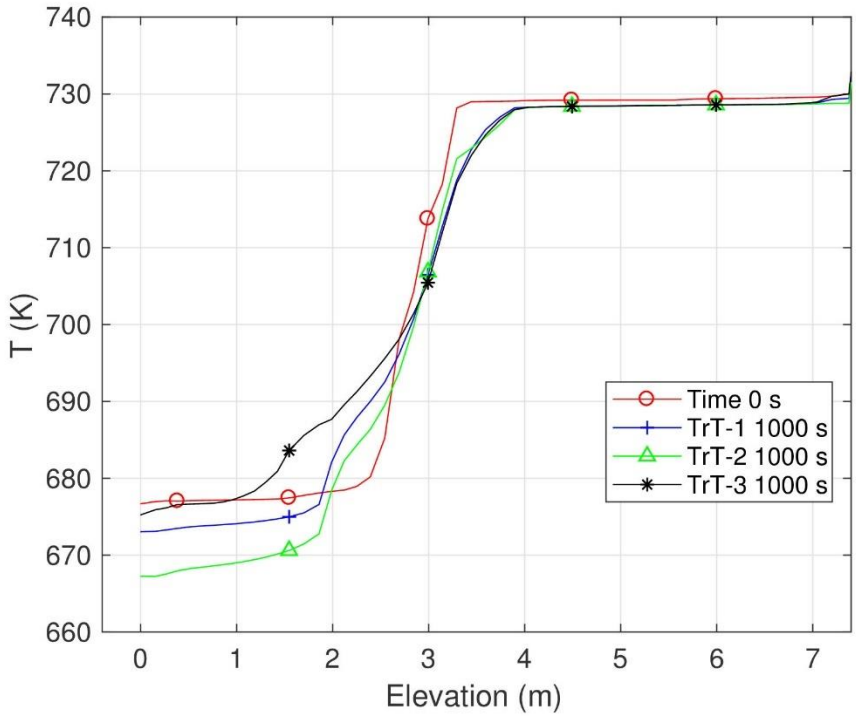

Figure 61. First comparison: thermal stratification

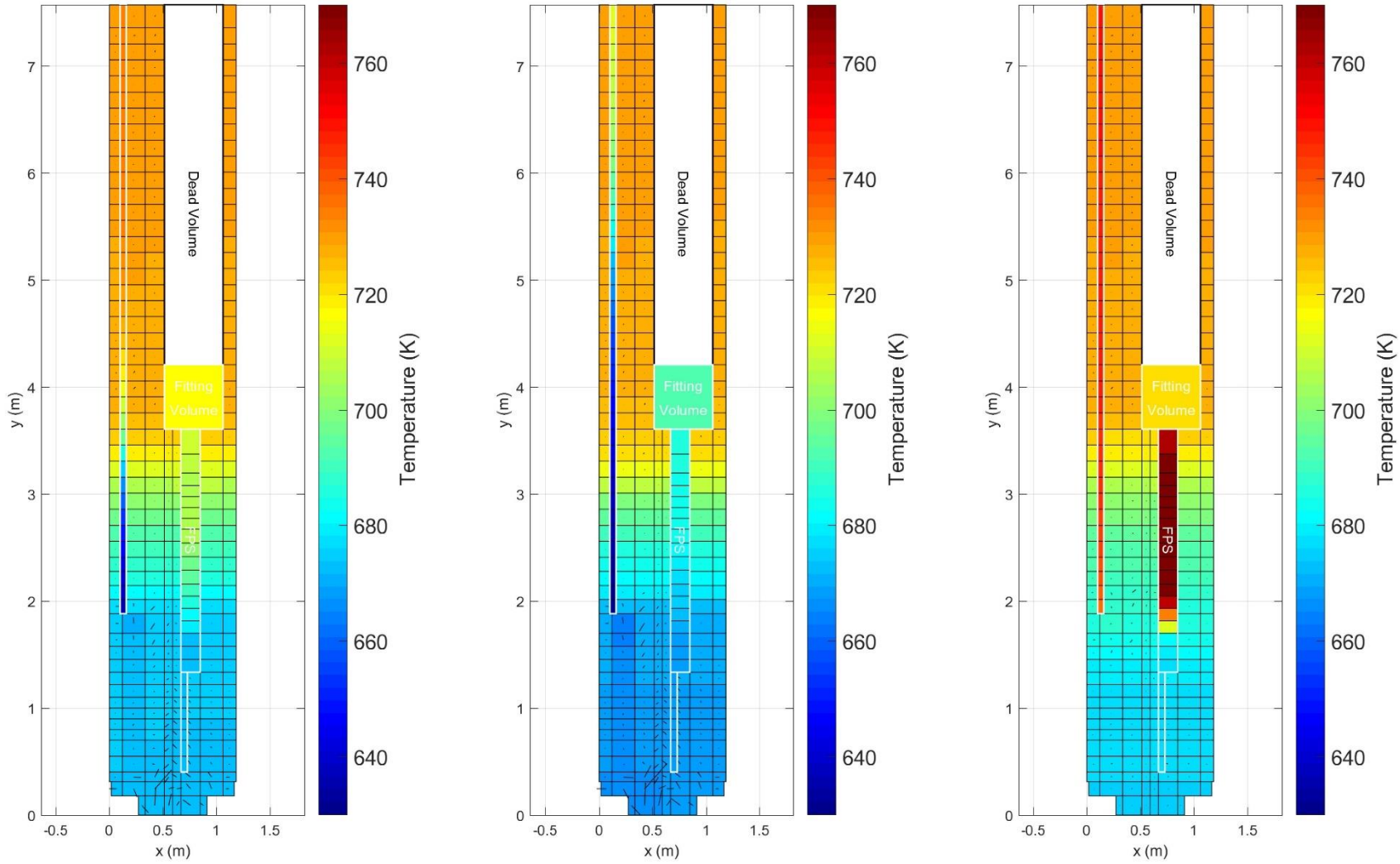

(a) TrT 1 (b) TrT 2 (c) TrT 3

Figure 62. First comparison: pool temperature

In order to evaluate the effect of the heat losses compensation, TrT 1 and 3 are repeated assuming the typical decay heat curve, as shown in Figure 52. Figure 63 compares LBE temperature at the inlet and outlet temperature of the HS and SG observed in TrT 1 and 4. The main discrepancy is the outlet temperature of the FPS, where the difference of the thermal power supplied affects the LBE temperature which, in TrT 4, is constantly lower than TrT 1. Because of the duration of 1000 seconds and the low primary mass flow rate, no difference for the temperature field is found between the two simulations at the inlet section of the SG; this value only depends on the heat losses along the hot leg which is comparable in both the calculations. The difference at the SG outlet section is due to the slightly lower LBE mass flow rate during test 4 which causes a higher temperature drop across the steam generator. It is not enough to variate LBE temperature inside the pool though, since the large heat capacity of the liquid metal absorbs the slight difference of temperature, causing the same temperature at the inlet of the FPS (see Figure 65).

The same parameters are plotted in Figure 64, comparing the results of TrT 3 and 5. The main discrepancy is still found for the outlet temperature of the HS (about 60 K at the end of the calculation). Notwithstanding the average outlet temperature increases during test 5, at the end of the simulation the maximum temperature inside the HS is lower than the initial value. Another effect of the lower thermal power supplied is the decrease of the driving force that causes a primary mass flow near to zero; this is the reason for the large difference of the SG outlet temperature between the two calculations. After the restoration of the forward flow, in test 3, LBE mass flow rate is enough to move the hot liquid to the bottom edge of the SG, reducing the temperature drop across the component. Instead, in test 5, the reverse flow decreases the outlet temperature to the value of 685 K, which remains practically constant up to 1000 s, due to the quasi-stagnant conditions that occur after the dissipation of the reverse flow. This effect is also highlighted by the FPS inlet temperature, where the very low value of the LBE mass flow is not enough to decrease too much the temperature from the peak of 710 K.

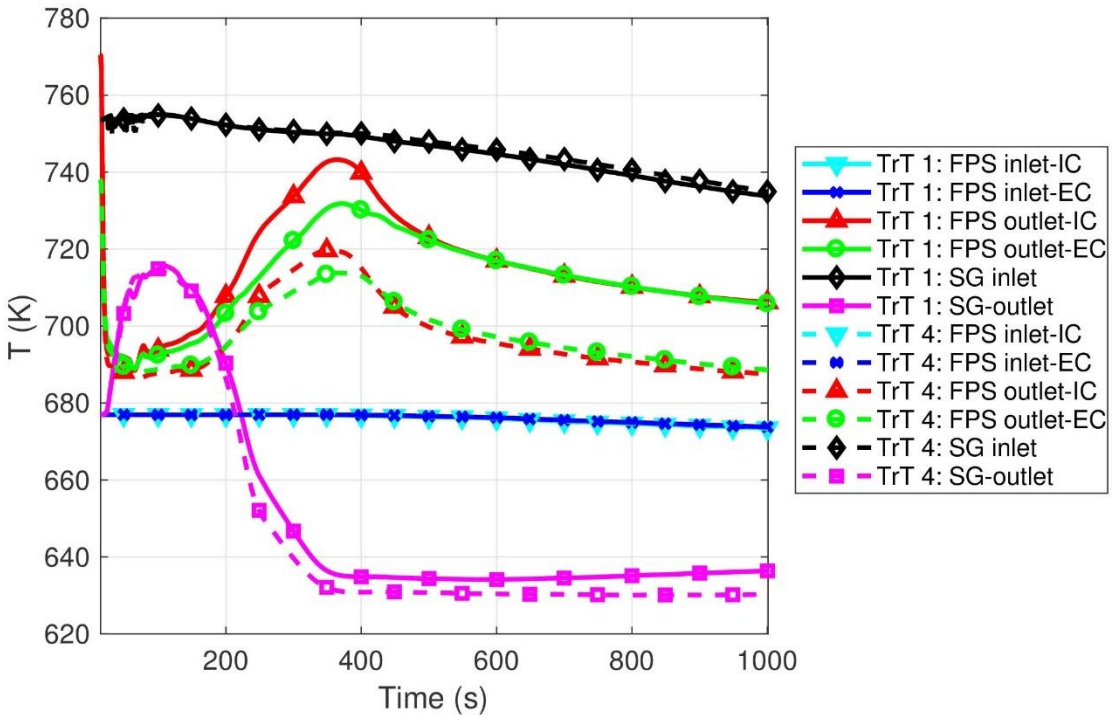

Figure 63. Second comparison: LBE temperatures

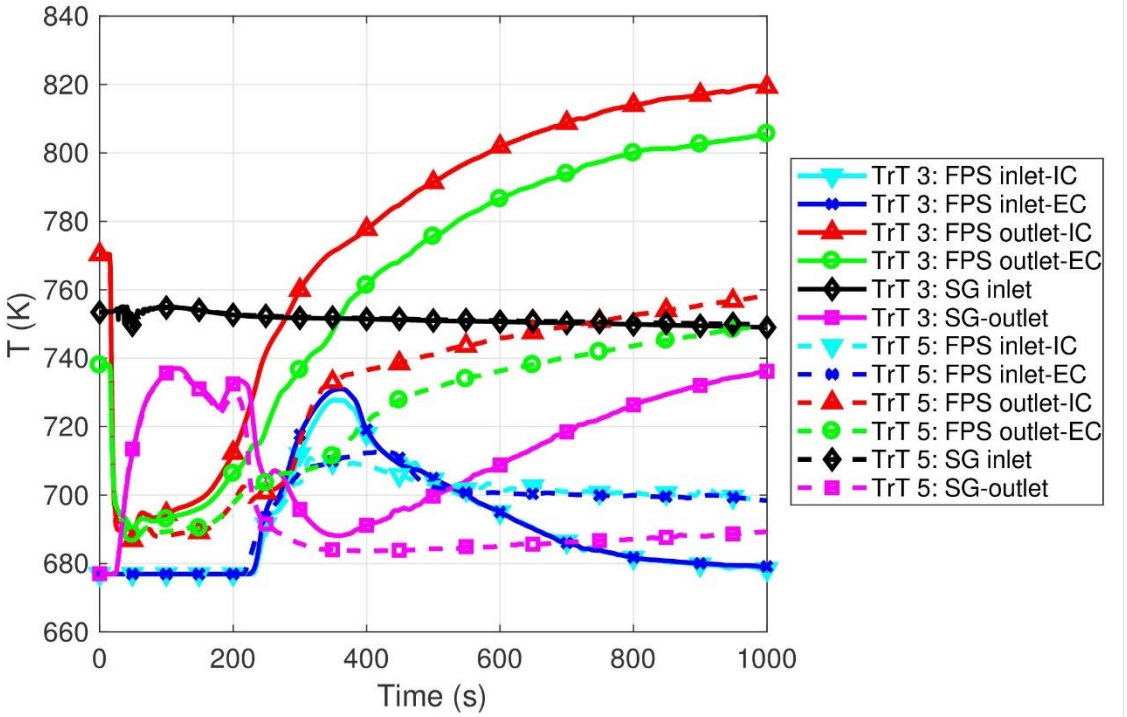

Figure 64. Third comparison: LBE temperatures

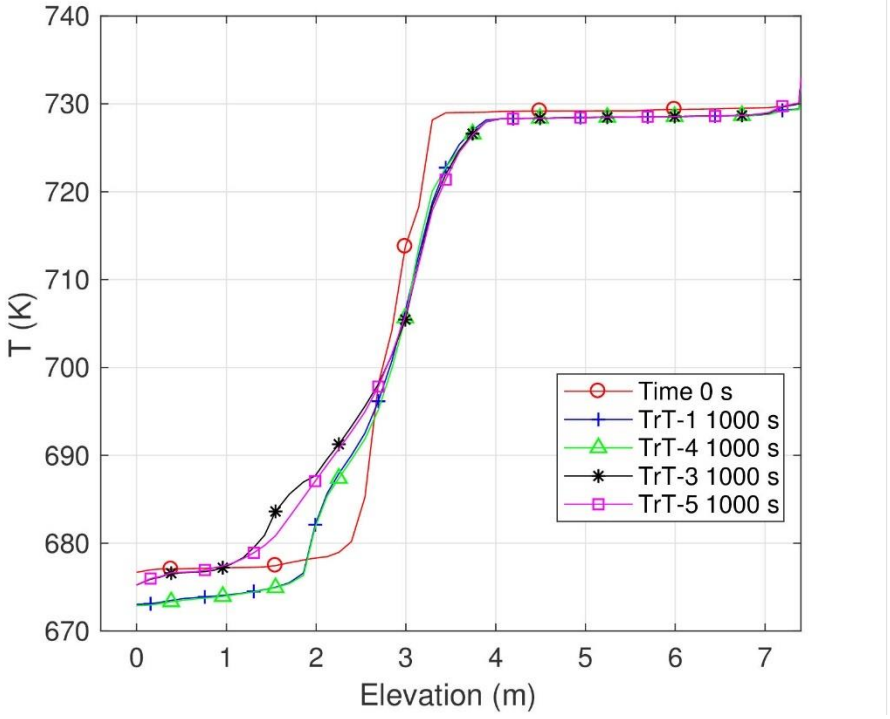

Figure 65. Second and third comparisons: thermal stratification

2.2.2.4 Conclusive remarks

The objective of the pre-test activity has been to evaluate performance of the DWBT SG installed within CIRCE facility. Simulations have been performed with RELAP5-3D© code, upgrading the validated model of CIRCE-ICE test facility.

The analysis has been aimed to investigate the transition from forced to natural circulation in loss of flow accident scenario. Full power steady-state conditions have been identified carrying out a sensitivity analysis considering different boundary conditions. Starting from the reference steady-state conditions, five transient calculations have been carried out: the transient tests 1 and 2 have simulated a protected loss of flow accident in which the SG has simulated the activation of the DHR system, reducing respectively feedwater mass flow rate to 10 % and 20 % of the nominal value. The transient test 3 has been identified to simulate the loss of primary pump plus the loss of DHR function in hot condition, reducing to zero the secondary mass flow rate. The three calculations are performed compensating the decay power with the heat losses towards the environment. In order to evaluate the effect of this assumption, transient tests 1 and 3 have been repeated using a no-compensated decay heat curve. The simulation results have highlighted that the HERO test section guarantees sufficient natural circulation conditions to remove the decay heat in the short term.

The calculations have provided useful information for the realization of the validation benchmark and the transient test 1 has been chosen as the reference scenario.

2.2.3 Post-test activity

2.2.3.1 Overview of the experimental campaign

Based on the results obtained in the pre-test activity, a set of three experimental tests has been carried out in the framework of the H2020 SESAME project. The tests consist in three protected loss of flow accidents (PLOFAs), occurred during the normal operation of the facility. The transients have been carried out managing the FPS power, the Ar injection system and the FW mass flow rate across the secondary loop [59].

Two of the three tests have been the subject of the post-test computational activity: Test 3 and Test 1.

2.2.3.1.1 Test 3

Test 3 has been selected for the validation benchmark promoted in the framework of H2020 SESAME project. The experiment consists in a PLOFA, simulating the loss of primary pump, the reactor SCRAM and the activation of the DHR system. Test starts at full power conditions, with 356 kW supplied to the HS and 2.75 Nl/s of argon injected to enhance primary circulation. Some uncertainties are related to measurement of the feedwater mass flow rate through the secondary loop. As reported in Ref. [59], assuming a water density of 640 kg/m3 and considering uniform distribution of the flow rate among the seven DWBTs, a total mass flow rate of 0.26 kg/s is obtained. This assumption is not confirmed by the experimental data; tube 1, that is not equipped with the turbine FM, is fed by higher mass flow rate, as demonstrated by the temperature acquired at the DWBTs outlet section. At the outlet of tubes 0, 3 and 4 superheated conditions are observed, whereas, at tube 1 outlet, saturated conditions are measured (TCs installed at the outlet section of tubes 2, 5 and 6 loss the signal during the test). The lack of information about steam quality at the outlet of tube 1, does not allow the estimation of the flow rate but a higher value is expected. In addition, the measured flow rate through tubes 0, 3, 4 and 5 highlights discrepancies in the magnitude of 10 %. In Ref. [59], an estimation of the FW mass flow rate is obtained from energy balance equation applied to the pre-heater, but this value is affected by uncertainty of the system efficiency. For these reasons, the Coriolis measurement is assumed as boundary condition for the full power calculation. This flow meter is installed downstream the volumetric piston pump and its measurements are affected by large fluctuations, probably induced by the pump (an accumulator is installed between pump and

flow meter to reduce the oscillations), which represent a large source of uncertainty. For the simulation, the mean value of 0.34 kg/s measured by the Coriolis FM is considered. FW is pre-heated to the inlet temperature of 609 K and the pressure of steam discharge line is regulated to 172 bar [59].

The transition of FPS power, FW inlet conditions and Ar injection occurs at the same time. The HS thermal power decreases to 5% of the nominal value in 240 s, following a characteristic HLM-cooled reactor decay heat curve; the Ar injection decreases to zero in 124 s, simulating the presence of a pump flywheel and the FW mass flow rate is reduced to 30% of the nominal flow reproducing the activation of a DHR system, maintaining the same inlet temperature and outlet pressure on the secondary loop [59].

2.2.3.1.2 Test 1

Test 1 consists in a protected loss of flow accident, starting from full power steady-state conditions. The main difference compared to Test 3 is the decreasing curve assuming for the gas injection, that, regarding Test 1, does not reproduce the presence of a pump flywheel.

The test starts at full power steady-state conditions obtained with the FPS power of 352 kW, argon flow rate of 2.75 Nl/s and FW total mass flow rate of 0.245 kg/s (even if significant uncertainties affect the measurement of the secondary MFR). The PLOFA sequence is reproduced reducing the FPS power to about 20 kW, following the same curve of Test 3, simulating the loss of primary pump by decreasing the Ar flow rate from 2.75 to 0 Nl/s with a linear trend in a time lapse of 10 s and reproducing the loss of heat sink and the consequent activation of the DHR system reducing the FW mass flow rate up to 30 % of the nominal value in a time lapse of 2 s [59][63].

2.2.3.2 Description of the thermal-hydraulic model

The geometrical scheme adopted for the post-test computational activity is based on the model presented in section 2.2.2.1. The comparison between blind calculations and experimental data showed some discrepancies that suggested a revision of the nodalization scheme in order to better reproduce the experimental sequence [61]. The differences could be, in large part, explained by the not uniform feedwater distribution through the seven DWBTs. In addition, after the transition event, the thermocouple installed at the inlet section of tube 6 measured a superheated temperature that could be explained by a blockage occurring along this tube. These considerations suggested to improve the thermal-hydraulic model, including a detailed nodalization of the secondary loop. Furthermore, the model used for blind simulations predicted reverse flow condition through the hot leg of the primary system in the first minutes after the transition event, that is not acquired by the instrumentation [61]. The analysis performed during the post-test phase highlighted the relationship between reverse flow and pressure drops through the primary system: the whole pressure drops were well predicted by the code, as confirmed by the steady-state LBE mass flow rate, but the distribution of the pressure losses through the flow path seemed to be wrong. In particular, the model over predicted the pressure drop through the SG and, when LBE flow rate assumed low values, the mass flow through the SG was stopped and a reverse flow condition was observed on the hot leg. In order to reduce this effect, the thermal-hydraulic model has been enhanced with an improved distribution of the pressure losses through the primary flow path.

The main difference compared to the geometrical scheme presented in section 2.2.2.1 is related to the secondary loop. The model (presented in Figure 66) includes the feeding pipe downstream the pre-heater, the manifold, seven DWBTs separately simulated, the steam chamber and the steam line up to the valve V3. For the secondary system, heat losses toward the environment are not considered. Each DWBT model includes two vertical channels, reproducing the feedwater descending side and the annular riser (simulated with the annulus component). Seven heat structure components (each one composed of 48 heat structures) simulate the heat exchanged between descending and ascending secondary side. Two time-dependent volumes are considered, imposing feedwater inlet conditions downstream the pre-heater and secondary system pressure at the steam

line outlet. The total feedwater mass flow rate is imposed with a time-dependent junction (TDJ). A K-loss coefficient is considered at the inlet of each DWBT, to consider local pressure drop induced by the turbine flow meter. The operation of secondary system is affected by uncertainties, mainly due to the lack of some parameters that make it difficult to understand the experimental operation. In the following, parameters acquired, and quantities not recorded by the monitoring system are summarized:

- Tube 0: FW flow rate is acquired over the whole test; the water/steam temperature is measured in 4 sections along the annular riser;
- Tube 1: FW flow rate is not acquired. During the full power operation, at the outlet section of the annular riser, the TC measured saturated temperature but no information about the static quality is available. The saturated conditions are reached due to the absence of the turbine FM, which reduces the pressure drops and, therefore, increases FW flow rate in this tube;
- Tube 2: FW flow rate and steam outlet temperature are not acquired;
- Tube 3: FW flow rate is acquired up to the transition event and steam outlet temperature is collected over the whole test;
- Tube 4: FW flow rate and steam outlet temperature are acquired over the whole test;
- Tube 5: FW flow rate is measured up to the transition event and steam outlet temperature is not acquired;
- Tube 6: FW flow rate and steam outlet temperature are not collected.

For these reasons, K-loss coefficients at the DWBTs inlets are calibrated in order to obtain correct steam temperature at the outlet of the bayonet element 0, 1, 3 and 4, during the full power operation. Given that turbine flow meters inserted in the tubes number 0 and 5 measure the same flow rate, the same K-loss coefficients are considered for these tubes. The rest of the feedwater mass flow rate is divided equally between tubes 2 and 6, for which no information is available. These assumptions are affected by the uncertainty related to the flow rate along tube 0, in which saturated conditions are obtained at the outlet section but information about steam quality is not available. In addition, a blockage is supposed to occur within the bayonet element number 6, trying to explain the superheated condition acquired at the inlet of this tube. To reproduce the blockage occurring after the transition event, a trip valve component is included within the DWBT number 6. The position of the valve was the subject of a sensitivity analysis. Four positions were considered:

- at the DWBT inlet section;
- into the annular riser, 650 mm above the bottom edge;
- into the annular riser, 2925 mm above the bottom edge;
- into the annular riser, 5325 mm above the bottom edge.

The blockage supposed close to the turbine flow meter did not allow the feeding of the bayonet element, causing boiling of the whole liquid phase contained within the DWBT 6. At the inlet section, temperature increase was overestimated of about 30 K. When the blockage was supposed to occur within the annular riser, steam came back up to the inlet section, where saturated conditions were obtained; superheated steam condition was not reached. The other three cases showed the same results, proving that inlet temperature did not depend on the position of the blockage within the annular riser. For the post-test simulation, the blockage is supposed to occur 5325 mm above the bottom edge of the bayonet element.

The main dimensions of the improved thermal-hydraulic model are summarized in Table 8.

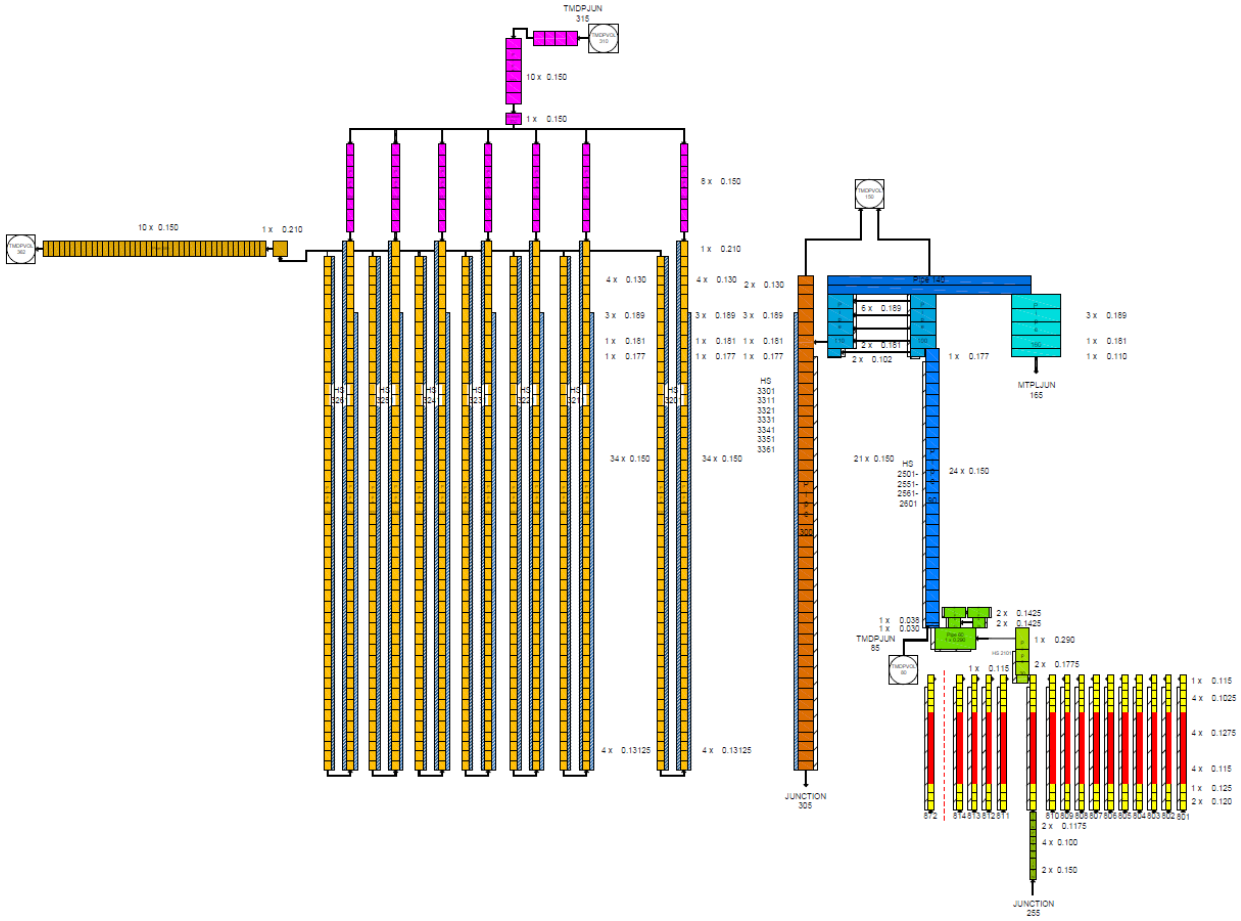

Figure 66. Post-test simulations: thermal-hydraulic model of 1D region

Table 8. Post-test simulations: model dimensions

Parameter	Number of components
Hydrodynamic volumes	3599
Hydrodynamic junctions	8134
Heat structure mesh points	37953

2.2.3.3 Simulations results

2.2.3.3.1 Test 3

Initial conditions for Test 3 transient simulation have been obtained with a full power calculation, assuming the boundary conditions presented in section 2.2.3.1.1. Table 9 summarizes the simulation results, comparing them with experimental data. Discrepancies between simulation and experiment are compared with the measurement uncertainties and they are highlighted in green when the discrepancy is contained within uncertainty bands, and in red in the other case.

As mentioned in section 2.1.1, the experimental acquisition of LBE mass flow rate is affected by large uncertainties. R5-3D calculates a primary flow rate of 31.4 kg/s, underestimating the average value acquired by

the FM [66], even if the discrepancy is included within the uncertainty band. The good evaluation of the code is confirmed by the mass flow rate obtained by the energy balance (EB) equation, applied to the FPS, which provides LBE mass flow rate equal to 31.1 kg/s.

At the FPS inlet, the LBE temperature evaluated by R5-3D is compared with the average value of the temperature acquired by three thermocouples, highlighting a good agreement. Three TCs, placed at 120° from each other, measure LBE temperature at the FPS outlet holes. The average experimental data is compared with the mean temperature calculated by R5-3D at the highest control volume of channels 55, 61 and 67, showing a good agreement between experiment and calculation. Temperature drop between the FPS outlet and the SG inlet sections is due to the heat losses along the primary flow path. As shown in Table 9, the code well reproduces heat losses towards the pool, obtaining a good estimation of LBE temperature at the SG inlet holes. At the outlet section, experimental acquisitions show a large spread on the LBE temperature, highlighted by the large uncertainty reported in Table 9. The code shows an underestimation of LBE temperature drop across the SG, obtaining a large discrepancy with the experimental data.

On the secondary side, pressure losses through the DWBTs are calibrated in order to obtain a good estimation of the steam temperature at the outlet sections of tubes number 0, 1, 3 and 4. This assumption causes an overestimation of the flow rate through tubes 0, 3, 4 and 5. The discrepancies could be due to the lack of information presented in section 2.2.3.2.

Figure 67 shows the vertical trend of LBE temperature inside the pool during the full power steady-state operation. The elevation is shown on the x axis, assuming the 0 at the bottom of the pool. Acquisitions of the TCs installed on rods A (Figure 67 (a)) and H (Figure 67 (b)) are compared with LBE temperature evaluated by R5-3D in the exact positions of the TCs. The analysis aims to assess the capability of MULTID component to reproduce three-dimensional thermal-hydraulic effects typical of large pool. As expected, experiment shows that, at the same axial level, LBE assumes the same temperature in different azimuthal positions, whereas a relevant vertical stratification phenomenon occurs between 1.5 and 2.5 m, at the SG outlet level. The simulation is in good agreement with experimental data. The qualitative trend is well reproduced, predicting the relevant stratification phenomenon. In the upper part of the pool (between 2.5 and 7.8 m) an almost uniform profile is simulated, under predicting the experimental data of about 2 degrees. The magnitude of the stratification (about 50 K) is well reproduced and LBE temperature in the lower part of the pool (between 0 and 1.5 m) is in good agreement with experiment. Figure 68 (a) provides a useful representation of LBE temperature within the test facility, observing the most relevant section that includes the FPS and the SG. The temperature within the pool is uniform from 2.5 to 7.8 m, assuming a value of about 745 K. This is due to the large amount of heat losses from the TS hottest part, in particular from the FPS and the fitting volume which are not insulated (the FPS is insulted with a double wall shell filled with stagnant LBE). Between 1.5 and 2.5 m, cold LBE, exiting the SG, cools the lower pool, causing the vertical stratification. Figure 68 (b) shows the error distribution in the same axial section. Being the LBE temperature uniform at the same vertical levels, the TCs on rod A is considered for the comparison. In order to cover the whole pool along z- coordinate, the experimental temperatures are interpolated between two contiguous acquisition points, following the black line presented in Figure 67 (a). The representation shows the good agreement between the simulation and the experiment, except from 1.4 to 2 m, where discrepancy increases up to 40 degrees, explained by the prediction of the stratification level about 0.25 m above the experimental data.

Table 9. Test 3 – Full power calculations: main results

Parameter	Unit	Experiment	Uncertainty	R5-3D	Error
LBE MFR	kg/s	34	25%	31.4	-7.6%
Av. FPS inlet T	K	692.8	2.0	693.6	0.8
Av. FPS outlet T	K	769.8	2.0	769.5	-0.3
Av- SG inlet T	K	759.9	2.0	761.3	1.4
Av. SG outlet T	K	674.1	12.0	687.1	13.0
TFM-T0	kg/s	0.0372	0.0044	0.0430	0.0058
TFM-T3	kg/s	0.0408	0.0044	0.0479	0.0071
TFM-T4	kg/s	0.0394	0.0044	0.0480	0.0086
TFM-T5	kg/s	0.0372	0.0044	0.0430	0.0058
TC-C0-O70	K	647.0	2.0	644.4	-2.6
TC-C1-O70	K	625.9	2.0	626.3	0.4
TC-C3-O70	K	633.9	2.0	633.9	0.0
TC-C4-O70	K	633.5	2.0	633.9	0.4

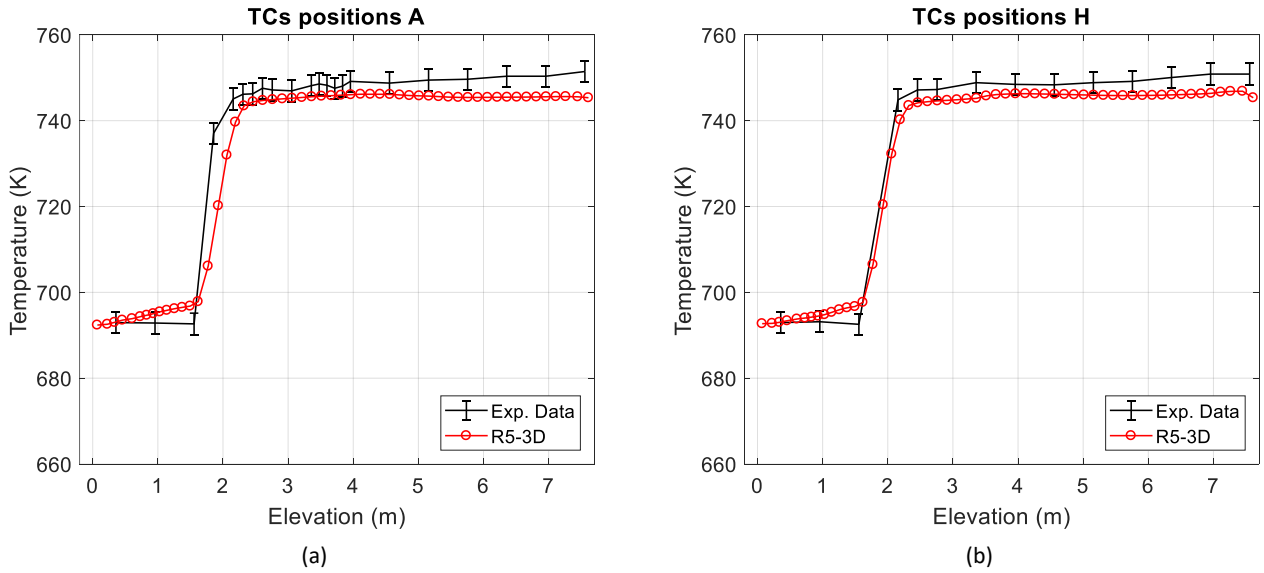

Figure 67. Test 3 – Pool thermal stratification: full power steady-state conditions

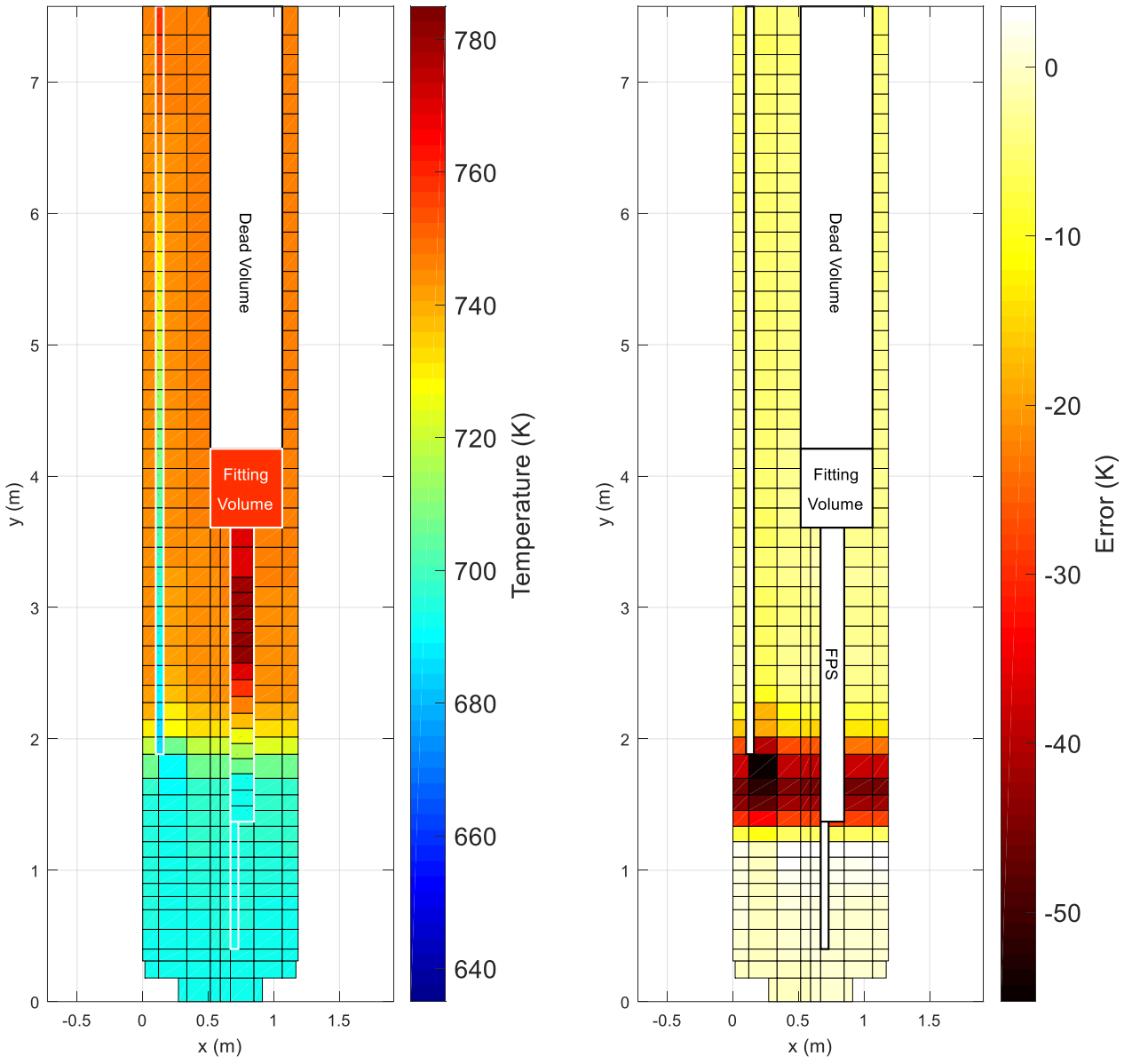

(a) (b)

Figure 68. Test 3 – Pool temperature

Starting from the full power steady-state conditions, transient analysis has been carried out. The boundary conditions are summarized in section 2.2.3.1.1. In the following plots, experimental data are compared with two calculations: case 1 (#1) assumes a total FW mass flow rate equal to 0.078 kg/s (reference value [59]) and case 2 (#2) adopts the value of 0.047 kg/s. The blind simulation highlighted an overestimation of the power remove by the SG [61]. In case 2, feedwater mass flow rate has been calibrated in order to obtain the correct thermal power removed by the secondary system. Acceptability of this assumption will be analyzed in the following. In the plots,

experimental trends are presented with the mean value acquired by instrumentations (solid line) and their uncertainty bands (dotted line).

Figure 69 compares the LBE mass flow rate acquired by the Venturi FM with the EB flow rate and the primary flow obtained by simulations. The quick decrease occurring after the transition event is well reproduced by the code and the two calculations do not show visible differences. When argon injection is cut off, the experimental monitoring system acquired the minimum value of primary flow rate (about 3 kg/s), well predicted by case 1 and under predicted by case 2 of about 2 kg/s. As discussed in section 2.2.3.2, the improved thermal-hydraulic model provides a better estimation of the flow rate, avoiding the establishment of the reverse flow condition, observed in the blind simulations [61]. After that, the simulated flow rate increases slower than experimental data up to the new quasi steady-state condition. The natural circulation depends on the heat source (FPS power), the heat sink (power removed by SG) and the relative distance between them. The difference of secondary flow rate produces a discrepancy in terms of primary flow of about 1 kg/s between the two calculations. Both the results are included within the uncertainty band but case 2 provides the best estimation of the experimental acquisition. The EB value is outside the experimental uncertainty band but, in natural circulation, it is expected that the uncertainty increases over the reference value of 25%.

Figure 70 shows the temperature increase through the HS active length, comparing temperature acquired by thermocouples T-FPS-31, 35 and 36 with simulations results obtained in the exact position of instrumentation (respectively at the inlet and outlet section of the subchannel 01 and at the outlet section of the subchannel 29). At the top of the active length, the rapid temperature decrease is well predicted by the calculations, not presenting visible differences. When the FPS power reaches the decay heat value, LBE mass flow rate still assumes 50 % of the nominal value, causing the minimum temperature at the outlet of the HS active length. This effect is well predicted by both the simulations, reaching a minimum value of about 710 K. When the Ar injection system is cut off, and the LBE MFR assumes the minimum value, at the outlet section of the HS active length the LBE temperature rapidly increases up to the maximum value of 740 K, acquired by the TC T-FPS-35 at 155 s. Calculation #1 matches very well the experimental trend, assuming the same maximum temperature. At this time, the LBE mass flow calculated by R5-3D approaches the EB trend, proving that this value must be considered as the reference primary flow rate. Simulation #2 well reproduces the first seconds of the temperature ramp, but the maximum value is overestimated (about 8 degrees) and delayed (about 25 s) than the experimental data. This is explained by the under prediction of the primary flow rate up to 250 s. In the long term, case 1 predicts too high temperature gradient, leading to underestimation of the inlet temperature at FPS inlet (more than 2 degrees at the end of the test). At the outlet section, the over prediction of LBE mass flow causes a lower value of the temperature increase than the experiment and an underestimation of the outlet temperature of about 12 K at the end of the test. The lower secondary flow rate assumed in the second calculation, provides a better estimation of the temperature gradient (the inlet temperature approaches very well the experimental data) and the good agreement in terms of primary mass flow rate ensures a good prediction of the outlet temperature.

Figure 71 shows the temperature decrease through the SG primary side. Experimental temperatures are acquired at the SG inlet holes, at 4200, 3000 and 1500 mm from the bottom of the heat exchanger and at the SG outlet. At the top of the test section, the separator operates as a hot pool; the large amount of hot LBE reduces the cooling trend observed at the FPS outlet. This effect is well reproduced by simulations, even if R5-3D under predicts the inlet temperature after the transition. This is due to the SG modelling approach, collapsing the LBE subchannel in a single equivalent pipe. At the top of the SG, TCs are installed at the inlet holes and the higher temperature acquired by instrumentation than the computed values is explained by the boundary effects. Looking at the outlet section, both the calculations predict a peak temperature at about 95 s from the beginning of the test. This is due to the rapid decrease of the FW flow rate in the face of a slower primary flow reduction.

This behavior is not observed by experimental acquisitions. Along the SG, feedwater mass flow rate of 0.047 kg/s allows a better estimation of the whole temperature drop and of the heat exchanger efficiency in the different axial sectors. In case 1, the higher amount of temperature drop occurs in the upper part of the SG, from 3000 mm to the inlet holes. Instead, case 2 allows a better partition of the total temperature drop along the SG, matching very well experimental data in each monitored section. This is due to a better evaluation of the power removed by the SG and of the primary mass flow rate. The thermal power removed is shown in Figure 72, where experimental data is obtained with the energy balance equation applied to the SG primary side. Figure 72 shows that case 1 over predicts the power removed over the whole transient test (even if it is included within the uncertainty bands), whereas the secondary flow rate imposed to the calculation #2 has been calibrated to obtain the correct SG power.

Figure 73 shows thermal stratification at the end of transient test, comparing experimental data acquired on the support rods A and H with computational results. Due to unbalance conditions occurring after the transition from GEC to NC, the TCs observe a reduction of the average pool temperature (about 10 degrees), even if the qualitative vertical trend is maintained (thermal stratification is still observed between 1.5 and 2.5 m). R5-3D is able to reproduce the progressive pool cooling, matching very well LBE temperature in the upper part in both the calculations (740 K). At the bottom, the underprediction of SG outlet temperature leads to underestimation of LBE temperature within the pool by calculation #1 whereas case 2 is in good agreement with the experiment.

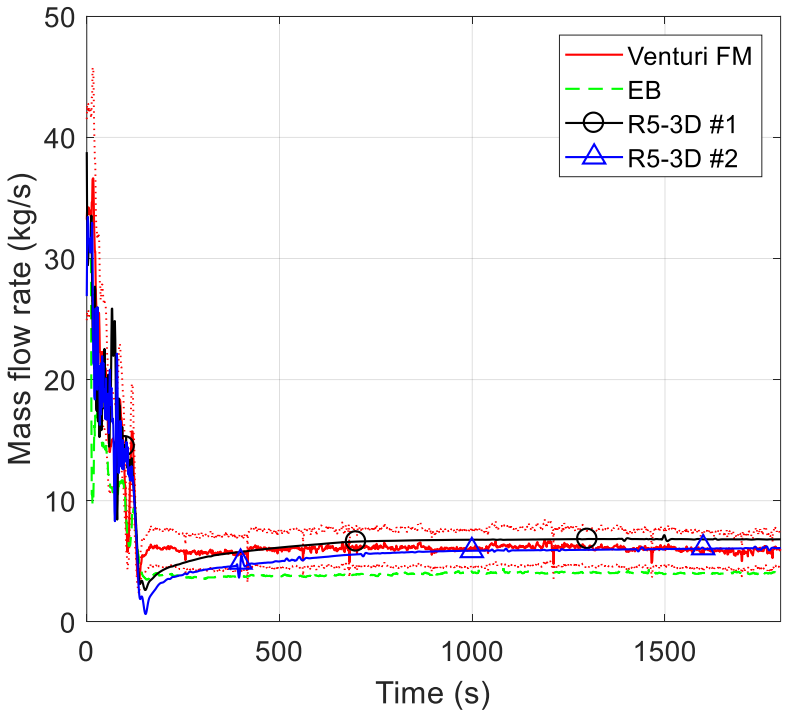

Figure 69. Test 3 – LBE mass flow rate

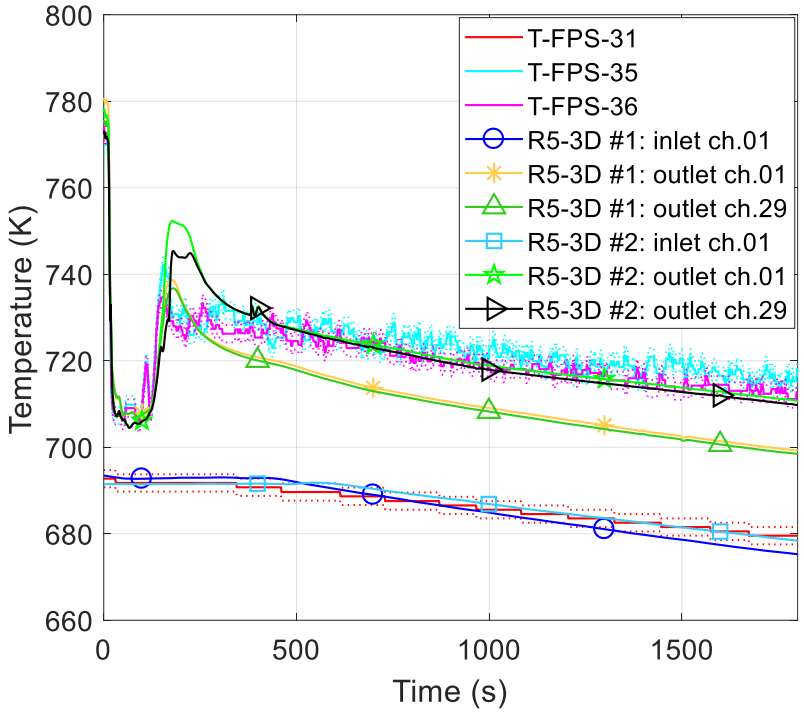

Figure 70. Test 3 – FPS inlet and outlet temperature

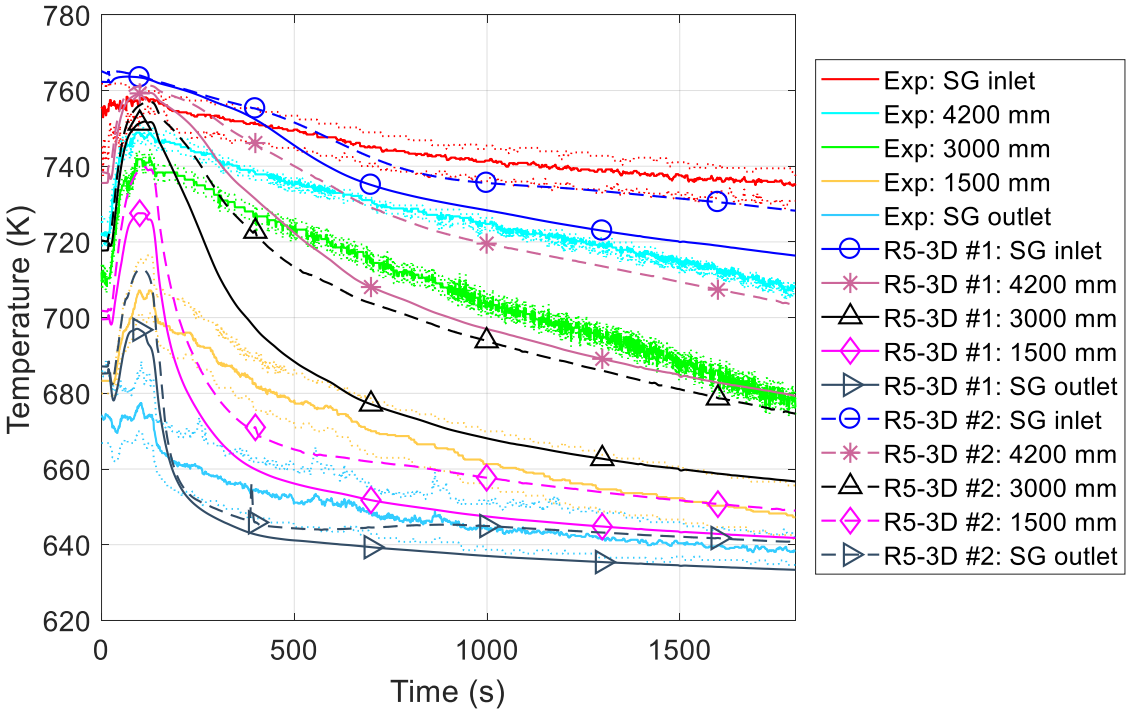

Figure 71. Test 3 – LBE temperature through the SG

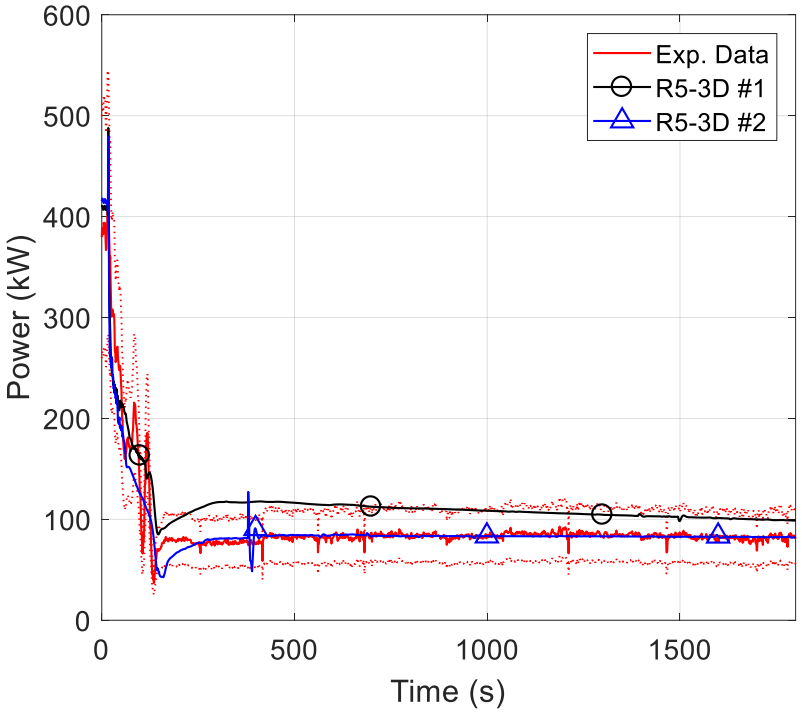

Figure 72. Test 3 – Power removed by the SG

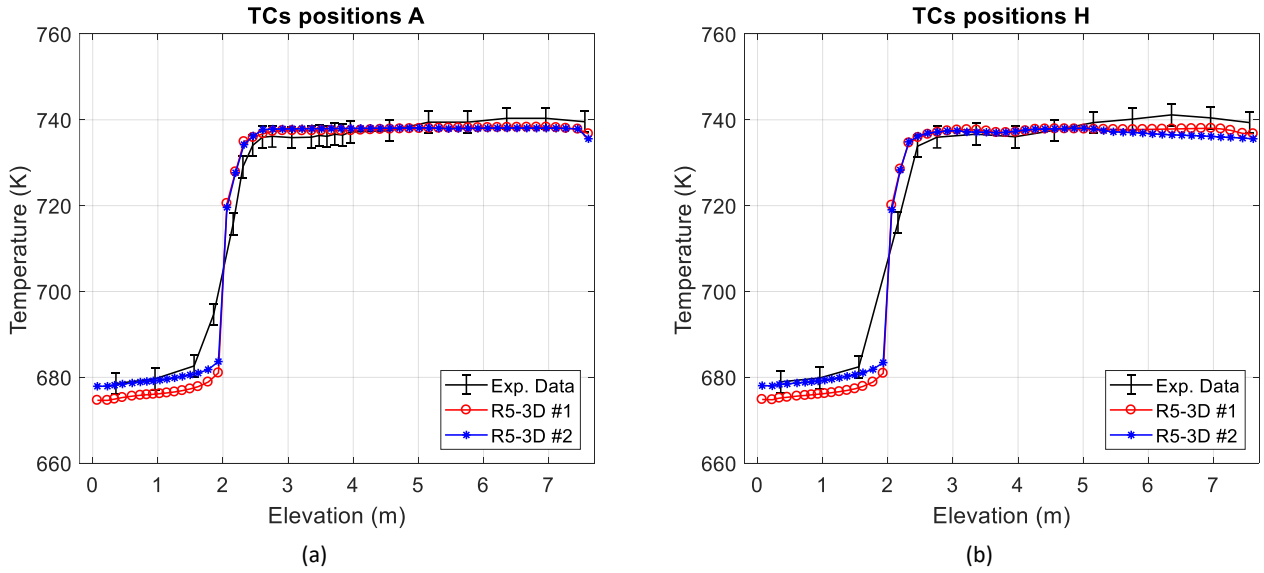

Figure 73. Test 3 – Pool thermal stratification: final conditions

Regarding the secondary loop operation, Figure 74 compares mass flow rate measured by turbine flow meters at the inlet sections of DWBTs 0 (a) and 4 (b) with simulations results. The others flow meters lost the signal after the transition event. For case 1, the total FW mass flow rate is assumed equal to the reference data of 0.078 kg/s [59]; Figure 74 shows that, in this case, R5-3D results are in good agreement with the best estimation of the experimental measurements. Reducing the total flow rate to 0.047 kg/s, the experimental acquisitions are under predicted, even if computational results remain within the uncertainty bands. Figure 75 shows steam

temperature at the outlet of tubes 0, 1, 3 and 4, comparing experimental data with simulation results. After the transition, R5-3D over predicts the sharp temperature increase, overestimating the maximum temperature of about 35 degrees in both the simulations. At the DWBTs outlet, steam assumes temperature only few degrees lower than LBE temperature on the primary side. It could be due to the thermal conductivity of the powder within the DWBT, which could be overestimated in the modelling. In fact, the differential thermal expansion of the third and fourth tubes which compose the DWBT, caused by the whole temperature increase, could create a thin layer of helium within the gap that operates as insulator, reducing the heat exchanged. R5-3D modelling does not take into account this phenomenon. After that, calculation #1 over predicts steam temperature gradient, observing a faster decrease than the experiment. Despite this, reducing the secondary flow rate, the gradient calculated by R5-3D is in good agreement with the experimental trend, even if steam temperature remains higher than the TCs acquisition over the whole test.

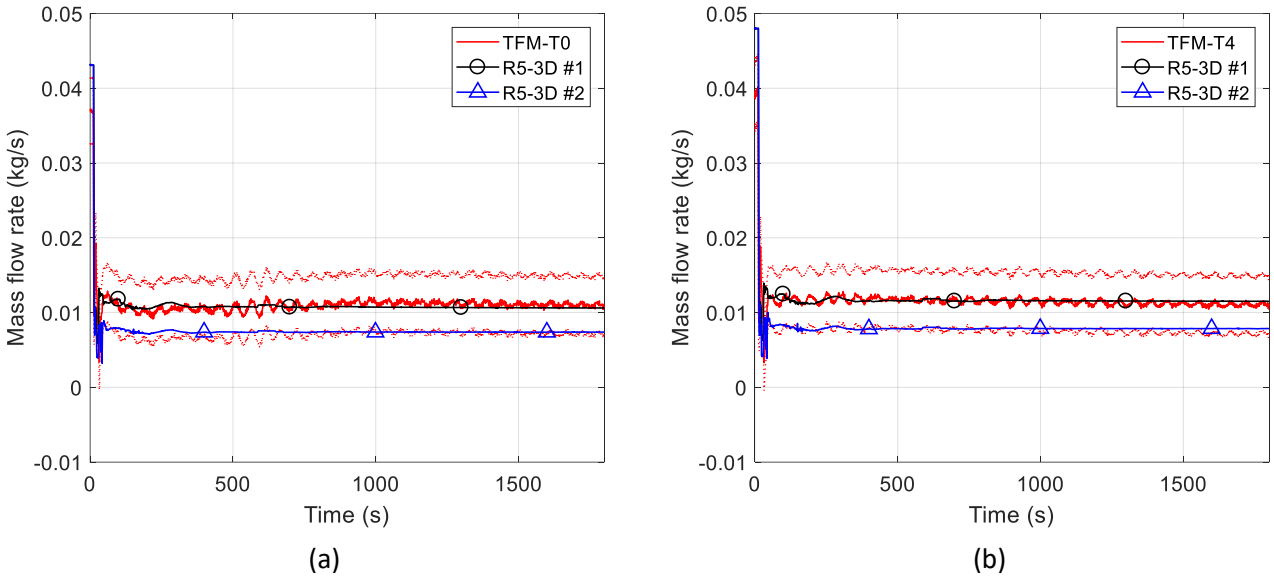

Figure 74. Test 3 – FW mass flow rate through DWBTs 0 and 4

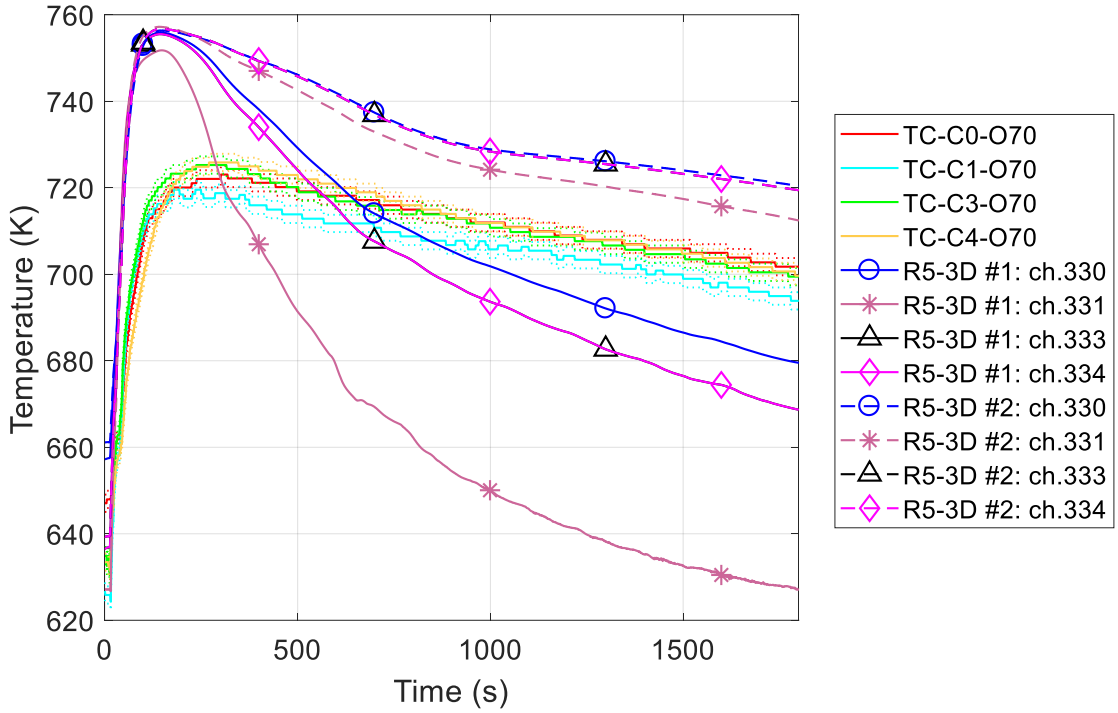

Figure 75. Test 3 – Steam temperature

2.2.3.3.2 Test 1

A preliminary full power calculation has been carried out in order to obtain the initial conditions for the transient analysis, assuming the boundary conditions presented in section 2.2.3.1.2. The main results are summarized in Table 10, comparing them with experimental data. Discrepancies between simulation and experiment are shown and highlighted in green if they are included within experimental uncertainties, or in red in the other case. Globally, simulation results are in good agreement with the experiment. The largest discrepancies are observed at the SG LBE side, where the temperature measured by the thermocouple TC-SG-01 suffers of an instability in GEC respect to the other two TCs (TC-SG-02 and TC-SG-03), because of its position in the separator. In fact, this TC is directly exposed to the rising LBE, mixed to the argon injected at the bottom of the riser and this turbulence affects the measure acquired. This could explain the large discrepancy observed. A similar behavior is observed at the outlet section, where it is difficult to evaluate an average temperature due to the large discrepancies acquired by the TCs.

On the secondary side, the experiment is well reproduced by R5-3D. As analyzed in section 2.2.3.3.1 for Test 3, the main discrepancies are due to the lack of information on the FW mass flow rate feeding each DWBT.

Table 10. Test 1 – Full power calculation: main results

Parameter	Unit	Experiment	Uncertainty	R5-3D	Error
LBE MFR	kg/s	34	25%	31.7	-6.7%
Av. FPS inlet T	K	420	2.0	418.4	-1.6
Av. FPS outlet T	K	493.5	2.0	495.0	1.5
Av- SG inlet T	K	480.0	5.0	485.1	5.1
Av. SG outlet T	K	403.7	8.0	413.9	10.2
TFM-T4	kg/s	0.036	0.0044	0.039	0.003
TFM-T5	kg/s	0.033	0.0044	0.039	0.006
TFM-T6	kg/s	0.035	0.0044	0.034	-0.001
TC-C0-O70	K	387.9	2.0	387.9	0.0
TC-C1-O70	K	353.0	2.0	353.9	0.9
TC-C3-O70	K	376.1	2.0	366.1	-10.0
TC-C4-O70	K	365.4	2.0	366.1	0.7

Starting from the full power steady-state conditions, the transient analysis has been carried out, applying the boundary conditions described in section 2.2.3.1.2, except for the FW mass flow rate that, assuming the lessons learned from Test 3, has been evaluated in order to remove the correct thermal power.

Figure 76 shows the LBE mass flow rate analysis. The quick MFR decrease, occurring after the transition event, is well predicted by R5-3D, reaching the minimum value of 1.5 kg/s. After that, the code underestimates primary flow rate in NC operation, even if the calculated trend is maintained within the experimental uncertainty bands over the whole test. Experimental and computational trends are compared with the EB MFR. In both full power steady-state condition and quasi steady-state condition after the transient, the EB trend approaches very well the calculated value. Discrepancies with experimental data are justified by the large uncertainties related to the Venturi acquisition at low value of mass flow rate.

Figure 77 compares LBE temperature acquired at the HS inlet (T-FPS-31) and outlet section (T-FPS-35 and T-FPS-36) with the simulation results. R5-3D provides good estimation of the temperature trend over the whole test. At the inlet section of the active length, the code well reproduces the cooling down derivative trend, matching the experimental acquisition up to the end. At the outlet section, the quick decrease of the LBE temperature is well predicted, even if some discrepancies are observed at the minimum peak, where R5-3D overestimates the minimum temperature of about 6 degrees. After that, temperature rapidly increases up to the maximum value; R5-3D approaches very well the acquisition of the thermocouple T-FPS-35, whereas the T-FPS-36 provides a measurement few degrees higher. Then, the temperature decreases following the cooling-down trend of the whole system and the calculation predictions are in good agreement with experimental data.

The main results of the subchannel analysis, carried out with CIRCE-HERO modelling, are presented in Figure 78, where the temperature profile obtained by the code in the radial direction at the outlet section of the HS, is compared with the experimental acquisitions, reported with their uncertainty bars. Four relevant instants are considered for the analysis: initial conditions, 20, 50 and 1000 s after the transition event. In the x-coordinate, 0 represents the position of pin 1. As expected, due to the uniform power profile, a flat temperature distribution is obtained by the calculation at the beginning of the test (0 s). This is confirmed by the representation of the temperature distribution within the bundle, obtained by the code (see Figure 79). At the beginning of the test, R5-3D provides a good prediction of the temperature profile, even if some discrepancies are observed (see Figure

78, 0 s), especially on the left boundary. After the transition event, the evolution of the temperature profile is well reproduced. At 20 s, the FPS outlet temperature is decreased below the average pool temperature and the heat exchanged through the HS shell determines the inversion of the temperature profile within the bundle, where internal subchannels are cooler than the external ones. This condition is presented in Figure 78 (20 s), that shows the capability of R5-3D to reproduce the quick temperature evolution in the first instants of the transient. After that, as observed in Figure 77, the LBE temperature increases up to the peak value, restoring the original temperature gradient within the bundle (see Figure 78, 50 s). Finally, LBE temperature decreases following the cooling-down trend of the whole system and the temperature assumes a flat profile within the bundle. Figure 78 (1000 s) shows a good agreement between simulation and experiment.

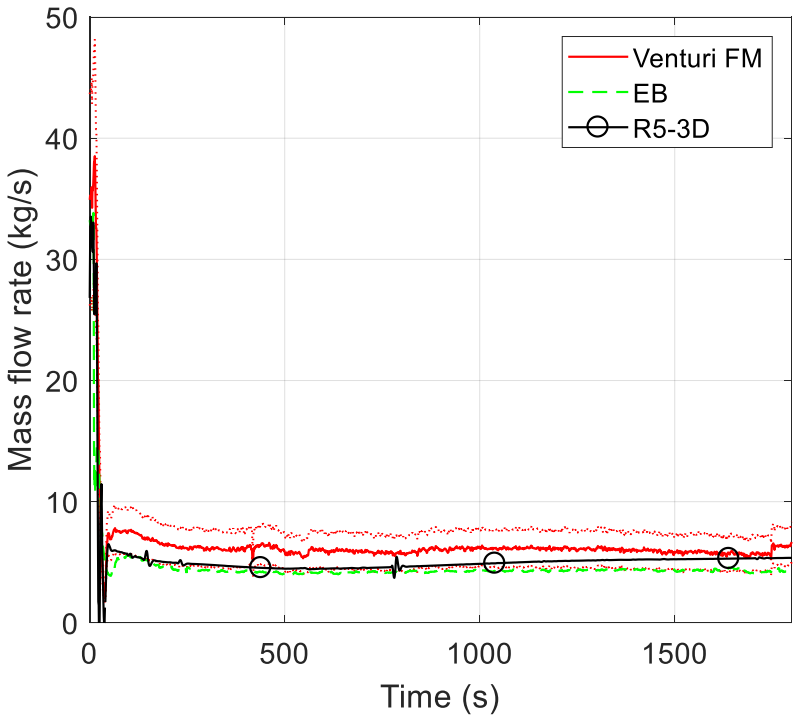

Figure 76. Test 1 – LBE mass flow rate

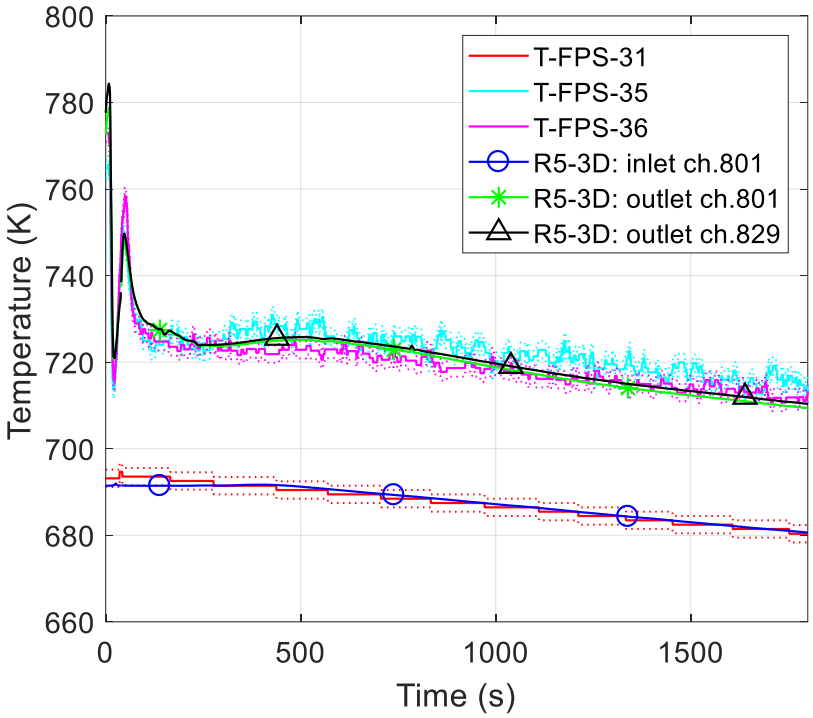

Figure 77. Test 1 – FPS inlet and outlet temperature

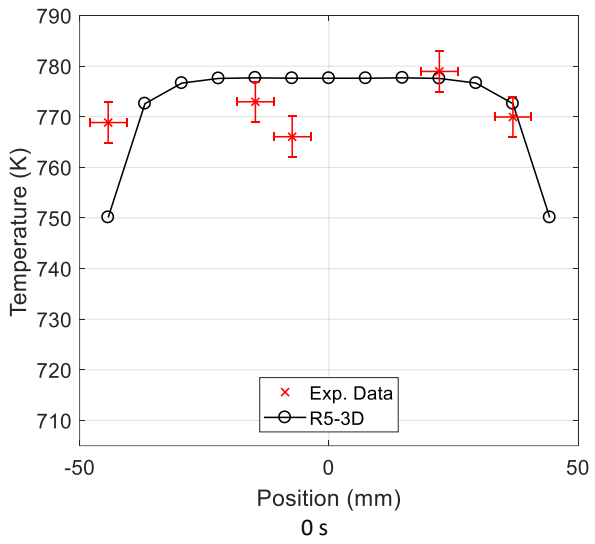

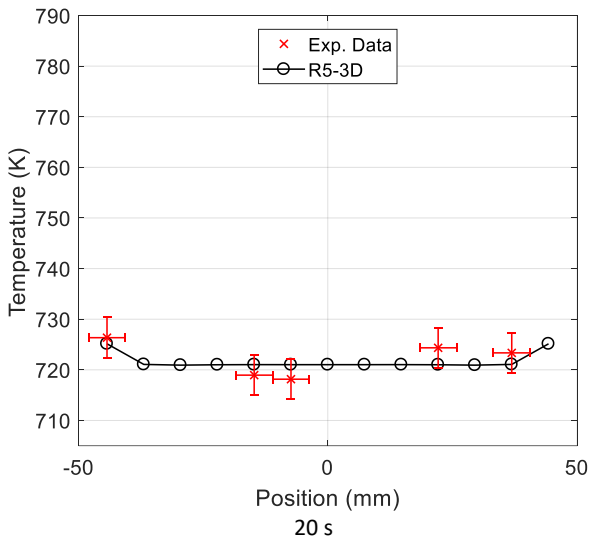

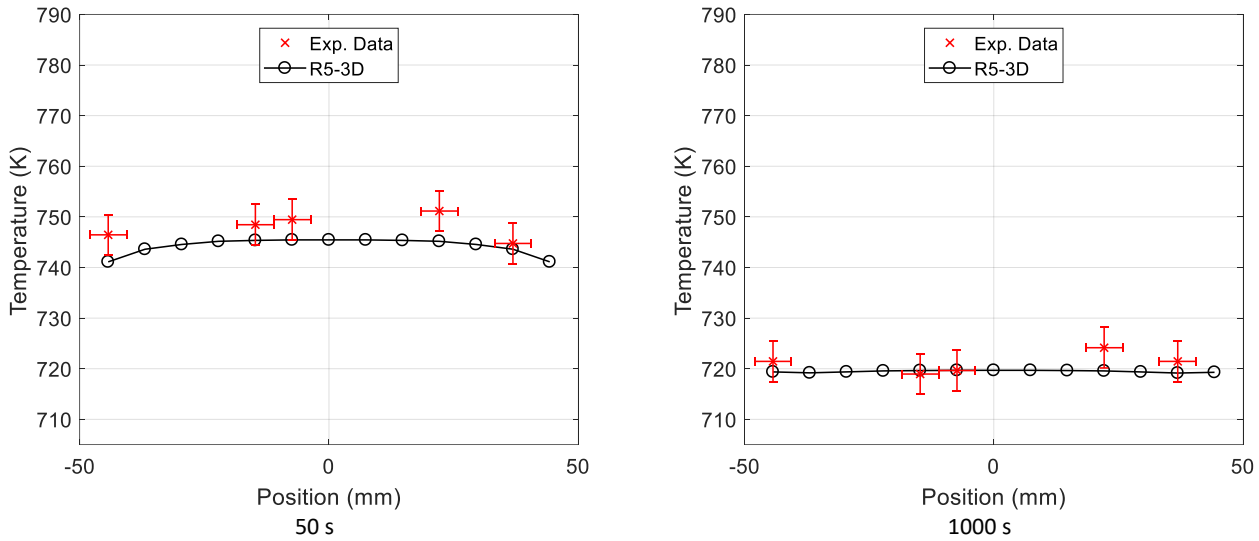

50 s 1000 s

Figure 78. Test 1 – Temperature profile at the outlet of the FPS active region

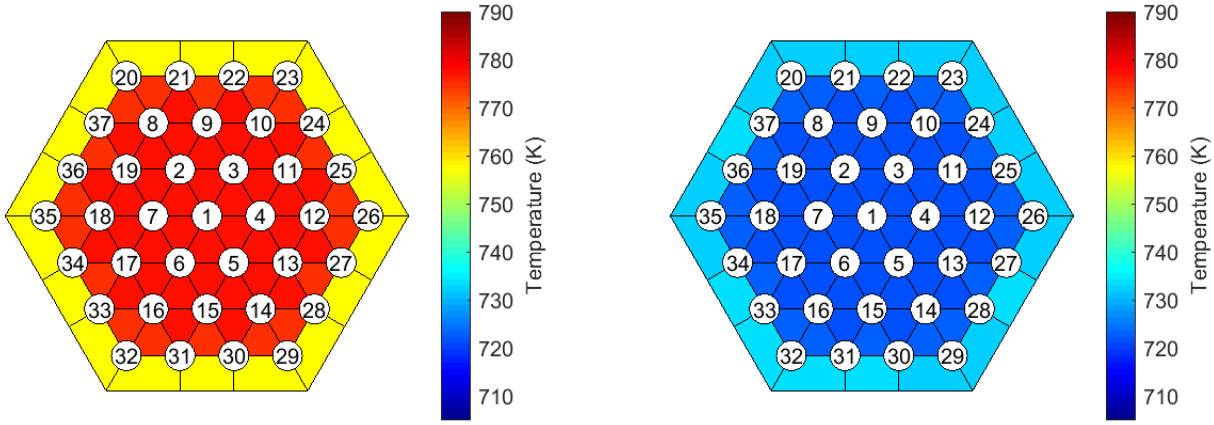

0 s 20 s

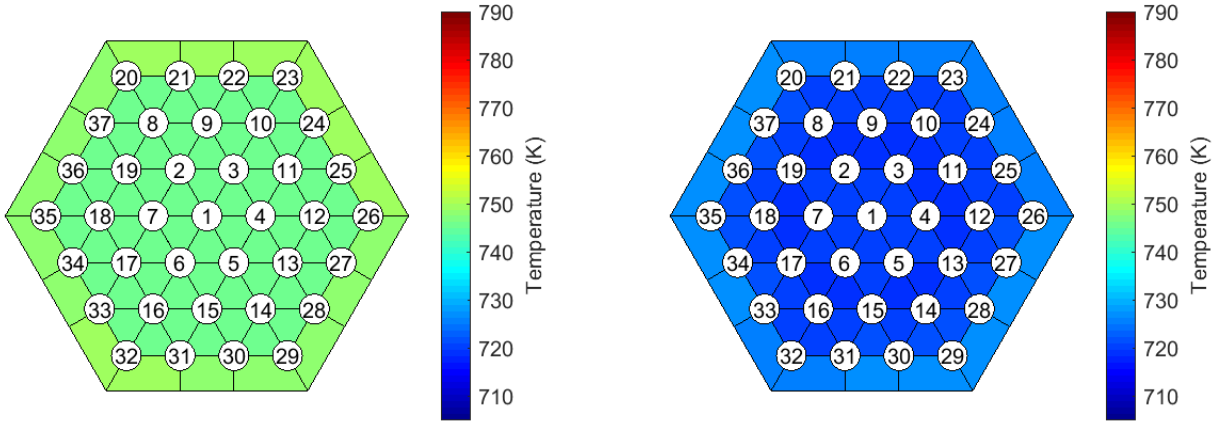

Figure 79. Test 1 – FPS outlet temperature: R5-3D calculation

Figure 80 shows inlet and outlet temperature of the LBE flowing through the SG. The separator operates as a hot pool, reducing the quick cooling trend seen at the FPS outlet section. This effect is well reproduced by the code. It provides a good estimation of the heat losses between hot leg and cold pool, confirmed by the good evaluation of the SG inlet temperature. At the outlet section, the quick temperature decrease is well reproduced in the first seconds after the transition event. This is due to the rapid reduction of the primary flow rate. After that, new quasi steady-state conditions are obtained and LBE maintains quite constant temperature at the outlet section of the unit. Figure 80 shows good agreement between simulation and experiment, except for the acquisition of the thermocouple T-C-07-L00, that shows some instabilities.

On the secondary side, the quick reduction of the FW flow rate causes the rapid steam temperature increase at the outlet of the DWBTs. Figure 81 compares the experimental acquisitions at the outlet of tubes 0, 1, 3 and 4 with simulation results. R5-3D predicts the sharp increase, even if the maximum temperature is overestimated of about 30 degrees. After that, the cooling down derivative trend is well predicted by the code. Discrepancies are probably due to the thermal conductivity of the powder, that represents one of the most relevant uncertainties of the calculations.

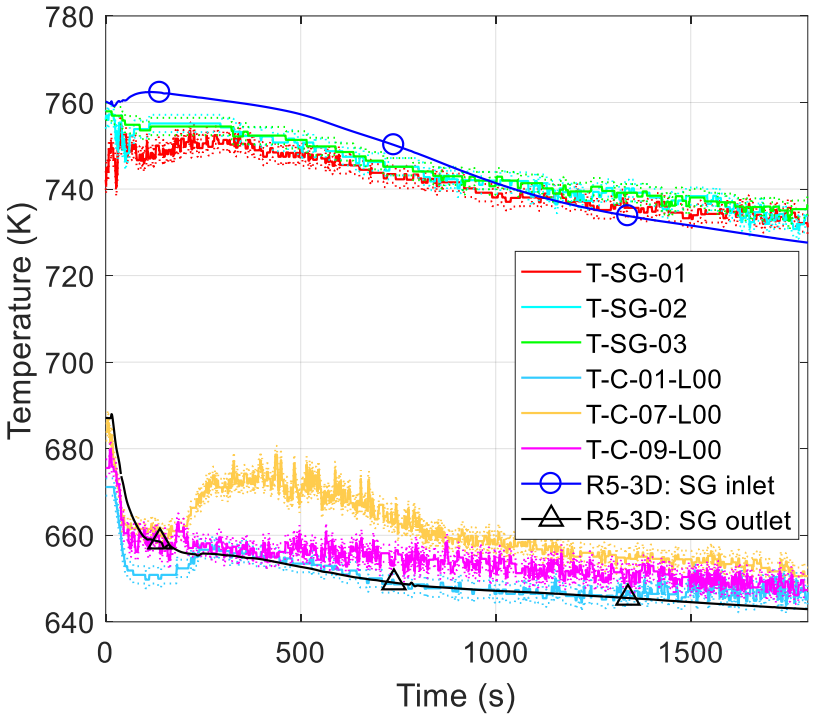

Figure 80. Test 1 – LBE temperature through the SG

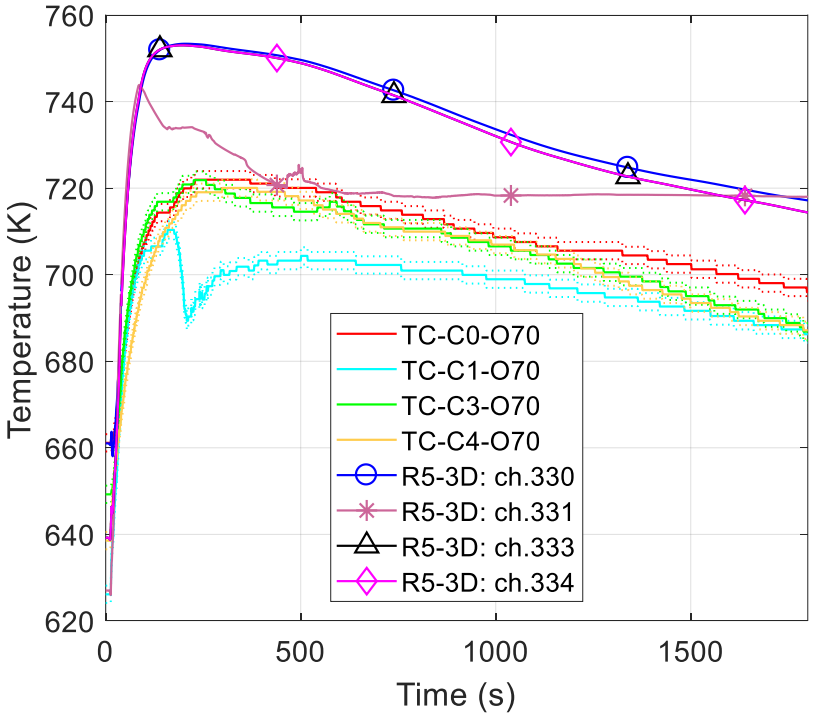

Figure 81. Test 1 – Steam outlet temperature

Figure 82 and Figure 83 analyze pool thermal stratification respectively at the beginning and at the end of the test. As presented in section 2.2.3.3.1 concerning Test 3, the experimental acquisition shows a relevant stratification phenomenon along the vertical direction and a quite uniform temperature at the same axial level. This is well reproduced by the code. The calculation results are acquired at the same position of the TCs, along the support rods A and H. R5-3D predicts uniform temperature at the same quote, and the vertical temperature trend approaches very well the experimental data: almost uniform temperature in the upper part of the pool, relevant stratification phenomenon (about 50 degrees) in between 1.5 m and 2.5 m, and uniform temperature at the lower part of the pool. In addition, the transition from GEC to NC is well reproduced.

Figure 84 provides a useful representation of the R5-3D results, considering the most relevant section of the facility, including the main components of the primary system. The relevant stratification phenomenon occurs at the SG outlet level. This is due to the heat losses between the hot leg and the main pool that warms the upper part of the pool. Downstream the SG outlet, the cold fluid, exiting the heat exchanger, cools the lower pool, causing the characteristic thermal stratification.

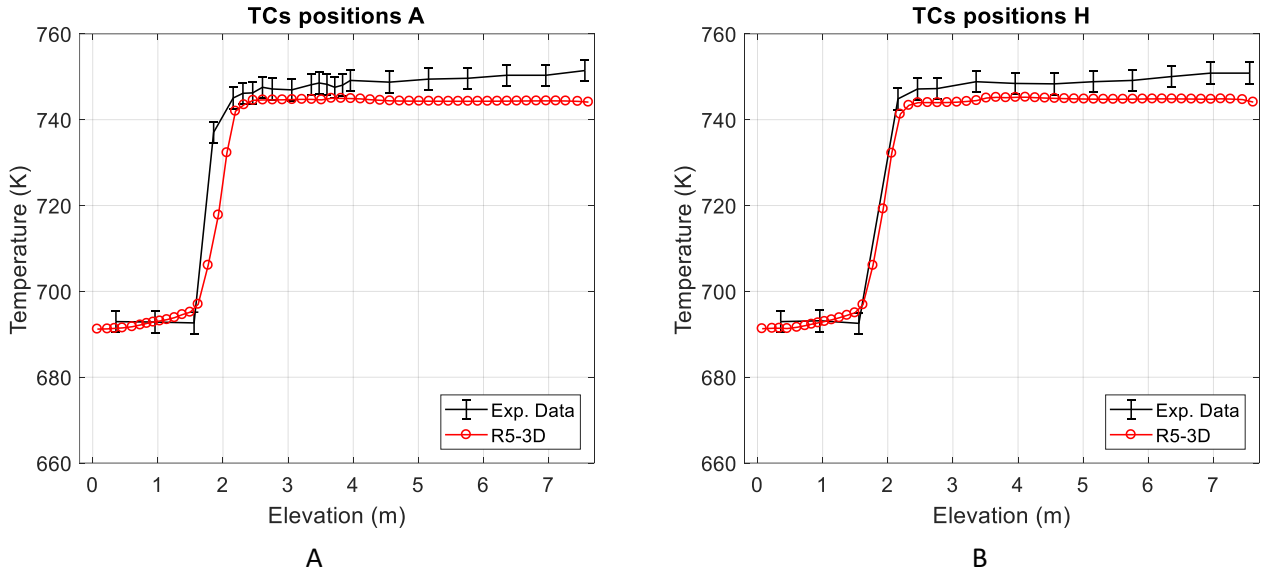

Figure 82. Test 1 – Pool thermal stratification: initial conditions

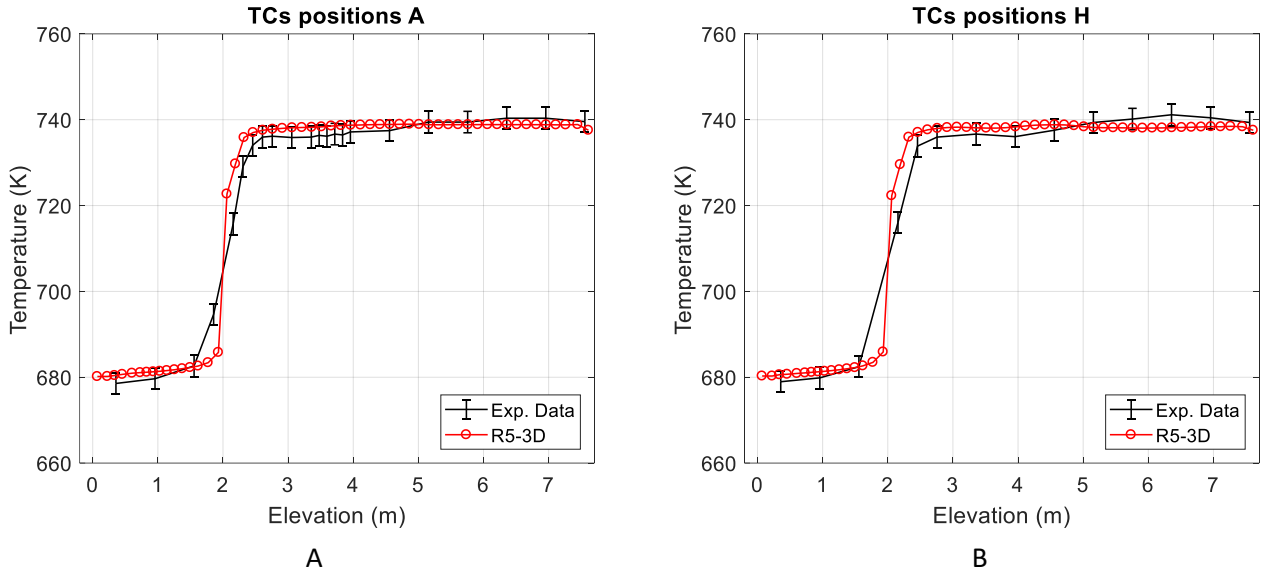

Figure 83. Test 1 – Pool thermal stratification: final conditions

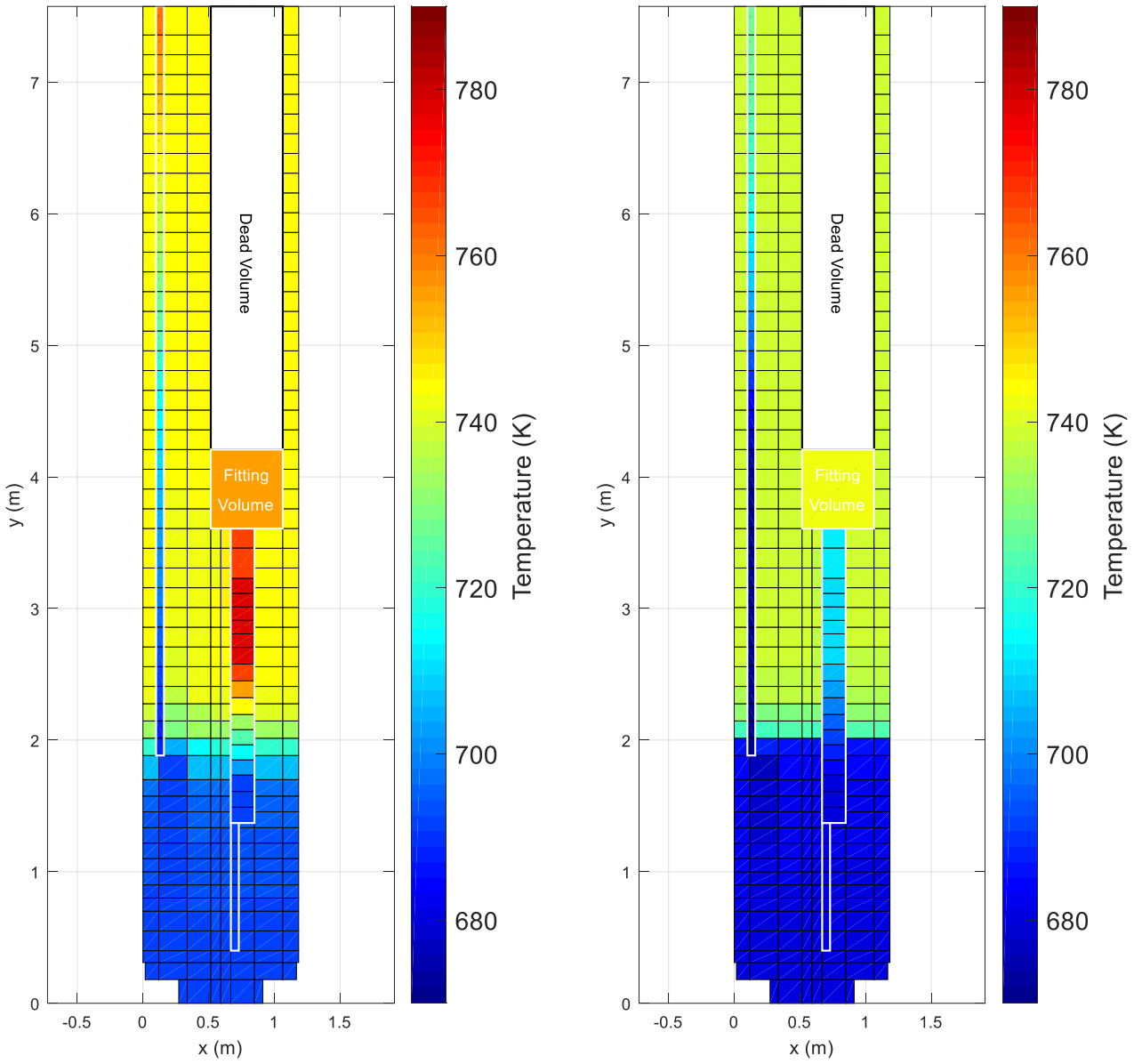

Figure 84. Test 1 – Pool thermal stratification: R5-3D results

2.2.3.4 Conclusive remarks

The experimental campaign performed on CIRCE-HERO test facility offered useful data for validation of computational codes, improved with capabilities to simulate innovative HLM nuclear systems. CIRCE-HERO facility was designed to reproduce an HLM-cooled pool-type reactor, testing a DWBT SG in a relevant configuration for ALFRED SG. The experimental campaign concerned three protected loss of flow accident, reproducing the primary pump cut off simulating the presence of a pump flywheel, the consequent reactor SCRAM and the activation of the DHR system.

One of the three test (Test 3) was proposed for a validation benchmark in the framework of the H2020 SESAME project. As a participant of the benchmark exercise, UNIROMA1 used CIRCE-HERO model to carry out blind-calculations. The open phase of the test benchmark highlighted the overprediction of the SG performances obtained with the blind simulation. The analysis of the experimental campaign suggested a revision of the thermal-hydraulic model, improving the nodalization scheme of the secondary loop to consider the asymmetries in the parallel tubes.

The research activity has aimed on the assessment of RELAP5-3D capabilities to reproduce the main thermal-hydraulic features of an HLM-cooled pool-type reactor, in safety relevant operation conditions. Regarding post-test analysis of Test 3, boundary conditions, provided by ENEA, have been applied for the full power calculations. Simulation results are globally in agreement with experimental data for all the primary circuit physical quantities monitored; some discrepancies are highlighted on the secondary side, where total mass flow rate is assumed equal to the best estimate measurement of the Coriolis flowmeter and pressure losses at the inlet of the bayonet elements are calibrated to obtain the correct steam temperature at each outlet. An overestimation of about 15% is observed on the flow rate through the DWBTs 0, 3, 4 and 5. Discrepancies are explained by the lack of some information which determines large uncertainties on the evaluation of secondary system boundary conditions. One of the main tasks of the simulation activity has been the assessment of MULTID capability to reproduce relevant thermal-hydraulic phenomena within a large pool. At this purpose, 119 TCs installed within CIRCE pool provide useful data for code validation. Comparison with experimental data highlights excellent capabilities of the multi-dimensional component to reproduce heat losses between hot leg and cold pool. The code is able to reproduce steady-state vertical profile of the temperature, matching very well the experimental thermal stratification occurring at the SG outlet level. In addition, MULTID component well reproduces the pool temperature trend over the whole transient test.

Starting from the full power steady-state conditions, two transient calculations have been performed, assuming the same boundary conditions, except for the total feedwater mass flow rate after the transition event. Case 1 assumes the reference value of the secondary flow rate (0.078 kg/s), obtained with the energy balance equation applied to the FW pre-heater. This calculation highlights an overestimation of the power removed by the SG; for this reason, a second calculation has been performed calibrating the total secondary flow rate to 0.047 kg/s which guarantees the correct SG power. Both the simulations are in good agreement with experimental data in the first 200 s, reproducing very well the first minutes after the transition event. After the Ar injection cut off, the first calculation provides a good estimation of the minimum value of the LBE MFR, underpredicted by the second calculation of about 2 kg/s. The long term behavior strongly depends on the feedwater mass flow rate. Case 1 shows an overestimation of the whole system energy unbalance, leading to the over prediction of the natural circulation contribution and of the cooling trend. The SG power balance analysis highlighted an overestimation of the power removed of about 30% of the experimental value. The large uncertainties related to the measurement of the secondary system quantities have suggested the calibration of the secondary flow rate to obtain the correct SG power removed. This assumption has been justified comparing the experimental flow rate, acquired at the inlet of the tubes 0 and 4, with the simulation results: the experimental data are underestimated but the calculation results remain within the experimental uncertainty bands. Looking at the primary system, the assumption of a lower FW flow rate leads to a better agreement with experimental data, providing a good estimation of the long term behavior. Some discrepancies are still maintained on the secondary side, where the steam outlet temperature is over predicted by the code. The differences could be due to a not perfect agreement of the powder thermal conductivity, which represents a large source of uncertainties. This opens the possibility to continue the post-test analysis for the secondary side, leading an improved experimental results analysis, despite of the good global results obtained.

The lesson learned from post-test of Test 3, has been applied to the simulation activity carried out on the experimental Test 1. Similar conclusions are obtained, confirmed the good capabilities of R5-3D to reproduce thermal-hydraulics of HLM-cooled system in safety-relevant operations. In addition, the subchannel analysis performed has highlighted a good prediction of the subchannel thermal-hydraulics within the FPS bundle in the postulated transient accident.

3 COMPUTATIONAL ACTIVITY ON PHÉNIX DISSYMMETRIC TEST

Phénix is a French pool-type sodium-cooled prototype reactor; before the definitive shutdown, occurred in 2009, a final set of experimental tests are carried out in order to increase the knowledge on the operation and the safety aspect of the pool-type liquid metal-cooled reactors. One of the experiments was the Dissymmetric End-of-Life Test which was selected for the validation benchmark activity in the frame of the H2020 SESAME project [36].

The experimental test, characterized by asymmetrical boundary conditions, is considered very interesting for the evaluation of the STH codes capability to reproduce relevant three-dimensional phenomena in a liquid metal pool-type reactor. The boundary conditions lead to a dissymmetrical distribution of the temperature inside the cold pool which is strongly related to the thermal-hydraulics of the primary flow path.

Seven organizations have participated to the validation benchmark [67]: CEA, with CATHARE code, UNIROMA1, in collaboration with ENEA, with RELAP5-3D© code, NRG, with SPECTRA code, Argonne National Laboratory (ANL), with SAS4A/SASSYS-1 code, Karlsruhe Institute of Technology (KIT), with ATHLET code, and the Institut de Radioprotection et de Sûreté Nucléaire (IRSN), with ASTEC-Na code.

The thermal-hydraulic model developed by UNIROMA1 and the main results obtained in the framework of the validation benchemark are presented in this chapter.

3.1 Description of Phénix reactor

Phénix is a 563 MW_{th} sodium-cooled pool-type fast reactor [68], with an electric output of approximately 250 MW_{el}, located at the Marcoule nuclear site, near Orange, France. Its construction began in November 1968 and the plant was first connected to the French national electricity grid in December 1973. From 1993 to the end of the electricity production in 2009, the reactor has been operated at a reduced power of 350 MW_{th} (140 MW_{el}) [69].

Figure 85 shows the reactor block [70], which is a suspended type: all the vessels are supported by the upper cover slab, which is provided with flanges for the replacement/maintenance of the reactor components. The main vessel, which ensures biological protection, has a diameter of 11.8 m and it contains about 800 tons of primary sodium. The main vessel is attached to the upper slab by means of 21 suspension hangers and it is closed by means of a flat roof, featuring penetrations for the components. Any possible sodium leak is contained within the double-enveloped vessel, which is welded to the upper part of the main vessel. The roof and the double-envelope vessel are thermally insulated. The third vessel represents the primary containment; it is welded to the underside of the slab and it is attached to the reactor pit. The role of the third vessel is to contain radioactive products in case of severe accidents [70]. Below the core, the strongback, together with the conical shell, has the function of supporting the above structures and redirecting about 10 % of the operating flow to the Vessel Cooling System (VCS). Above the strongback, the diagrid connects the Primary Pumps (PPs) to the core, suppling the primary coolant to each Sub-Assembly (SA). The reactor core consists of an array of hexagonal assemblies, represented in Figure 86. Each assembly has an overall length of 4.3 m; the fuel is mixed uranium-plutonium oxide [71] [72]. The central fissile zone is divided into two regions having different enrichment, and it is surrounded by annular fertile zones, Axial Reflector Assemblies (ARA), and lateral neutron shielding rods. The reactor control is ensured by means of 6 control rods and 1 safety rod, that represent the complementary shutdown system (Système d'Arrêt Complémentaire, SAC).

The core is located inside of the primary vessel (see Figure 85), which separates the hot from the cold pool in the main vessel. The hot sodium, exiting the core, flows into the hot pool and subsequently moves into the six

intermediate, straight tube heat exchangers (see Figure 85 and Figure 87), marked as IHX and DOTE in Figure 87. The primary coolant flows downward through the shell side of the IHX and it is discharged into the cold pool. Three vertical-axis primary pumps ensure the primary coolant circulation, drawing the sodium from the cold pool and pumping it into the diagrid through three connector pipes. The six IHX, in groups of two, represent the interface between the primary system and three secondary loops. Each secondary loop is equipped with a mechanical pump located inside the expansion tank, a buffer tank and the auxiliary systems, which ensure the sodium storage, filling, and purification. Each secondary loop feeds secondary sodium to a steam generator that supplies the thermal power to a tertiary circuit operating with water as a fluid in a conventional Rankine cycle.

From 1993 until the final shutdown of the reactor in 2009, the secondary loop No. 2 was not operating and the two corresponding heat exchangers (called DOTE in Figure 87) were plugged. The Primary Pump No. 2 (PP2) was instead operating normally.

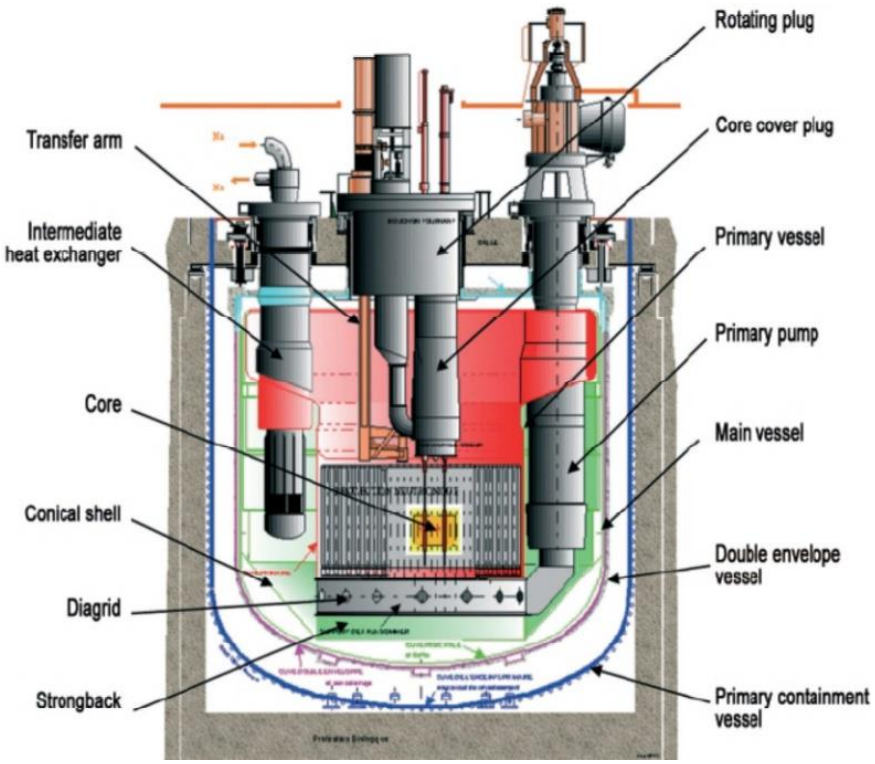

Figure 85. Scheme of the Phénix reactor block [70]

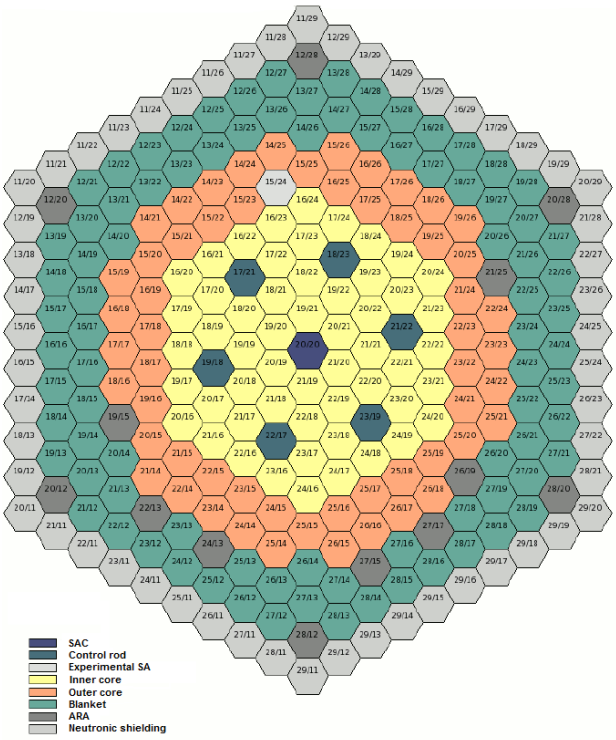

Figure 86. Top view of the core [72]

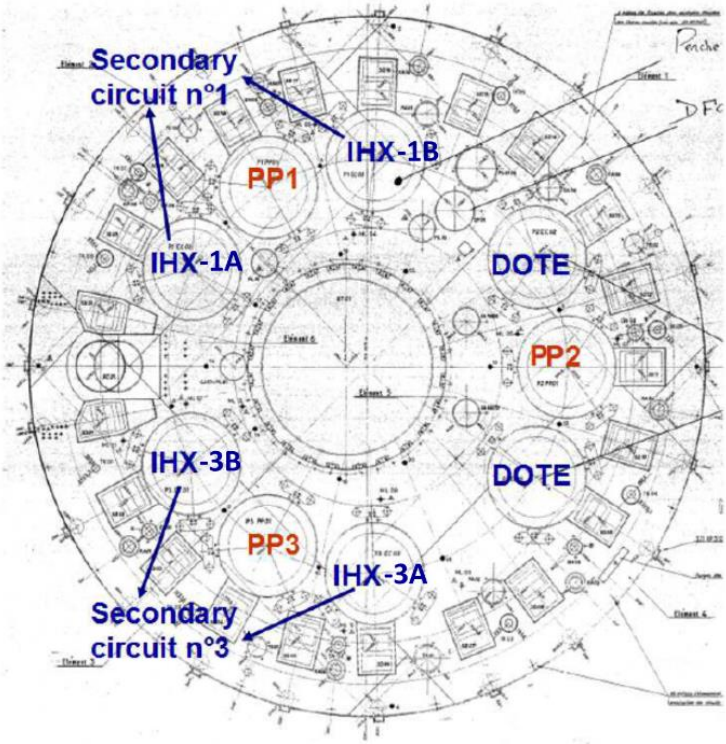

Figure 87. Top view of the reactor [70]

3.2 Overview of the dyssimmetric test

In 2009 two dissymmetrical tests were performed, one on each of the operating secondary loops (LOOP 1 and LOOP 3). The results of these tests support liquid metal reactor plant design. As the results of the tests were similar, thus proving test repeatability, only the test on LOOP 1 was considered in this study [73].

The test taken into consideration in this research work started from nominal steady-state conditions, i.e. full power and flow rates, followed by a sequence of events summarized in Table 11. The initiating event was the trip of the secondary coolant pump (on LOOP 1), with the speed reduced from 700 to 100 rpm in about 13 s. This resulted in azimuthal and axial asymmetry in the cold pool, with the reduction in cooling resulting in a rapid temperature increase in the cold pool at the outlet of IHX 1. After 5 seconds from the beginning of the test, automatic shutdown occurred (with the control rods inserted at a velocity of 1.4 mm/s for 45 s) and the speed of the secondary pump in LOOP 3 was reduced from 700 to 110 rpm in about 60 s, after the turbine trip signal.

At 48 s the SCRAM command was operated, and the test terminated after 1800 seconds.

The operating parameters have been provided by CEA to the benchmark participants; the measurement uncertainties have been included in the data sheet, as following:

- +/- 5 MWth on the thermal power before the SCRAM;
- 10 % for the decay heat power;
- +/- 5 K on the temperatures;
- +/- 5 % on the flow rates.

Table 11. Dissymmetrical test: main events sequence

Time (s)	Action
0	Secondary pump trip (on loop 1): speed reduced from 700 to 100 rpm in about 13 s
5	Automatic shutdown: insertion of the control rods (1.4 mm/s) for 45 s
	Turbine trip
	Secondary pump speed reduced (on loop 3) from 700 to 110 rpm in about 60 s
48	SCRAM
1800	End of benchmark test

3.3 Description of the thermal-hydraulic model

The Phènix modelling is composed of an overall number of 6940 hydraulic volumes, 11840 hydraulic junctions, 6888 heat structures and 40170 heat transfer nesh points. The development of the nodalization scheme is described in Ref. [73] and [74], analyzing different modelling approaches assessed during the blind-calculation phase of the validation benchmark.

The model mainly consists of:

- MULTID component, modelling the pools, the diagrid and the core bypass;
- Mono-dimensional model, reproducing the zones where a predominant 1D flow is expected (i.e. hexagonal fuel assemblies, heat exchangers, pump suction, feeding conduit, VCS and gas plenum).

The multi-dimensional component is composed of 35 axial lengths, 6 radial rings and 12 azimuthal sectors. The first three radii (R in Figure 88) are chosen to divide the core region in three zones (fuel zone, blanket-reflector zone, and natural circulation zone), and the fourth, fifth and sixth radii are chosen to uniformly divide cold and hot pools (radius 4 measures up to the axle of the IHXs and the PPs, radius 5 is chosen to have the azimuthal sectors with the same area of radius 4, and radius 6 corresponds to the primary vessel inner diameter). The number selection of azimuthal meshes is based on the PPs and IHXs geometrical positions (see Figure 88). The axial mesh lengths of the cold and hot pool regions and of the other components (reactor zone, skirt and PPs pipes, IHX, and VCS) are consistent with the vertical sliced approach (see Figure 89). Each 1D component is placed in accordance with the 3D geometrical specifications and the relevant elevations are preserved (see Figure 90). In order to represent the actual amount of fluid contained in each volume of MULTID component, volume factors and junction factors are used.

The reactor core modelling is divided into three main regions, corresponding to the division presented in Figure 86:

- the inner and outer core (corresponding to the innermost 7 rings of assemblies): an overall number of 127 parallel pipes reproduces each fuel assembly (one pipe for each assembly);
- the blanket zone (rings greater than 7): it is modeled with 36 equivalent pipes, simulating the radial blanket, the ARAs and the storage assemblies (for the cooling of spent fuel) grouped separately, according to their azimuthal configuration;
- the shielding zone: it is modelled with 24 equivalent pipes which include the neutronic shielding and boron carbide shielding elements.

The model of each FA in the core regions is rather detailed to represent the relevant geometric characteristics (20 control volumes per each FA pipe component). The detailed modelling approach applied for the reactor core has been developed in order to allow multi-physics calculations using RELAP5-3D© for the thermal-hydraulics and PHISICS for neutronics.

Calibrated K-loss coefficients, depending on flow conditions, have been introduced at the FA inlets; they have been evaluated on the basis of the MFR and the overall dynamic pressure drops data in nominal steady-state conditions, provide by CEA to the benchmark participants [75]. Several heat structures (20 per each FA modelling) are considered to reproduce the power generated by the fission reaction. Concerning the dissymmetric test benchmark, the thermal power has been provided by CEA and introduced as boundary condition in the model. In addition, heat losses between FA and core bypass wrap are simulated with 3722 heat structures, reproducing the heat conduction through the wrap thickness, assuming the thermophysical properties of the structural materials provided by CEA [75].

The three primary pumps are simulated separately. Each one is composed of a vertical pipe in which coolant flows upward, reproducing the annular inlet to the component, connected with the corresponding region of the cold pool, with the pump component and with the vertical pipe which contains the primary coolant flowing downward to the diagrid. The nodalization scheme is showed in Figure 91. The homologous curves of the pump components are set-up using Phénix reference data [75]. Each of the six IHX are modelled separately. The primary side is simulated with a pipe component connected upstream and downstream with the correspondent region of hot pool and cold pool (see Figure 88). The IHXs secondary sides are modeled separately with pipe components from an inlet and outlet collectors (dummy) and fed with imposed boundary conditions. Figure 91 shows the representative nodalization scheme of the heat exchangers. Primary and secondary sides of DOTE components (Figure 88) are modeled and disabled closing the connections between the IHXs No. 2 and the hot pool, to prevent the primary coolant to flow through them. The VCS modelling is presented in Figure 91; it is simulated

with a pipe component connected upstream with the diagrid (MULTID component) and downstream with the corresponding regions of the cold pool. Several heat structures are included into the model to consider the heat losses between the hot and cold zones of the reactor (through the primary vessel, the IHXs and pumps shell) and the heat exchanged between the cold pool and the VCS.

The pressure drop in the rod bundle is evaluated using the Cheng & Todreas correlation for laminar, turbulent and transition flows [76]. Specifically, the standards R5-3D wall friction correlations were modified as to reproduce the Cheng & Todreas formulation, simulating a wire-wrapped rod bundle by form loss coefficient with a *Re* dependence, as described in Ref. [25] and [77].

Concerning the HTC evaluation, default correlations have been applied, except for the calculation of the coefficient across the primary side of the IHXs. The intermediate heat exchangers are characterized by *p/d* equal to 1.43 and Graber & Rieger correlation [78] has been selected for the HTC evaluation:

$$Nu = 0.25 + 6.2\frac{p}{d} + \left(-0.007 + 0.032\frac{p}{d}\right) Pe^{\left(0.8-0.024\frac{p}{d}\right)} \tag{11}$$

As described in section 2.1.3, an HTC multiplicative factor equal to 1.4 has been imposed, in accordance with the selected correlation.

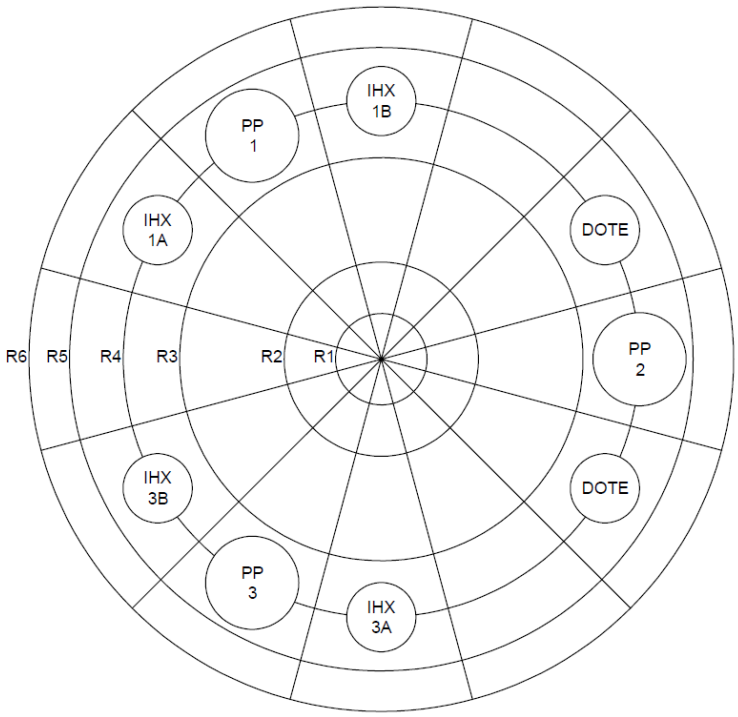

Figure 88. Overview of radial and azimuthal meshes of MULTID component

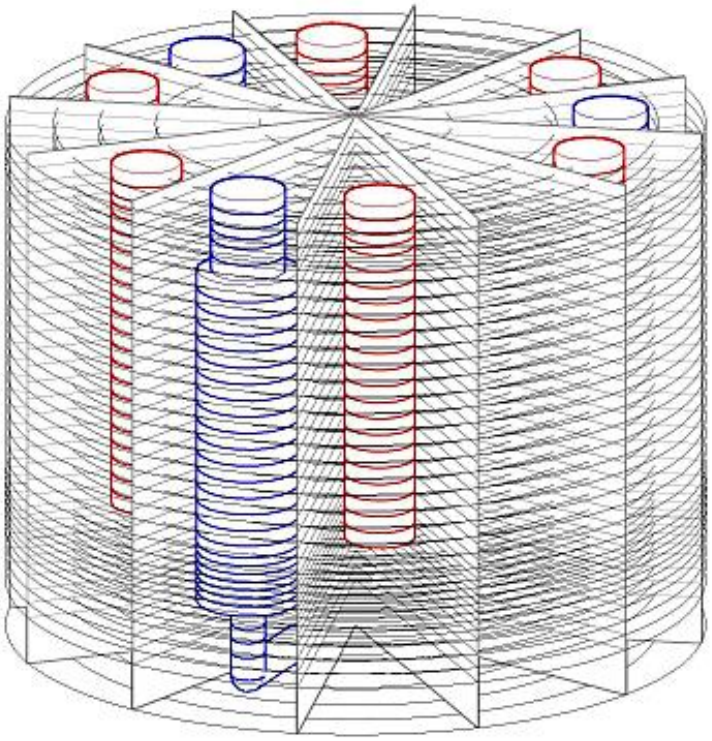

Figure 89. Scheme of MULTID component

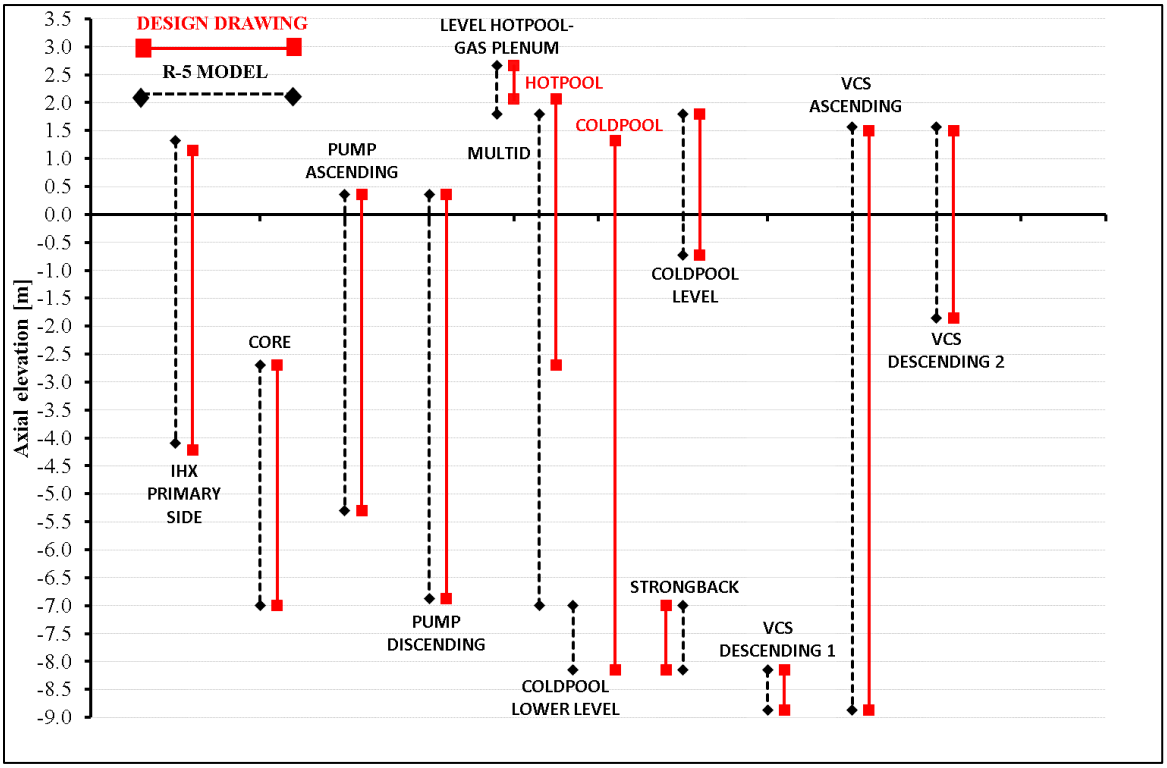

Figure 90. Comparison of Phénix relevant heights

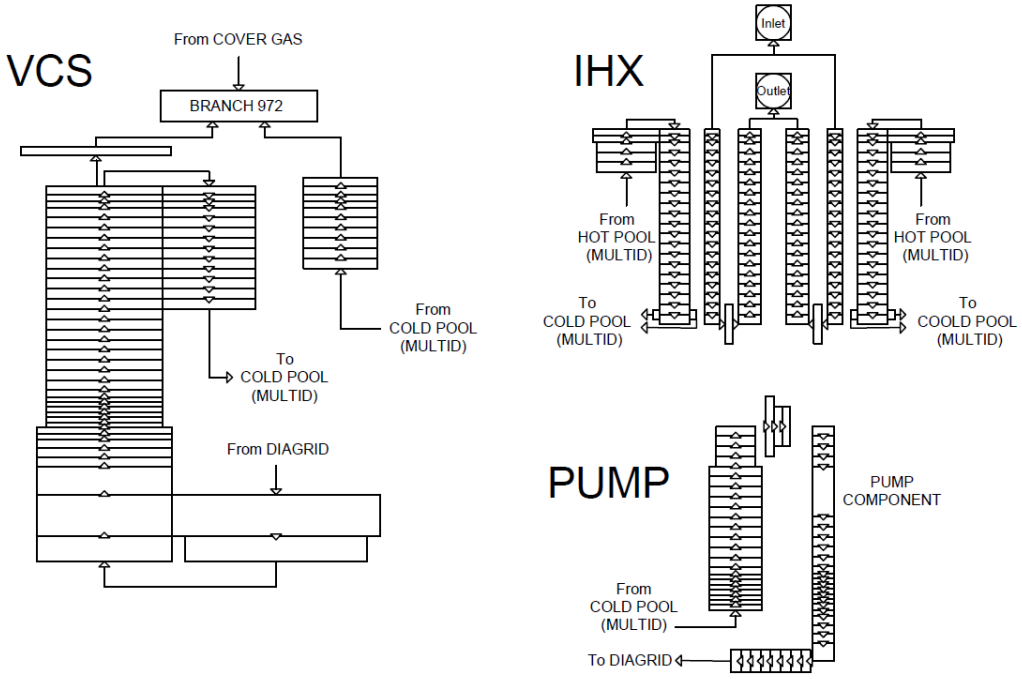

Figure 91. Overview of the nodalization scheme of PPs, IHXs and VCS

3.4 Simulations results

In order to obtain the initial conditions for the transient test, the full power operation is first analyzed. Table 12 summarizes the nominal (full power operation) boundary conditions applied and Table 13 the comparison of R5-3D results and experimental data. As shown in the Table 13, the code is able to provide an excellent evaluation of the full power conditions, containing the discrepancy respect to the experimental data within the measurement uncertainties.

Figure 92 shows the sodium temperature within the primary system, considering a relevant section. The picture represents the full power steady-state condition, highlighting a slight thermal stratification within the cold pool, at the level of the IHXs outlets.

Table 12. Nominal boundary conditions

Quantity	**Unit**	**Value**
Primary circuit balance	MW	341
Secondary system IHX inlet temperature	K	594
Secondary system IHX outlet temperature	K	787
Mass flow rate through IHX-1A secondary side	kg/s	347

Table 13. Steady-state calculation

Quantity	Unit	Experimental data	Simulation result	Error
IHX secondary side inlet temperature	K	594	594	0 K
IHX secondary side mass flow rate	kg/s	347	347	0%
PP total mass flow rate	kg/s	2209	2211	1%
IHX secondary side outlet temperature	K	784	787	+3 K
Core inlet temperature	K	658	660	+2 K
Core outlet temperature	K	807	806	-1 K
IHX primary side inlet temperature	K	793	792	-1 K
IHX primary side outlet temperature	K	658	660	+2 K
Core mass flow rate	kg/s	1988	1992	0%
VCS mass flow rate	kg/s	221	219	0%
IHX primary side mass flow rate	kg/s	497	498	-1%

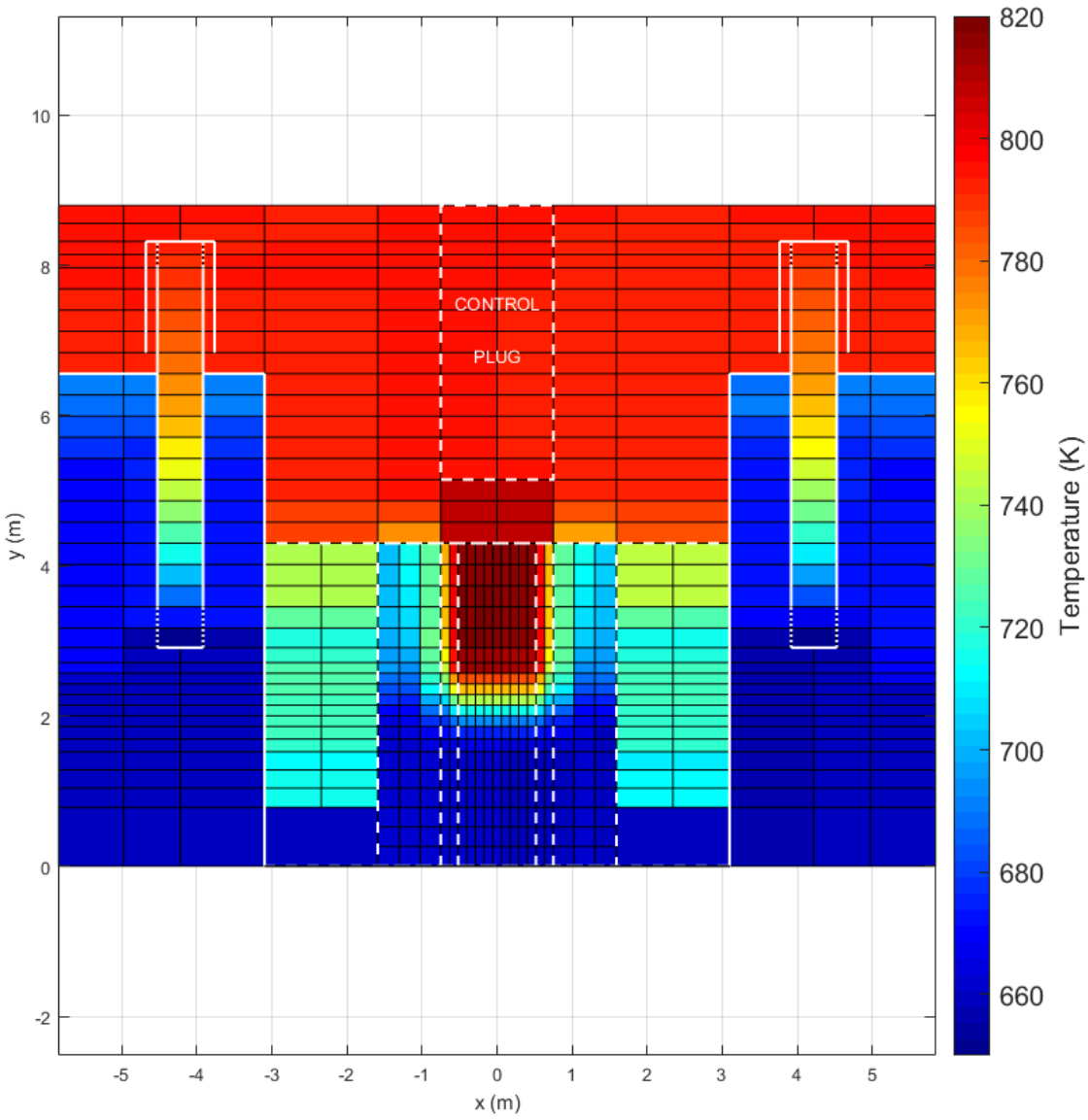

Figure 92. Steady-state conditions

Starting from the steady-state results, the dissymmetric test is reproduced following the sequence of events shown in Table 11. At the beginning of the test, secondary mass flow rate through LOOP 1 (L1) decreases, causing the fast reduction of the thermal power removed by the IHX-1A and IHX-1B. Figure 93 shows the experimental thermal power removed by LOOP 1 (IHX-1A + IHX-1B) and LOOP 3 (IHX-3A + IHX-3B), comparing them with simulation results in the first 200 s of the transient. The delay in power reduction by LOOP 3 (L3), due to the delay time of the pump trip on LOOP 3, is also highlighted in Figure 94. The plots show a good agreement between the simulation and the experiment. During the first 30 s, the thermal power removed by LOOP 3 increases up to 85% of the total power; at this time, the power removed by LOOP 1 reaches and maintains the value of about 20

MW, while the power removed by LOOP 3 continues to decrease, reaching the same value of LOOP 1 at about 70 s. Then, the symmetrical distribution of the power is completely restored at 200 s.

The quick decrease of the power removed by L1 leads to a hot shock at the IHX-1A and IHX-1B primary side. Figure 95 shows the comparison of calculated IHX-1B outlet temperature with thermocouples acquisition. After 35 s from the beginning of the test, the experimental temperature reaches a peak value of 766 K. R5-3D is able to predict the quick increase of temperature, even if overestimating the maximum value of about 8 degrees. The slower speed decrease of the secondary pump on LOOP 3 causes a similar peak temperature at the IHX-3A and IHX-3B outlets. The effect is an asymmetric distribution of the temperature inside the cold pool, as shows from Figure 15 to Figure 19, reproducing the evolution of the temperature within the reactor in the first 120 s. The figures show the sodium temperature in a relevant sliced of the reactor, represented with the red line in Figure 96.

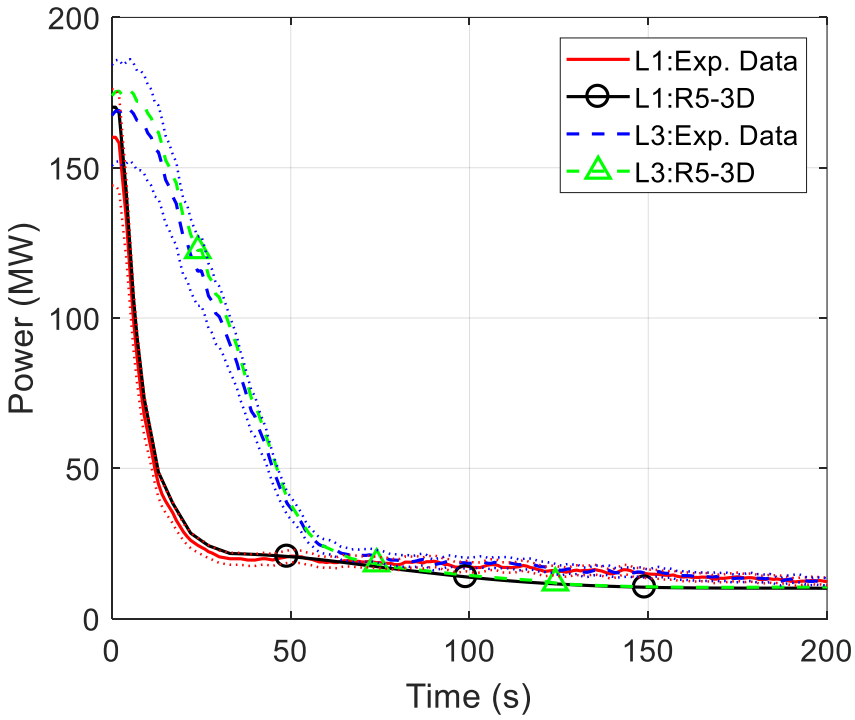

Figure 93. Power removed by IHXs

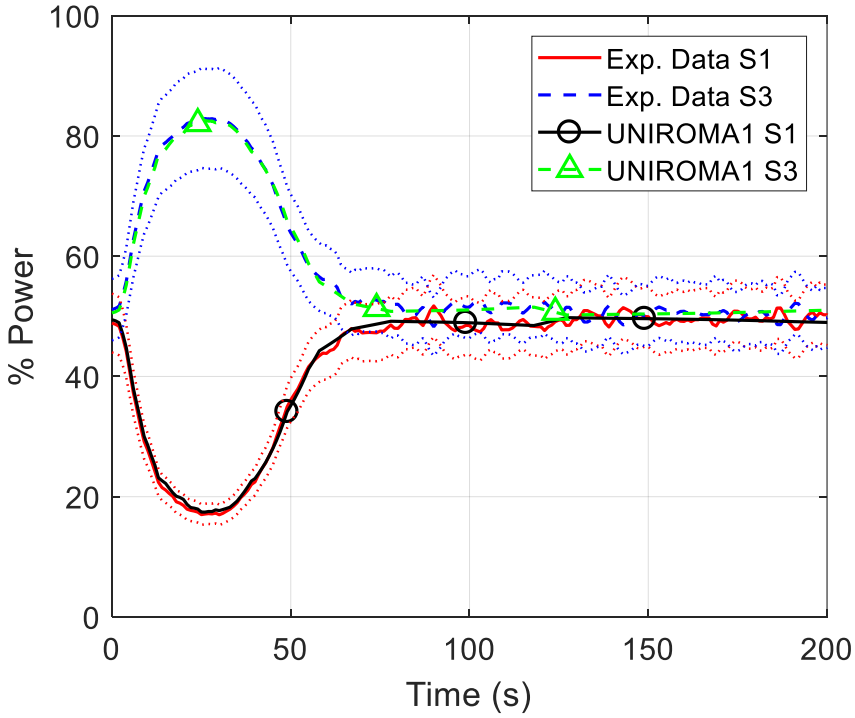

Figure 94. Power removed by L1 and L3 (%)

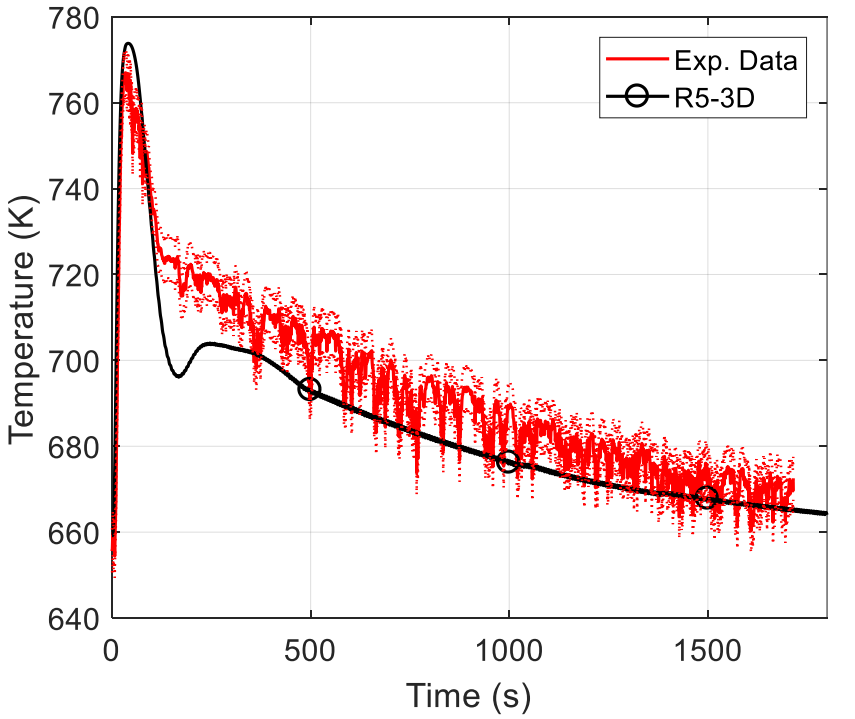

Figure 95. IHX-1B outlet temperature

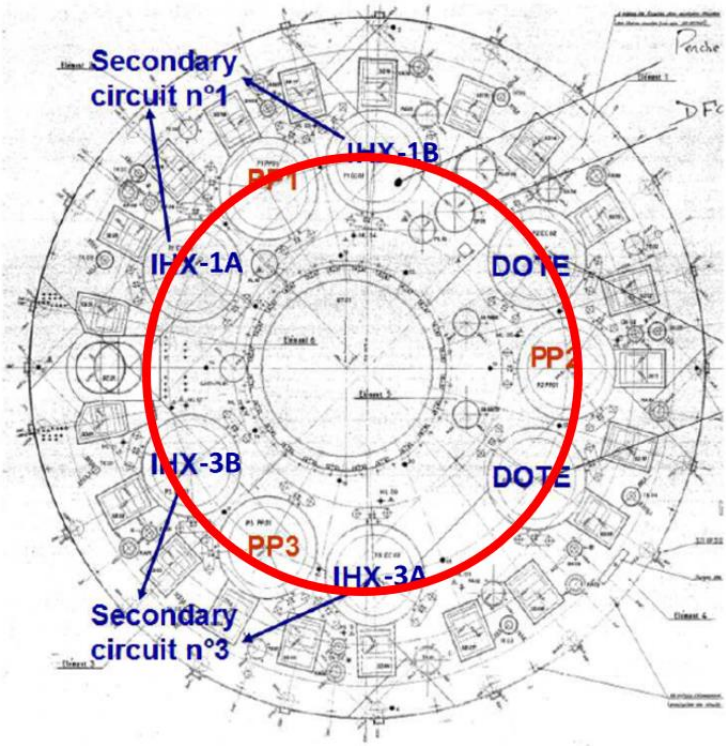

Figure 96. Relevant slice

The multi-dimensional modelling approach provides results in high resolution within the pools. Figure 97 shows the initial conditions evaluated by R5-3D. In these figures, the x-axis represents the theta- coordinate, showing the axial temperature distribution calculated in the control volumes between radius 4 (R4) and radius 5 (R5) on the r-coordinate (see Figure 88). At the beginning of the transient test (full power steady-state condition), hot pool does not present relevant thermal stratification, showing uniform temperature in each sector. Within the cold pool, a significant thermal stratification is observed; the axial level of the stratification move from 3.5 m, where the cold sodium exit the active IHXs (see "**X**" and "**O**" in Figure 97), to 2.5 m, where the cold sodium is drawn into the pump conduits (theta 4, 8 and 12). In the first seconds of the transient, the decrease in thermal power removed by LOOP 1 causes a small increase in temperature at the IHX1 exit (see "**X**" in Figure 98), as analyzed in Figure 95. Subsequently, after 30 s, the hot fluid moves to the upper part of the cold pool, in the volumes around IHX1 (see theta 1 and 11 in Figure 98), and the cooler fluid moves downward (from theta 2 to 10 and 12 in Figure 98). This effect results in a peak temperature observed by the TCs located at the PP1 inlet section, shown in Figure 102 (664 K at 50 s), also predicted by the code, even if the magnitude is underestimated of 3 degrees. At the beginning of the test, the temperature acquired at the inlets of the three primary pumps are the same and R5-3D provides a good prediction of these parameters (see form Figure 102, Figure 103 and Figure 104). After the transition event, the asymmetric conditions reached within the cold pool, lead to a different temperature distribution at the pumps inlets, as observed at the PP1 inlet.

Between 30 and 60 s, the secondary flow decrease through the LOOP 3 leads to a peak temperature at the IHXs 3 outlets (see "**O**" in Figure 99). At this time, the upper part of the cold pool is completely heated by the hot fluid exiting from IHX1; for this reason, the hot sodium exits from IHX3 and moves downward, reaching the PP3 inlet section (see "**Y**" in Figure 99). The hot sodium movement within the cold pool, predicted by R5-3D, leads to a peak temperature of about 680 K at the PP3 inlet (Figure 104), which is not observed by the thermocouples.

After that, the average temperature within the cold pool increases uniformly (see Figure 100) and, after 120 s from the beginning of the test, the thermal stratification level has been moved downward up to 1.8 (Figure 101). The temperature increase within the cold pool causes the temperature increase at the PPs inlets, where the maximum temperature of 704 K is reached. As shown in Figure 102, Figure 103 and Figure 104, the maximum temperature is well predicted by R5-3D, even if the calculation shows two consecutive peaks instead of the single experimental one. This is probably due to some discrepancies highlighted in the temperature distribution within the cold pool in the first 120 s. After that, sodium temperature decreases uniformly at the PPs inlets and R5-3D reproduces well the overall pool cooling.

The average core outlet temperature is compared in Figure 105. Due to the automatic shutdown, occurring at 5 s, the core power decreases in a time-lapse of 40 seconds. The primary pumps continue to operate and the primary mass flow rate through the core remains quite constant during the test (a little variation occurs due to the temperature variation of the sodium). It leads to a cold shock at the core outlet. The fast temperature decrease is well predicted by the code, matching very well the experimental acquisitions and the minimum temperature of 680 K. After that, the core outlet temperature increase following the qualitative trend of the seen at the PPs inlets. The simulation shows a good prediction of the temperature increase, even if the two peaks observed at the PPs inlets are also predicted at the core outlet. Finally, the temperature decreases to the final value and R5-3D provides a good estimation of the overall cooling.

The rapid temperature decrease, acquired at the core outlet, is also observed within the hot pool with a delay; it is visible at the inlets of the intermediate heat exchangers, plotted in Figure 106, Figure 107 and Figure 108. Experimental data highlights a thermal inertia effect due to the large volume of sodium contained into the hot pool. In fact, the lower temperature peak observed at the outlet section of the reactor core, is not acquired at the IHXs inlets. The main discrepancies between experiment and calculation are observed in these parameters. In fact, R5-3D seems to underpredict the thermal inertia within the hot pool, obtaining a cold peak temperature at the IHXs inlets.

The temperature distribution within the reactor vessel is presented in Figure 109, Figure 110 and Figure 111, concerning three relevant instants: the time of the minimum and maximum temperature at the core outlet after the transition and the final condition. As shown by the representations, a progressive cooling of the whole reactor occurs and a thermal stratification within the hot pool is observed from the beginning of the transient test, moving up to 8 m at the end of the test.

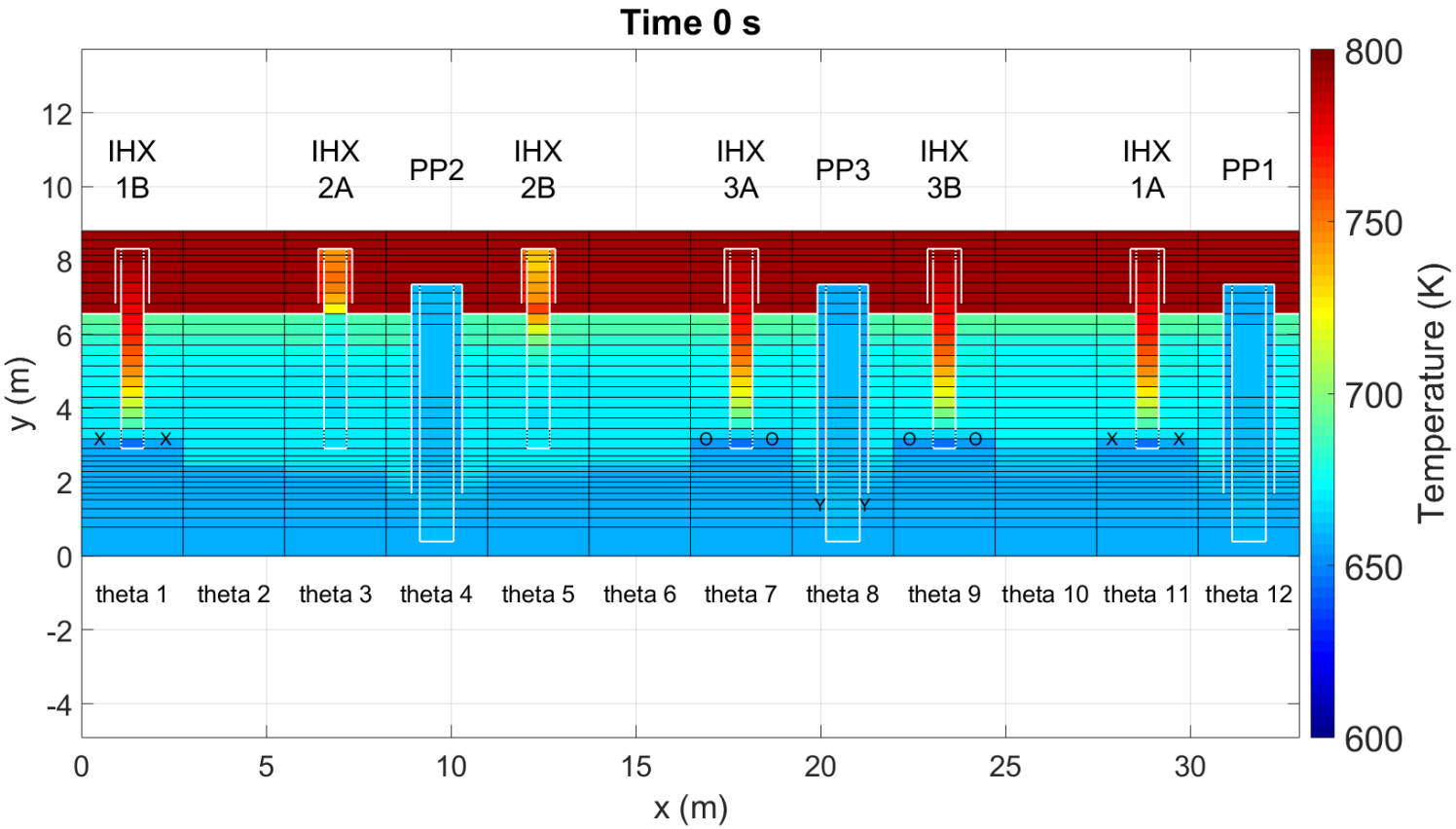

Figure 97. Primary system temperature: initial conditions

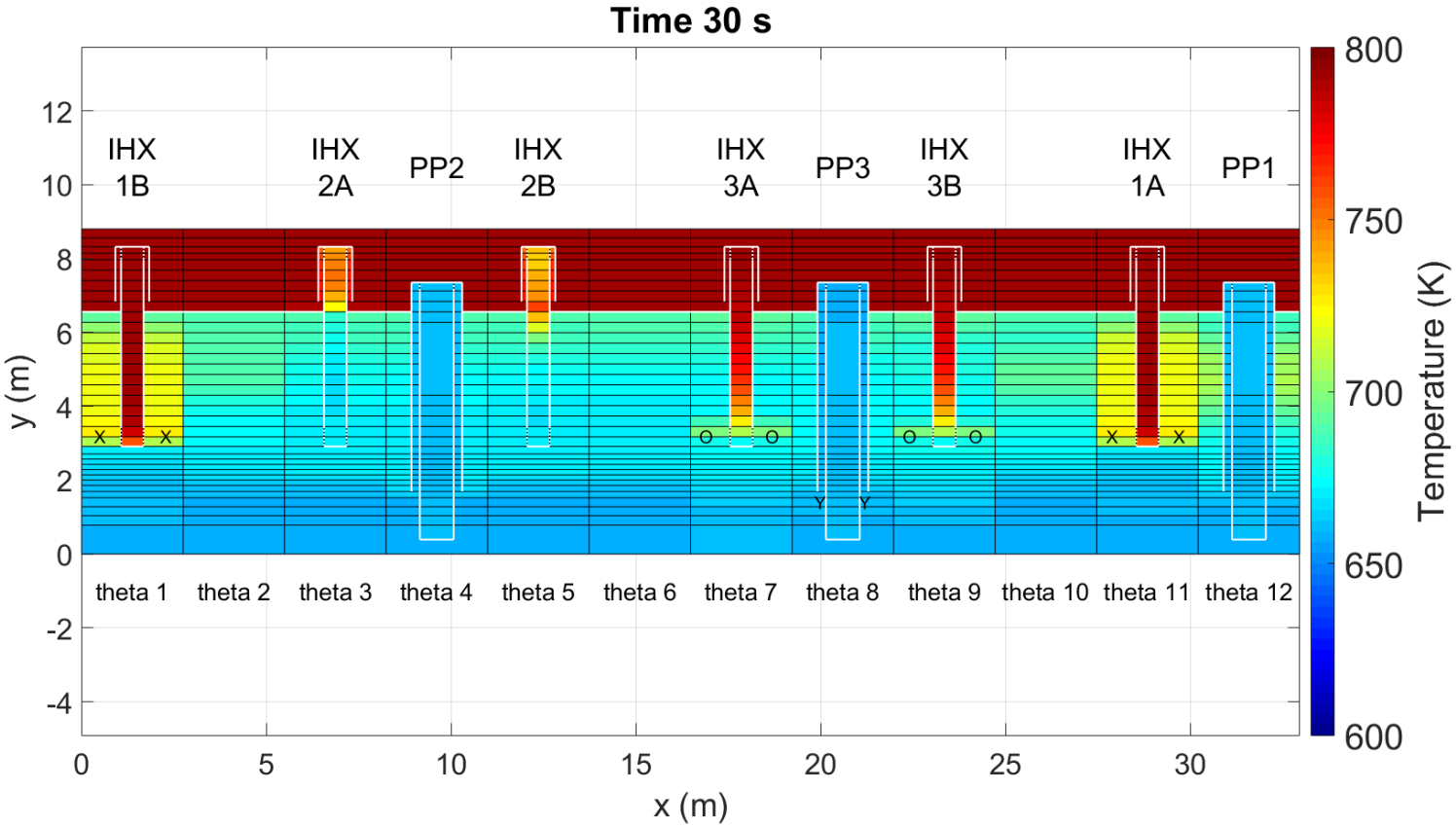

Figure 98. Primary system temperature: 30 s

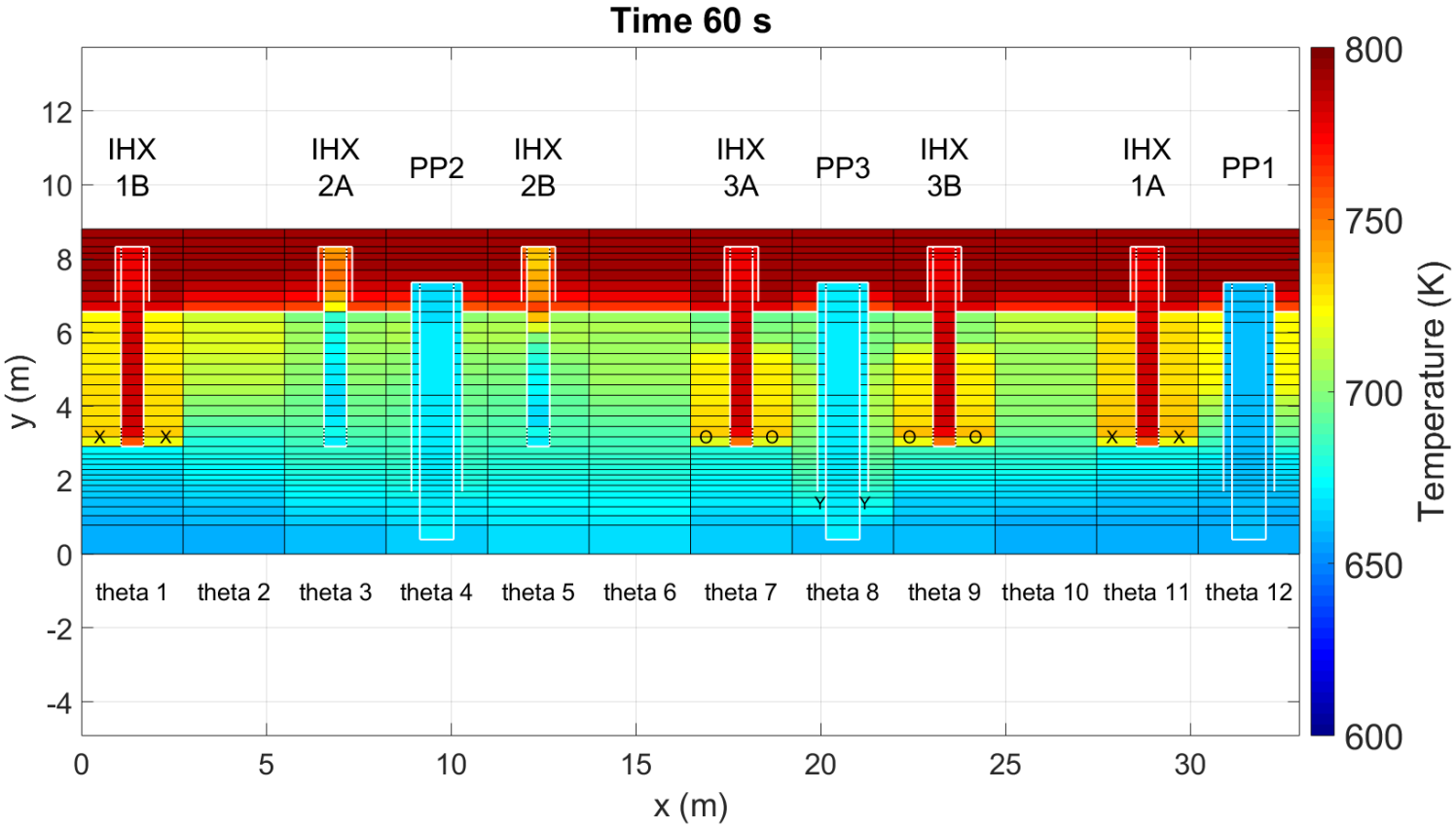

Figure 99. Primary system temperature: 60 s

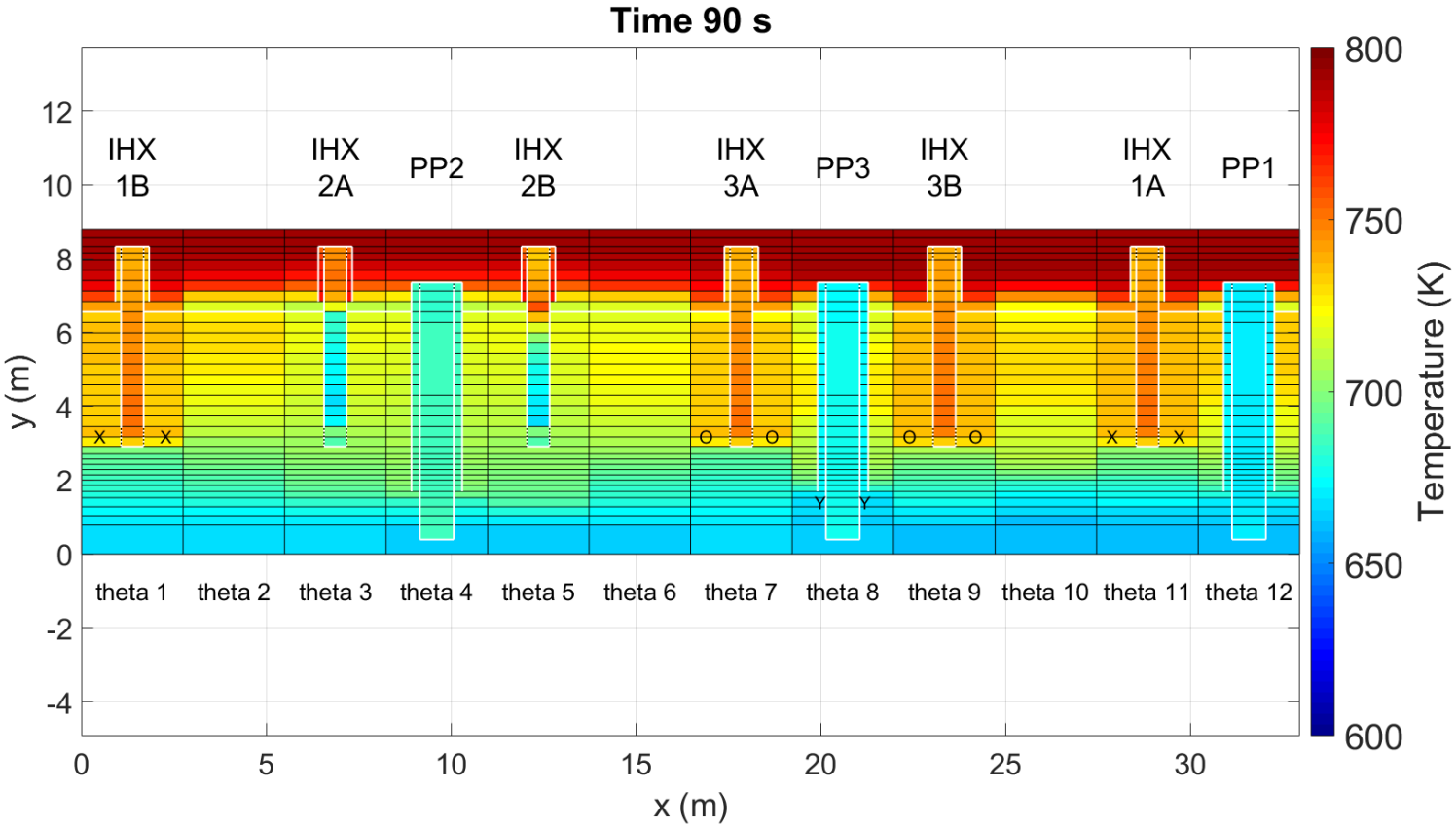

Figure 100. Primary system temperature: 90 s

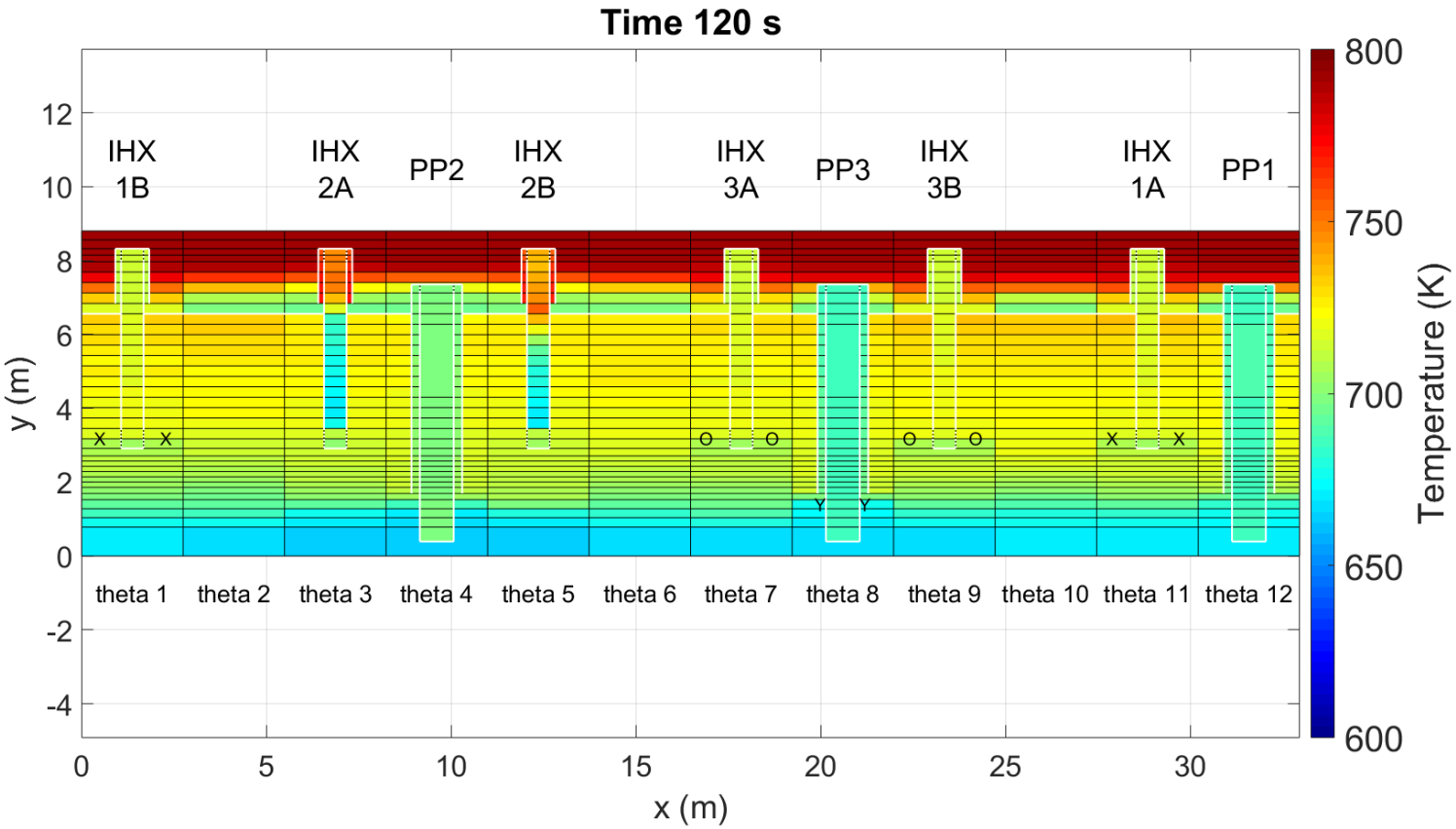

Figure 101. Primary system temperature: 120 s

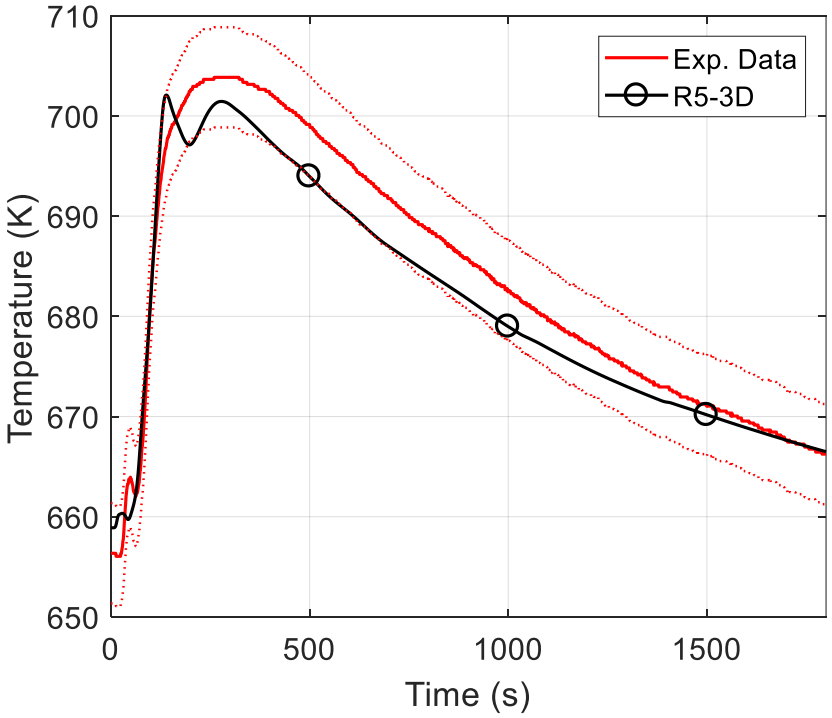

Figure 102. PP1 inlet temperature

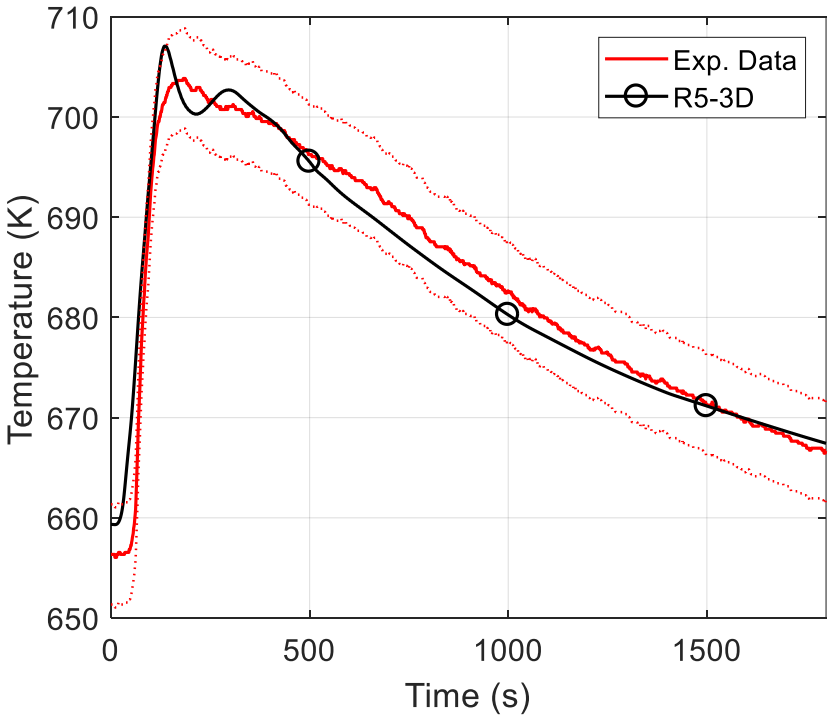

Figure 103. PP2 inlet temperature

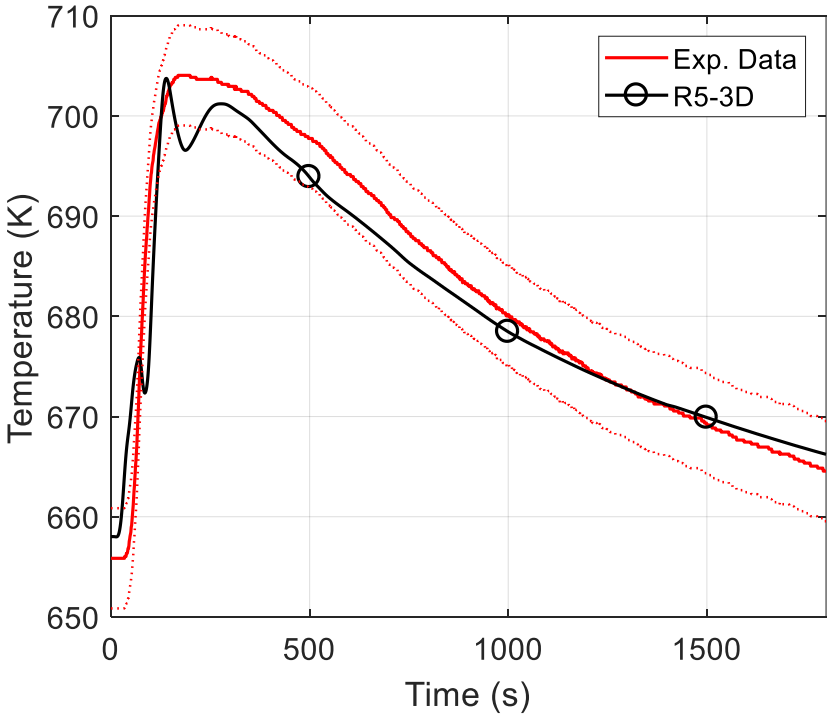

Figure 104. PP3 inlet temperature

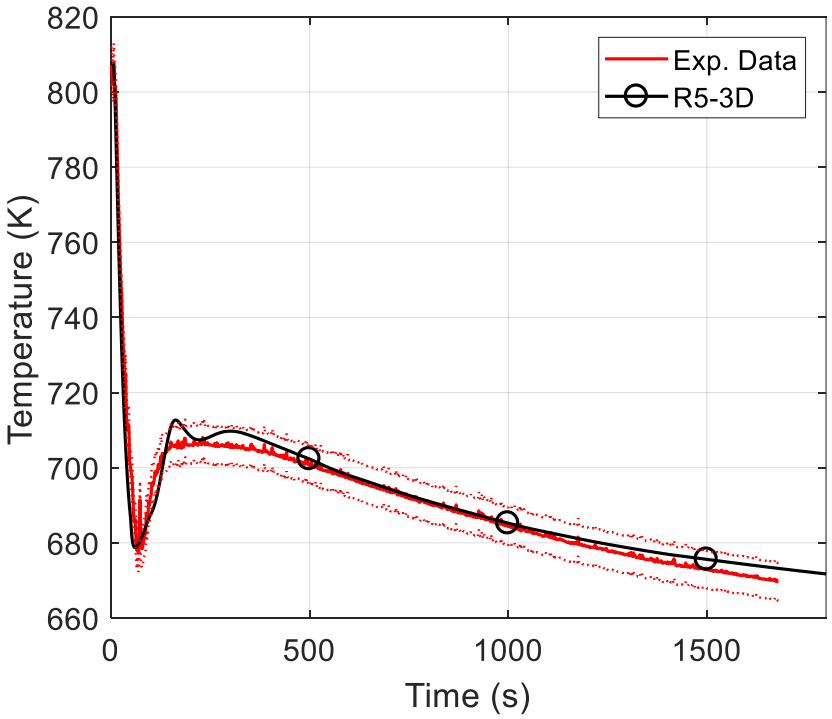

Figure 105. Core outlet temperature

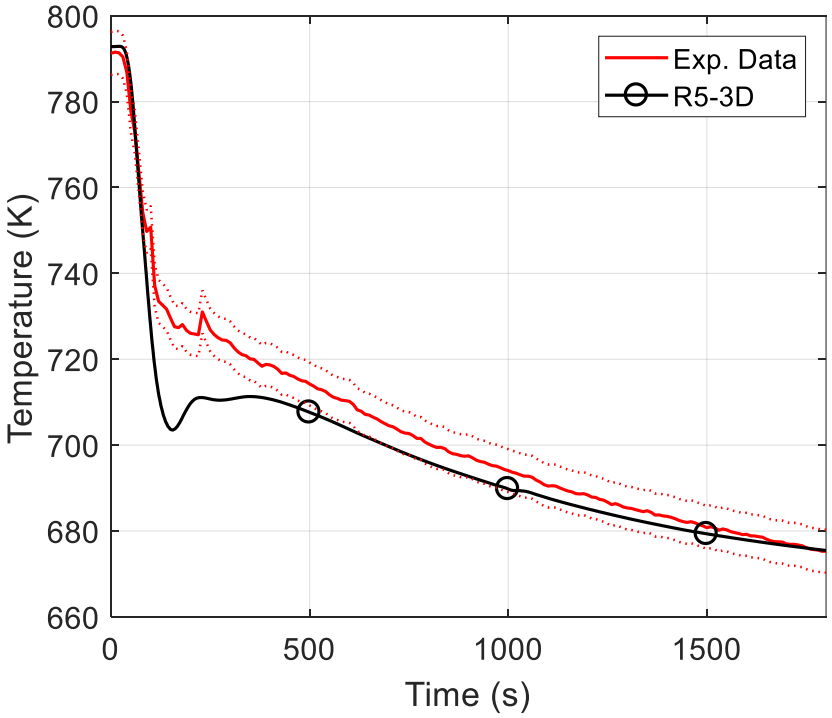

Figure 106. IHX-1A inlet temperature

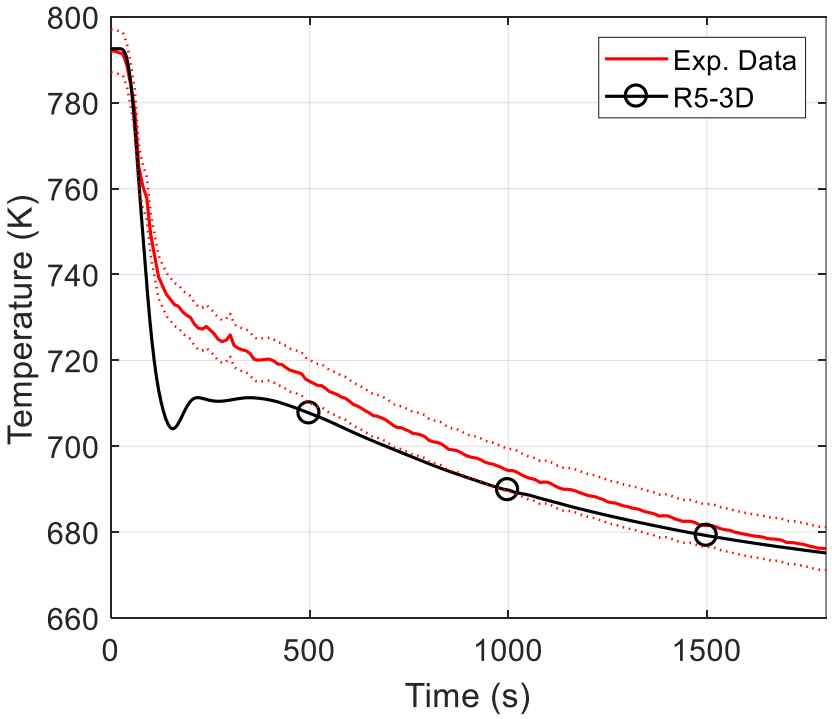

Figure 107. IHX-3B inlet temperature

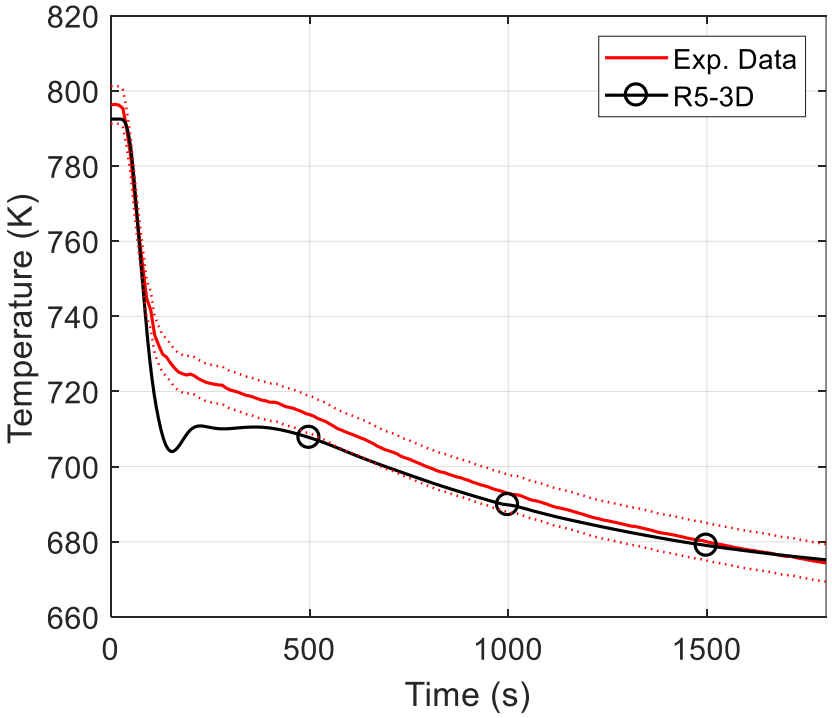

Figure 108. IHX-3A inlet temperature

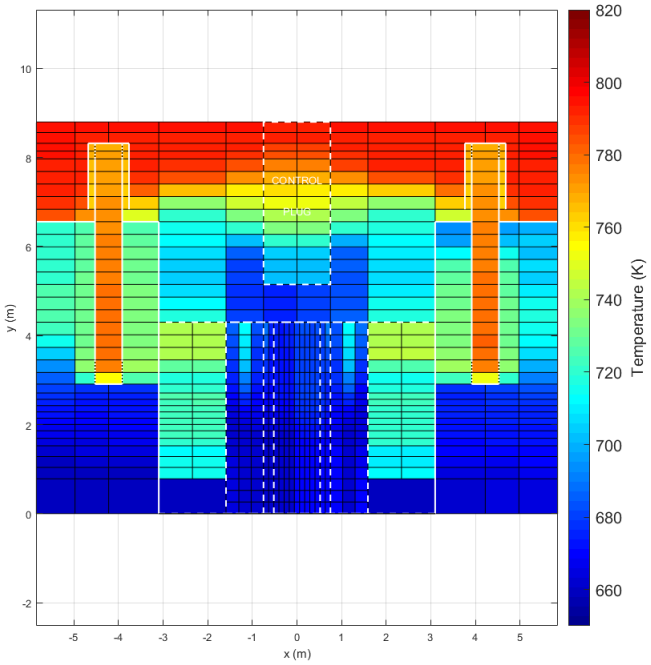

Figure 109. Temperature distribution: 60 s

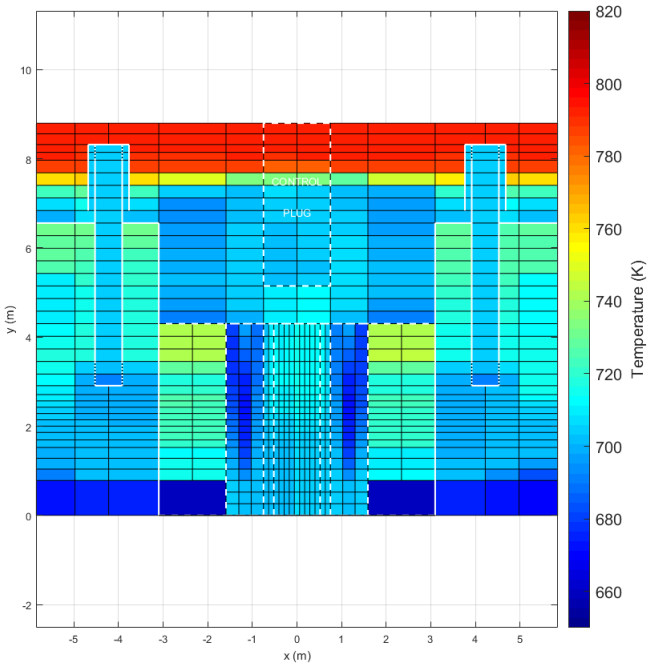

Figure 110. Temperature distribution: 160 s

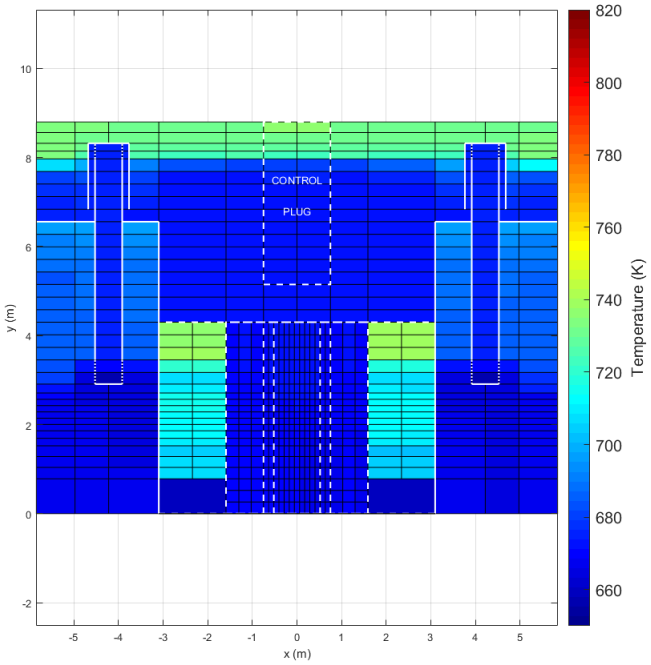

Figure 111. Temperature distribution: final condition

3.5 Conclusive remarks

The Phénix Dissymmetric End-of-Life Test offers useful experimental data for the validation of thermal-hydraulic system codes, especially regarding their capability to predict thermal-hydraulic asymmetries in liquid metal pool reactors. “Sapienza” University of Rome, in collaboration with ENEA Brasimone RC, developed a thermal-hydraulic model of Phénix using RELAP5-3D©, focused on the evaluation of the main phenomena which are expected to occur under asymmetrical boundary conditions. At this purpose, a detailed three-dimensional nodalization of the pools is developed. In addition, the core is analyzed assembly per assembly and the PPs and the IHXs are separately modelled.

The full power calculation has highlighted good capability of the code to reproduce the normal operation of the reactor. Starting from the steady-state results, the transient calculation has been performed assuming the dissymmetric test boundary conditions provided by CEA. The asymmetric distribution of the flow rate through the secondary loops leads to an asymmetric operation within the primary system, which is well predicted by R5-3D. The asymmetrical operation of the two secondary systems leads to a dissymmetric evolution of the thermal-hydraulics within the cold pool. Good agreements have been observed between experiment and simulation. In particular, the movement of the hot sodium within the cold pool is well predicted by the code, which is able to predict the local peak temperature at the PP1 inlet. At this regard, the three-dimensional momentum equation adopting the MULTID modelling seems to provide a good instrument for the evaluation of the temperature and flow distribution within large volumes.

4 COMPUTATIONAL ACTIVITY ON PERSEO FACILITY

Safety and reliability have been recognized as important issues for the development of innovative GEN IV reactors. The development of nuclear reactors cooled by liquid metal is strongly correlated to these goals, presenting peculiar characteristics related to the thermophysical properties of the coolant. Although the main parameters that influence the DHR operation in LWRs are well known, LMFRs present additional challenges related to the possibility of the coolant freezing, that may occur in long term DHR operation, when the power removed from the primary system could exceed the residual decay power. So, innovative DHR systems for LMFR applications must consider two conflicting requirements:

- efficient decay heat removal, guaranteeing core temperatures according to the safety limits of the materials;
- preventing coolant freezing.

In order to meet the objectives fixed by GIF [2], innovative DHR system must reduce the probability and the magnitude of core damage without relying on continuously generated power, such as normal AC power, i.e. a passive decay heat removal system. A passive system must ensure the operation without external power source, based on simple physical principles like gravity. However, in accordance with the International Atomic Energy Agency (IAEA) standards [79], a passive system can be actuated with active components that, using an independent stored source, start the passive operation with a single-action (for example valves).

One of the most promising passive DHR system is composed of an isolation condenser (IC) immersed in a dedicated pool, which operates as a final heat sink. This solution is supposed to be used in ALFRED [80]. The main issues related to the application of this system for safety of LMFRs will be analyzed in depth in section 5.2.1.

Several studies and experimental campaigns were involved in the development of this system and their integration in innovative nuclear reactors, investigating the decay removal capabilities and providing experimental data useful for code validation. In this framework, a benchmark activity has been proposed within the OECD/NEA/CSNI/WGAMA “Thermal-hydraulics of passive safety systems in water-cooled reactors”, concerning the experimental campaign performed on PERSEO (in-Pool Energy Removal System for Emergency Operation) facility. The activity has aimed to investigate capabilities of STH codes to reproduce heat transfer in a full scale HX submerged in a water pool.

“Sapienza” University of Rome has participated in the benchmark exercise using RELAP5-3D©. After a brief description of the facility and of the experimental campaign, the nodalization scheme developed by UNIROMA1 will be presented and the main results will be discussed.

4.1 Description of the test facility

PERSEO is a full-scale facility built at SIET (Società Informazioni Esperienze Termoidrauliche) laboratories in Piacenza (Italy). The experimental facility aims to study an innovative passive DHR concept, based on an IC operating in natural circulation, submerged in a pool. PERSEO was built by refurbishing the existing PANTHERS (Performance Analysis and Testing of Heat Removal System) IC-PCC (Isolation Condenser – Passive Containment Cooling) facility, used in the past to investigate thermal-hydraulic performances of a full-scale module of a Small Boiling Water Reactor (SBWR) in-pool HX [81].

Figure 112 shows the scheme of the PERSEO facility. The primary system is mainly composed of a pressure vessel, characterized by an overall volume of 43 m^3 and a total height of 13 m, and the isolation condenser. The two main components are connected through a steam pipe line and a condensate drain line.

The pressure vessel supplies steam at fixed conditions. It is part of the multipurpose GEST (GEnerator Separator Tests) facility [83], conceived to maintain the saturation condition typical of a BWR primary system or PWR secondary system, but its adaptability allows to supply steam in a large wide of thermodynamic conditions, coming from the nearby EDIPOWER power station (steam supply in Figure 112). The level within the pressure vessel is controlled through a valve installed in the condensate discharge line, connected at the bottom of the vessel (see Figure 112). The IC heat exchanger is composed of two cylindrical headers and 120 vertical tubes. The upper header is fed by the steam line and the bottom header is connected to the drain line.

The secondary side of the facility is composed of two pools: the HX Pool (HXP) and the Overall Pool (OV). The HXP is characterized by an overall volume of 29 m^3 and a total height of 5.7 m. It contains the IC, allowing the heat exchange from primary to secondary sides. A vacuum breaker valve, installed at the top of the HXP, opens when the pressure within the pool becomes lower than the atmospheric pressure. The OP (173 m^3 and 5.8 m height) represents the final heat sink of the PANTHERS PCC facility (the heat exchanger of the facility is still present within the pool). In this configuration of the facility (PERSEO), it represents the water reservoir. The two pools are connected at the bottom by a water line, equipped with a triggering valve (F 045 in Figure 112), and, at the top, with a steam duct, provided with an injector allowing the mixing of the steam into the OP, limiting the thermal stratification phenomenon (see Figure 112). In addition, the OP is equipped, at the top, with a boil-off pipe, allowing the steam discharge, and, at the bottom, a water discharge line, operated through a dedicated valve (F 031 in Figure 112).

In steady-state conditions, before the beginning of a transient test, the pressure vessel is maintained in saturated conditions, with a required liquid level, controlled by supplying the desired steam from the EDIPOWER power station and the water discharge through the discharge line. In this condition, the steam line, the primary side of the IC and the drain line are filled by saturated steam. On the secondary side, the triggering valve is closed; the OP is filled by cold water at the desired level and the HXP is full of air or steam, depending on the test specifications. The transient test starts opening the triggering valve; the cold water moves from the OP into the HXP. The IC is flooded by cold water and the heat exchange takes place. On the primary side, the steam condensation leads to the establishment of the natural circulation, and the steam conditions are maintained constant through the EDIPOWER power station. On the secondary side, the steam created within the HXP is driven by the steam duct into the OP, where it is condensed or discharged depending on the water level [82] [84].

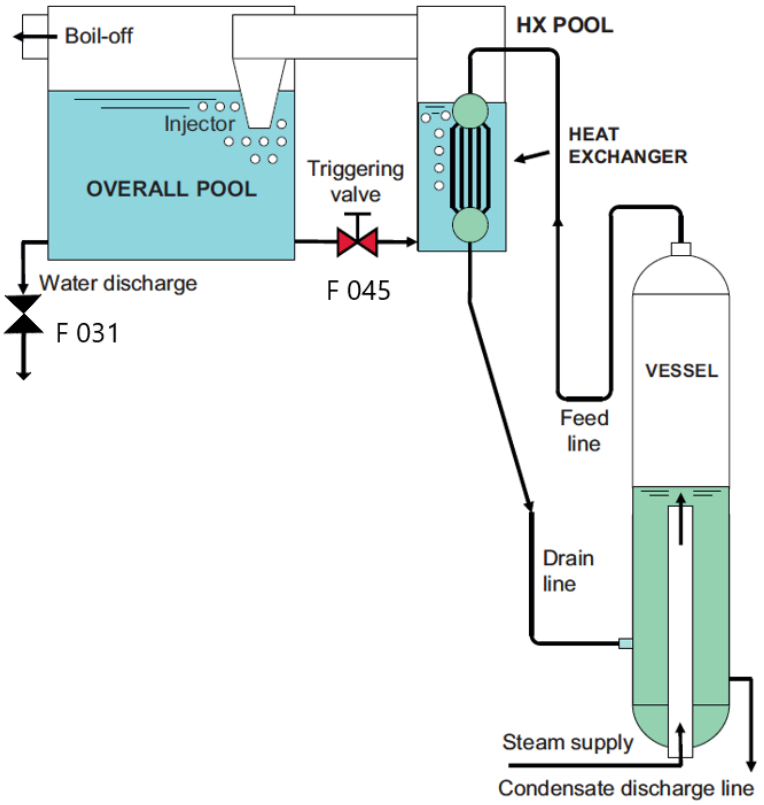

Figure 112. PERSEO facility: scheme [82]

4.2 Overview of the experimental test

Among the several tests performed within the experimental campaign, Test 7 has been chosen for the benchmark exercise, due to the completeness of the test. It is a full pressure test (70 bar) in which both the system stability and the long term operation are investigated. The test is divided in two relevant parts:

- Part 1: it is a stability test aimed to investigate the behavior of the system considering two different water levels within the HXP: 1.4 and 3.5 m;
- Part 2: it aims to verify the long term cooling capability of the system. For this purpose, the water level decrease within the OP is accelerated by opening the valve F 031 (see Figure 112), simulating the normal depletion of water due to the boiling within the HXP.

The whole Test 7 is devoted to characterize the in-pool and in-tube heat transfer and the thermal-hydraulic coupling of the two pools during the operation of the innovative DHR concept.

4.2.1 Test 7 Part 1

The experimental test starts in steady-state conditions with the primary system operated at 70 bar. The steam and drain lines and the HX are filled with saturated steam and no mass flow rate is observed within the primary loop. The HXP is full of air and the OP is filled with cold water. The triggering valve is closed, and no mass flow rate is observed between the two pools.

Starting from the steady-state conditions, the Part 1 of the test was performed. The test starts at 10000 s and it is characterized by three phenomenological windows (PhW). Table 14 identifies the three PhW, describing the

boundary conditions and summarizing the relevant thermal-hydraulic aspects observed in each one [82]. The opening and closure time of the triggering valve is summarized in Table 15.

Table 14. Test 7 Part 1: phenomenological windows

PhW	Boundary time	Description	Relevant aspects
1	10000 s - 11260 s	HXP level is increased in two steps (1.4 and 3.4 m). Consequent increase of the power exchanged	HXP level increase
			OP level decrease
			MFR increase in-tube side
			Power removed increase
			Progressive covering of the HX within the HXP
			System instability with cold water - steam interface at the injector (string condensation shocks)
2	11260 s - 11845 s	Quasi-steady operation maintained when the HXP level reaches 3.4 m	Quasi-steady power removed
			Quasi-steady MFR in-tube side
			Initial boil off in the HXP
			Mixing of the OP water due to the steam acceleration by the injector
3	11845 s - 14784 s	Boil off in the HXP with a consequent level reduction and heat exchange decrease	Boil off in the HXP
			HXP level decrease
			OP level increase
			Power removed decrease
			MFR decrease in-tube side
			Progressive uncovering of the HX within the HXP
			Thermal stratification in the OP, due to the reduction of mixing for the steam FR decrease

Table 15. Test 7 Part 1: triggering valve events timing [82]

Event	Time (s)
First opening	10475
First closure	10608
Second opening	10621
Second closure	10655
Final opening	11039
Final closure	11260

4.2.2 Test 7 Part 2

Test 7 Part 2 starts from the final conditions of Part 1. Three phenomenological windows are individuated and described in Table 16. The opening and closure time of the triggering valve (F 045) and of the water discharge valve (F 031) are summarized in Table 17.

Table 16. Test 7 Part 2: phenomenological windows

PhW	Boundary time	Description	Relevant aspects
1	0 s - 531 s	HXP level is increased in one step with a consequent increase of the power exchanged	HXP level increase
			OP level decrease
			MFR increase in-tube side
			Power removed increase
			Progressive covering of the HX within the HXP
2	531 s - 2282 s	Quasi-steady operation maintained when the HXP level reaches 3.3 m	Quasi-steady power removed
			Quasi-steady MFR in-tube side
			Initial boil off in the HXP
			Instabilities in the OP water level
3	2282 s - 5735 s	Boil off in the HXP with a consequent level reduction and heat exchange decrease	Boil off in the HXP
			HXP and OP level decrease as a consequence of the water drained by F 031
			Power removed decrease
			MFR decrease in-tube side
			Progressive uncovering of the HX within the HXP

Table 17. Test 7 Part 2: triggering valves events timing [82]

Event	Time (s)
F 045 Opening (in 26 s)	300
F 031 opening	1150
F 045 closure (in 123 s)	3338

4.3 Description of the thermal-hydraulic model

Figure 113 shows the nodalization scheme developed for the simulation activity. The thermal-hydraulic model consists of two main systems: the primary system, including pressure vessel, steam line, heat exchanger and drain line, and the secondary system, including the two pools and the connections between them.

The pressure vessel is modelled with two vertical pipes (110 and 090 in Figure 113), reproducing the steam conduit and the annular volume between the steam conduit and the vessel's walls. Steam inlet conditions are imposed with the time-dependent volume (TDV) 100, connected with the lower part of the steam conduit using a single junction. A branch component (BRANCH 120 in Figure 113) connects the two vertical pipes with the steam plenum of the pressure vessel, modelled with a single pipe (130 in Figure 113). Steam moves into the HX, flowing through a pipeline (STEAM LINE in Figure 113), simulated with three pipes (010, 020 and 030 in Figure 113). The heat exchanger is composed of the two headers and the tube bundle. The upper and lower headers are modelled with two pipes (040 and 060 in Figure 113), each one composed of six control volumes. The bundle is reproduced with a single equivalent pipe (050 in Figure 113), assuming the total flow area, the hydraulic diameter of a single tube and the total heat transfer area. The condensate moves into the pressure vessel, flowing through the drain line, which is simulated with two pipes (070 and 080 in Figure 113). The lower plenum of the component 090 is connected with a TDV, reproducing the condensate drain system.

Concerning the secondary system, two solutions have been evaluated to reproduce the two pools: a mono-dimensional approach, using parallel pipes with cross junctions, and a more detailed three-dimensional approach, developing two MULTID components. Even if thermal stratification within the OP has been selected as a relevant aspect to be investigated (see Table 14), this phenomenon does not determine predominant thermal-hydraulic effects into the pool, due to the injector that accelerates the steam providing relevant mixing effects. As shown in sections 2.1.4 and 2.1.5, the mono-dimensional modelling approach for a large volume provides satisfactory results in the simulation of 3D pool thermal-hydraulics. The MULTID component improves the resolution of the results, even if much higher computational cost is needed, that sometimes does not justify its adoption. For this reason, the mono-dimensional modelling approach has been selected for the simulation of the two pools. Each one is modelled with three vertical pipes, composed of 60 control volumes, connected with several cross junctions. The OP and the HXP are connected with the steam duct, modelled with the pipe component 210, including the injector, and the water line, simulated with two pipes (230 and 240 in Figure 113) and with the triggering valve, simulated with a motor valve component.

The upper volumes of the HX pool are connected with two time dependent volumes:

- TDV 207, connected with the upper volume of component 200; a trip valve component (VACUUM BREAKER VALVE in Figure 113) opens when the pressure within the pool becomes lower than the atmospheric pressure;
- TDV 209, connected with the upper volume of component 201; a trip valve component is set in order to maintain the atmospheric pressure within the HXP in the first seconds of Test 7 Part 1.

In addition, two time dependent volumes are connected with the overall pool:

- TDV 227, connected through a single junction with the upper volume of component 220, simulating the atmosphere;
- TDV 229, connected with the lower volume of component 221; a trip valve component is set to reproduce the water discharge in TEST 7 Part 2.

The whole nodalization scheme is developed adopting the sliced modelling approach and the local pressure losses are simulated with constant K-loss coefficients calculated according the geometry data provided to the benchmark participants. The heat losses towards the environment are taken into account with several heat structures, imposing the temperature of the environment (288 K) and the heat transfer coefficient on the outside surfaces (6 W/m^2 K).

Regarding the heat exchange between primary and secondary systems, 44 heat structures are used for the thermal coupling between the HX and the HXP. As found in the literature [84][85][86], a multiplicative factor must be applied to the heat transfer coefficient on the tube and pool side. In fact, considering the thermal-hydraulic conditions of Test 7, the correlations implemented in R5-3D for the HTC evaluation work out of the validity range, underestimating the experimental HTC. For this reason, a multiplicative factor equal to 2.4 has been introduced in both the HX sides.

The main parameters of the thermal-hydraulic model are summarized in Table 18.

Table 18. PERSEO model: main parameters

Component	**Number of hydraulic volumes**	**Number of junctions**	**Number of heat structures**	**Overall Volume (m^3)**
Vessel	98	96	99	36.92
Steam Line	187	186	187	1.71
HX	32	31	44	1.92
Condensate line	158	157	158	0.52
HXP	180	295	186	26.9
Steam duct	66	65	66	12.1
OP	180	295	306	163.66

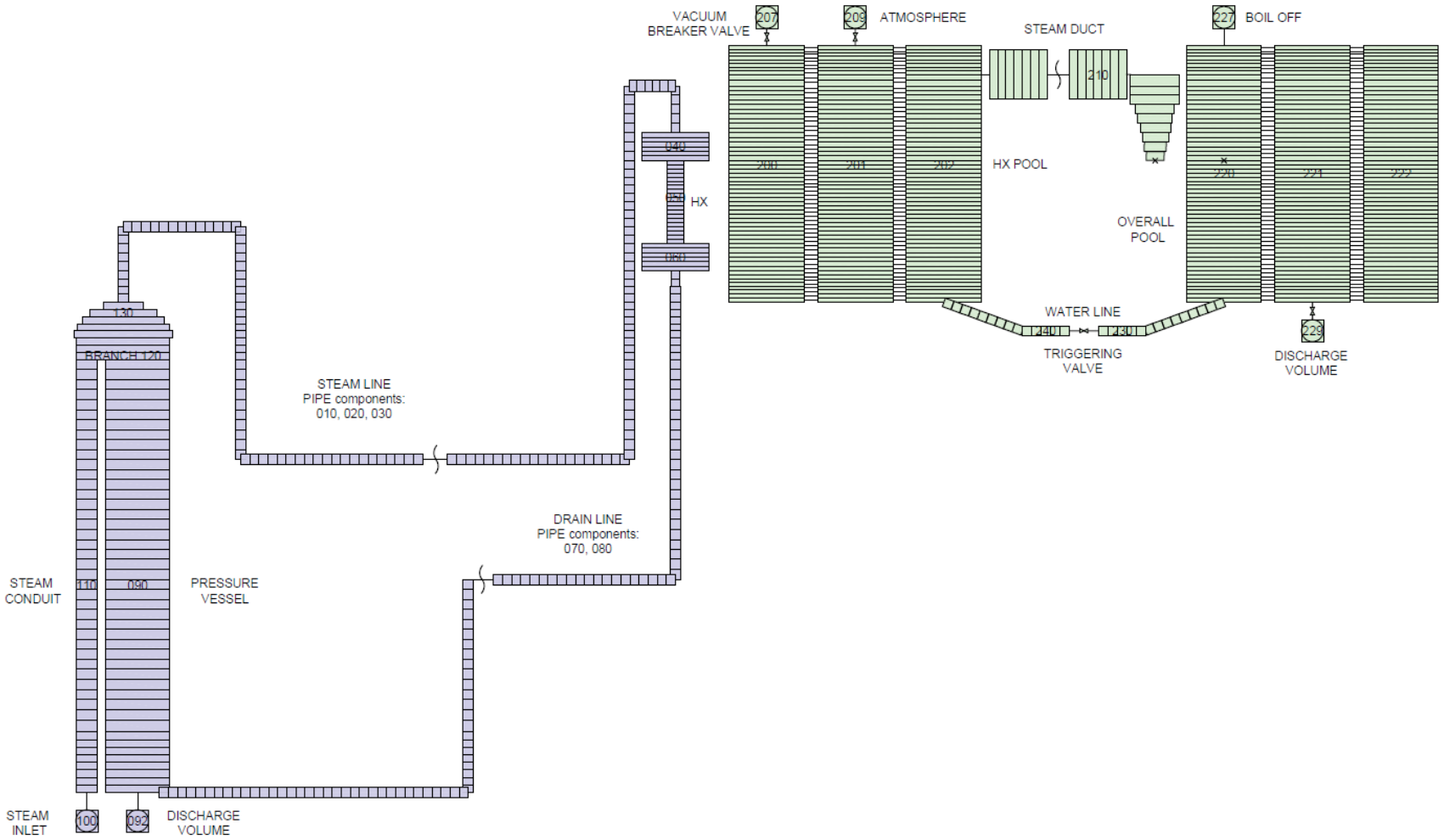

Figure 113. PERSEO: nodalization scheme

4.4 Simulations results

4.4.1 Test 7 Part 1

The initial conditions for simulation of Test 7 Part 1 are imposed as boundary conditions, following the initial experimental data in a reasonably accurate way. Within the primary system, saturated conditions at 70.3 bar are considered (the initial steam and condensate flow rate is set to 0). On the secondary side, the pressure is set to 1 bar. Inside the HXP the water level is initialized at 0.276 m from the bottom of the pool and the rest of the volume is filled with dry air; temperature increases from the bottom to the top of the pool from 351 to 528 K, as specified in the experimental initial conditions. In order to maintain a constant pressure within the HXP in the first minutes of the test, the upper volumes are connected to a time-dependent volume with a trip valve component, which remains open in the first 460 s, ensuring the atmospheric pressure inside the HX pool. The OP is filled with water up to 4650 mm from the bottom. A uniform temperature of 288 K is considered. The triggering valve is initialized closed.

The following figures compare the experimental acquisition (red line) with the calculated results (black line). The absolute maximum error related to the main monitored quantities are summarized in Table 19 [84]:

Table 19. PERSEO facility: measurement errors [84]

Quantity	Maximum absolute error
HXP level	+/- 0.04 m
OP level	+/- 0.04 m
HXP relative pressure	+/- 0.35 kPa
OP temperatures	1.3 K
Exchanged power	500 kW

The first phenomenological window (10000 – 11260 s) consists in the first activation of the system; the triggering valve opens, water flows from the OP to the HXP, filling the latter up to 3.4 m in two consecutive openings (see Table 15). R5-3D model provides a satisfactory prediction of the main phenomena occurring in this phase, even if some discrepancies with the experiment are observed.

Figure 114 and Figure 115 show respectively steam and condensate flow rate through the primary system. At the beginning of the test, a low value of the water flow rate through the primary loop is measured, probably due to the heat losses towards the environment which promotes a visible natural circulation. As presented in section 4.3, the nodalization scheme includes the modelling of the heat losses, considering constant values for the HTC on the outer walls and for the environment temperature. The overall value of the heat losses is not compared with experimental data but the initial flow rate within the primary system is well predicted, proving the good evaluation of the heat dissipations. In this phase, the experimental value of the thermal power exchanged between the HX and the HXP is about 2200 kW (average value). As expected, being the HXP filled by dry air, R5-3D does not observe a significant heat exchanged (Figure 116). Discrepancy between experimental and simulated values could be due to the calculation methodology adopted for the evaluation of the experimental power. This is an indirect experimental measurement, based on the energy balance equation applied to the primary side of the IC.

The pressures within the primary system is depicted in Figure 117. It is maintained constant over the whole test, except between 11000 and 11700 s, when the condensation rate leads to depressurization of the system, immediately balanced by the EDIPOWER power station that supplies the steam to the pressure vessel. The primary pressure is entered as boundary condition in the R5-3D model, matching satisfactorily the experimental data. Figure 118 and Figure 119 show the temperature in two relevant positions of the primary system, respectively in the steam and condensate lines. The comparison between experimental and simulated temperatures highlights a discrepancy of about 5 degrees in both the acquisitions. This should be due to the measurement uncertainties, since, at the beginning of the test, primary system would be in saturation condition (as imposed in the R5-3D calculation); instead, experimental acquisitions observe superheated steam.

On the secondary side, in the first PhW, a satisfactory prediction is observed within the HXP, even if the code underestimates the thermal stratification. Figure 122, Figure 123 and Figure 124 show the temperature in three relevant axial positions within the HXP: respectively 0.5 m (below the lower header), 2.5 m (about the middle level of the tube bundle) and 3.8 m (above the upper header) from the bottom of the pool. Before the first opening of the triggering valve, the HXP is full of air. In this condition, R5-3D underestimates the thermal stratification (see Figure 123 and Figure 124), even if this phenomenon does not affect the thermal-hydraulics of the system, due to the negligible power exchanged in this phase. Figure 125 shows the pressure within the HXP, that, in the first instants of the test, is maintained constant with the TDV.

At 10475 s, the first opening of the triggering valve occurs. Regarding Test 7 Part 1, the specifications provided to the benchmark participants include the opening and closure instants, but not the opening and closure rates of the triggering valve. For this reason, the rates are evaluated in order to reproduce in the most accurate way the HXP filling, that could determine a relevant source of uncertainties in the calculations. The HXP level is presented in Figure 120, where a good agreement is observed between simulation and experiment, even if the code underestimates the maximum level after the first opening of about 0.1 m. The discrepancy could be due to a not perfect simulation of the first opening rate and it could explain the underprediction of the power exchanged between 10475 and 11450 s (see Figure 116) and the absence of the slow water consumption in the simulation results (visible in the experimental HXP level decrease in Figure 120). The underestimation of the power leads to an under prediction of the primary flow rate in this phase (see Figure 114 and Figure 115). According to the analysis above presented, the first OP level decrease is well predicted by the code, even if a slight overestimation of the level is visible after the first opening (see Figure 121).

After the second opening, the HXP level increases up to the maximum value. Figure 120 shows a good agreement of the level increase, even if the maximum level is overestimated by the code of about 0.14 m, due to a not perfect opening rate of the valve. The level increase leads to a rapid increase of the power exchanged between the HX and the HXP and, therefore, a quick increase of the condensation rate and of the flow rate through the primary system. R5-3D predicts very well the increase rate, even if, the overestimation of the level leads to the slight overprediction of the power and of the primary flow rate (see Figure 116, Figure 114 and Figure 115). Figure 128 shows the pressure drop across the HX; the code provides a satisfactory prediction of the minimum value, even if the pressure decrease occurs about 200 s earlier than experimental data. As expected, the absolute value of the pressure drop follows the primary flow rate, reaching the maximum value at the same time of the maximum FR. The experimental flow rate reaches two consecutive peaks, determining the two pressure peaks observed in Figure 128. The R5-3D results have a different peaks value on the flow rate, with the first overestimated and the second underestimated; this could explain the discrepancies observed in Figure 128.

On the secondary side, at 10460 s the trip valve connecting the HXP and the atmosphere closes and, as a consequence of the water boiling, the pressure starts to increase. Figure 125 shows a good agreement between

simulation and experiment, even if the maximum pressure is predicted a bit earlier by the code. This should be related to the over prediction of the power exchanged in the first seconds after the second opening. Regarding the temperatures, after the injection of the cold water, the experimental acquisitions shows the temperature decrease up to the saturated value, as predicted by the code (see Figure 122, Figure 123 and Figure 124). The steam produced within the HXP is driven towards the OP, through the steam duct. Figure 129 shows the pressure losses through the steam injector, providing an estimation of the steam flow rate. As presented in the figure, a good agreement is observed in the first PhW between calculation and experiment.

The second PhW consists in the quasi-steady operation at the maximum power (11260 -11845 s). The qualitative quasi-steady-state condition is well predicted by the code, even if its duration is predicted shorter than the experimental acquisition. This is clearly shown in Figure 114, Figure 115 and Figure 116. This could be explained by the higher power exchanged and the consequent higher boiling rate within the HXP, demonstrated by the overestimation of the pressure losses across the steam injector observed in the first seconds of the second PhW (see Figure 129), highlighting a higher value of the steam flow rate.

The third PhW consists in the level decrease within the HXP and, therefore, the reduction of the power exchanged between the HX and the HXP (11845 – 14784 s). The simulation results are globally in good agreement with experimental data. Due to the shorter quasi-steady operation, the HXP level decrease starts earlier, but the rate is comparable with experimental data. Power reduction, shown in Figure 116, is caused by the level decrease and the progressive HX uncovering, that highlights a good agreement between experiment and simulation. The decrease rate is well predicted, and the R5-3D power trend assumes typical stepwise change due to the nodalization scheme. A similar trend is observed in the primary flow rate. The shorter quasi-steady operation causes the discrepancies within the HXP, and the consequent earlier HX uncovering, causes the discrepancies shown in Figure 123 and Figure 124, where the earlier level decrease predicted by R5-3D leads to the earlier temperature increase, and in Figure 130, that highlights an earlier uncovering of the upper header. The OP level is shown in Figure 121; the comparison highlights a good agreement between simulation and experiment. Some oscillations are observed in the calculation, probably due to the condensation rate of the steam coming from the HXP. Regarding the OP temperature, the code is able to reproduce the temperature increase due to the steam condensation, but the thermal gradient of the stratification phenomena is underestimated at the end of the test. A multi-dimensional modelling approach could improve the results, but the increase of the computational cost could be not justified if this aspect is not so relevant.

The maximum time step adopted for Part 1 calculation has been set to 0.001 s and the computational time has been 12 h 10 min.

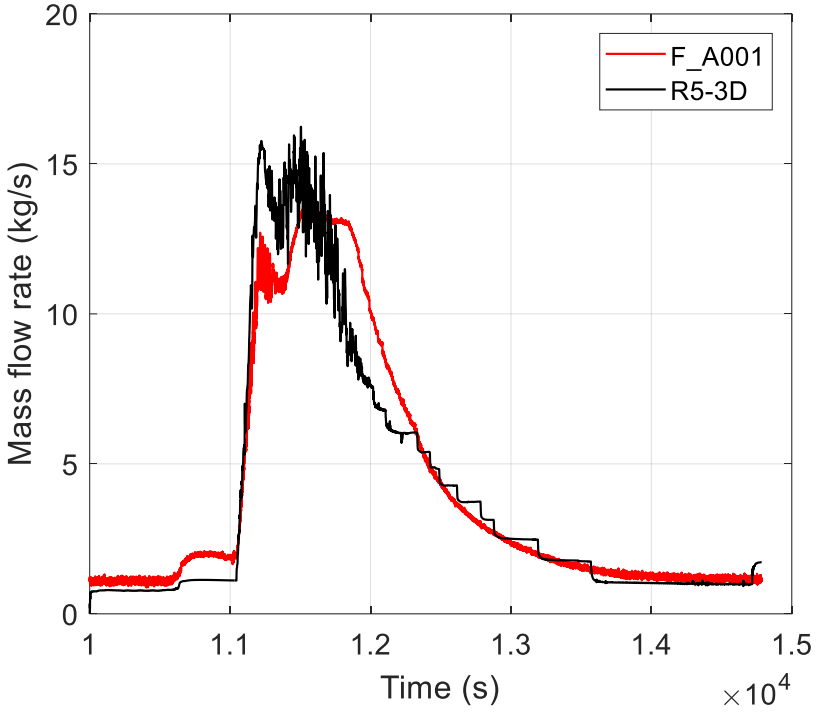

Figure 114. Test 7 Part 1: steam flow rate

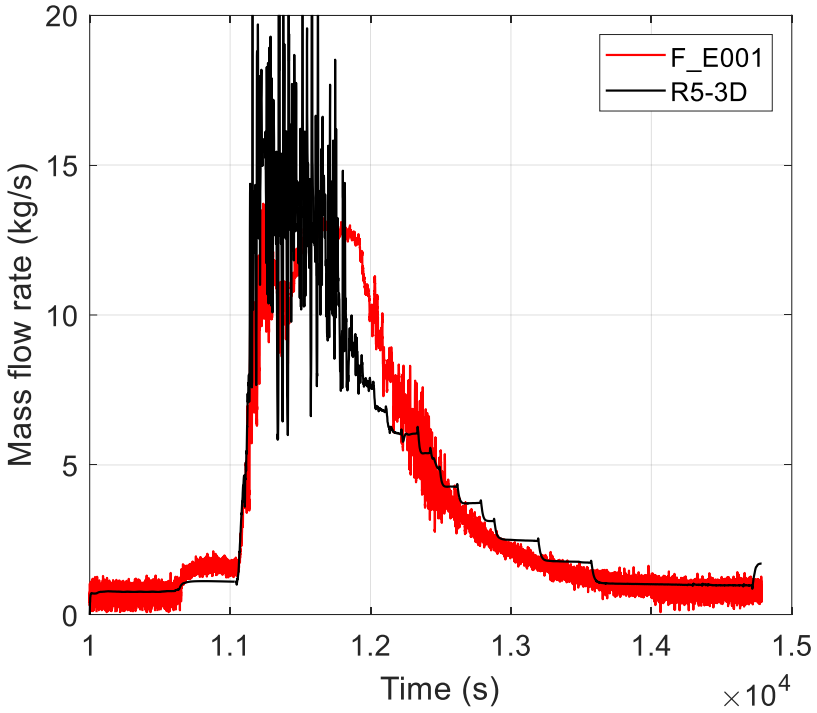

Figure 115. Test 7 Part 1: condensate flow rate

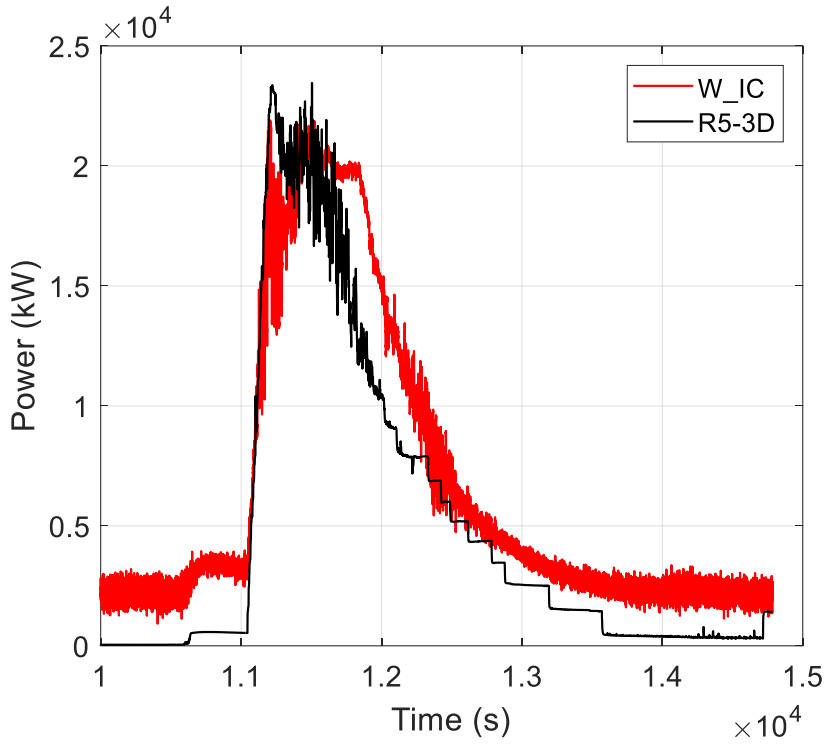

Figure 116. Test 7 Part 1: HX power

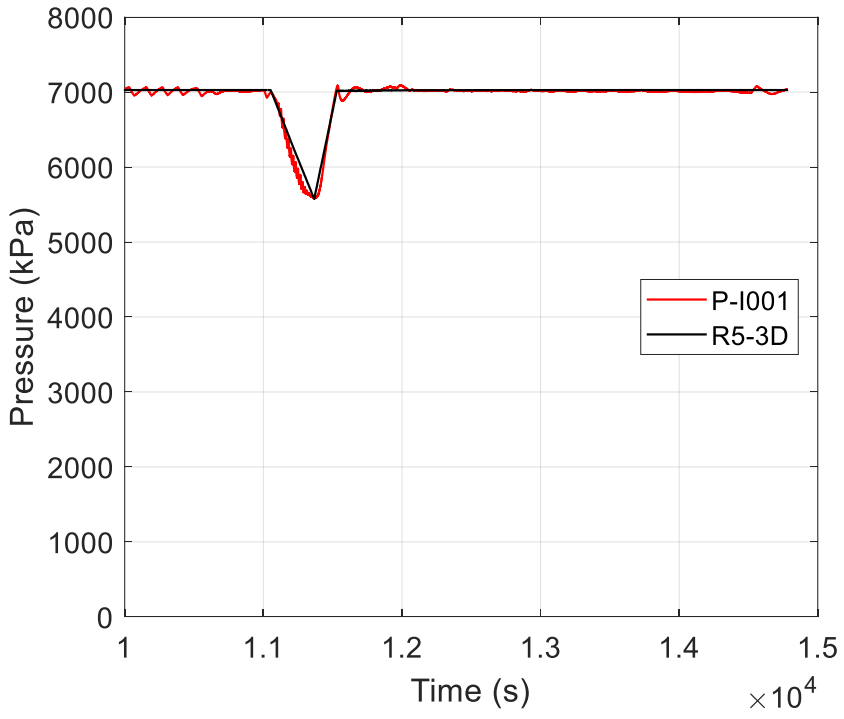

Figure 117. Test 7 Part 1: primary pressure

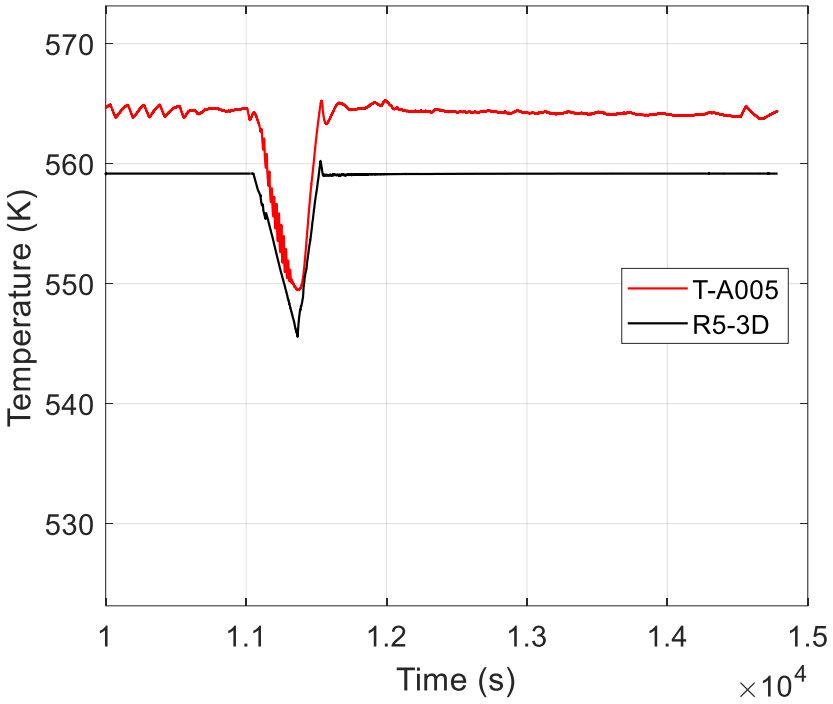

Figure 118. Test 7 Part 1: steam temperature

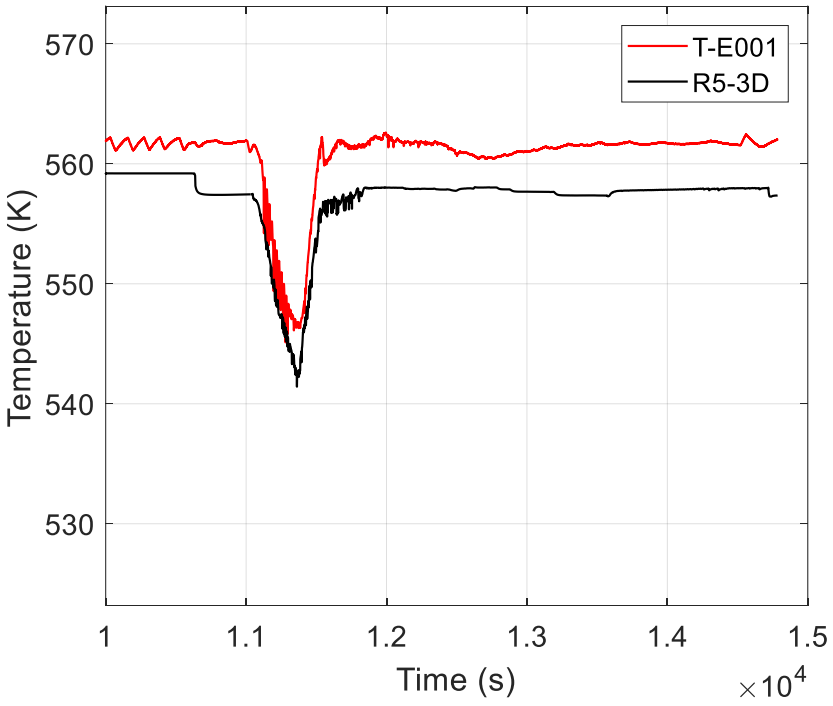

Figure 119. Test 7 Part 1: condensate temperature

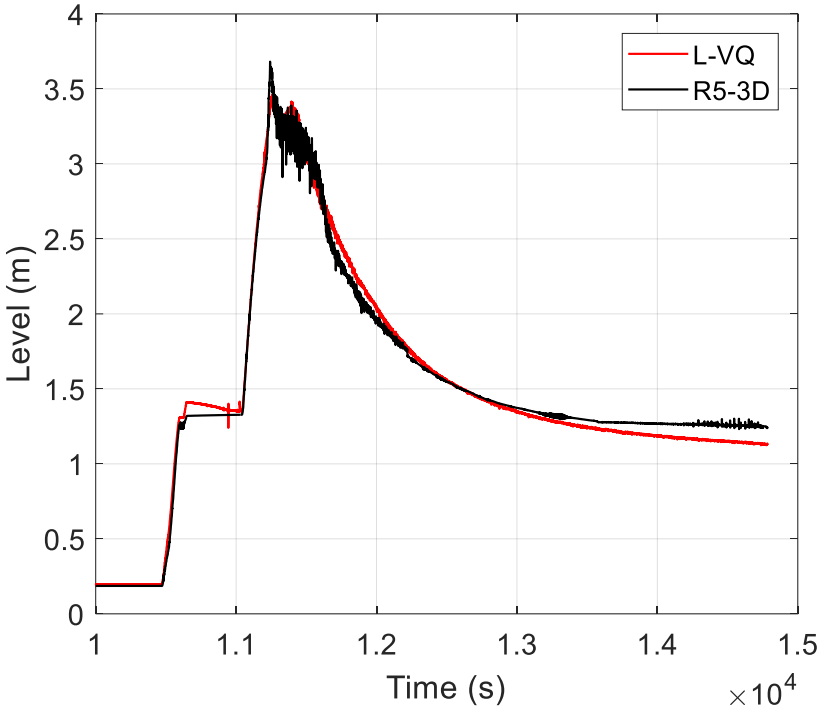

Figure 120. Test 7 Part 1: HXP level

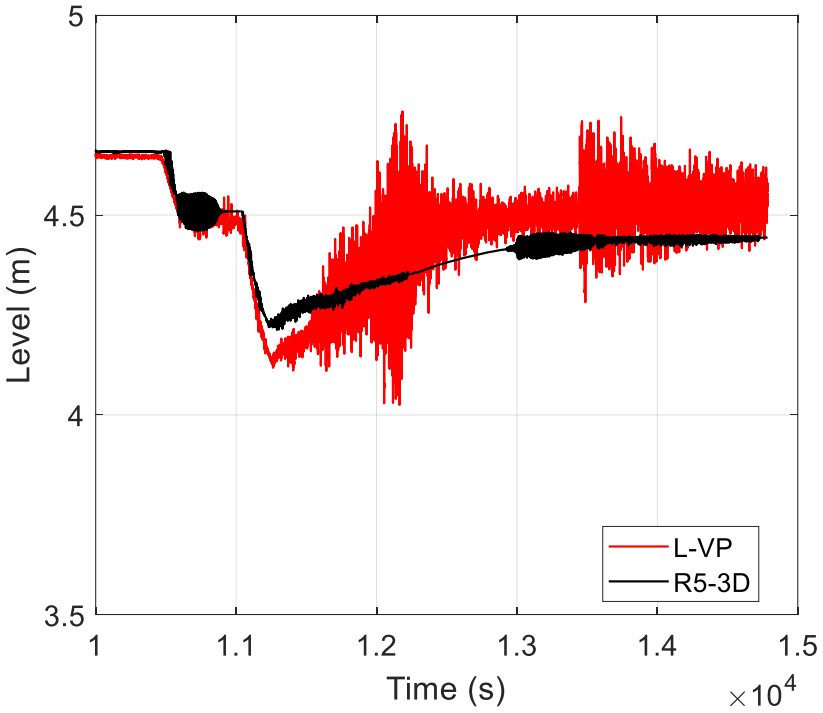

Figure 121. Test 7 Part 1: OP level

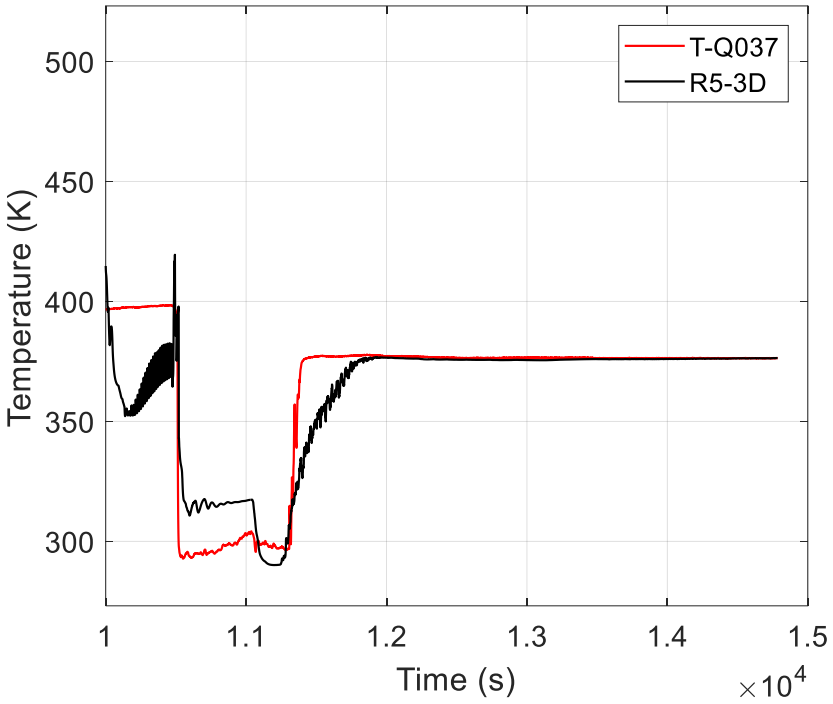

Figure 122. Test 7 Part 1: HXP temperature T-Q037

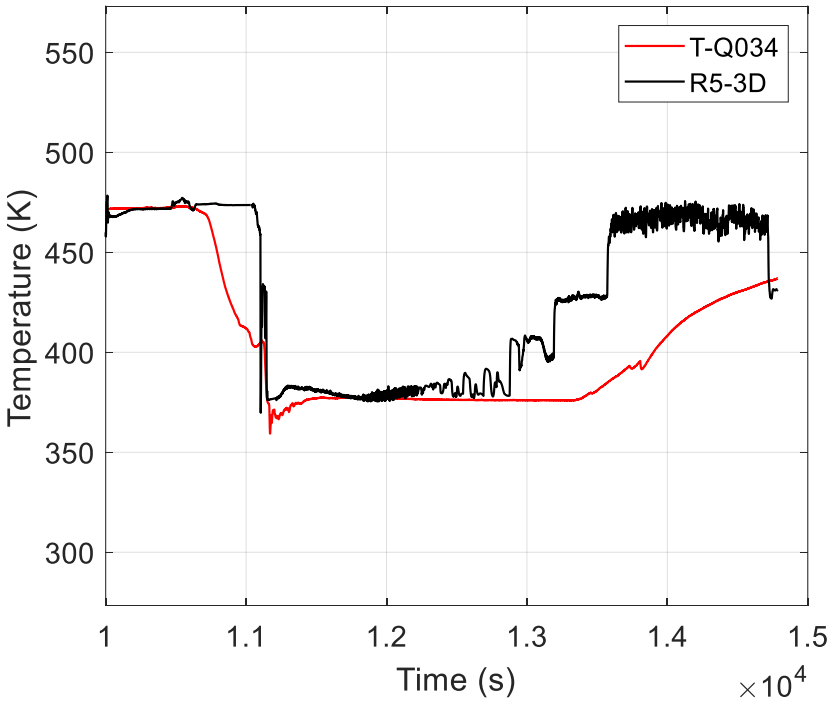

Figure 123. Test 7 Part 1: HXP temperature T-Q034

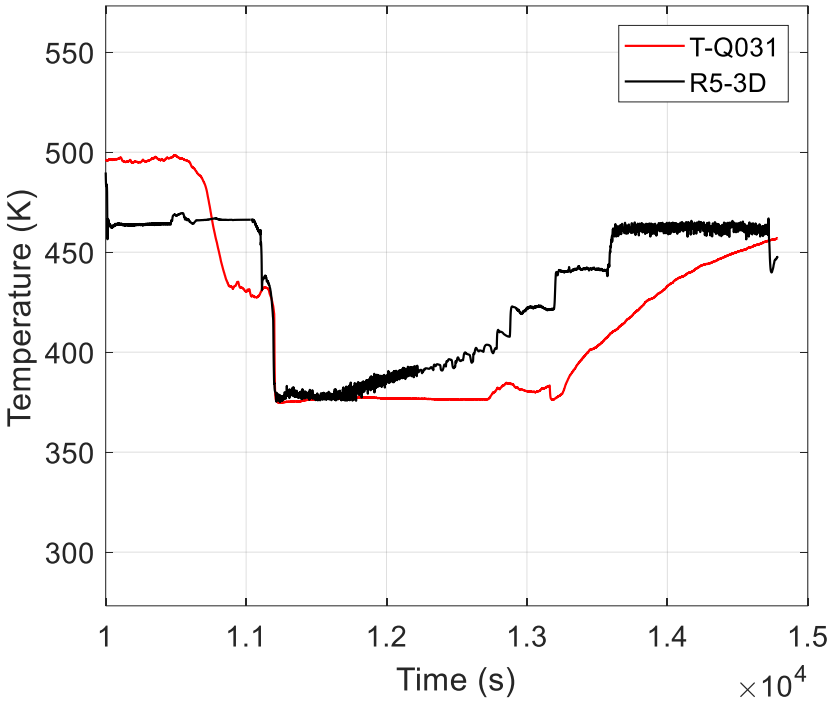

Figure 124. Test 7 Part 1: HXP temperature T-Q031

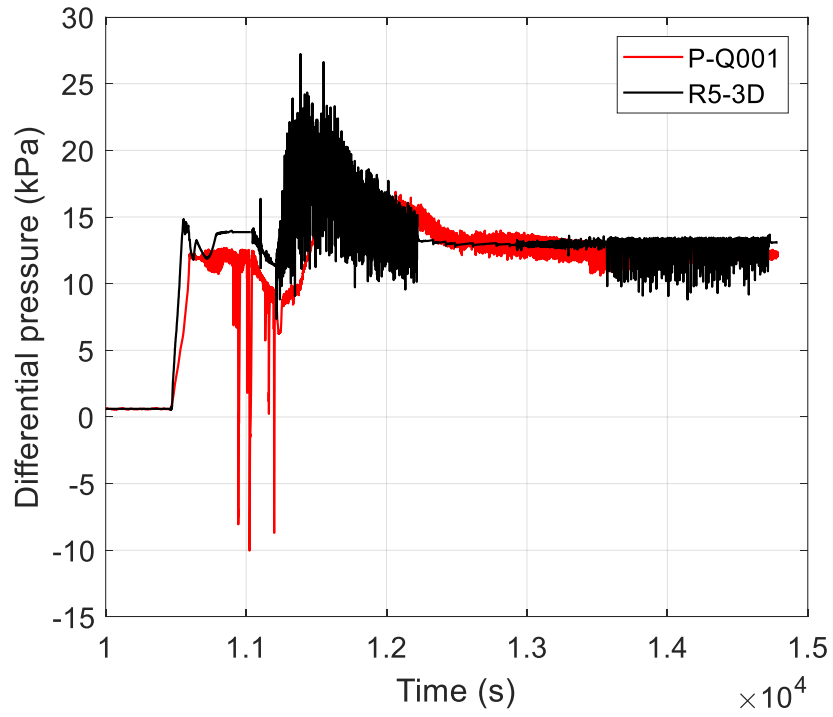

Figure 125. Test 7 Part 1: HXP relative pressure

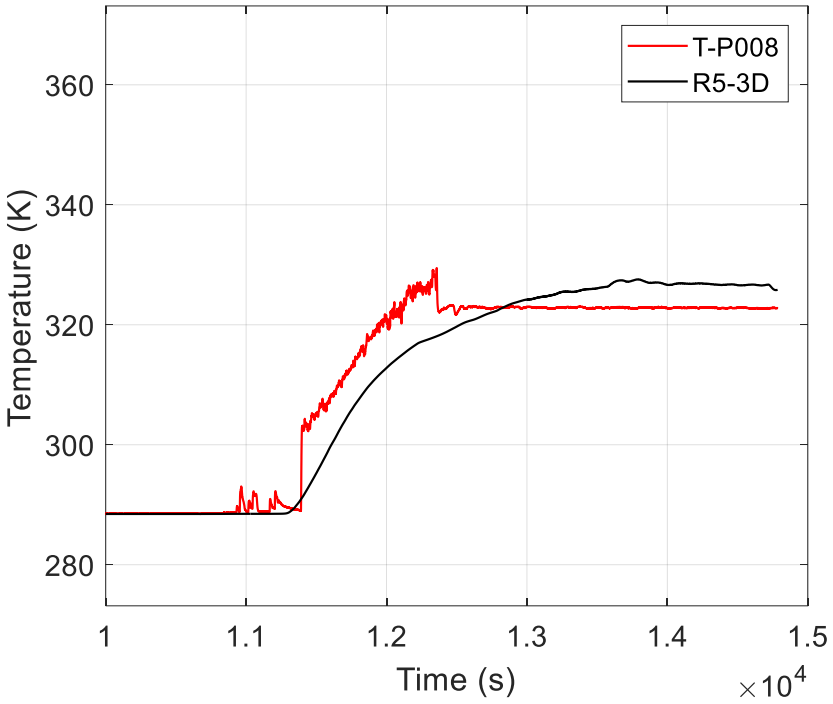

Figure 126. Test 7 Part 1: OP temperature T-P008

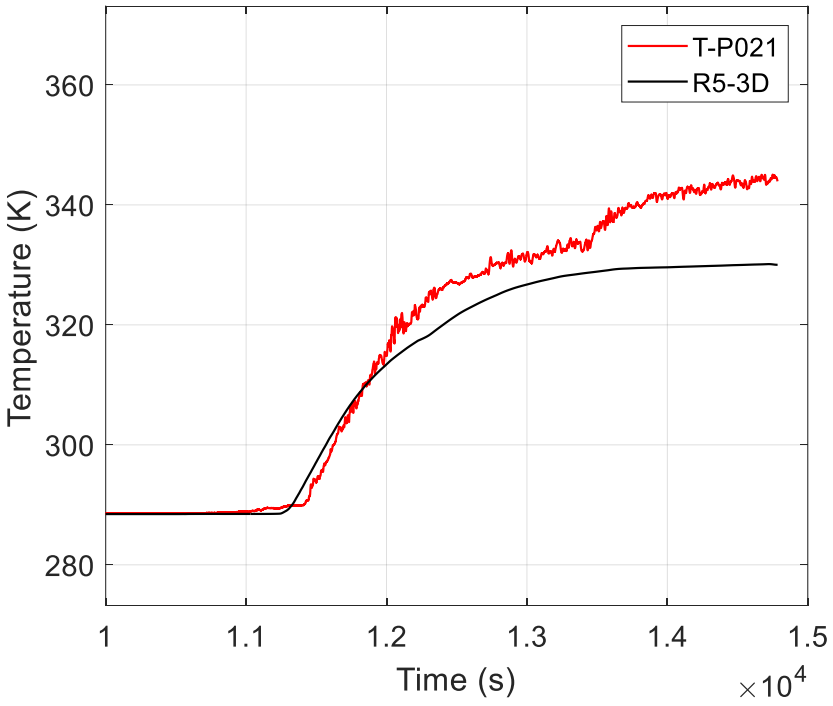

Figure 127. Test 7 Part 1: OP temperature T-P021

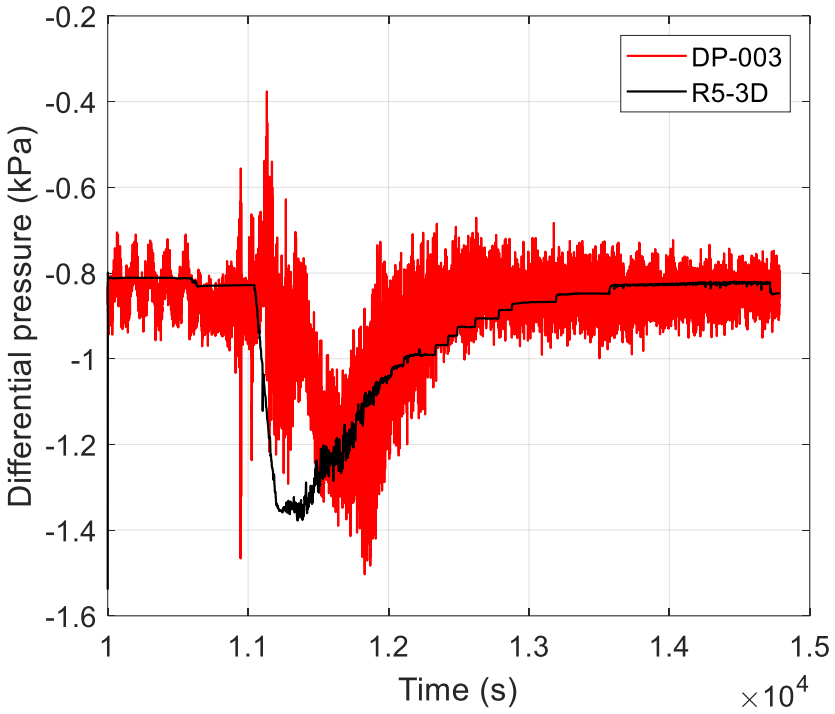

Figure 128. Test 7 Part 1: HX pressure drop

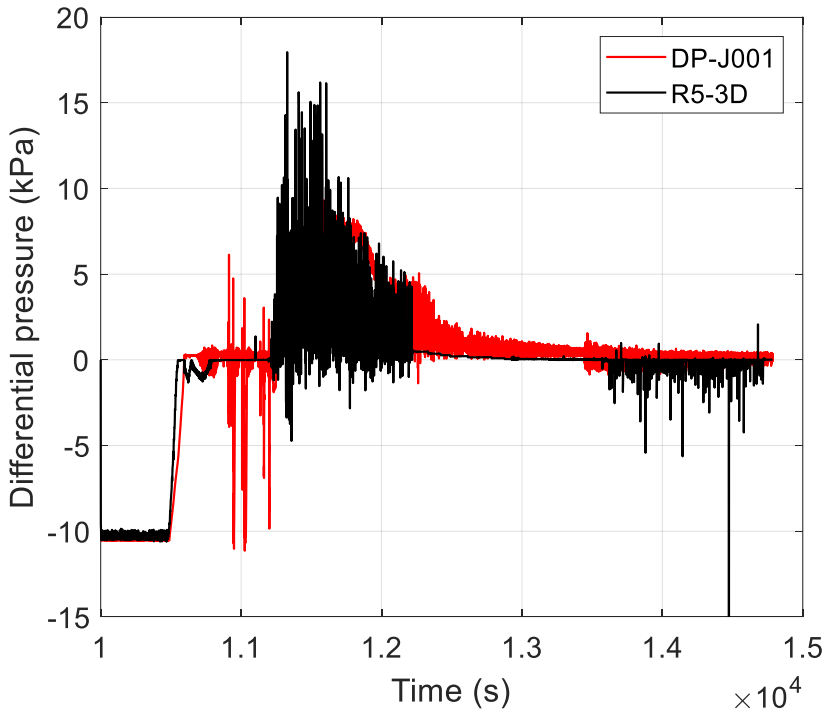

Figure 129. Test 7 Part 1: Injector pressure drop

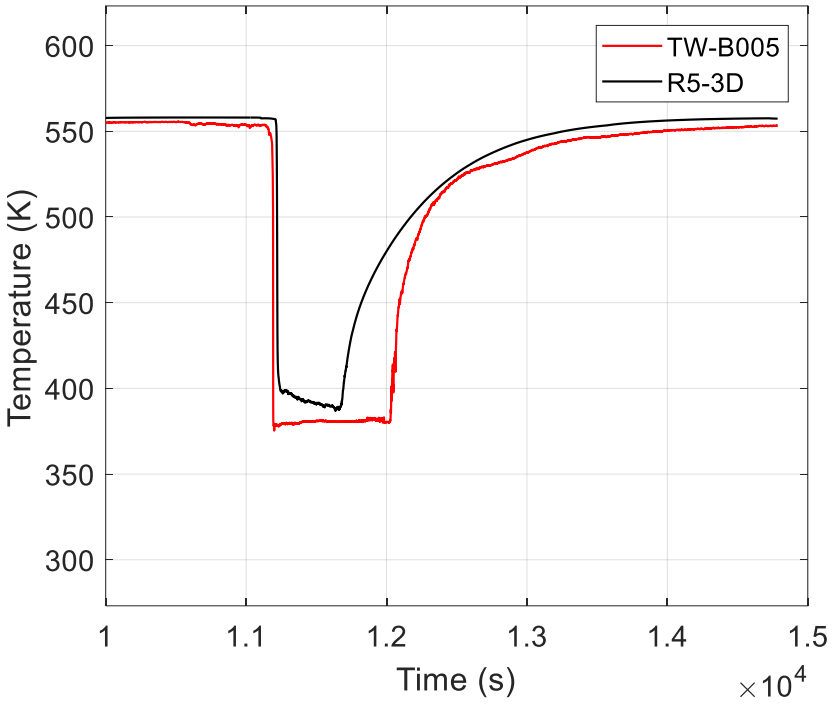

Figure 130. Test 7 Part 1: HX upper header outer wall temperature

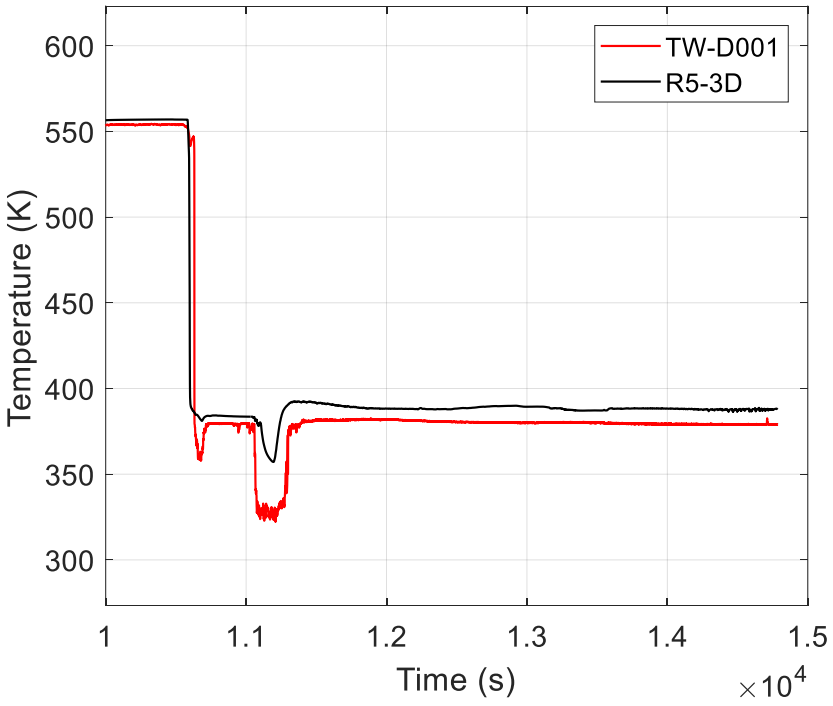

Figure 131. Test 7 Part 1: HX lower header outer wall temperature

4.4.2 Test 7 Part 2

Test 7 Part 2 starts from the final conditions of Part 1. The initial conditions are in good agreement with experimental data. Some discrepancies are observed, as discussed section 4.4.1: lower power exchanged between HX and HXP, underprediction of the temperature inside the primary system (about 5 degrees), and underestimation of the thermal stratification phenomenon within the two pools.

The first PhW consists in the activation of the system (0 – 531 s), opening the triggering valve. For this part of Test 7, both the opening and closure instants and rates are provided to the participants.

The opening causes a rapid increase of the HXP level, well reproduced by the code (see Figure 138). The maximum level is well predicted, even if R5-3D predicts a peak about 50 s before the experimental one. On the OP side, the level decrease is well reproduced by the code, which is also able to reproduce the oscillations observed in the experimental acquisitions during the first 531 s (Figure 139). The HXP level increase, and the consequent HX covering, causes the rapid power rise. Figure 134 shows the comparison between the experimental evaluation of the power and the simulated value, highlighting a good agreement. As a consequence of the condensation within the HX pool, the primary fluid starts to flow through the primary system. The experimental acquisitions and the simulated values are compared in Figure 132 and Figure 133. The quick flow rate increase is well reproduced, even if the maximum value is slightly overestimated by R5-3D.

On the HXP side, the injection of the cold water causes the low temperature peak in the bottom part of the pool, as shown in Figure 140; this effect is reproduced by the code, even if the minimum temperature is underestimated of about 10°C and it is predicted about 50 s earlier, following the faster level increase inside the HXP. The same discrepancy in the timing is observed in the upper part of the pool, where saturated conditions are rapidly obtained (see Figure 141 and Figure 142).

The second PhW consists in the quasi-steady-state conditions observed between 531 and 2282 s. After the maximum peak, the level within the HXP maintains a constant value (unless the fluctuations) of about 2.4 m. R5-3D is able to predict this phenomenon, also providing a satisfactory reproduction of the fluctuations. This condition leads to a constant value of the power exchanged and of the primary flow rate. The code provides a good evaluation of the power exchanged between the HX and the HXP, also reproducing the oscillations observed in the experimental acquisitions. The primary flow rate is slightly overestimated. The condensation of the steam within the HX tubes causes the decrease of the total pressure difference across the HX, due to the gravitational contribution (see Figure 146), well predicted by the code.

Concerning the secondary side, the water boiling produces a quick pressure increase within the HXP (Figure 143), well reproduced by R5-3D, even if the steam flow through the steam duct seems to be under-predicted (Figure 147 shows an underestimation of the pressure losses across the injector by R5-3D). The steam, flowing from the HXP to the OP, causes the temperature increase within the OP, where saturation conditions are reached; Figure 144 and Figure 145 show a good agreement between experiment and calculation.

The third PhW consists in the deactivation of the system (2282 – 5735 s). The OP discharge valve is opened, causing the decrease of the water level into the OP and the HXP. The reduction of the HXP level produces the power decrease and the reduction of the primary flow rate. This sequence is well predicted by the code. At 3338 s the triggering valve closes and the HXP level rapidly decreases as shown in Figure 138. The consequent HX uncovering leads to the rapid power decrease and the reduction of the primary flow rate, which are well reproduced by R5-3D, showing the typical stepwise trend also observed in Test 7 Part 1. The reduction of the condensation causes the increase of the pressure difference across the HX, due to the reduction of the gravitational term. This phenomenon is well reproduced by the code up to 4660 s, when the depressurization of the primary system

occurs causing the discrepancy between the simulation and the experiment (see Figure 146). On the secondary side, the reduction of the boiling rate causes the pressure decrease within the HXP, predicted by R5-3D (Figure 143), and the temperature increase in the upper part of the pool, producing a relevant thermal stratification at the end of the test, which is qualitatively predicted by the code (see Figure 140, Figure 141 and Figure 142).

At the end of the test, the code predicts very well the flow rate across the primary system. The power exchanged between the HX and the HXP presents the same discrepancies observed at the beginning of Test 7 Part 1 and Part 2, underestimating the experimental value.

The maximum time step for Part 2 calculation has been set to 0.01 s and the computational time has been 6 h 18 min.

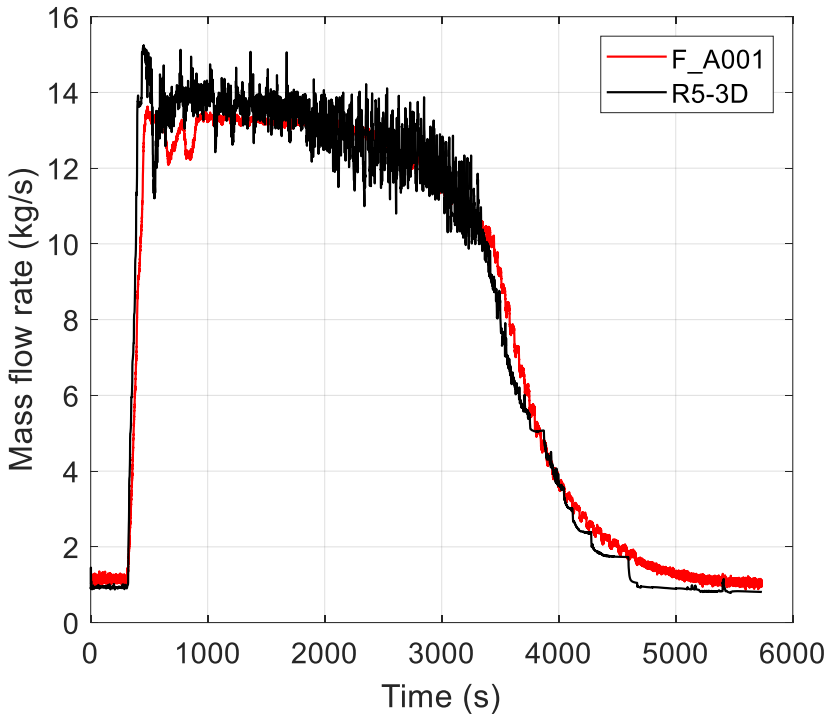

Figure 132. Test 7 Part2: steam flow rate

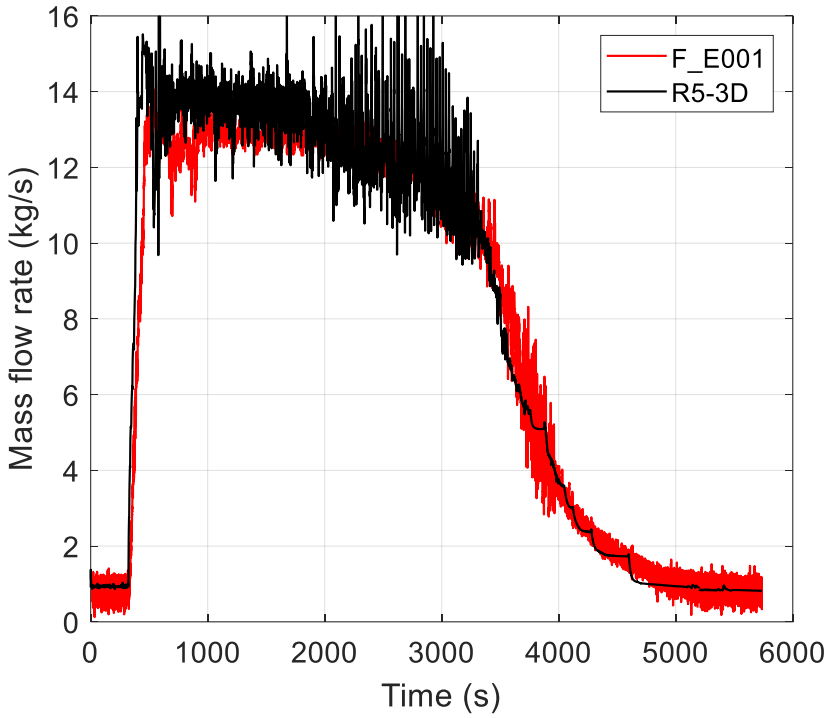

Figure 133. Test 7 Part2: condensate flow rate

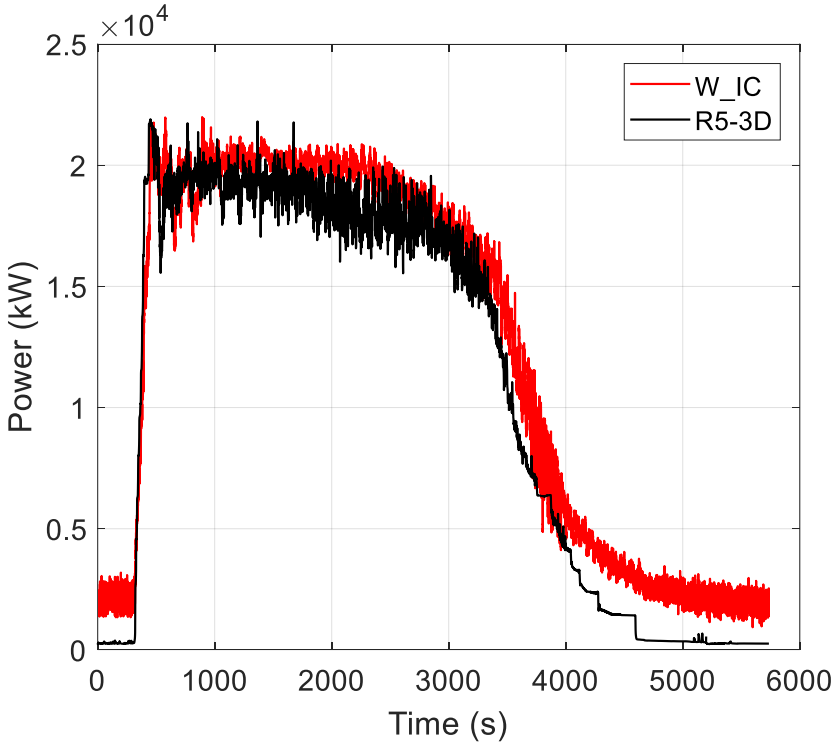

Figure 134. Test 7 Part2: HX power

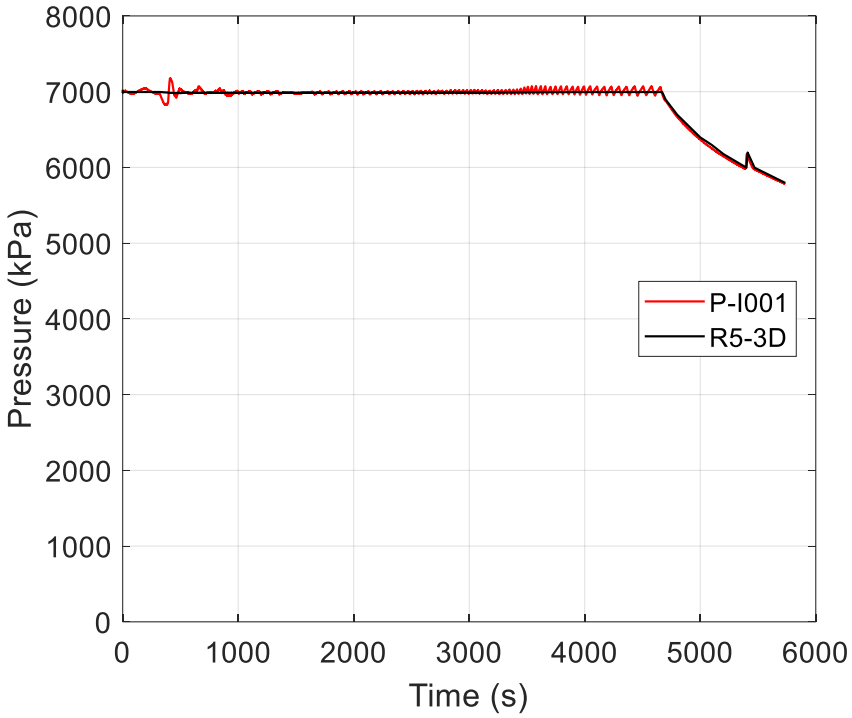

Figure 135. Test 7 Part2: primary pressure

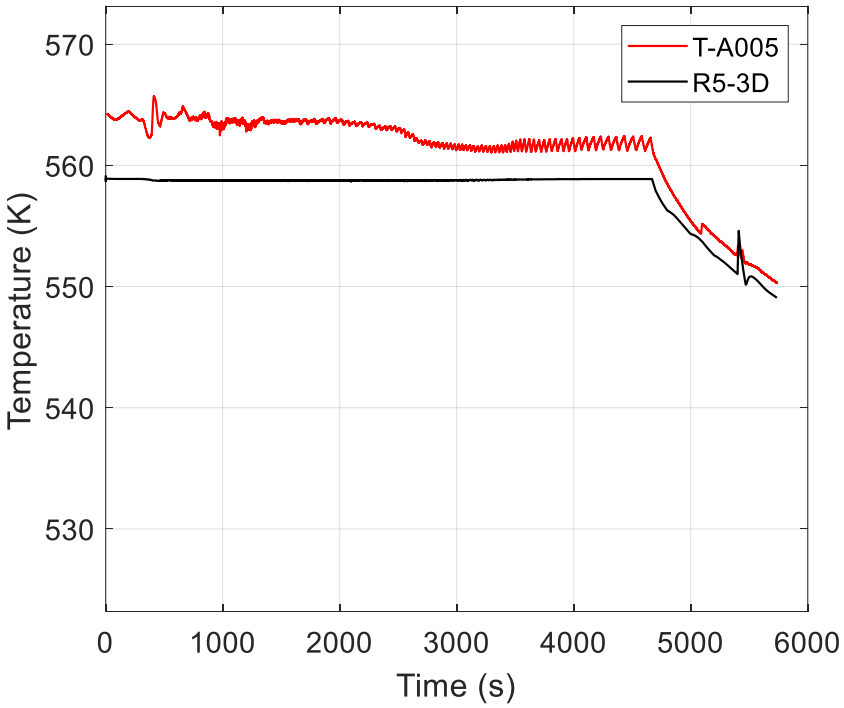

Figure 136. Test 7 Part2: steam temperature

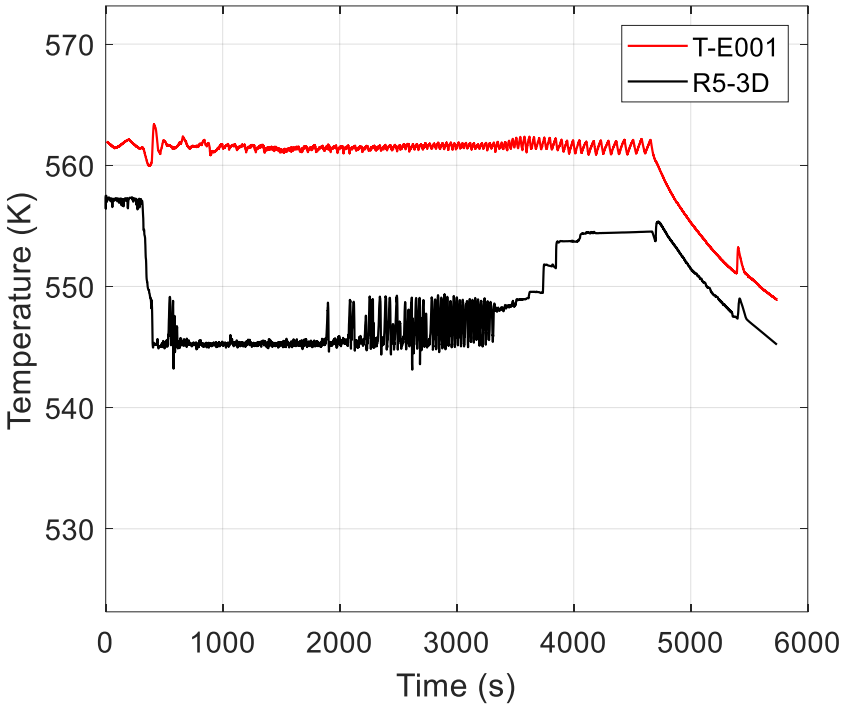

Figure 137. Test 7 Part2: condensate temperature

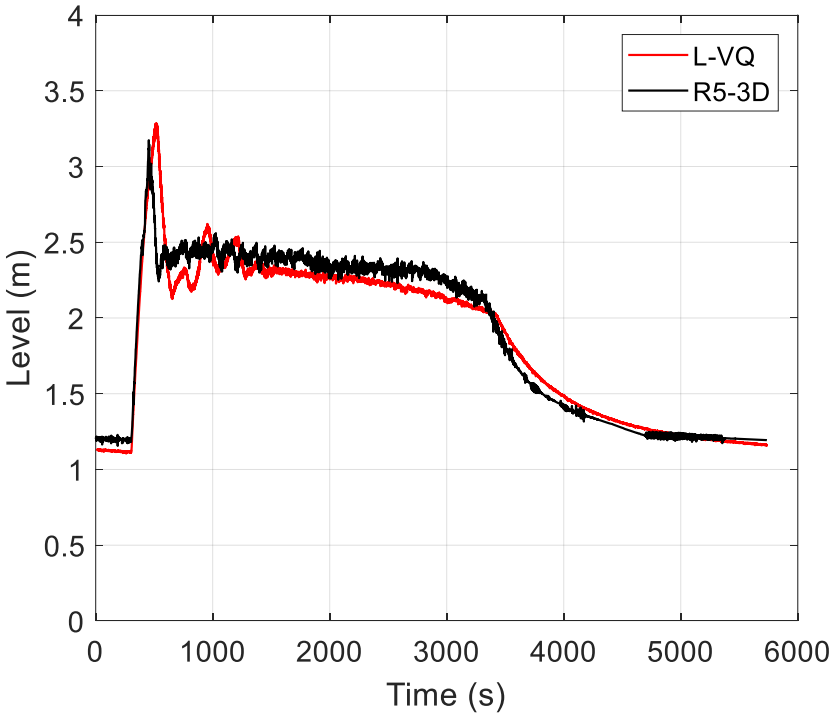

Figure 138. Test 7 Part2: HXP level

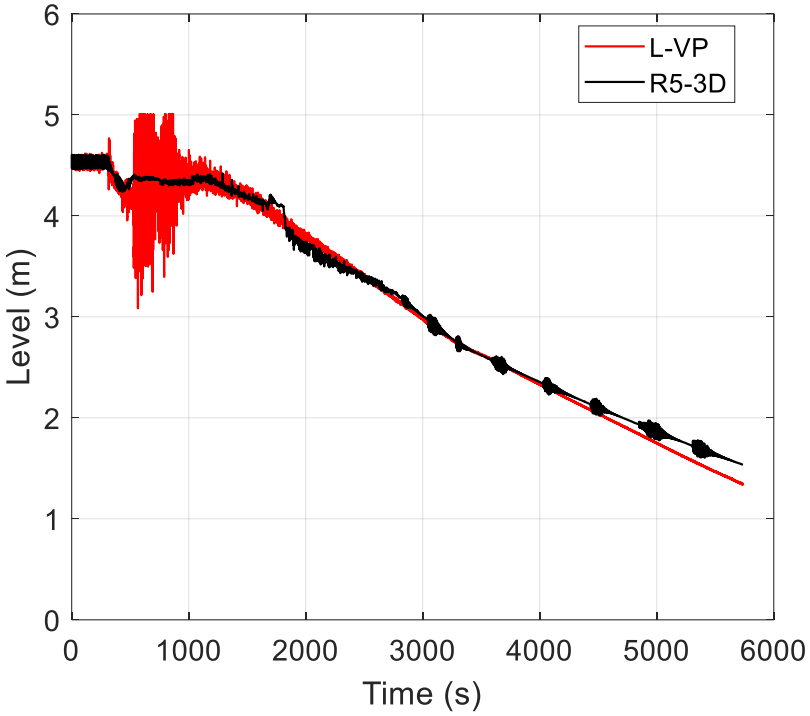

Figure 139. Test 7 Part2: OP level

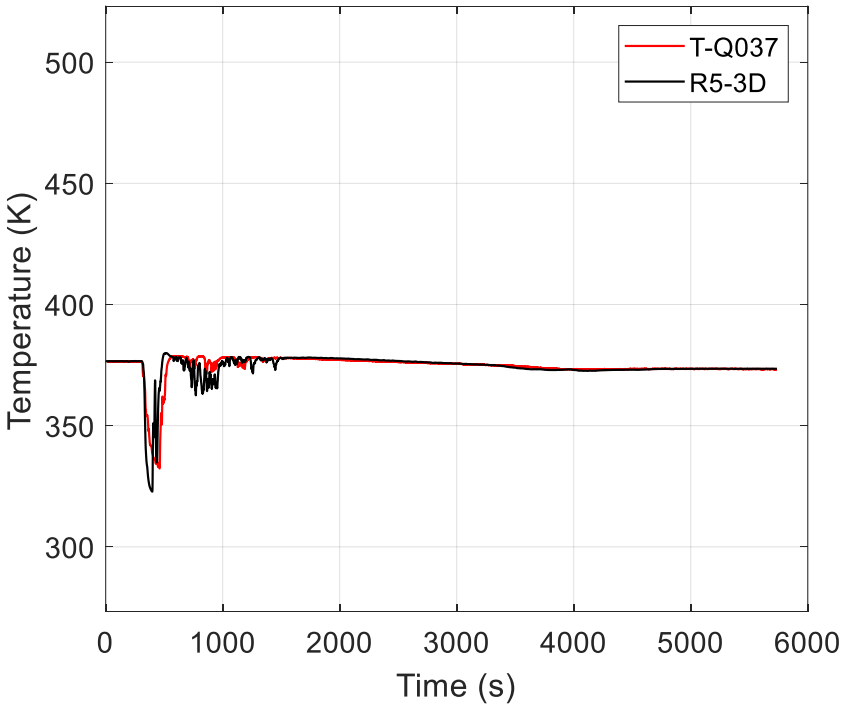

Figure 140. Test 7 Part2: HXP temperature T-Q037

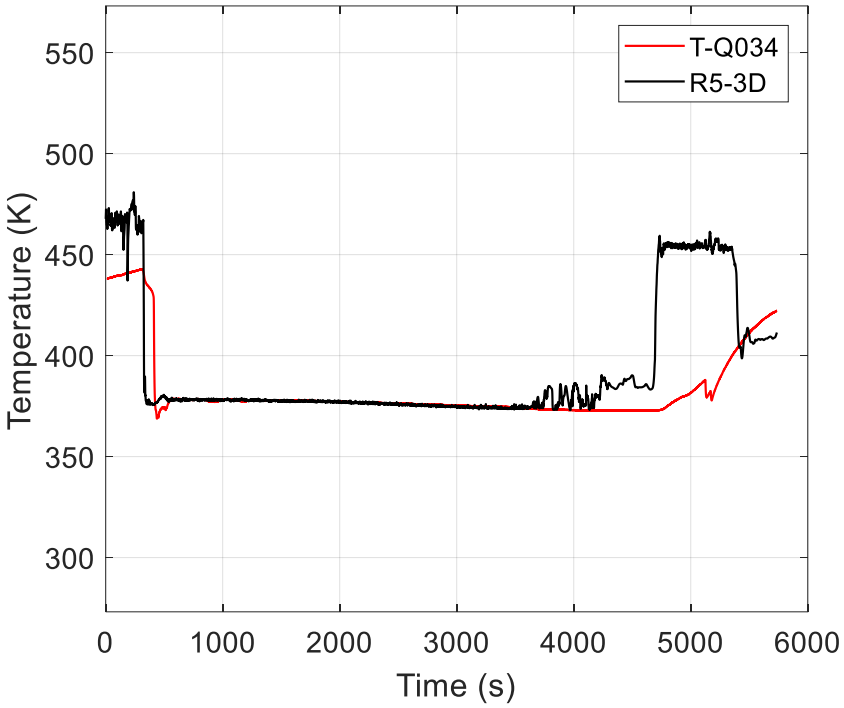

Figure 141. Test 7 Part2: HXP temperature T-Q034

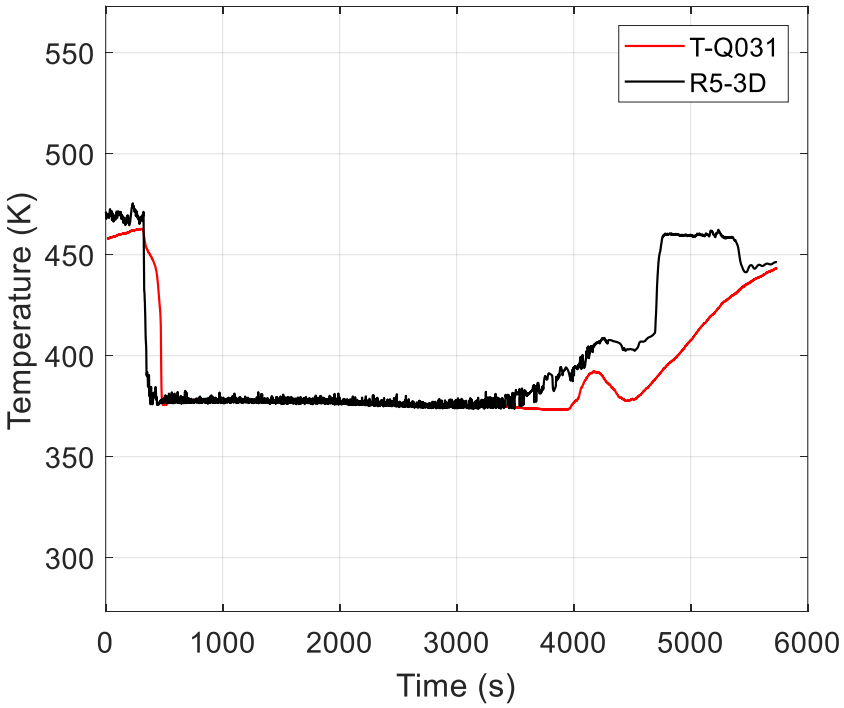

Figure 142. Test 7 Part2: HXP temperature T-Q031

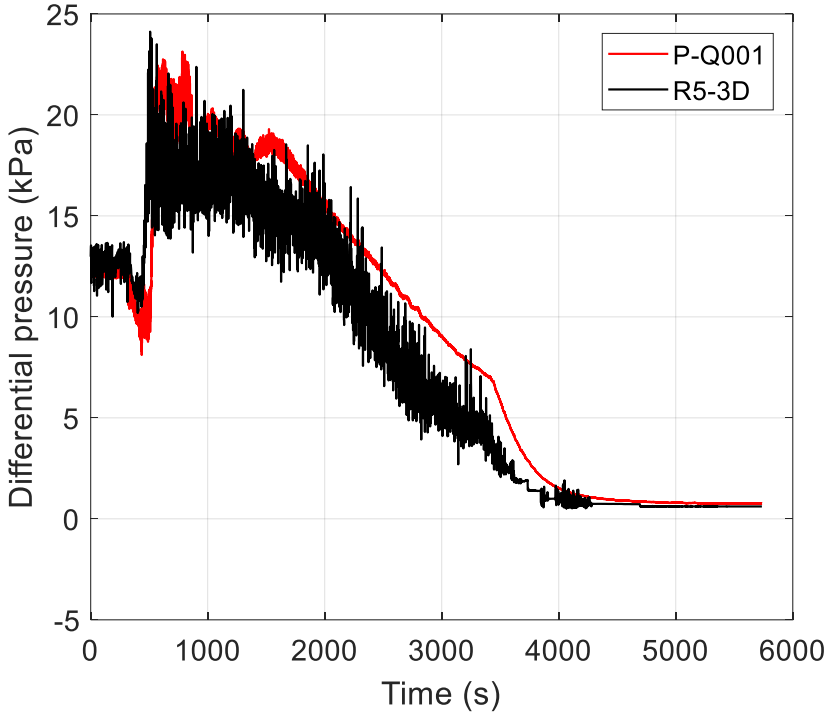

Figure 143. Test 7 Part2: relative pressure HXP

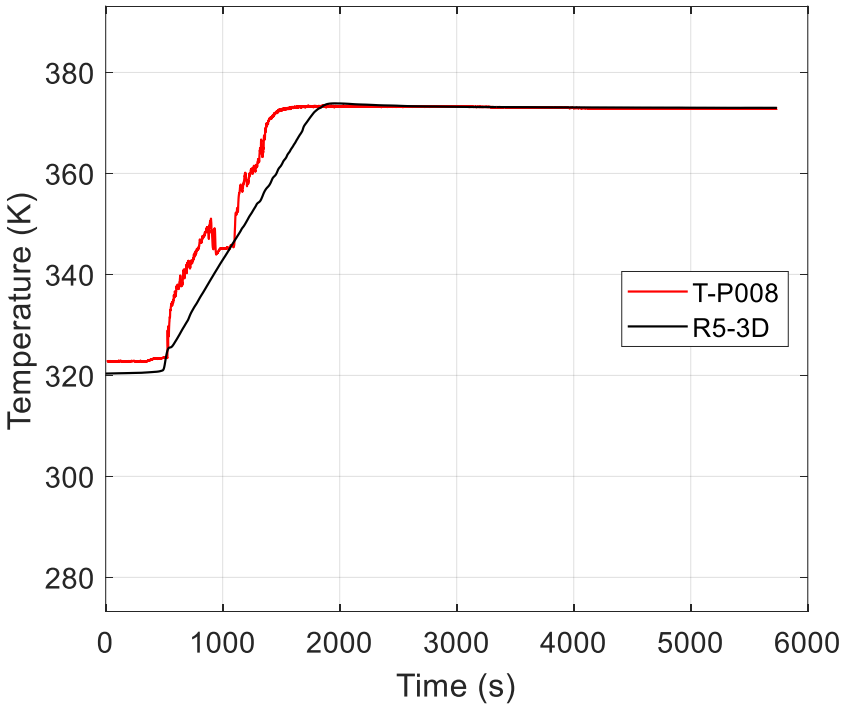

Figure 144. Test 7 Part2: OP temperature T-P008

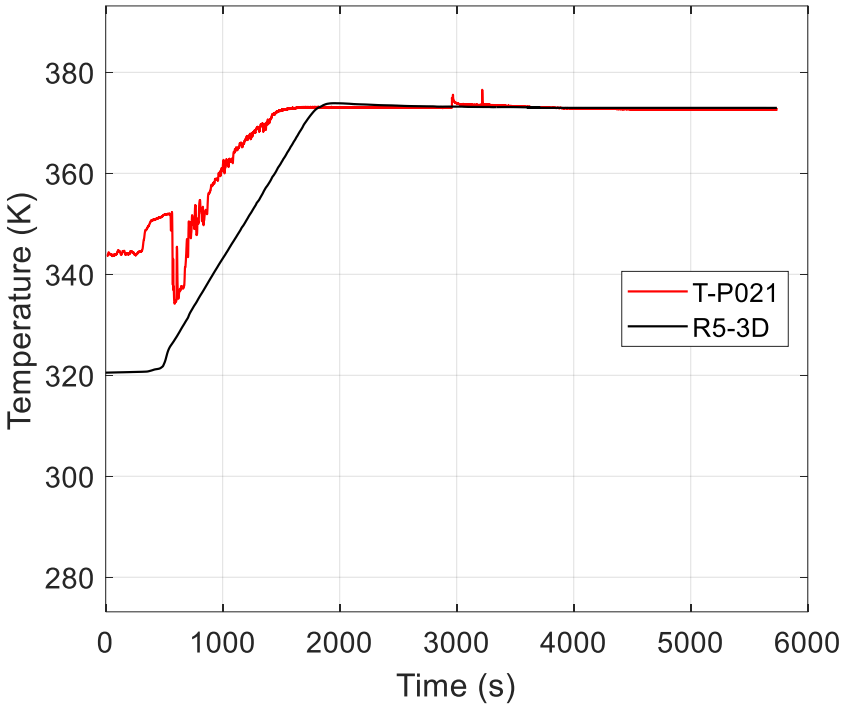

Figure 145. Test 7 Part2: OP temperature T-P021

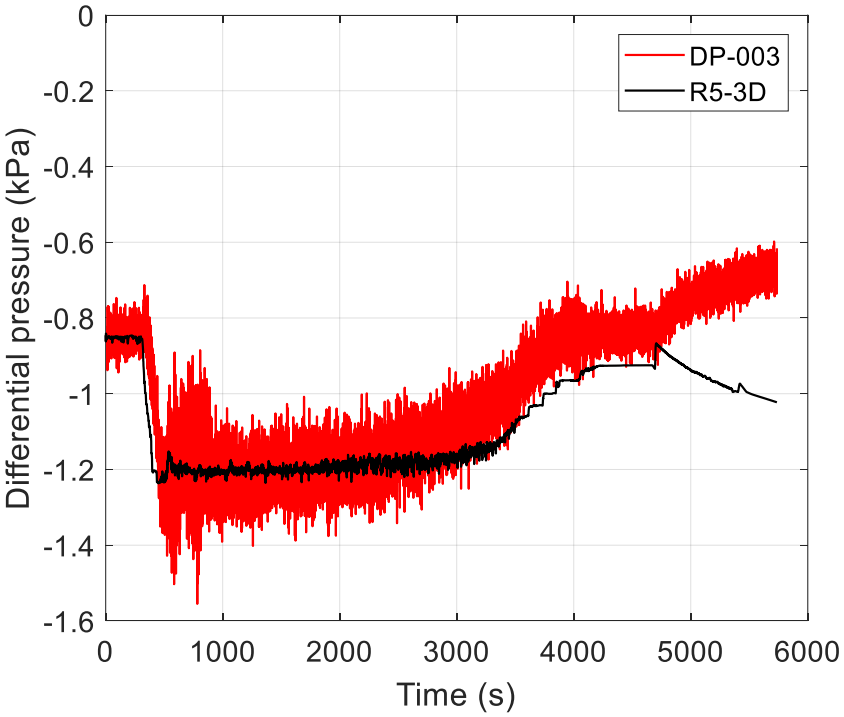

Figure 146. Test 7 Part2: HX differential pressure

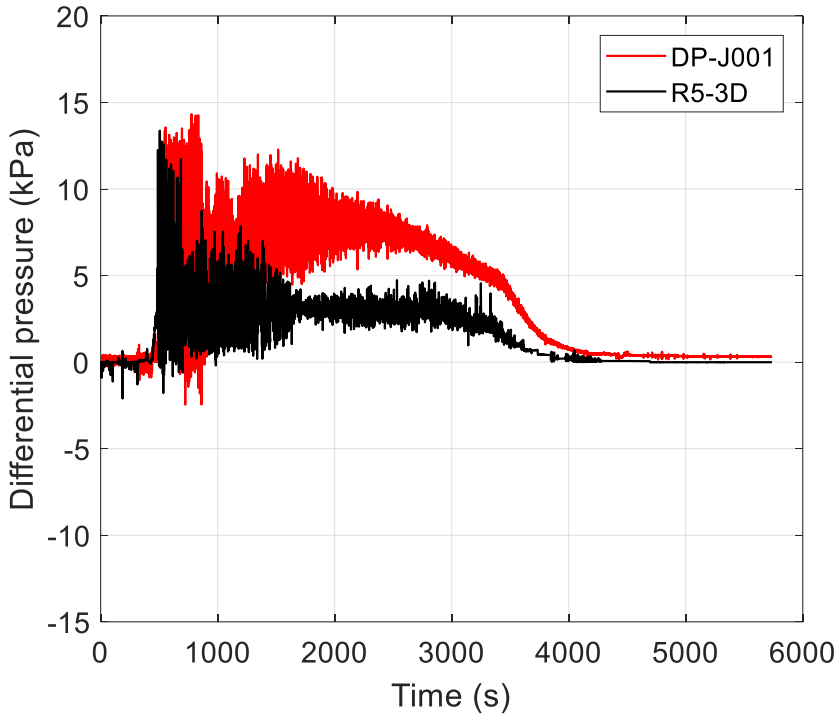

Figure 147. Test 7 Part2: injector differential pressure

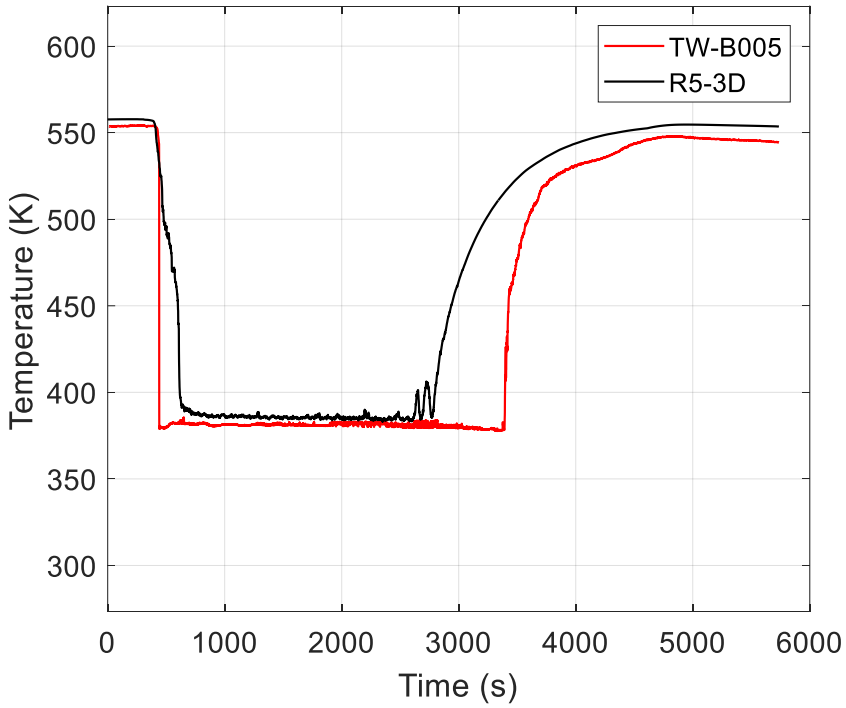

Figure 148. Test 7 Part2: HX upper header outer wall temperature

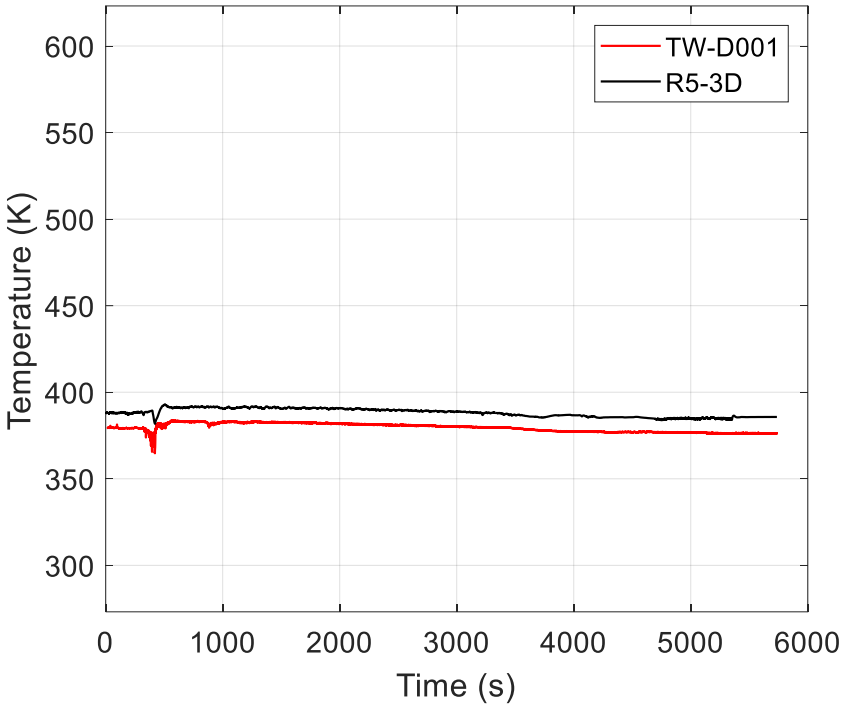

Figure 149. Test 7 Part2: HX lower header outer wall temperature

4.5 Conclusive remarks

The experimental campaign performed on the PERSEO facility provided useful data for the assessment of the STH code capabilities for the simulation of passive systems operating in natural circulation. For this purpose, the Test 7 Part 1 and Part 2 has been selected for the benchmark exercises promoted in the framework of the OECD/NEA/CSNI/WGAMA "Thermal-hydraulics of passive safety systems in water-cooled reactors".

"Sapienza" University of Rome took part in the exercise benchmark developing a nodalization scheme of PERSEO facility with RELAP5-3D©. A mono-dimensional model has been developed, including the pools modelling. All the main phenomena occurring in Test 7 Part 1 and Part 2 have been reasonably predicted by the code, even if some criticalities have been highlighted.

The main limitation observed in R5-3D calculations, and in almost all the codes adopted in the benchmark exercise, is the significant underestimation of the power exchanged between the HX and the HXP. This can be attributed to the under prediction of the HTC in both the tube-side and pool-side, where the condensation under natural circulation conditions and the pool boiling are outside of the validity ranges of the correlation fully integrated in the code. For this reason, the main improvement adopted in the nodalization has been the application of a constant multiplicative factor (2.4) to the HTC on both the sides.

Another criticality highlighted by the comparison between the experiment and the calculation, has been the capability to reproduce the thermal stratification within the pool. However, this discrepancy was expected, because of the choice to simulate the pools with a mono-dimensional modelling approach, in order to reduce the computational costs. This choice could be justified because the thermal stratification does not lead to relevant effects, occurring at the beginning and at the end of the transients, when the passive system is no in

operation. The good agreement highlighted in the operation of the passive system, confirms that the missing prediction of the thermal stratification does not prevent a correct prediction of the experimental data.

5 COMPUTATIONAL ACTIVITY ON ALFRED REACTOR

ALFRED is the European LFR demonstrator, developed and designed to test and qualify technological feasibility of an industrial size LFR. Initially, the ALFRED reference concept was developed in the frame of the LEADER project, within the European 7th Framework Programme (FP) [87]. In the last years, a revised concept of the reactor has been proposed, responding to the main specific issues highlighted in the previous configuration [88].

"Sapienza" University of Rome, in collaboration with ANSALDO NUCLEARE and ENEA, promoted two computational campaigns concerning the safety analysis of the two concepts developed for the Advanced Lead Fast Reactor European Demonstrator. The know-how, acquired with the numerical activities described in previous chapters, has been applied to support the design of the LFR demonstrator.

5.1 The ALFRED reference concept: LEADER project

The LEADER project started in April 2010, in the framework of the European 7th FP, aiming to develop a conceptual design of an LFR industrial size plant and a scaled demonstrator for the LFR technology (ALFRED). The objective was to construct ALFRED reactor in a relatively short term. At this regard, the main purposes of the project were [87]:

- to define the main suitable design and characteristic guidelines for the demonstrator;
- to use, as much as possible, components and technologies already available in short term;
- to evaluate safety aspects and to perform preliminary safety analysis;
- to minimize the costs of the demonstrator.

Within the third point, UNIROMA1 developed a detailed thermal-hydraulic model with R5-3D, carrying out the preliminary safety analysis.

5.1.1 Description of the ALFRED reference configuration

The reference configuration of ALFRED reactor is a pool-type lead-cooled fast reactor of 300 MW_{th}. In order to limit corrosion effects, the operative temperature is maintained in the range of 673-753 K, controlling the amount of oxygen dissolved in the coolant. Eight integrated SG-PP units promote the circulation of the primary coolant and remove the fission power. The SG secondary cooling systems are fed with water at 608 K and 188 bar. Super-heated steam enters the turbine at 723 K and 180 bar to produce a net electrical power of about 125 MW_{el} [87].

Figure 150 shows the ALFRED reactor block [87]. It presents a simple primary flow path. The cold lead moves upward through the reactor core and then enters the eight pump conduits. The hot coolant flows upward through the riser, and it feeds the SGs passing through the inlet holes obtained on the SGs shells. Lead is cooled and then discharged in the lower plenum of the cold pool.

All the primary components are contained within the Reactor Vessel (RV) (yellow structure in Figure 150), a cylindrical tank with toro-spherical bottom head. It is anchored to the reactor cavity from the top. The reactor pit is covered by a steel layer, named Safety Vessel (SV). The volume between the RV and the SV is designed in order to contain the primary coolant in case of RV leakage, covering the SG inlets in any accidental case, in order to maintain the safety operations. The Safety Vessel is cooled by the cooling system of the cavity concrete.

The RV contains the Inner Vessel (IV) (green structure in Figure 150) that accomplishes two functions: it supports the reactor core and it separates the hot plenum from the cold pool. At the top, the upper grid (blue) is designed to push down the fuel assemblies during the reactor operations. At the bottom, the lower grid, anchored to the IV, allows the coolant to enter the active region, moving upward across the core and exiting the active zone

through the eight circumferential PP conduits, included in the IV structure. The primary axial pumps are installed into the hot legs, surrounded by the steam generators tube bundles, placed inside the SG casings. Each SG consists of 542 bayonet tubes with an active length of six meters. The SG concept is the same presented in section 2.2.1 and its thermal-hydraulics has been investigated in CIRCE-HERO experimental campaign. Each PP and SG are integrated in a single vertical unit, located inside the annular volume between the IV and the RV, as shown in Figure 150 (b). The axial distance between the middle of the core and the SG mid-plane, relevant for the instauration of the natural circulation, is about 1.87 m.

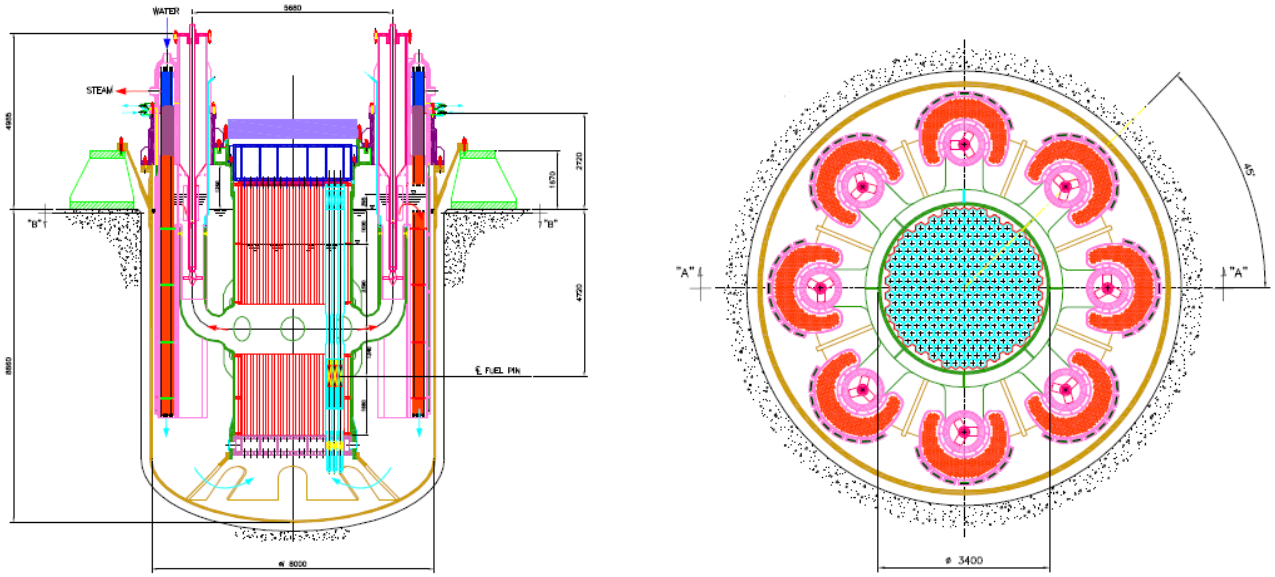

(a) (b)

Figure 150. ALFRED reactor block: vertical (a) and horizontal (b) views

Figure 151 shows the core configuration [87]. It consists of 171 fuel assemblies: 57 FAs composing the inner core (green in Figure 151), 114 composing the outer core (blue). Twelve control rods (CRs) (red) and four safety rods (SRs) (purple) accomplish the control and safety operations, and 108 dummy elements (white) fulfill the IV shielding.

Each FA consists of a bundle of 127 pins with an active length of 60 cm and a large fuel rod pitch to improve the natural circulation. MOX fuel is used with two different enrichments for inner and outer core. The pins are arranged in a hexagonal wrapper to provide a more stable core geometry and an easier handling. A spike, fixed to the lower grid, allows the coolant entrance through multiple openings and a funnel, above the core active region, permits the fluid exit through several holes. The multiple inlets/outlets design solution is adopted to avoid an instantaneous total blockage. At the top, a ballast avoids the assembly buoyancy within the liquid lead. Figure 152 shows the FA axial design (total height is 8 m) with cross-sectional geometry at key locations [87].

Two diverse, redundant and separate shutdown systems are proposed: the CRs system, used for regulation during reactor operations and for SCRAM in case of emergency, and the SRs system, designed only for the reactor SCRAM. Each CR consists of a bundle of 19 pins contained inside a cylindrical shroud and cooled by the primary lead. The absorber material is B4C (90% 10B) and it is characterized by an active length of 68 cm. Control rods enters the core from the bottom and they are actuated by motors during reactor operations. When fully

extracted, the top of CR absorber region is 4 cm below the bottom of the fuel. The control rods are also provided with an electromagnetic connection whose release, in case of emergency, causes their rapid insertion within the core by buoyancy. The four SRs have the same absorber material of the CRs, but they are extracted upward and inserted downward against buoyancy force. They consist of 12 pins cooled by the primary lead and arranged inside a cylindrical shell. The SRs are inserted by a pneumatic system drive. If this system fails, a tungsten ballast, added at the top of the SRs, provides a sufficient weight to oppose the buoyancy and to insert the SRs into the core with a lower speed. The absorber length is 84 cm and, when fully extracted, the distance from the top of the fuel is 12 cm [89].

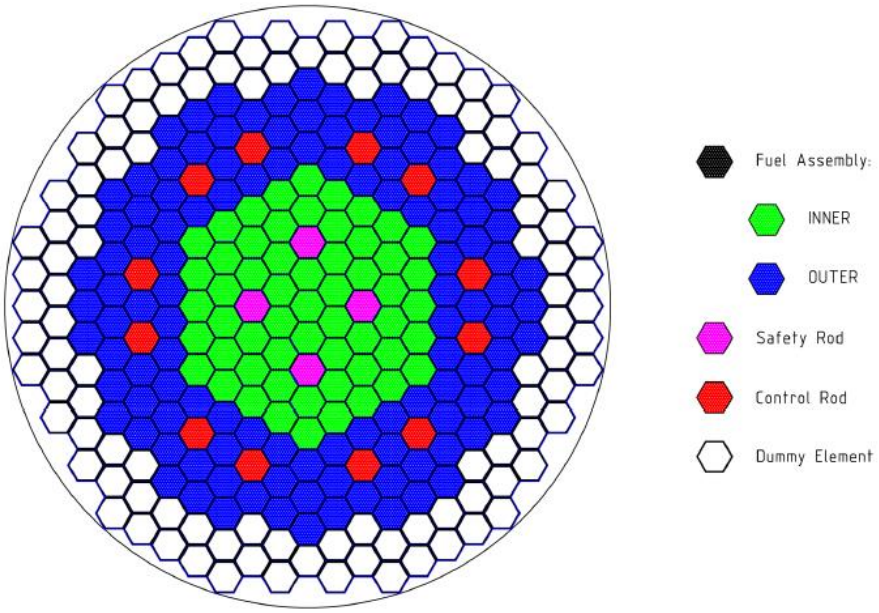

Figure 151. ALFRED core configuration [87]

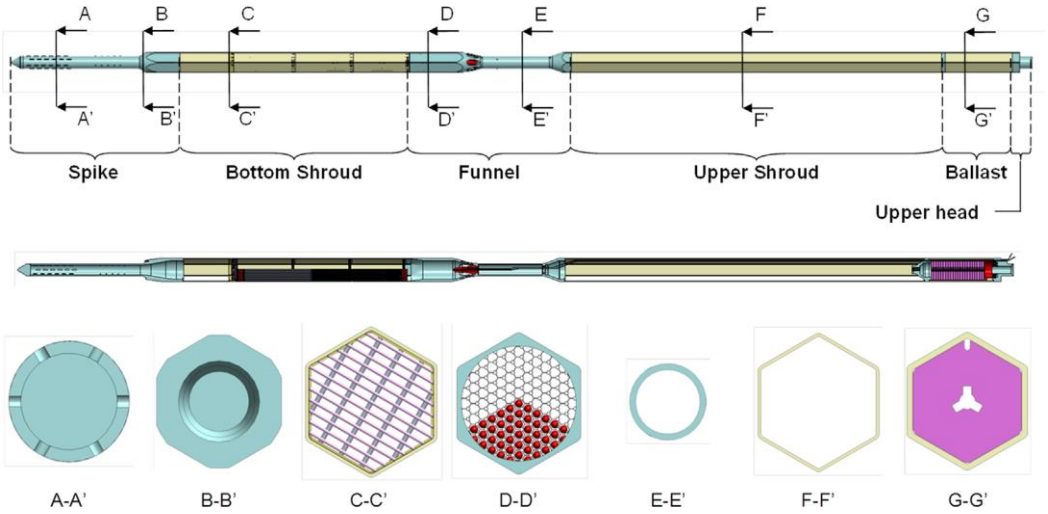

Figure 152. FA geometry [87]

5.1.2 Description of the thermal-hydraulic model

The computational activities concerning CIRCE facility (section 2) and Phénix reactor (section 3) provide useful guidelines for the simulations of complex LM-cooled pool-type systems. The lesson learned from the code validation activity has been applied for the realization of a thermal-hydraulic modelling of the ALFRED reactor.

Figure 153 shows the nodalization scheme developed for the primary system of ALFRED reactor. The model mainly consists of a three-dimensional region, reproducing the cold pool, the lower plenum, the core bypass and the hot region above the core, and a mono-dimensional region, simulating the rest of the system.

Three MULTID components are developed, identified by the numbers 100, 101 and 110 in Figure 153. Component 100 (hollow cylindrical geometry) reproduces the annular volumes between the RV and the IV. It is composed of 53 axial levels, 3 radial meshes and 8 azimuthal intervals. Volume and junction factors have been calibrated to take into account the volume occupied by the internal components (i.e. SG-PP units and pump conduits; see Figure 150 (b)). The MULTID component 110 simulates the cold pool lower plenum. It is conceived in cylindrical geometry, composed of 7 radial meshes, 8 azimuthal intervals and 9 axial levels. The firsts four radial meshes reproduce the region below the reactor core, and the last three simulate the bottom region of the annular downcomer. Calibrated volume and junction factors have been considered to account the actual lead volume of the toro-spherical bottom head. The third MULTID region, component 101, simulates the core bypass and the hot plenum above the reactor core. Radial and azimuthal nodalizations have been developed according the firsts four radial meshes of component 110 and axial meshing is obtained according the sliced modelling approach. Volume and junction factors have been calibrated to consider the volumes occupied by the core assemblies.

Several multiple junctions are introduced to realize the hydraulic connections between each MULTID component and between the three-dimensional region and the mono-dimensional one.

The 1D model includes the reactor core, the hot region above component 101 (see 120 in Figure 153), the cover gas volumes (components 160 and 130), the SG-PP units and the secondary side of the bayonet tubes. The reactor core is simulated assembly per assembly in the active region (FAs, CRs and SRs) and collapsing all the dummy elements in a single equivalent pipe. The core modelling consists of an overall number of 189 pipes, each one composed of 30 axial hydrodynamic volumes. The axial quotes for nodalization have been chosen to be consistent with the assembly design derived from Ref. [89]. Calibrated K-loss coefficients have been adopted at the inlet of the assemblies, supplying the total primary flow rate in order to obtain a coolant temperature

distribution as flat as possible at the core outlet, in full power steady-state conditions. Heat structures are connected to each pipe component to simulate the thermal power deposited in any core assembly by gamma and neutron emissions due to fission processes. Calibrated multiplicative factors (equal to 1.26) have been introduced to correct the HTC coefficients in accordance with Ushakov correlation [53]. Specific correlations are used to evaluate pressure drops in FAs spike, funnel, spacer grids and rod bundle [90].

The eight SG-PP units are separately modelled and connected with the corresponding regions of the hot plenum and of the cold pool. The steam generator modelling approach has been investigated in section 2.2 and adopted for the ALFRED model. The primary side is modelled with a single pipe, simulating the free volume between the SG case and the tubes, and the DWBTs are collapsed in two pipes per each SG: one for the descending side and one for the annular riser. Several heat structures simulate the heat exchanged between primary and secondary sides and between water descending side and water/steam annular riser, as presented in section 2.2.2.1.

All the heat exchange between the components, and the heat losses towards the environment are simulated with several heat structures, developed according to the reference data on the geometries and materials [91].

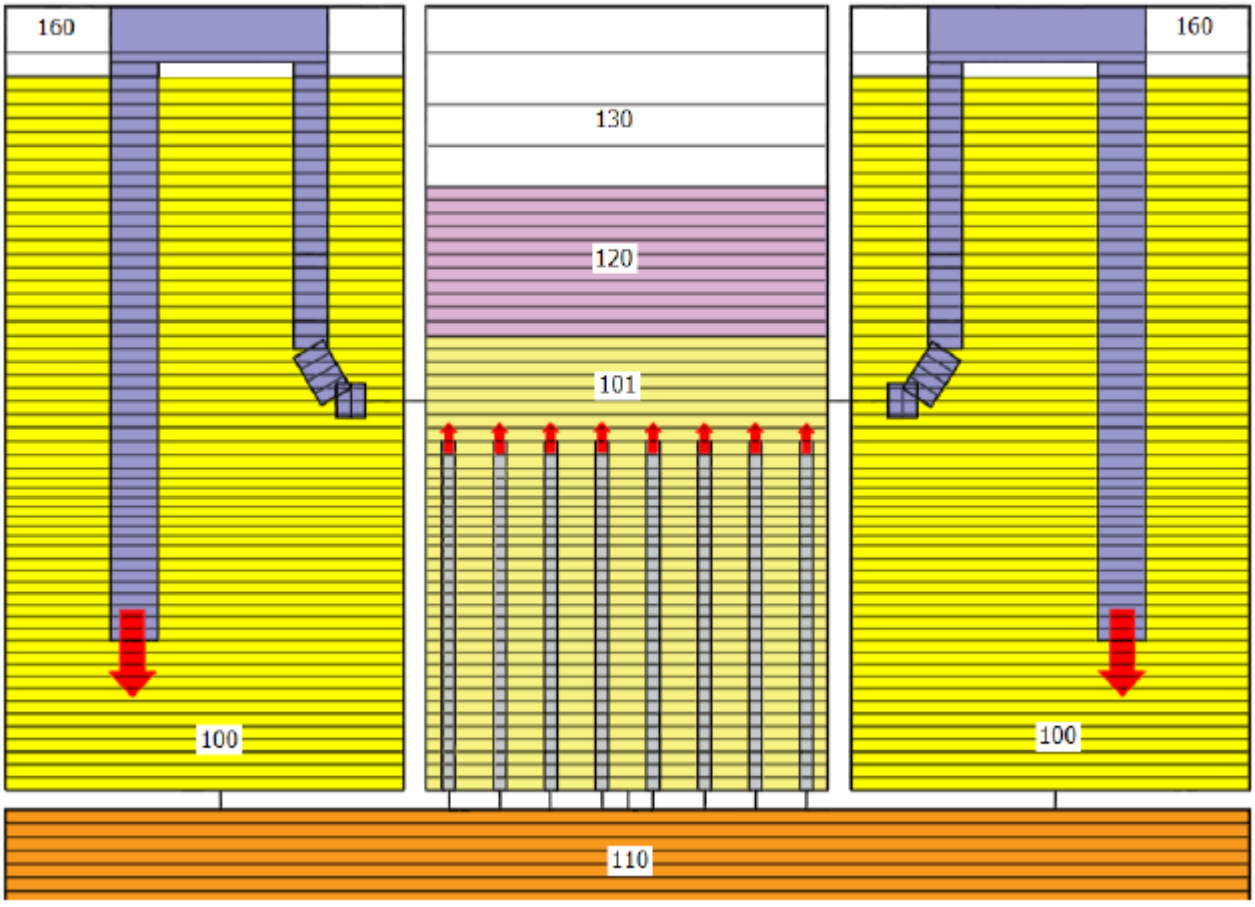

Figure 153. ALFRED primary system: nodalization scheme

5.1.3 Application of the RELAP5-3D/PHISICS coupling methodology for the evaluation of the full power steady-state conditions within the reactor core

This section presents the methodology applied for the evaluation of the core parameters at full power steady-state conditions. For this purpose, a coarse thermal-hydraulic nodalization scheme of ALFRED reactor has been adopted, in order to reduce the computational cost (which can be a critical point for coupled calculations). The main purpose of this activity has been to investigate capability of the RELAP5-3D/PHISICS coupled codes to simulate LFR transients, in particular, to reproduce ALFRED core power spatial evolution and its effects on the main thermal-hydraulic parameters during two unprotected scenarios: unprotected loss of flow (ULOF) and unprotected transient of over-power (UTOP). In addition, the core power distribution, calculated with the coupling methodology at the beginning of life (BOL) steady-state conditions, has been used as boundary conditions for the full power steady-state calculations, using the detailed nodalization scheme presented in section 5.1.2.

This section presents the analysis of the core critical configuration at BOL conditions; the transient analysis of the postulated accidents is discussed in section 5.1.5.

5.1.3.1 Neutronic kinetic and thermal-hydraulic model of ALFRED reactor

Figure 154 shows the thermal-hydraulic model adopted for the coupled calculation [92]. A coarse nodalization scheme of the pool and of the SG-PP units has been adopted, whereas the geometrical meshing of the reactor core and of the cover gas plenum is the same of the one presented in section 5.1.2.

All the primary system components are modelled with 1D approach, maintaining the axial meshing of the model presented in section 5.1.2. The eight SG-PP units are collapsed in a single equivalent one, preserving the total hydraulic and heat transfer features. This modelling approach reduces the required CPU time, without influencing the reactor behavior under symmetrical conditions. The cold pool is simulated with two annular components, linked with several cross junctions, in order to consider the buoyancy effects within the large volume.

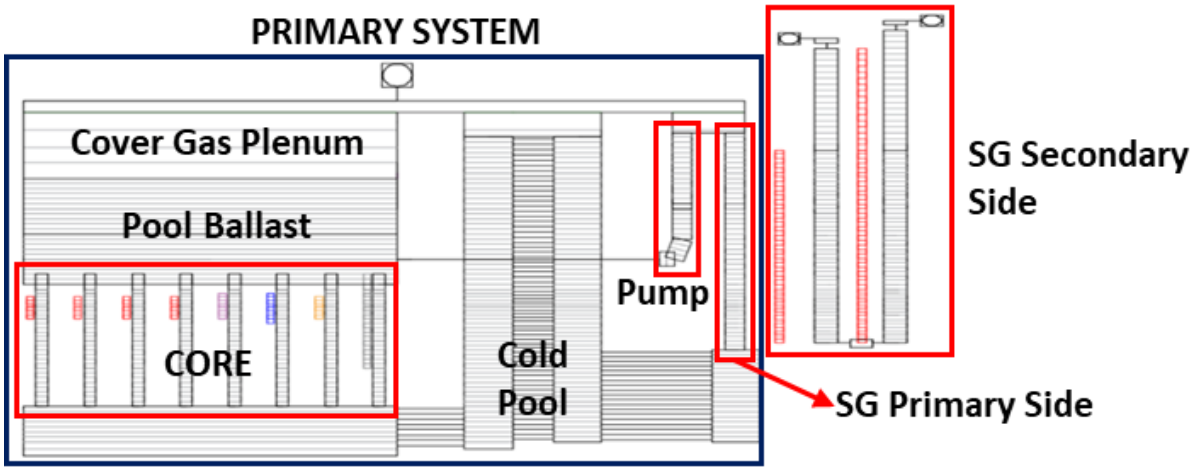

Figure 154. Simplified thermal-hydraulic model

PHISICS toolkit uses the nodal method to solve the second-order formulation of the transport equation in an unlimited number of energy groups. For all the core materials, starting from a N-dimensional Cartesian grid, PHISICS interpolates linearly the self-shielded macroscopic cross sections previously calculated with ERANOS code [93], which adopts a 33 energy groups structure and the P1 approximation for scattering treatment and evaluates thermal expansion and Doppler effect (JEFF 3.1 nuclear data library). The dimensions of the Cartesian grid are core thermal-hydraulic parameters, such as fuel and coolant temperature, density of the coolant or boron concentration. The number of tabulated dimensions and the points per dimension are unlimited [94][95]. For the purposes of ALFRED neutronic kinetic (NK) calculations, five fuel temperatures in the range of 603-3373 K and five coolant temperatures in the range of 603-1373 K have been selected to constitute a 25 points-2D interpolation grid. The axial distribution of core materials, simulated for each assembly type, is shown in Figure 155. The NK nodalization foresees 36 axial mesh and, radially, a neutronic node associated to each assembly. Material compositions have been derived from [96]. Non-reentrant current boundary conditions are used to close the neutronic problem [92].

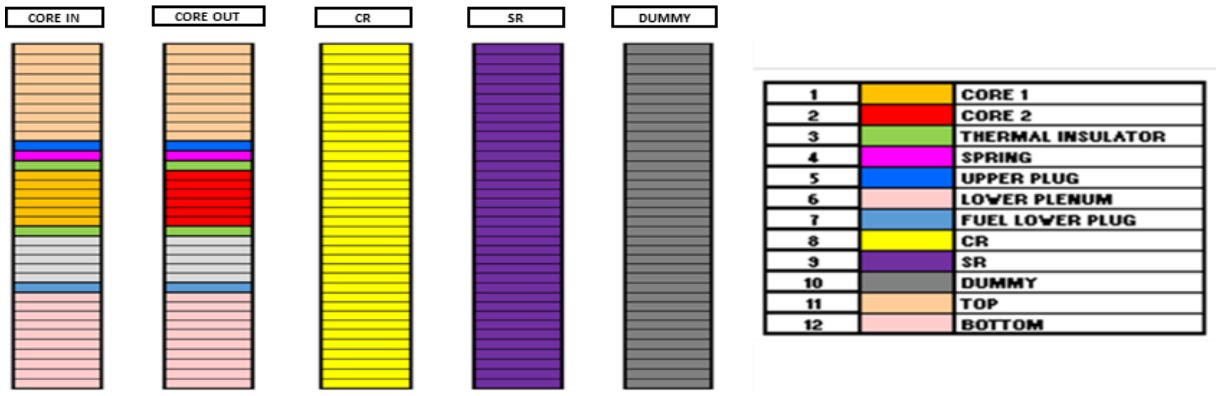

Figure 155. ALFRED core NK nodalization: material axial distribution for each assembly type

5.1.3.2 Full power steady-state calculation

Fission power, lead outlet temperature and centerline fuel temperature have been computed for each FA and their radial distributions are shown in Figure 156, Figure 157 and Figure 158. Fission power decreases moving from the center towards the periphery of the core, with a partial increase in the first ring of the outer core (which presents a higher fuel enrichment). The maximum value is in the central FA (2.34 MW). Figure 159 represents, assembly per assembly, the relative error computed in absolute terms between the mass flow rate obtained by simulation and the one derived from [90]. Its maximum value is 0.32%, so mass flow distribution is reproduced in the model with adequate accuracy. Combining the fission power computed by PHISICS and the assembly flow rate adopted, the resulting distribution of the lead outlet temperature is quite flat. The difference between the maximum and minimum coolant temperatures at the core outlet is about 23 K. One of the main design parameters for ALFRED core is the maximum fuel temperature of 2273 K [90]. The deviation of the simulation result (2310 K) from this reference value is about 1.6 %. Figure 158 represents the centerline fuel temperature radial distribution at the axial level where the maximum value of this parameter occurs (0.35 m from the bottom of active fuel). Figure 163 shows axial and radial distributions of the neutron flux, obtained considering the FAs contained in the core diameter which goes from top-right to bottom-left corner and the axial levels from the bottom of active fuel (BAF) to top (TAF). The neutron flux has nearly symmetrical profiles in both directions, with a maximum value at the core center (2.56E+15 n/(cm^2 s)).

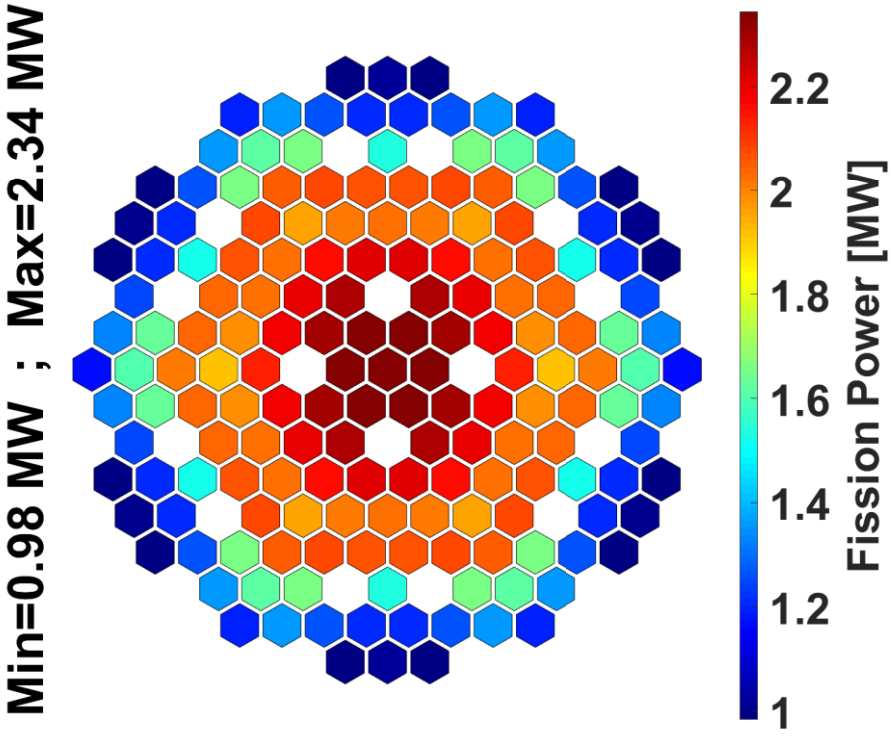

Figure 156. Fission power

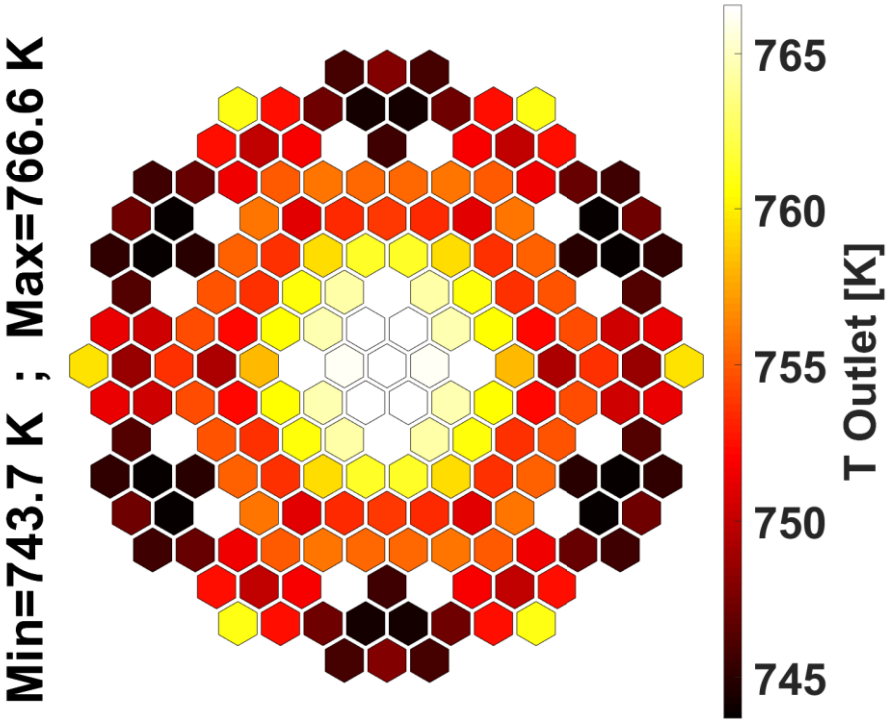

Figure 157. Pb outlet temperature

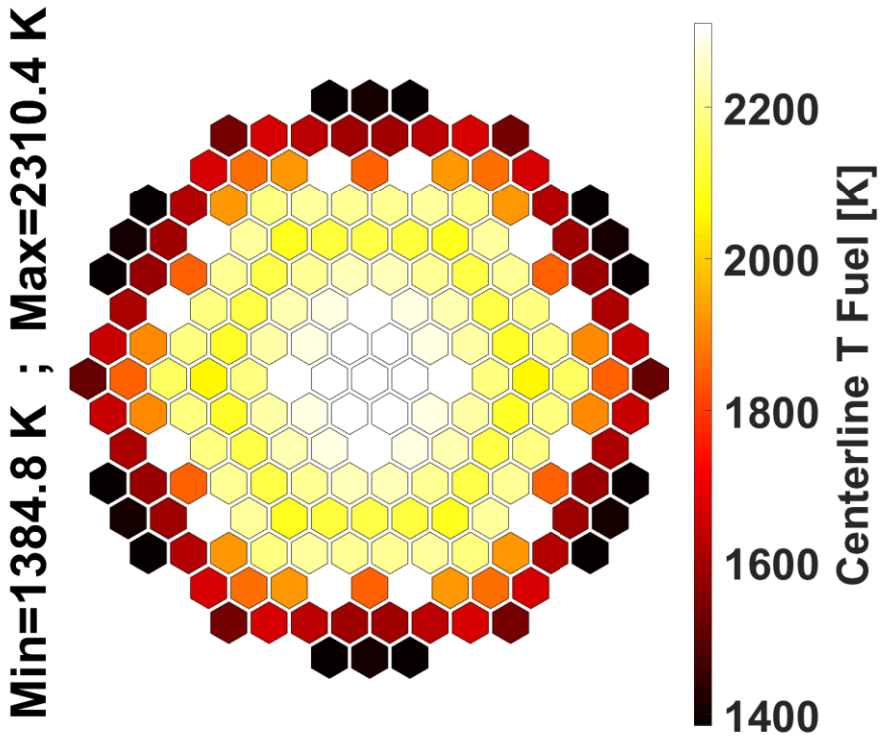

Figure 158. Centerline fuel temperature

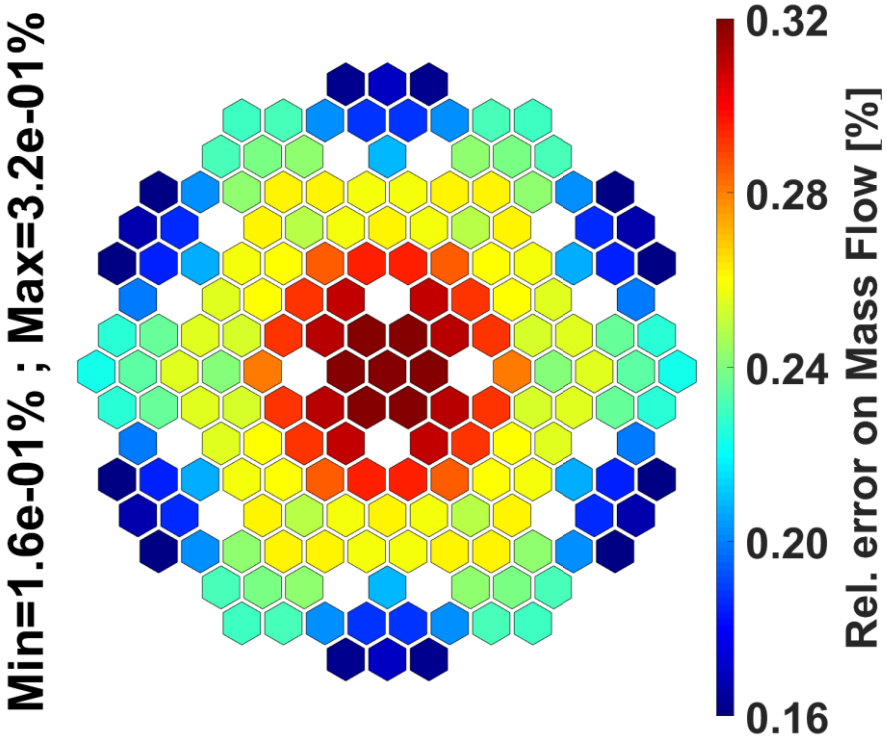

Figure 159. Relative error on mass flow

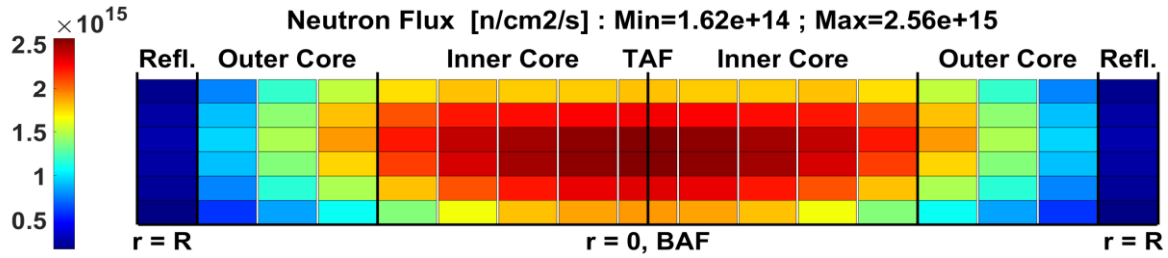

Figure 160.Neutron flux

5.1.4 Full power steady-state calculation

The fission power distribution, presented in section 5.1.3.2, has been used as a boundary condition for the full power steady-state calculation adopting the detailed thermal-hydraulic model presented in section 5.1.2. The main objective has been to investigate the thermal-hydraulics of the reactor under normal operation. In particular, the attention has been focused on the pool thermal-hydraulics.

The reference boundary conditions, derived from [91] and summarized in Table 20, have been applied.

Table 20. ALFRED full power calculation: boundary conditions

Boundary conditions	Unit	Value
Reactor core power	MW	300
Primary MFR	kg/s	25590
Secondary MFR	kg/s	192.8
Steam pressure	bar	180
FW inlet temperature	K	608

Figure 161 shows the Pb mass flow rate distribution through the active core. It is quite uniform within the inner core, decreasing towards the outer region. Combining the primary MF distribution and the fission power provided by the NK-TH calculation, Pb temperature at the outlet section of the core shows a quite flat distribution, as shown in Figure 162. The difference between the maximum and the minimum temperature is about 28 K.

Figure 163 shows Pb temperature within the whole primary system, at full power steady-state conditions, considering a representative section which includes the reactor core and two SG-PP units. Cold Pb moves from the lower plenum into the reactor core, where the primary fluid increases the temperature. The hot liquid metal is collected within the hot volume above the core and it is driven through the PP conduit. After that, the primary coolant enters the SG, is cooled and it is released within the pool at about 3 m from the bottom. A relevant thermal stratification phenomenon (about 70 K) is observed between 5.5 m and 6.5 m. The establishment of the thermal front is caused by the almost stagnant conditions of the Pb in the upper part of the pool. Cold lead,

exiting the SG, moves downward towards the core inlet region. This means that the upper part of the pool (between 3 m and 9 m) does not take part in the primary flow path. The large amount of heat losses from the hottest parts of the system (i.e. outlet core region, pool ballast, PP conduits) warm the almost stagnant Pb within the pool and the hot fluid is collected in the upper part, due to buoyancy forces. Thermal stratification represents a crucial issue, inducing relevant thermal stress to the RV, that leads the designers to develop a revised concept of the reactor.

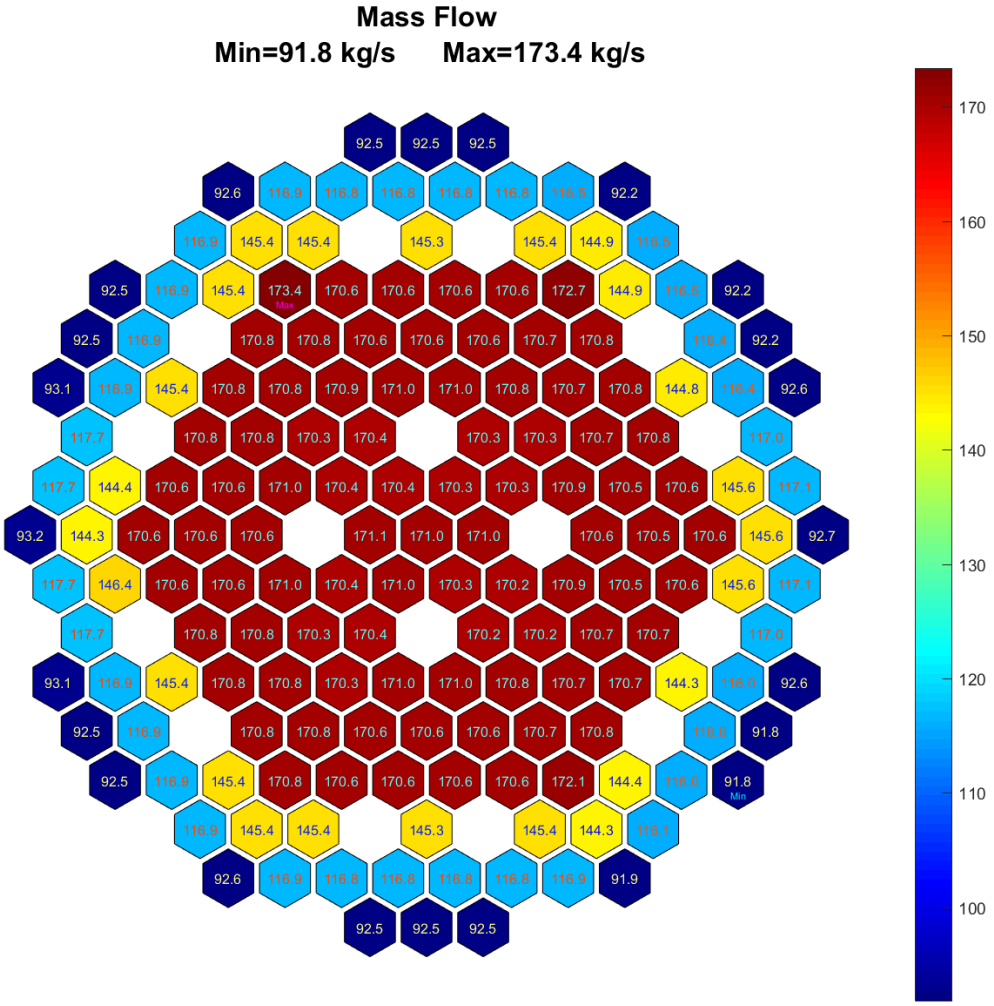

Figure 161. Mass flow rate distribution

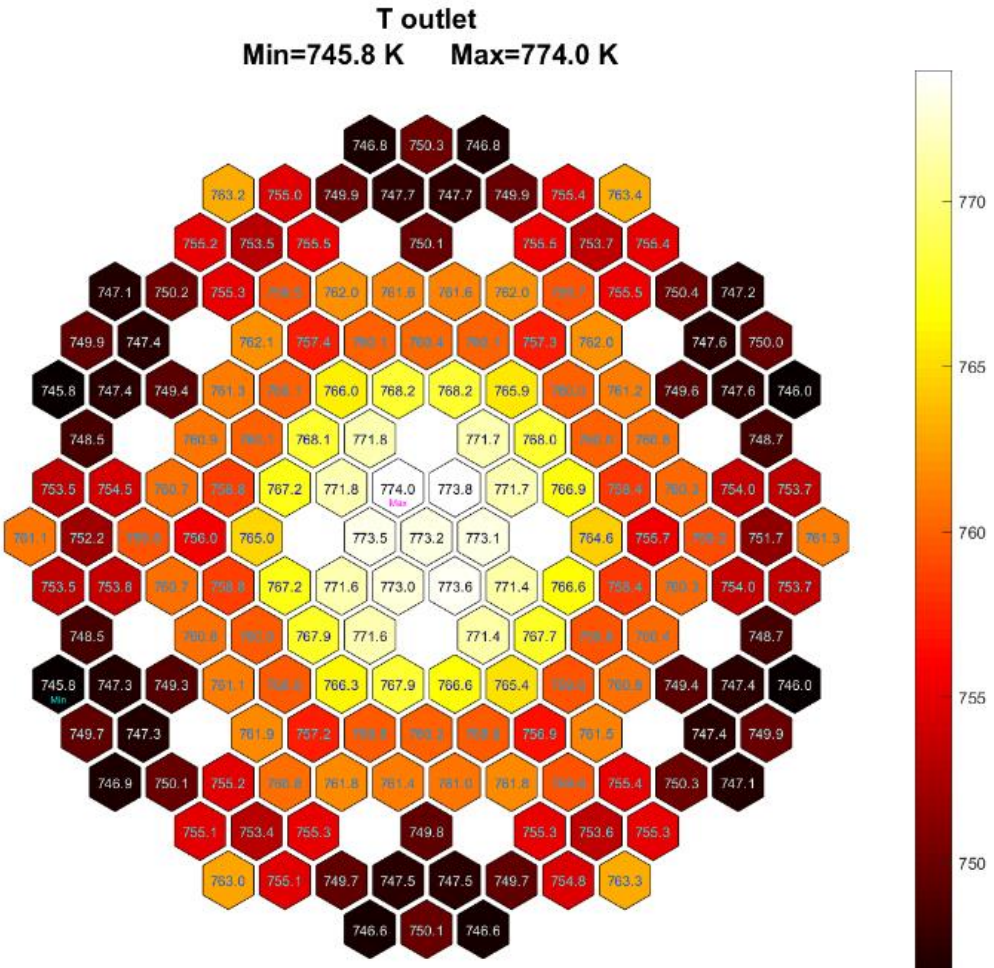

Figure 162. Active core: Pb outlet temperature

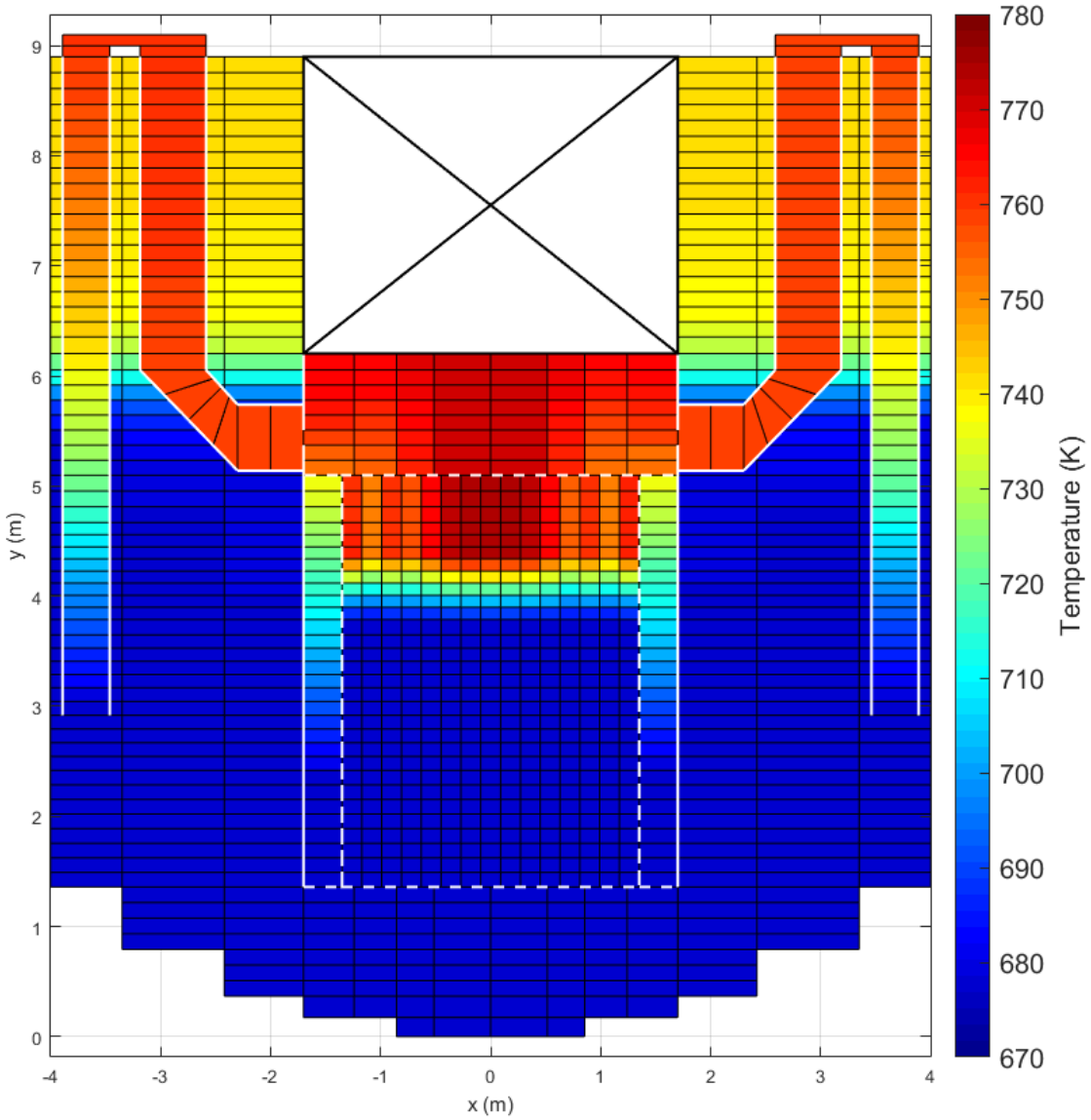

Figure 163. Primary system: Pb temperature

5.1.5 NK-TH calculations: transient analysis

The full power steady-state results described in section 5.1.3.2 are used as boundary conditions for two selected transient accidents: the unprotected loss of flow and the unprotected transient of overpower. The main results are analyzed in the following sections [92].

5.1.5.1 ULOF transient

The unprotected loss of flow transient is initiated by the loss of power supply to all primary pumps. The reactor SCRAM is supposed to fail, and the core power is driven by reactivity feedbacks. During this transient, the

secondary system is supposed to remain in normal operation with no control of the feedwater flow rate. Starting from the full power steady-state condition, the loss of all primary pumps takes place after 2 seconds of simulation. After an initial undershoot, with a minimum of 4567 kg/s, the natural circulation flow rate tends to the asymptotic value determined by the primary system pressure drops and the design height difference between core and SG mid-planes (see Figure 164 (a)). The new value, almost constant, is 5905 kg/s (about 23 % of the nominal MFR). Because of the prevalent negative reactivity feedback, the total core fission power follows the same time trend but with enhanced overshoot and undershoot values. However, after these initial oscillations, also this parameter stabilizes to about 205 MW (Figure 164 (b)). At the transient beginning, the unbalance between primary FR and fission power within the core leads to a sudden increase of the Pb outlet temperature and of the clad temperature, followed by stabilization to a new equilibrium value higher than the initial condition (Figure 164 (c) and (d)). ALFRED core design foresees a maximum allowable clad temperature of 1023 K [90]. During the transient simulation, this parameter increases up to 1036 K, exceeding the reference value of about 1.3 %. Finally, the centerline fuel temperature, depending on the linear heating rate, decreases during this accidental scenario following the fission power behavior (Figure 164 (d)).

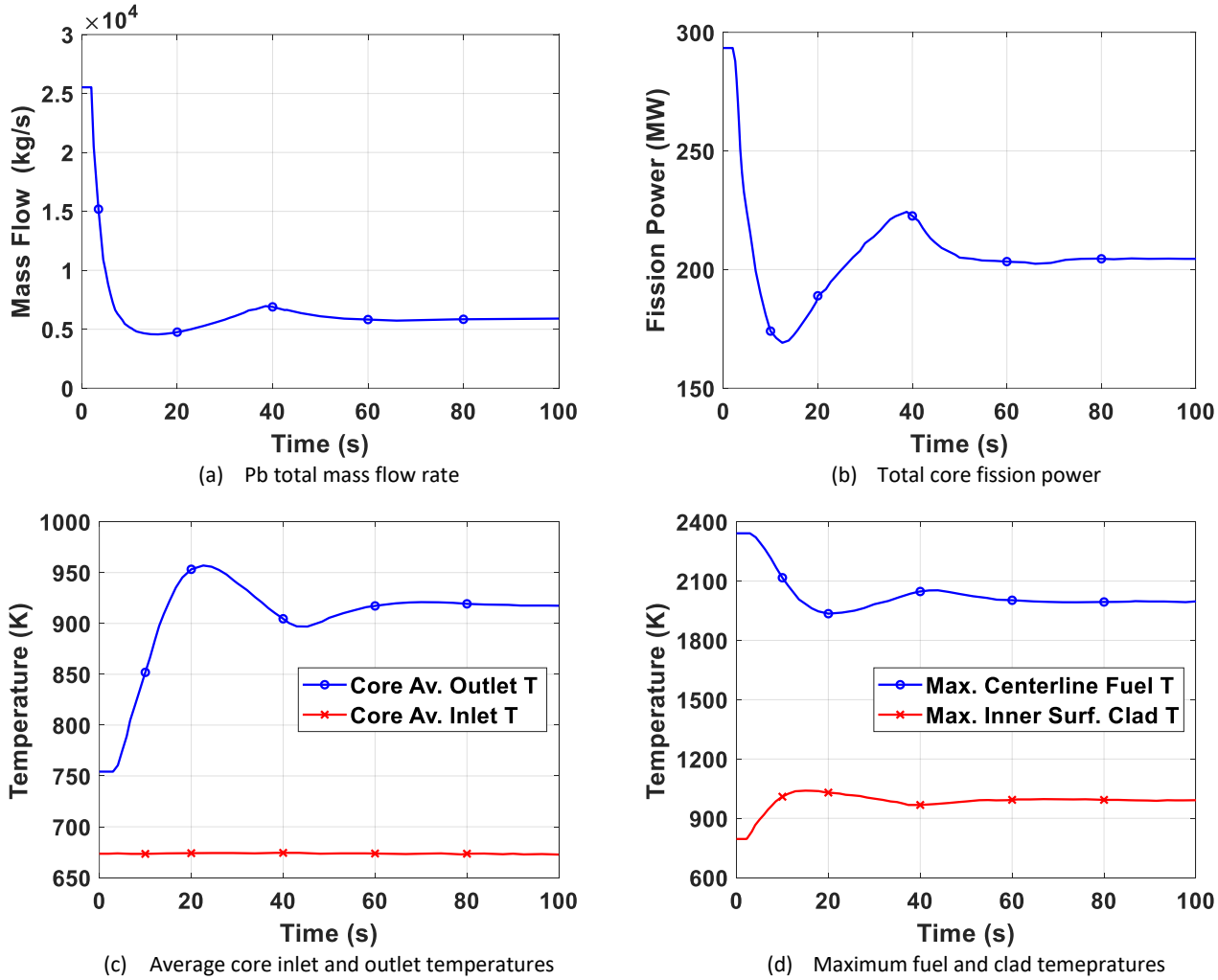

(a) Pb total mass flow rate

(b) Total core fission power

(c) Average core inlet and outlet temperatures

(d) Maximum fuel and clad temepratures

Figure 164. ULOF transient: main results

5.1.5.2 UTOP transient

The unprotected overpower transient is initiated by unexpected positive reactivity insertion. The one simulated is of 250 pcm in 10 s. It represents the possible reactivity perturbation induced in the core as a result of steam generator tube rupture, FA flow blockage or core compaction. The transient is unprotected, assuming the reactor SCRAM to fail. The secondary circuits are supposed to remain in normal operation with no control of the feedwater flow rate. The primary system is maintained in forced circulation. The reactivity insertion is simulated by moving all the control rods out of the core of about 1.3 cm in 10 s with a constant withdrawal rate. Starting from the full power steady-state condition, the reactivity insertion takes place after 2 seconds of simulation. The core power immediately increases (Figure 165 (a)) and, consequently, also coolant and structures temperatures rise (Figure 165 (b) and (d)). The power excursion is limited by the prevalent negative reactivity feedback. Among major contributions to it, there is the Doppler effect, due to the fuel temperature increase and the fuel expansion. After the initial peak, the system evolves towards a new equilibrium state at higher power (about 350 MW) presented in Figure 165 (a). The new Pb temperature at the core outlet is maintained at about 770 K (Figure 165 (b)). The maximum fuel and clad temperatures occur in the central FA: the former rises up to 2575 K, value sufficiently lower than the MOX melting temperature (about 2973 K), the latter increases up to 818 K, far lower than the maximum allowable value of 1023 K (Figure 165 (c) and (d)).

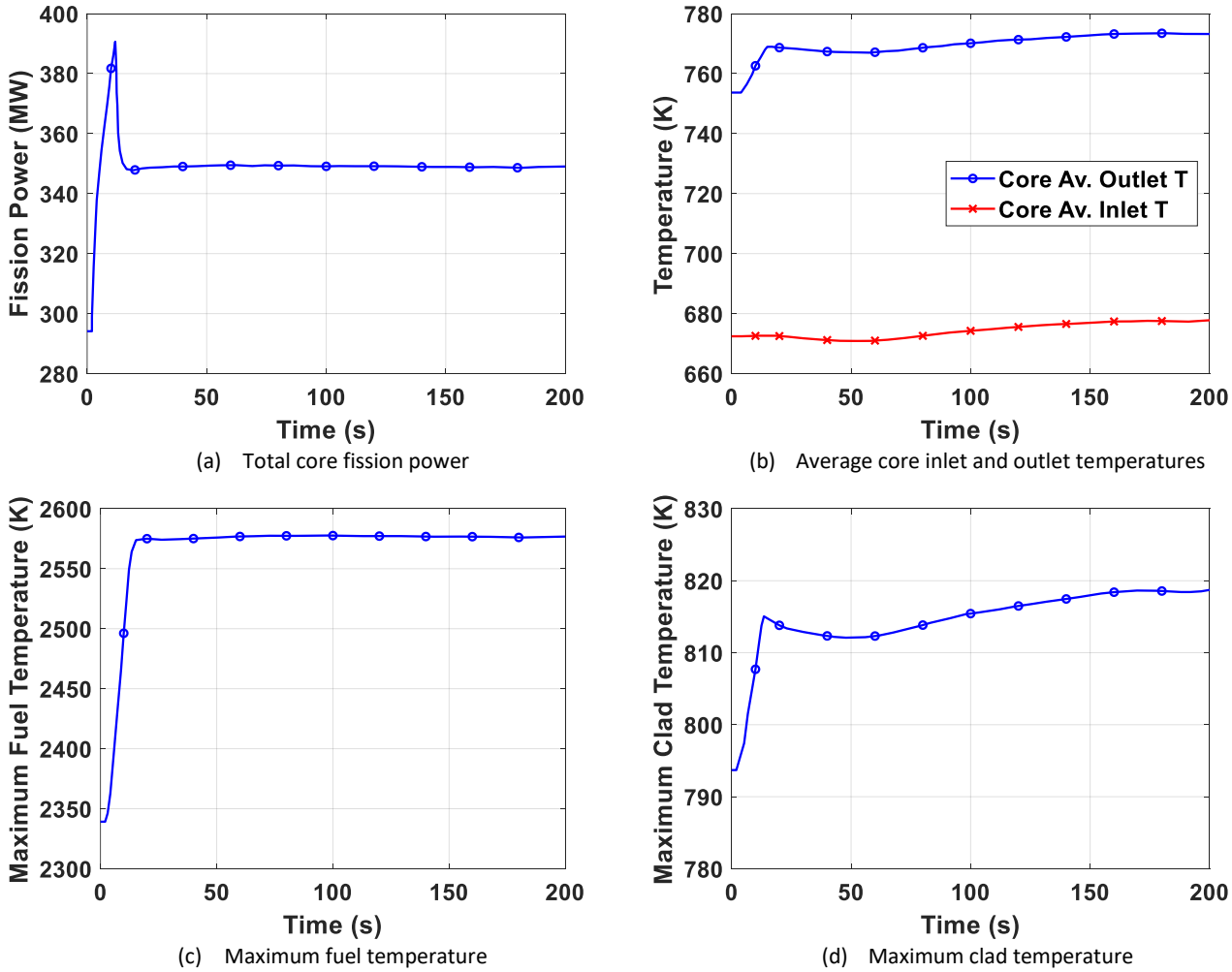

(a) Total core fission power

(b) Average core inlet and outlet temperatures

(c) Maximum fuel temperature

(d) Maximum clad temperature

Figure 165. UTOP transient: main results

5.1.6 Conclusive remarks

The numerical activity concerning the reference concept of ALFRED reactor has been mainly focused on the analysis of the full power steady-state conditions, investigating the main issues related to the design features. In addition, NK-TH coupled calculations have been performed to obtain the BOL conditions to carry out safety analysis under postulated accidental scenarios.

For the NK-TH methodology, a coarse thermal-hydraulic model has been developed, aiming to reduce the computational costs, which can be a relevant issue for the coupled procedure. The nodalization scheme has been mainly focused on the reactor core operation. A preliminary full power steady-state calculation has been performed in order to evaluate the fission power distribution at BOL conditions. The full power results have been used as boundary conditions for the simulation of two postulated accidents: ULOF and UTOP. The results, presented in section 5.1.5, have provided a realistic evolution of the main neutronic and thermal-hydraulic parameters monitored. The transient analysis has highlighted good agreements with the results obtained by other research institutes, adopting different numerical codes [97].

The fission power distribution, obtained with the coupled calculation, has been used as boundary condition for a detailed analysis of the primary system at full power operation. A more detailed model has been developed, maintaining the core nodalization scheme. The eight SG-PP units have been separately modelled, and the pool of the reactor has been simulated with a MULTID component, following the know-how acquired from the numerical activity described in the previous chapters. The full power results highlighted the establishment of a relevant thermal stratification (about 70 K) in the upper part of the pool, where the molten lead is almost stagnant. This effect represents a critical issue for the reactor operation, leading the designers towards a revised concept of the demonstrator.

5.2 A revised concept of ALFRED reactor

At the end of the LEADER project, the common efforts between ANSALDO NUCLEARE, ENEA and the Institute for Nuclear Research (ICN) (Romania) were confirmed in December 2013, within the FALCON (Fostering ALFRED Consortium) international consortium [88]. In this framework, a new strategic vision has been conceived, aiming to accelerate the commissioning and the operation of ALFRED. A staged approach, summarized in Table 21, has been proposed to reduce the time-to-market of the LFR technology [98]. The idea is to start operations at low power and low temperature, that will be progressively increased using the reactor itself to qualify the next step of operation and the R&D programme which will advance in parallel with the demonstrator operation. Three levels of power are foreseen, (100, 200 and 300 MW), maintaining the same primary flow rate and allowing the planned temperature increase in three stages. The first one will be committed to the investigation of two relevant concerns for LFR technology: compatibility of lead with structural materials and lead chemistry control. Design conditions of the following stages will need a qualification programme before their operations.

Table 21. ALFRED main parameters in the stages of operation [98]

Parameters	Units	Stage 0 (Commissioning)	Stage 1 (Low T)	Stage 2 (medium T)	Stage 3 (High T)
Core inlet temperature	K	663	663	673	673
Core outlet temperature	K	663	703	753	793
Core thermal power	MW	≈ 0	100	200	300

Based on the outcomes of LEADER project, a technical review of the reactor reference configuration is undergoing. Three main topics have been investigated in the revised design [88]:

- thermal stratification occurring in the upper part of the cold pool;
- steam phase entrainment in case of SGTR accident, and consequent transport of voids within the reactor core, potentially causing positive reactivity insertion;
- lead freezing in long term accident scenario, where active control logic is not applicable for DHR passive systems.

The following section presents an overview of the ALFRED revised concept.

5.2.1 Overview of the improved concept

Even if LEADER outcomes highlighted three main sources of concerns, several features of the ALFRED reference configuration have been maintained in the revised design undergoing. First of all, the pool-type geometry has been confirmed, allowing a compact and robust design and preventing out-of-vessel primary systems. The reactor core configuration has been mostly confirmed (mixed oxide fuel, hexagonal wrapped FA, large p/d promoting the instauration of natural circulation) and two redundant SCRAM systems have been maintained. Once-through SGs and axial primary pumps, located through the hot leg, are confirmed and two diverse, redundant and fully passive DHR systems are also considered for the revised configuration. In addition, the RV is maintained surrounded by an additional safety boundary, allowing the decay heat removal in case of vessel break [88].

On the other hand, three main issues suggested the need for a technical review of the ALFRED configuration [88], performed by a dedicated task force. The revised concept has been mainly focused on an improved configuration of the pool and on the development of an anti-freezing DHR system.

Numerical activities performed on the reference configuration of ALFRED, such as the one presented in section 5.1.4, highlighted the occurrence of thermal stratification phenomenon within the upper part of the pool. This region of the pool is not involved in the primary flow path, creating an almost stagnant region where the hottest walls of the inner vessel warm the primary fluid. Buoyancy effects determine the establishment of the thermal front. Another consequence of the reference pool thermal-hydraulics is the possible void transport through the reactor core, in case of SGTR. The steam, released within the SG primary side, could be transported by the primary flow rate and collected in the lower part of the pool. As presented in Figure 150 (a), a preferential flow path could promote the transport of the steam within the core, leading to void formation and possible positive reactivity insertion. Therefore, a technical revision has been proposed in order to improve the pool thermal-hydraulics. An internal structure (IS) (the green structure in Figure 166) has been introduced within the reactor vessel, forcing the cold lead, exiting the SG, to move towards the free level. Through several slots located on the outer walls of the IS, in the upper part, the primary coolant moves into the downcomer obtained in the annular region between the RV and the IS, flowing towards the core inlet. This solution avoids the stagnation of the coolant in the upper part of the pool, preventing the establishment of the thermal stratification. In addition, in case of SGTR, steam is transported by the primary flow path up to the free level and purged into the cover gas system, where it is separated from the liquid metal due to gravitational forces, preventing the void formation within the reactor core. Moreover, the IS introduces a hot pool in the upper part of the reactor, separating the PP and SG units and improving the Pb inlet conditions of the SGs [88].

The main technological drawback is the increase of the RV diameter, even if it is considered still acceptable. In addition, the improvements introduced in the pool thermal-hydraulics should be verified, mainly focusing on the following aspects:

- suppression of the thermal stratification, in both forced and natural circulation;
- establishment of natural circulation conditions able to remove the decay heat power;
- slots configuration, compatible with all conditions, including the reduced free level following a reactor vessel break.

For this purpose, “Sapienza” University of Rome, in collaboration with ANSALDO NUCLEARE, has developed a detailed nodalization scheme of the new configuration of ALFRED (relevant for stage 2, see Table 21). The description of the thermal-hydraulic model and the analysis of the simulations results are presented in sections 5.2.2 and 5.2.3.

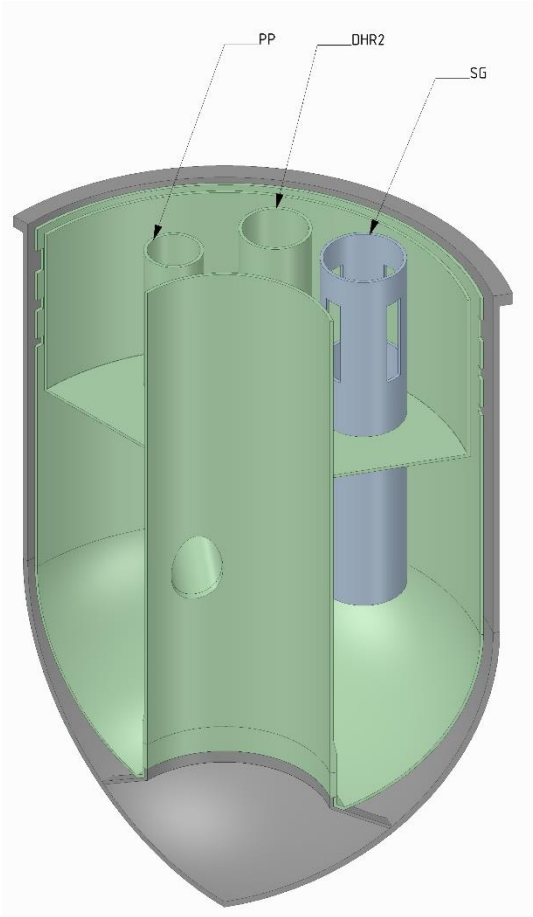

Figure 166. internal view of the ALFRED revised configuration [88]

The main components of the primary system are the reactor core, the primary pumps and the steam generators. While maintaining the main geometrical parameters of the previous configuration, the new concept of ALFRED core is characterized by several adjustments aimed to improve neutronic and thermal-hydraulic features and to allow qualification of fuel elements coating required at high temperatures [26]. Figure 167 shows the cross-sectional view of the new ALFRED core. It is composed of an overall number of 151 assemblies surrounded by additional 102 dummy elements. The active region is divided in two parts: the inner zone, composed of 56 FAs, and the outer zone, of 78 FAs. The inner position (blue in Figure 167) represents a special region for the in-pile

irradiation experiments, where components and materials, to be used in the following stages, can be tested under neutron irradiation at representative temperature conditions. Control and safety functions are carried out by 12 CRs and 4 SRs. The assemblies maintain the same qualitative configuration of the previous concept, even if some adjustments have been introduced in order to reduce pressure drops across the core and to improve neutron economy. The longer active region than the reference configuration, allows to decrease the number of the overall pins required for the nominal power, reducing the whole number of FAs and thus the core radius [26]. Another peculiarity of the new FA is the introduction of a dummy pin at the center of each assembly. This decision was taken in order to exploit for in-core monitoring of the operational parameters, which is a key purpose for a reactor demonstrator [26].

One of the main differences from the reference reactor concept, is the number of SG-PP units. In the revised configuration of ALFRED, primary circulation is promoted by three axial primary pumps, drawing the primary coolant from the core outlet region and discharging it within the hot pool. Through dedicated holes, the hot Pb enters three SGs, flowing downwards across the shell-side. Concerning stage 2, each SG is composed of 880 bayonet tubes, characterized by an active length of 6 m. Unlike the reference concept, in the new configuration of the reactor, bayonet elements are not equipped with double-wall assembly, thanks to the improved pool thermal-hydraulics which guarantees the evacuation of any possible steam leaks following a SGTR event. This solution allows to preheat FW flowing in the descending side, which has a role in the DHR operation. Reduction of the number of primary components guarantees sufficient space to place additional auxiliary and safety systems.

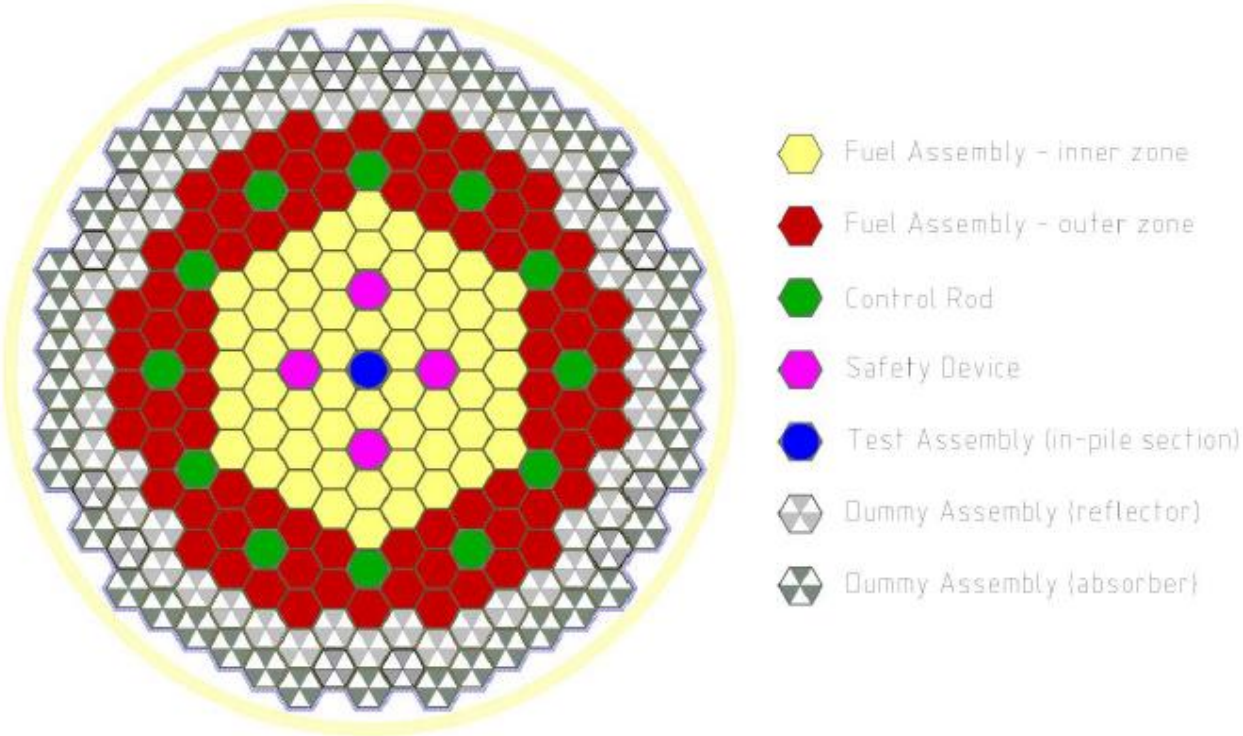

Figure 167. Core map of the revised ALFRED core [26]

As mentioned in section 4, in case of an accident, the DHR system implemented in ALFRED should be able to remove the decay power guaranteeing safety conditions, i.e. preventing to exceed the maximum temperature limits and the coolant freezing. This has been selected as one of the three main challenges for the new ALFRED concept. In the previous configuration of the reactor, DHR function was accomplished by an IC immersed in a dedicated pool, acting as final heat sink. The dimension of the water pool was evaluated in order to guarantee decay power removal for the grace time (i.e. 72 h). The DHR system was conceived to use the SG, in order to limit the number of components within the RV. For this reason, the IC was connected with feedwater and steam lines. The IC was designed to limit the maximum temperature within the primary system during the first hours of the transient. In case of passive safety systems, operator actions are forbidden within the grace time period, and the application of active systems is limited to simple operations, such as the activation of a valve powered by independent sources of energy, being them pressurized fluids or batteries. For this reason, the power removed by the DHR was basically constant and, following a postulated SBO transient, the temperature at the outlet section of the SG reached the freezing conditions within the first 6 hours, lower than the conventional grace time [88].

The solution proposed in the frame of the revised concept, has been to reduce the heat power removed by the DHR system by passively injecting non-condensable gases within the IC tubes. The technological solution has been presented in Figure 168 [80]. Few modifications have been implemented in the safety system, in order to modulate the power removed following the residual decay heat. The main improvements have been the introduction of a nitrogen tank, connected to the lower header of the IC, and the addition of an IC inlet isolation valve. The secondary system is equipped with five valves:

- feedwater isolation valve;
- steamline isolation valve;
- safety relief valve;
- safety system inlet valve;
- safety system outlet valve.

During normal operation of the reactor, feedwater and steamline valves are opened and safety relief valve and the two IC valves are closed. In this condition, feedwater enters the SG at 608 K, flowing through the normal feedwater line. Referring to the stage 2 operation, the boiling occurs within the bayonet tubes (BTs) annular riser and superheated steam, at 708 K and 175 bar, exits the SG, moving towards the power conversion system (PCS). In these conditions, the IC is filled by non-condensable gases at 110 bar, in thermal equilibrium with the water pool, that is at ambient conditions. In case of accidental scenario, feedwater and steam line isolation valves close. The water contained between the two valves boils and the pressure within the secondary system increase until 190 bar, which is the actuation set-point of the DHR inlet valve. At this time, steam flows into the IC, pushing the nitrogen in the non-condensable tank. The safety system starts to exchange power and the steam condensates within the IC tubes, creating a liquid level inside the piping downward the IC. After a second signal, the DHR outlet valve opens and the natural circulation is established through the secondary loop. The orifice installed downward the safety system outlet valve is conceived to guarantee a liquid level after the second valve opening and to limit the quantity of nitrogen that flows towards the SG. In the first phase of the transient, about the total amount of non-condensable is contained in the gas tank, and the system operates with steam in saturated conditions. As the power removed by the DHR exceeds the one removed from the SG, the secondary system starts to depressurize. If the non-condensable were not present, the depressurization would be fast, and the water temperature would decrease below the Pb freezing point. For this reason, the DHR system is equipped with the N_2 tank. Following the secondary system depressurization, the nitrogen contained within the gas tank starts to flow towards the IC, with a FR proportional to the pressure reduction. The non-condensable

concentration increases within the IC tubes, degrading the heat exchange. In this way, the depressurization rate is reduced, and safety conditions are maintained until the secondary system remains above 123 bar (corresponding to the water saturation pressure at the Pb solidification temperature). An in-depth analysis of the safety system is presented in Ref. [80].

The DHR system consists of two redundant and diversified systems. The first one is composed of three loops connected to the three SG in order to reduce the number of components within the RV. It is redundant itself, allowing the failure of one of the three loops. The second one is currently under development.

The computational activity, presented in section 5.2.3, aims to verify the safety cooling capability of this innovative system, under a protected station blackout.

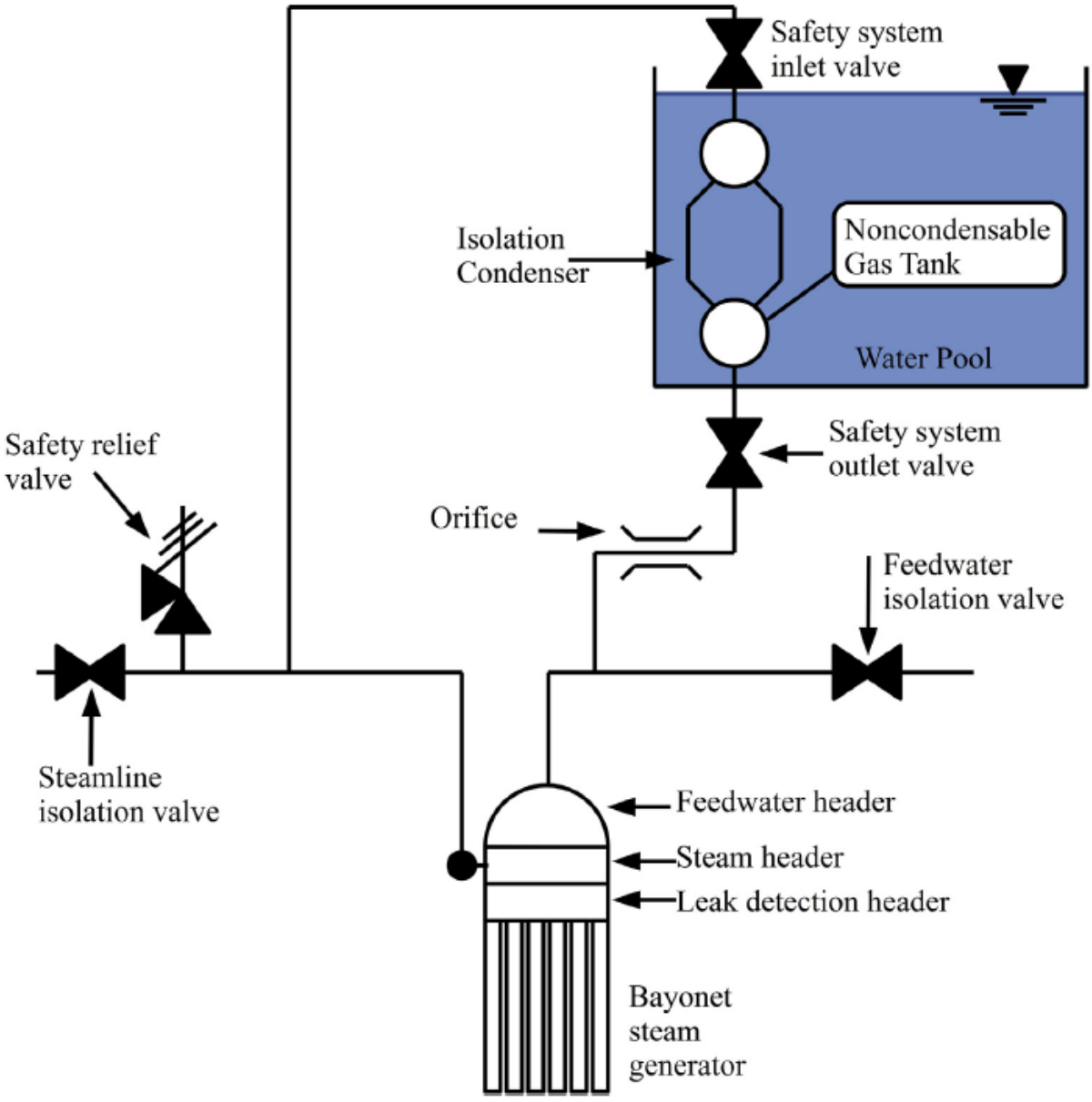

Figure 168. Layout of the DHR system [80]

5.2.2 Description of the thermal-hydraulic model

A detailed thermal-hydraulic model has been developed in order to evaluate the capability of the new configuration to lead the reactor in safety conditions after a postulated SBO accident.

The nodalization scheme basically consists in a three-dimensional and a mono-dimensional region, following the modelling approach validated within the Phénix dissymmetrical test benchmark (see section 3). The first one reproduces the pools and the core bypass and the second one simulates the rest of the system. Figure 169 shows the whole nodalization scheme and Figure 170 depicts the disposition of the main components within the RV.

Two MULTID components have been developed. The component 100 (green in Figure 169) reproduces the core bypass and the pool region below the reactor core. It is conceived to provide a detailed discretization of the pool region below the core. It is composed of 3 radii which delimit the regions of the inner active core (yellow in Figure 170), of the outer active core (red) and of the dummy elements (grey). The component is divided in 9 azimuthal sectors and 23 axial meshes, according to the reactor geometry provided by ANSALDO NUCLEARE. Concerning the core bypass, volume and junction factors have been calculated to take into account the volume occupied by the core assemblies. In order to obtain the reference mass flow rate through the bypass, junction factors and calibrated K-loss coefficients are introduced, simulating the presence of the lower grid. The second MULTID component (number 110 in Figure 169) reproduces the pools, in the region between the IS and the RV. In Figure 169, red lines represent the junction closed, to reproduce the characteristic geometry of the pools. In the upper part, the holes obtained on the IS allowing the Pb passage, are obtained with junction factors, calibrated in order to maintain the actual flow area at the correct axial level. The bottom volumes, depicted in gold in Figure 169, have been excluded from the computational grid closing all the junctions related to each face of the control volumes. In addition, along the RV boundaries, volume factors have been calculated to reproduce the actual Pb volume in the lower head of the reactor. The different regions of the pools, simulated by the MULTID component 110, have been highlighted with different gradations of yellow in Figure 169: the darkest one represents the hot pool (at the top of the RV), the medium one represents the intermediate pool (the region where the cold Pb exits from the SG and moves upwards towards the gas plenum) and the clearest one simulates the annular downcomer between the IS and the RV. The MULTID component 110 globally consists of 45 axial levels, 9 azimuthal sectors and 4 radii. The axial meshing, developed adopting the sliced modelling approach, maintains the relevant elevations of the reactor geometry provided by ANSALDO NUCLEARE. The mesh reference length adopted is about 200 mm; such a value allows an accurate evaluation of the thermodynamic properties variations along the flow path and limits the computational cost, although ensuring an accurate discretization of the large volume. The selection of radial and azimuthal meshing is related to the reactor symmetry. As shown in Figure 170, the azimuthal division has conceived to includes each relevant component within a single azimuthal sector. The radial discretization is basically related to the characteristic geometry of the pool; the first two radii are fixed by the hot pool dimensions and the third and the forth are defined by the annular region between the hot pool walls and the IS and between the IS and the RV. Calibrated volume and junction factors are inserted to consider the volume occupied by the internal components, including the second DHR system (under development), which is not simulated but its obstruction within the pool is considered. The primary loop obtained by the IS and the RV is completed with several cross junctions that connects the two MULTID components in the region below the core (see the black arrows in Figure 169).

The mono-dimensional region reproduces the main components of the reactor. Within the RV, the 1D model simulates the reactor core, the SGs, the primary pumps and the hot region above the core. SGs and PPs are separately simulated and connected in the correct region of the MULTD components. Hot lead, exiting the core,

is drawn by the three primary pumps; it moves upward through the PPs conduits and flows into the cold pool, passing through the PPs outlet holes, simulated by several cross junctions connected at different 5 axial levels. The PPs are simulated with R5-3D pump components, based on the information provided by ANSALDO NUCLEARE. The difference in altitude between PPs outlet and SGs inlet holes is conceived to avoid the thermal stratification establishment within the hot pool, exploiting the buoyancy of hot fluid. It moves upward and enters the SG unit; the steam generator modelling approach, verified with experimental data obtained from CIRCE campaigns (see section 2), is adopted for ALFRED SG: primary side is collapsed in a single equivalent pipe (per each SG) and bayonet elements are reproduced with two parallel pipes, simulating the descending tube and the annular riser. A fouling/plugging margin of 10 % is applied. In order to allow the possibility to perform calculations based on asymmetrical boundary conditions, the SG secondary sides are modelled separately and a set of three TDVs imposes the FW inlet conditions though each secondary loop, and other three TDVs fixe the steam outlet pressure. Steam line and FW line are intercepted respectively by steam and condensate lines of the DHR system. The modelling approach developed and verified within the PERSEO numerical activity (see section 4), has been adopted for the simulation of the safety system. The three DHR systems are separately modelled and each one is coupled with one of the three secondary loops. The isolation condenser is modelled with two pipes, simulating upper and lower manifolds, and a single equivalent pipe, simulating the IC bundle. The water pool is modelled with three parallel pipes connected with several cross junctions, reproducing buoyancy effects. The main differences between PERSEO and the actual configuration of ALFRED DHR are the actuation logic and the presence of the non-condensable tank. Concerning the actuation logic, this is provided by four valves, as presented in section 5.2.1. The time-dependent junction inserted downward the FW inlet TDV, carries out two functions: it simulates the operation of the secondary pump, setting feedwater flow rate in normal operation, and it operates as the FW isolation valve, stopping the secondary inlet flow rate after the postulated initiator event. The steam line isolation valve is modelled with a motor valve component, that closes after the initiator event, and the safety system inlet and outlet valves are simulated with trip valve components: the first one opens when the pressure on the secondary system reaches the actuation set-point (190 bar) and the second one opens after a defined delay. In addition, a motor valve component simulates the safety relief valve, opening when steam pressure exceeds 200 bar, discharging the steam towards the environment. The non-condensable tank is simulated with a vertical pipe and connected by an additional pipe to the lower manifold of the IC. During the full power operation, the DHR valves are closed and the IC and the non-condensable tank are filled by nitrogen at 110 bar. The 1D model is completed by the pipe 111 (see Figure 169), reproducing the hot region above the core, and by 5 additional pipes (not shown in Figure 169) that reproduce the Pb free level and the gas plenum in the upper region of the RV. The pressure of the gas plenum is controlled by a TDV. As presented in section 5.1.4, the hot region above the core plays a relevant role in the formation of the thermal stratification within the main pool. In the model presented in Figure 169, this region is simulated by a single pipe, accounting for the free volume between the assemblies. In this component, the thermal stratification model has been activated.

The active core region is divided in 18 sectors, consistent with the nodalization scheme of the MULTID component 100. The inner core is split in 9 azimuthal sectors, each one reproducing 1/9 of the whole inner zone. Eight equivalent pipes simulate eight identical sectors, connecting the inlet sections with the correspondent region of the MULTID component 100. The ninth sector is split in three parallel pipes, reproducing the hottest fuel pin, the hottest fuel assembly and the rest of the sector. The outer active core is simulated with 9 identical vertical pipes, consistent with the MULTID nodalization scheme. The reactor core modelling is completed by the SRs, the CRs and the dummy elements, collapsed in three equivalent pipes. The reactor power is supplied by several heat structures, implementing the radial distribution, based on Ref. [26], and the axial distribution, based on the information provided by ENEA Bologna.

The heat exchange between the main components are simulated with several heat structures, based on the reference geometry provided by ANSALDO NUCLEARE. For the preliminary calculations, the HTC is evaluated with the correlations implemented in R5-3D: Westinghouse correlation for bundle geometry and Seban & Shimazaki for non-bundle geometry [41].

The whole thermal-hydraulic model has been developed adopting the sliced modelling approach, using a mesh reference length of about 200 mm (the ratio between the length of adjacent nodes has been limited to 1.13), except for the hottest pin, where a more detailed nodalization has been applied in order to obtain a more accurate axial temperature distribution (meshing equal to 101.25 mm). All the local pressure losses have been simulated with K-loss coefficients, based on the reference geometry of the reactor.

The calculations related to the full power operation and to the postulated SBO accident, performed with the most recent thermophysical properties correlations of Pb [56] implemented in R5-3D as presented in Ref. [57], are presented in section 5.2.3.

In addition, the model has been improved with the subchannel analysis of the hottest FA; the nodalization scheme is the same presented above, except for the hottest FA (also including the hottest pin), whose nodalization scheme is presented in Figure 171. The subchannel modelling consists of an overall number of 252 parallel pipes, divided in:

- 6 inner subchannels (from 1 to 6 in Figure 171);
- 209 central subchannels (from 7 to 216);
- 36 lateral subchannels (from 217 to 252);
- 6 corner subchannels (from 253 to 258).

The modelling approach has been developed based on the numerical activity performed on CIRCE experimental data (see section 2). Several cross junctions connect adjacent subchannels at each axial level and the K-loss coefficients associated to the cross-flow have been calculated with the following equation, developed for *p/d* lower than 1.44 [55]:

$$K_{CF} = \left(z_p + 1\right) \cdot \left\{3.2 + 0.66 \cdot (1.7 - \bar{s})^{1.5} + \left(13.1 - 9.1 \cdot \frac{p}{d}\right) \cdot [0.8 + 0.2 \cdot (1.7 - \bar{s})^{1.5}]\right\} \cdot \varphi \cdot Re^{-0.27} \quad (12)$$

In accordance with Eq. 12, the form loss coefficient, dependent on flow conditions, assumes the following form:

$$K_{CF} = 4.79 \cdot Re^{-0.27} \quad (13)$$

The power distribution within the hottest FA has been implemented following the results presented in Ref. [26].

The main dimensions of the two thermal-hydraulic models are summarized in Table 22.

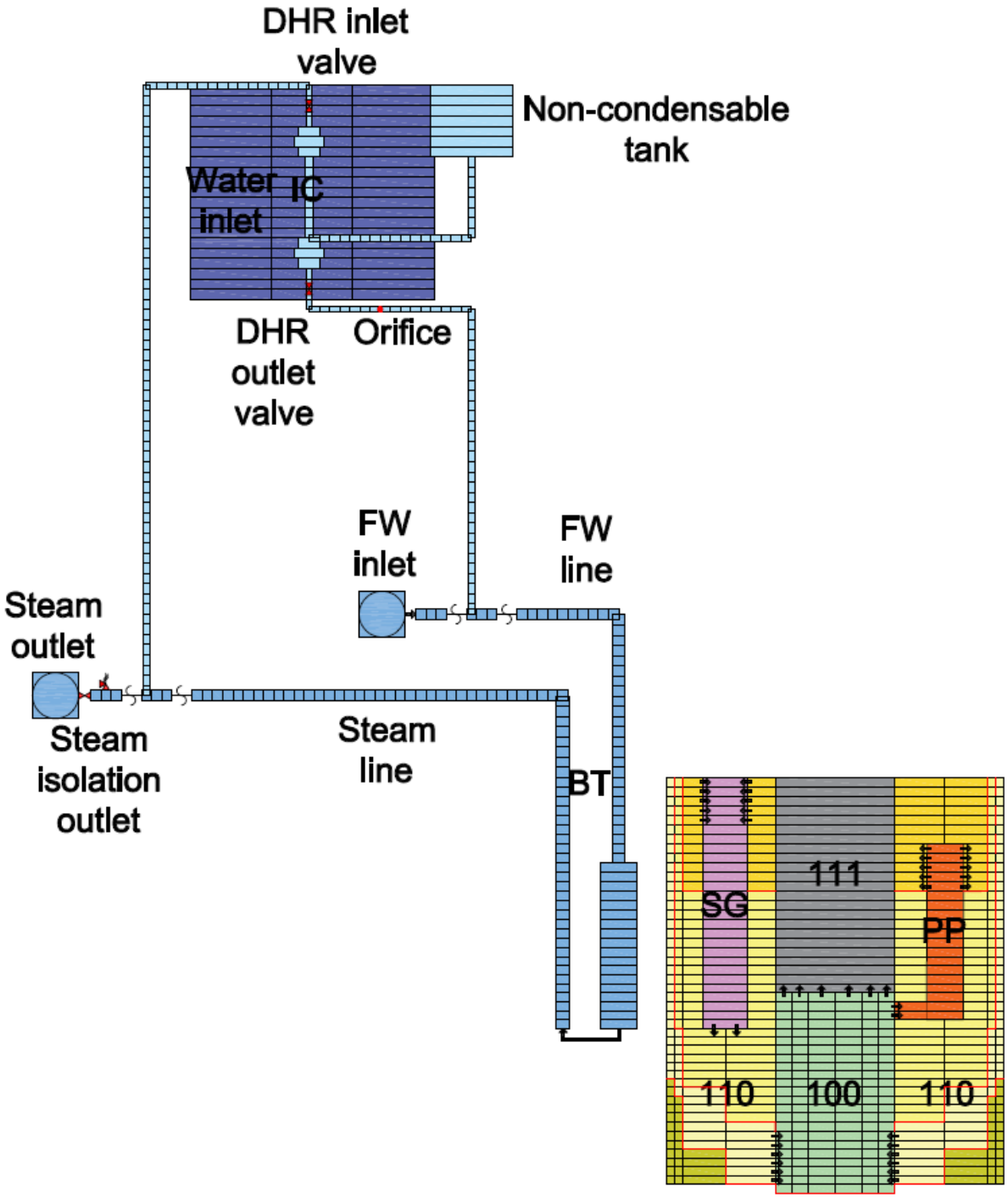

Figure 169. Nodalization scheme: ALFRED revised concept

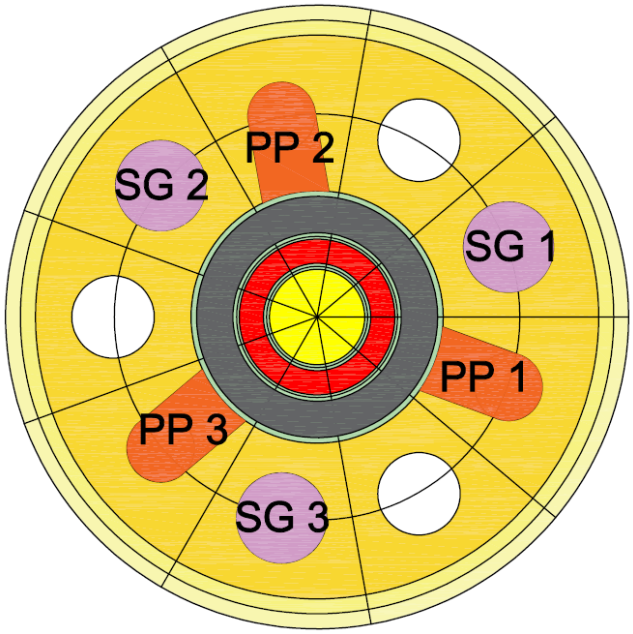

Figure 170. MULTID components: configuration

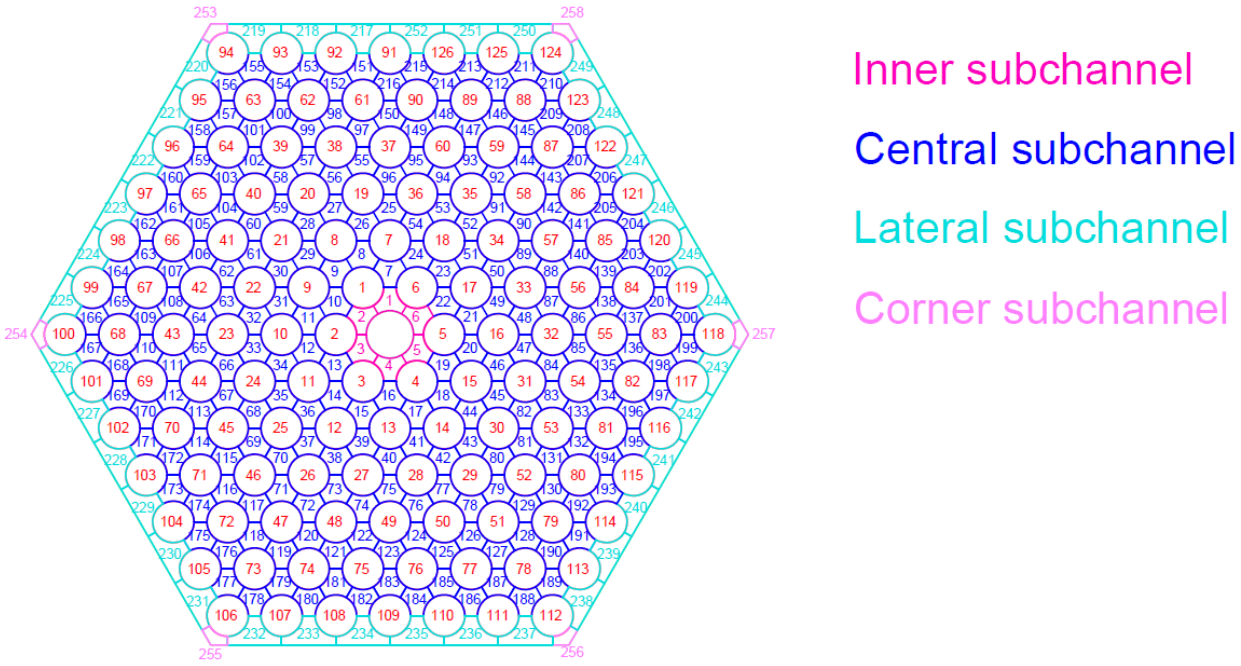

Figure 171. Subchannel modelling of the hottest FA

Table 22. ALFRED modelling: main parameters

Parameters	Reference model	Improved model
Number of hydrodynamic volumes	4036	5032
Number of hydrodynamic junctions	3759	6555
Number of heat structures	2254	3434
Number of heat structure mesh points	13728	27672

5.2.3 Simulations results

The numerical activity has regarded the stage 2 operation (see section 5.2). The fission power is 200 MW; it is supplied to the reactor core heat structures considering the power distribution presented in Ref. [26] (summarized in Table 23). The fission power is removed by SGs, each one fed by 44.3 kg/s of water, provided by a TDJ, at 608 K. Steam pressure is fixed to 175 bar by three TDVs at the outlet sections of the secondary loops (see Figure 169). The steam line isolation valve is initialized open and the two safety system valves and the relief valve are initialized close. The nitrogen pressure within the DHR system is set to 110 bar. In order to accelerate the convergence of the full power calculation, the hottest parts of the primary system (i.e. core outlet region, hot region above the reactor core and hot pool) are initialized at 753 K and the coldest one at 673 K.; the secondary system is set in thermodynamic equilibrium with the primary conditions. The initial mass flow rates through the primary and the secondary systems are null and the pressure within the primary system are inputted evaluating the gravitational effect.

Table 23. Boundary conditions: power distribution

Core zone	Thermal power (MW)
Inner core	95
Outer core	101
CR & SR	1.13
Dummy elements	2.07
Bypass core	0.8
Total power	200

Table 24 summarizes the main results of the full power steady-state calculation, obtained with 8000 s of problem time. The primary mass flow rate flowing through the reactor core is 17361 kg/s, increasing the temperature from 673.8 to an average value of 753.8 K (in accordance with the reference values, see Table 21). The coolant maximum temperature reached through the hottest subchannel is 795.6 K (close to the reference value presented in Ref. [98]) and the maximum cladding temperature is 820 K (below the limit of 823 K [26]). The hot primary coolant is drawn by the three primary pumps and it is collected within the hot pool. The difference between the average core outlet temperature and the Pb temperature at the inlet section of the SGs (about 1 degree) is due to the heat losses towards the cold pool. Each steam generator removes about 66.7 MW, decreasing the temperature of the primary coolant to 673 K. Heat losses from the hot walls determines the temperature difference of about 1 K between the SG outlet and the core inlet. On the secondary side, steam at 175 bar and 707.6 K is produced.

The total pressure drops through the primary system are calculated equal to 2 bar. According to the reference data [26], the primary flow rate through the core, also considering gagging, determines pressure losses equal to 1 bar. Concerning the SG, on the primary side the pressure drops are evaluated equal to 0.4 bar, and on the secondary side, the pressure drops across the bayonet elements are 0.75 bar.

One of the main objectives of the revised configuration of ALFRED was to avoid the thermal stratification establishment within the cold pool. The R5-3D calculation demonstrates the capabilities of the new concept; Figure 172 represents lead temperature within the RV, at full power steady-state conditions. The schematic view shows a relevant section of the RV, including the reactor core, one PP (on the left) and one SG (on the right). Comparing Figure 163 and Figure 172, the improvements allowed by the new reactor concept are highlighted: thermal stratification phenomenon is avoided in both the hot and cold pool. The level difference between the region above the core and the hot pool are determines by the pressure drops across the primary flow path.

Table 24. Full power calculation: steady-state results

Parameter	Unit	Value
Total primary mass flow rate	kg/s	17361
Core inlet temperature	K	673.8
Average core outlet temperature	K	753.8
Hottest subchannel outlet temperature	K	795.6
Maximum cladding temperature	K	820.0
Average SG inlet temperature	K	752.6
Average SG outlet temperature	K	673.0
SG power removed	MW	66.7
Pressure losses through the core	bar	1.00
Pressure losses through the SG (primary side)	bar	0.40
Total pressure losses through the primary system	bar	2.00
Pressure losses through the SG (secondary side)	bar	0.75
Steam temperature	K	707.6

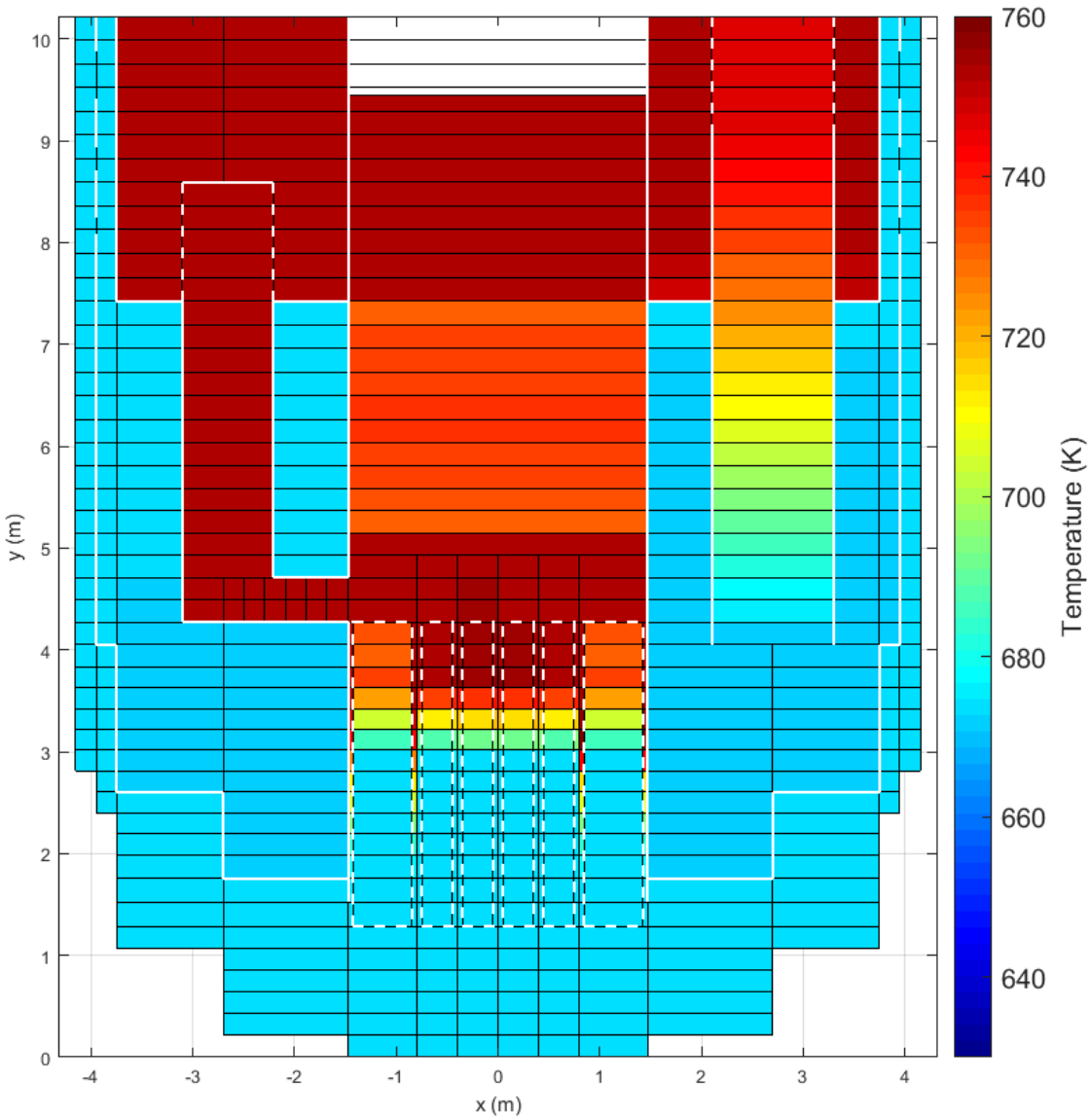

Figure 172. Full power steady-state condition within RV

Starting from the full power steady-state conditions, the transient test has been carried out. The transient simulation consists in a protected loss of offsite power (PLOOP), assuming the loss of power supplied to the primary and secondary pumps and the closure of the FW and steamline isolation valves, supposing a closure time of 2 seconds. The closure of the FW isolation valve is reproduced reducing to zero the mass flow rate imposed by the TDJs. The SCRAM command is supposed to occur with a delay of 1 s from the initiator event, considering the delay of the actuation system and the time required for the control rods insertion. The thermal power supplied to the core during the residual decay heat is shown in Table 25. During the PLOOP accident, one of the three loops (system 3 in the following analysis) composing the DHR system is supposed to be out of service; the

two isolation valves of this system close following the initiator event but the safety system inlet and outlet valves remain close over the whole transient, therefore the safety relief valves are triggered.

Table 25. Power fraction during the accidental scenario

Time from SCRAM (s)	Power fraction
0	100.00 %
1	6.70 %
60	3.96 %
600	2.60 %
3600	1.56 %
10800	1.12 %
36000	0.76 %
86400	0.61 %
259200	0.61 %

The initial conditions within the DHR system 1 are presented in Figure 173, showing the non-condensable fraction within the portion of the loop between the two points where the DHR streamline and condensate line intercept the main steam line and the FW inlet line. Figure 173 shows that, at the beginning, water and nitrogen are separated by the DHR valves: the steam line and the condensate conduit are filled by water and the IC and the non-condensable tank are full of nitrogen. As the isolation valves of the three secondary systems close, the secondary pressure starts to increase, reaching in few seconds the actuation set-point of the DHR inlet valve, fixed to 190 bar. Figure 174 shows the pressure within the three secondary loops in the first 250 s of the accident. At 3.2 s, the pressure reaches 190 bar, causing the opening of the DHR inlet valves of the systems 1 and 2; the third system is supposed out of service and the safety system inlet valves remains closed, leading to the pressure increase up to the safety relief valve opening set-point (200 bar). The consecutive openings and closures of the safety relief valve limit the pressure increase in the first minutes of the transient. Following the DHR inlet valves opening, the pressure within systems 1 and 2 quickly decrease down to the minimum value of about 151 bar. As the isolation valves close, the power removed by the SGs starts to decrease (see Figure 175), due to the reduction of the secondary flow rate. The DHR inlet valve opening, in systems 1 and 2, causes a fast increase of the secondary flow rate through the bayonet tubes, increasing the power removed by SGs 1 and 2, as shown in Figure 175 (see the peak power occurring at about 5 s). In system 3, the power continues to decrease up to the first opening of the safety relief valve; at this time (10 s) the first power peak is visible in Figure 175 (green line), followed by other lower peaks, related to the consecutive openings. The quick steam production within systems 1 and 2 leads to the pressurization shown in Figure 174, reaching the first equilibrium value. At this time, the safety system outlet valve is still close and steam pushes nitrogen into the non-condensable tank, due to the pressure difference. This condition is presented in Figure 176: steam fills the upper header and nitrogen is pushed within the non-condensable tank. When the DHR outlet valve opens (200 s after the opening of the DHR inlet valve), steam flow rate starts to increase, up to the first balance value of 1.43 kg/s. The mass flow rate across the secondary system 1 is shown in Figure 177. A first equilibrium condition is reached when the pressure within systems 1 and 2 assumes the almost constant value of 186 bar (see Figure 178, showing the pressure trend in the long term). In this phase the steam flow rate is almost constant (Figure 177) and nitrogen concentration is null in the IC upper header and negligible in the top and medium zone of the IC bundle. It assumes significant values in the lower part of the bundle and into the bottom header (about 35 %). This condition is depicted in Figure 179, representing the nitrogen concentration at 1 h, which remains almost constant up to 9 hours.

The first equilibrium phase ends when the power exchanged by the IC exceeds the power absorbed by the SG. This condition lead to the condensation rate increase, causing the pressure decrease shown in Figure 178. The pressure decrease causes the nitrogen expansion, which moves from the non-condensable tank to the IC unit. At 13 hours from the beginning of the test, the nitrogen concentration increases within the bottom header and in the medium and lower part of the IC bundle, reducing the condensation rate and so the heat exchanged by the unit. At 46 h, the non-condensable concentration reaches 85 % in the bottom part of the IC.

As the power decreases, the mass flow rate through the secondary system reduces up to a new equilibrium value of about 0.5 kg/s. The pressure decreases to 180 bar (higher than the limit of 123 bar, see section 5.2.1), maintained up to 25 h, when a slight increasing rate is observed.

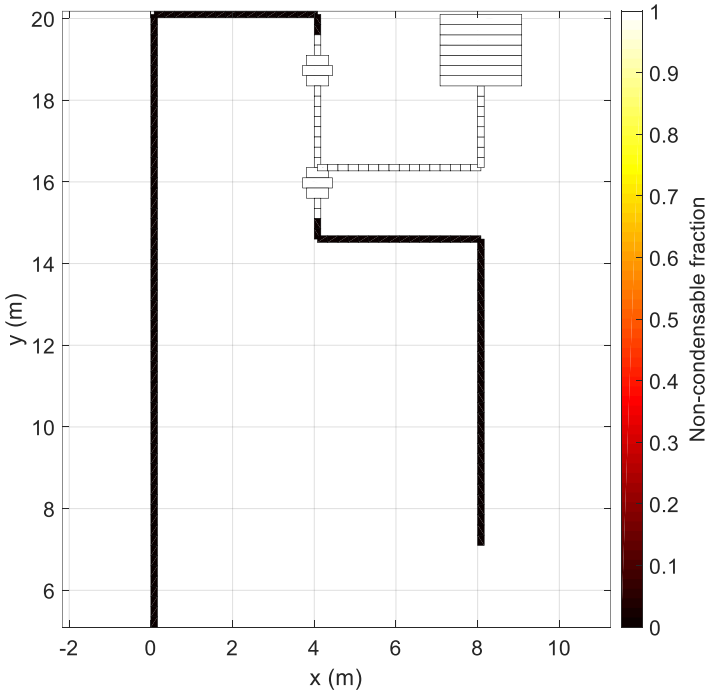

Figure 173. DHR system operation: initial conditions

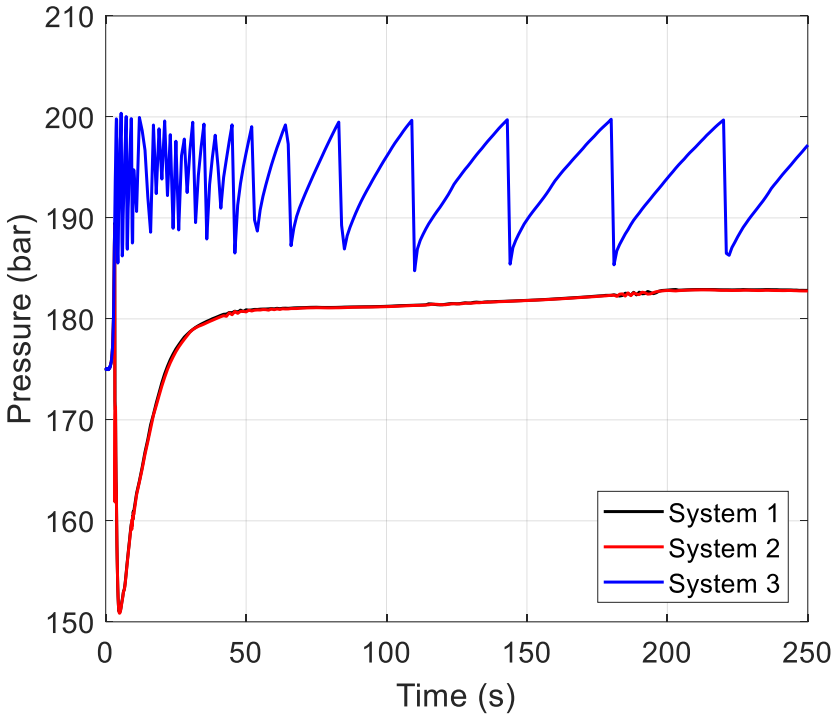

Figure 174. Pressure within the secondary systems: zoom on the firsts 250 s

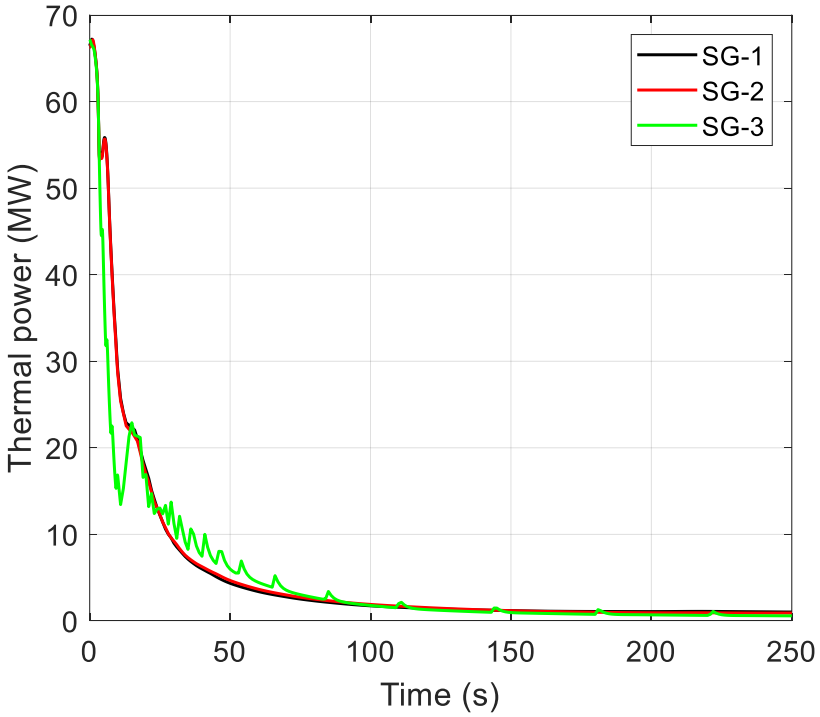

Figure 175. Power removed by the SGs: zoom of the firsts 250 s

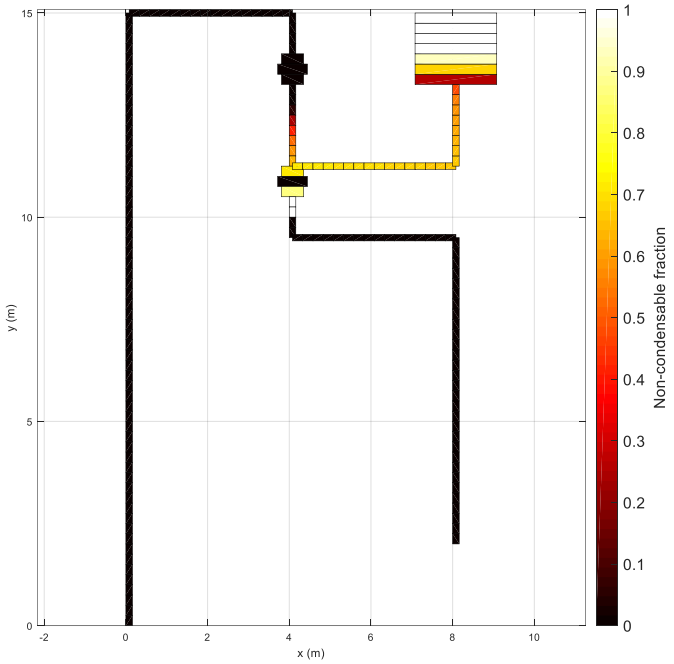

Figure 176. DHR system operation: 200 s

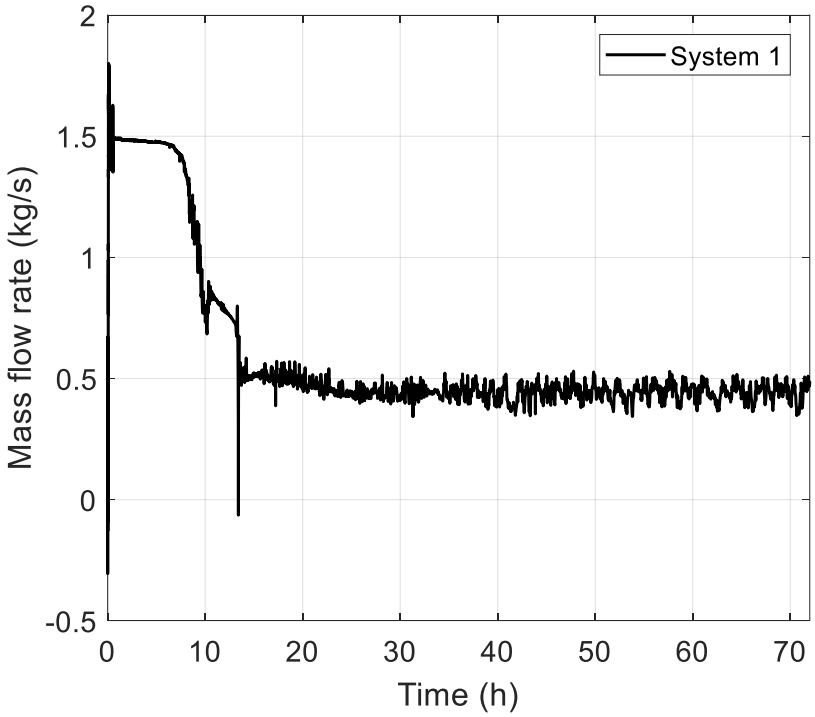

Figure 177. Steam flow rate across the secondary system 1

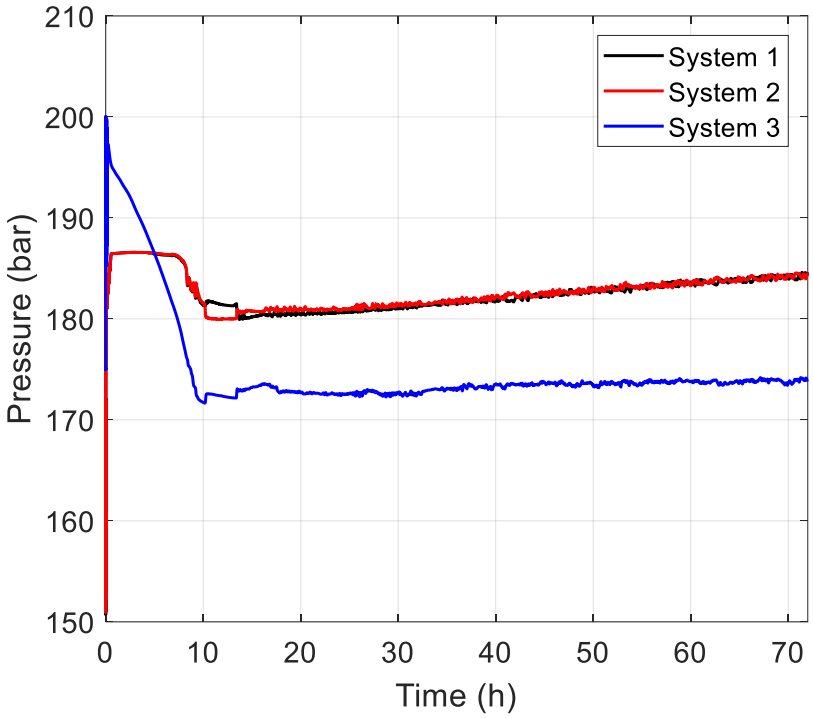

Figure 178. Pressure within the secondary systems

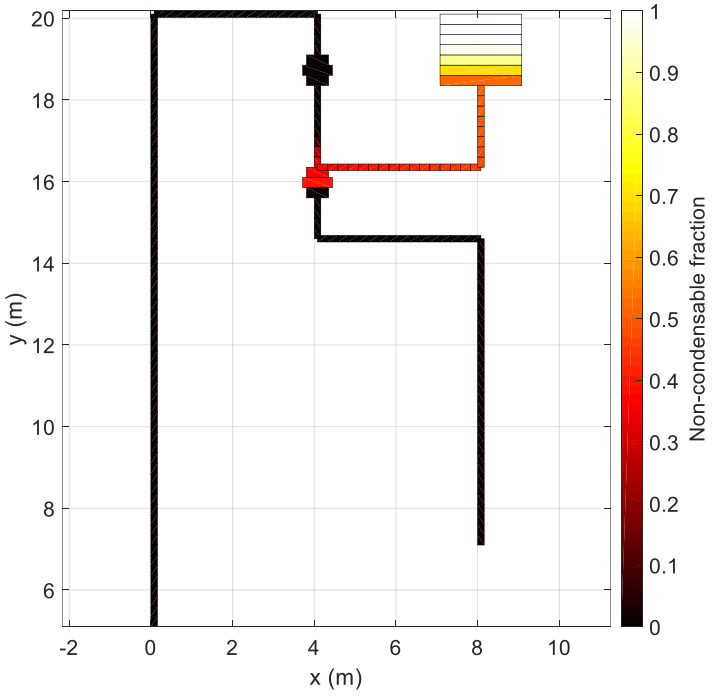

Figure 179. DHR system operation: 1 h

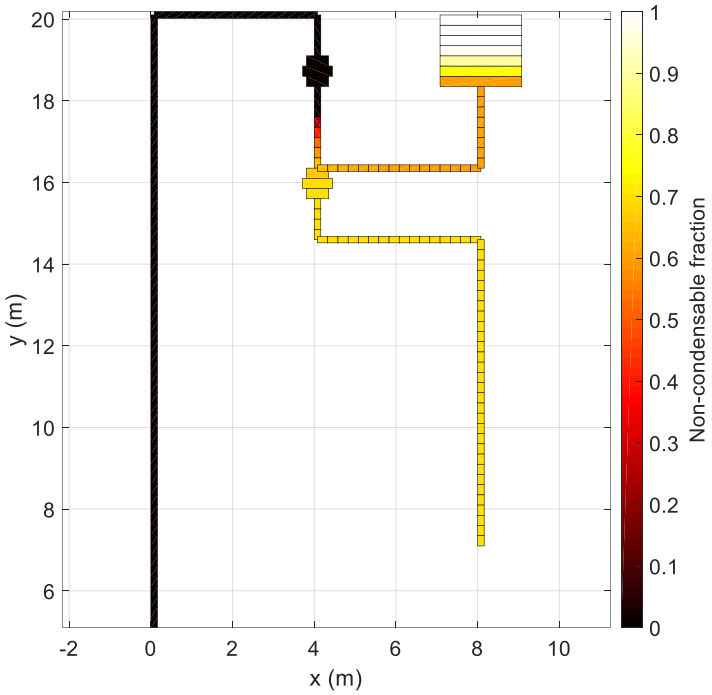

Figure 180. DHR system operation: 13 h

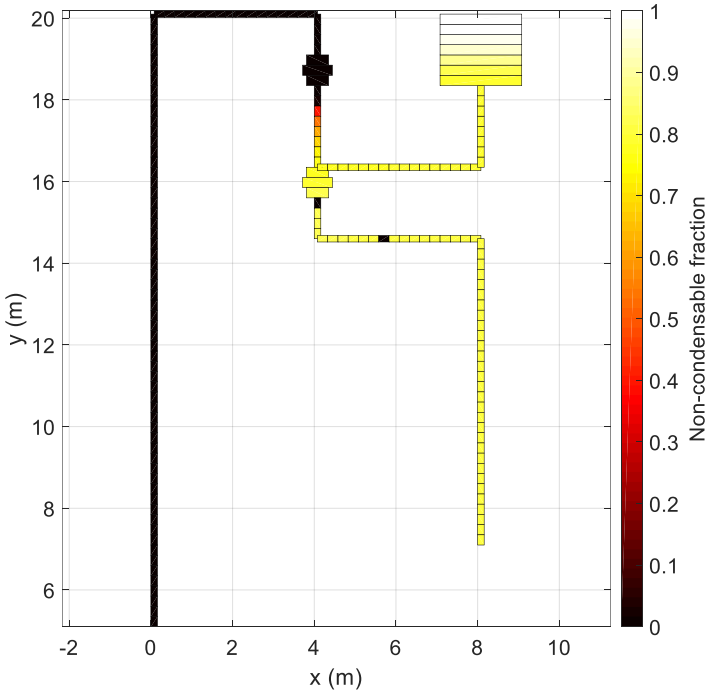

Figure 181. DHR system operation: 46 h

Figure 182 and Figure 183 compare thermal power removed by the three steam generators in the long term. As the pressure within the secondary system 3 decreases definitively below the safety relief valve set-point (see Figure 178), the coolant flow rate through the loop 3 is suppressed, and the power removed by SG-3 decreases to zero (see green line in Figure 183). The power removed by systems 1 and 2 follows the same trend of the secondary flow rate across the two loops; heat exchange assumes the almost constant value of about 1.85 MW up to 9 h. After the depressurization of the secondary systems and the consequent condensation degradation, the thermal power removed by the two SGs decreases to a new equilibrium value, equal to 0.61 MW (per each SG), balancing the residual decay heat (1.22 MW).

The natural circulation flow rate across the PP1 conduit is presented in Figure 184 and Figure 185. As the trip of the PPs occurs, the primary FR decreases, in accordance with the fission power reduction. In the first phase of the transient, the primary circulation is enhanced by the pump inertia; the minimum value of 240 kg/s (about 4 % of the nominal FR) is reached at 175 s (see Figure 184). At this time, the temperature difference between hot and cold lead decreases, as presented in Figure 186, where Pb temperatures at the SG inlet and outlet sections are shown in the first 5400 s of the transient. The peak temperature at the SG outlet is like the one analyzed in CIRCE-HERO activity (see section 2.2.3.3.1). As the power removed by the SG assumes the first equilibrium point, the temperature difference between hot and cold lead increases to the balance value of 28 K and the primary flow rate assumes the almost constant value of 310 kg/s, up to the depressurization of the secondary system. After that, a new equilibrium point is reached; the degradation of the condensation rate into the IC leads to the balance between the power removed by the DHR system and the decay power. Therefore, the temperature within the primary system assumes almost constant values, the temperature difference between the hot and cold Pb decreases to about 10 K (see Figure 187) and the primary MFR is reduced to the new equilibrium value of about 210 kg/s.

Figure 188 compares the feedwater temperature at the inlet of the BTs with the temperature acquired at the bottom of the annular riser and with the steam temperature at the BTs outlet. In the presence of non-condensable, water condenses at its partial pressure, depending on the nitrogen concentration within the IC bundle. Up to 9 hours from the beginning of the transient, nitrogen concentration is negligible, and condensation practically takes place at the total pressure of the system. In this phase, the DHR system operates mainly with steam. In Figure 188, the red line represents the temperature of the steam exiting the bayonet elements, which is in superheated conditions in the first 9 hours. It moves through the steam line and condenses, flowing across the IC tubes. Subcooled water exits the IC and flows towards the SG inlet (see the black line). The liquid water descends in the inner tube of the bayonet element, where it is preheated by the steam flow within the BT annular riser, reaching saturation conditions at the end of the descending side. After the depressurization of the system, due to the relevant nitrogen concentration within the IC bundle, water temperature at the outlet of the IC is significantly lower. Figure 188 shows that FW enters the BT at about 564 K (black line), equal to the saturation temperature at the water partial pressure, lower than the lead solidification point (about 600 K). Flowing through the BT descending side, the water is preheated, reaching the saturation temperature correspondent to the total pressure (nitrogen concentration is zero at the BT bottom), equal to 630 K (see blue line). Therefore, if in normal operation the heat exchange between descending tube and annular riser determines efficiency decrease, due to the steam condensation on the outer wall of the inner tube, in accidental scenario it assumes a relevant safety role, avoiding lead freezing and limiting the lower temperature to 630 K.

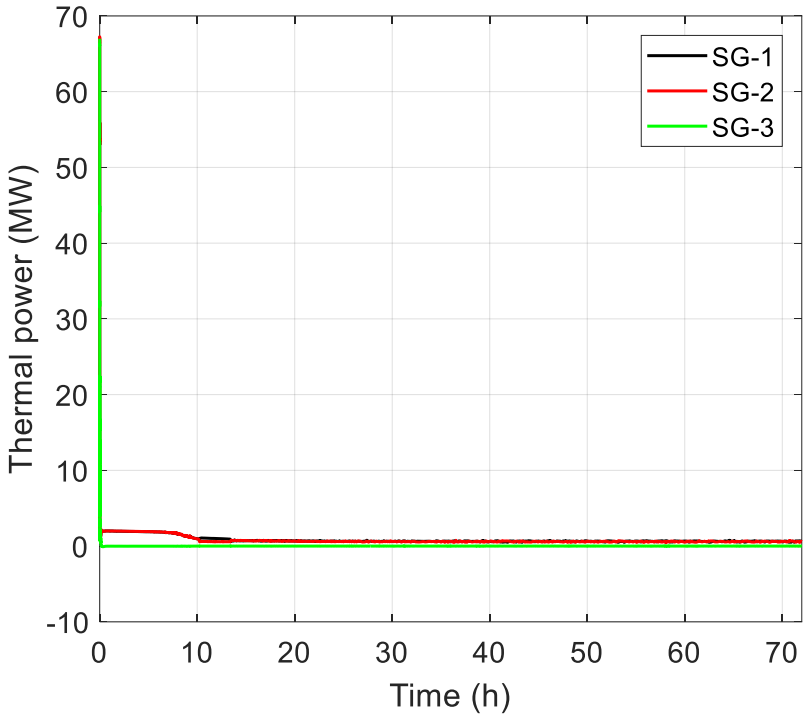

Figure 182. Power removed by the SGs

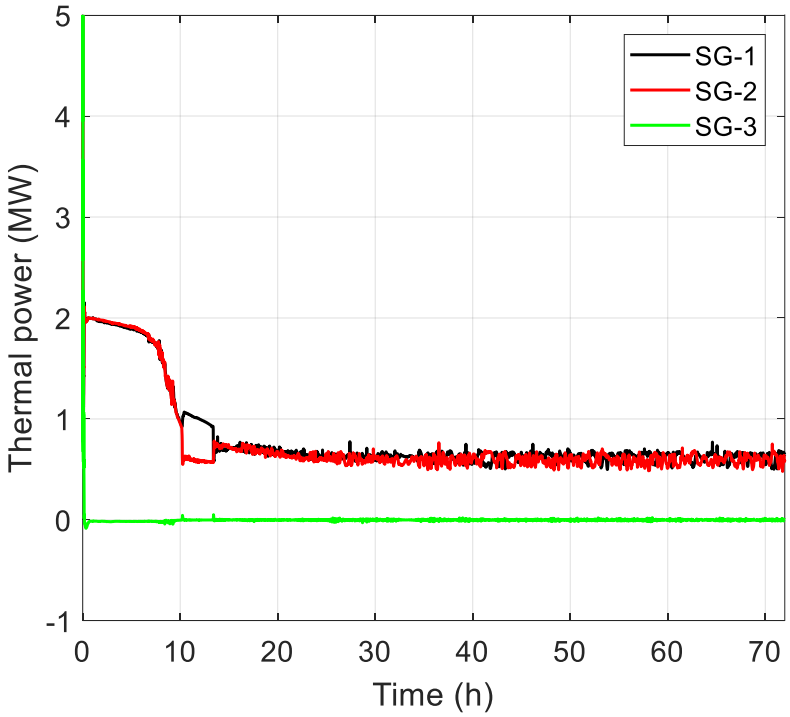

Figure 183. Power removed by the SGs: zoom on y-axis

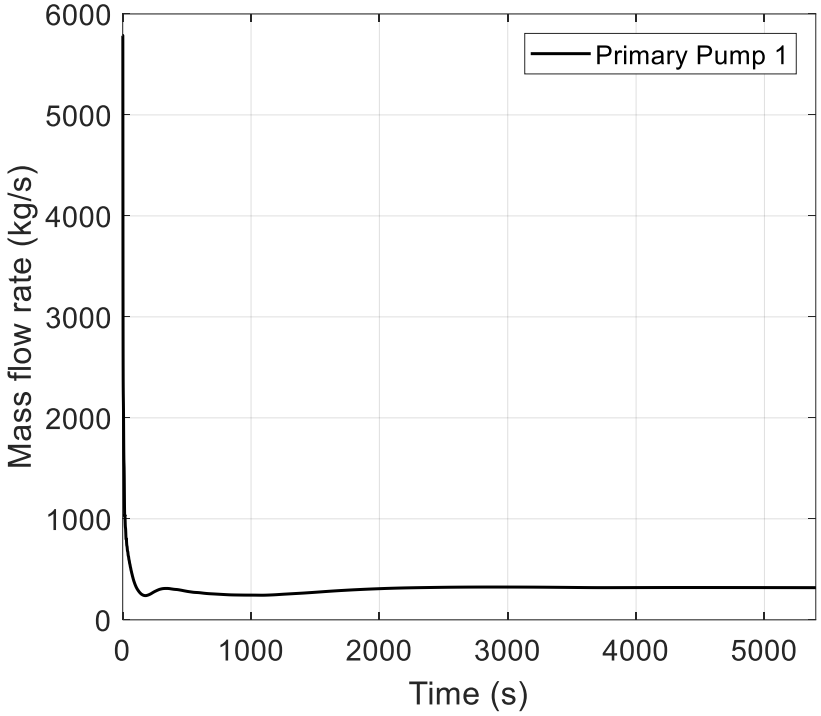

Figure 184. Primary mass flow rate: zoom of the firsts 5400 s

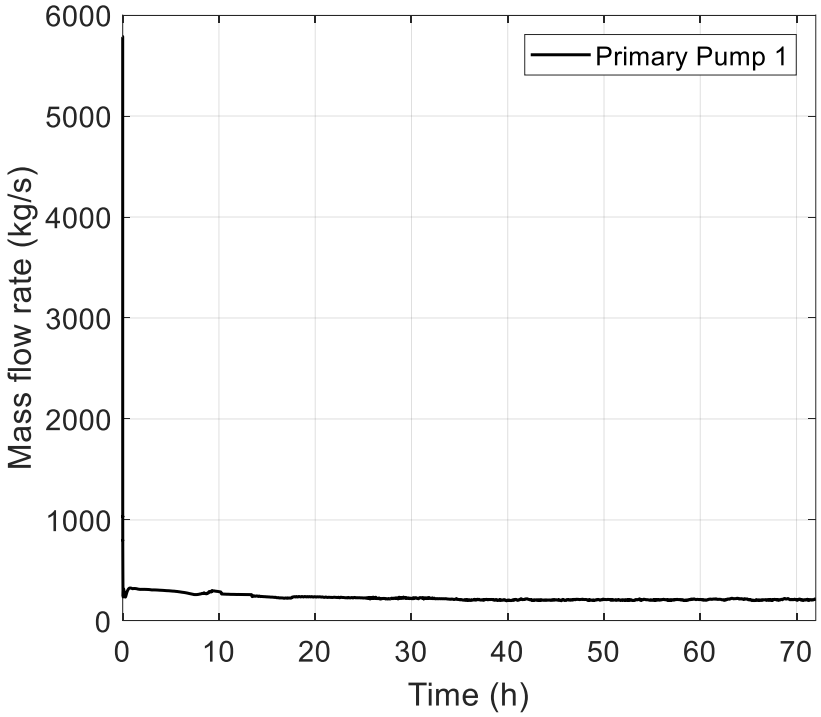

Figure 185. Primary mass flow rate

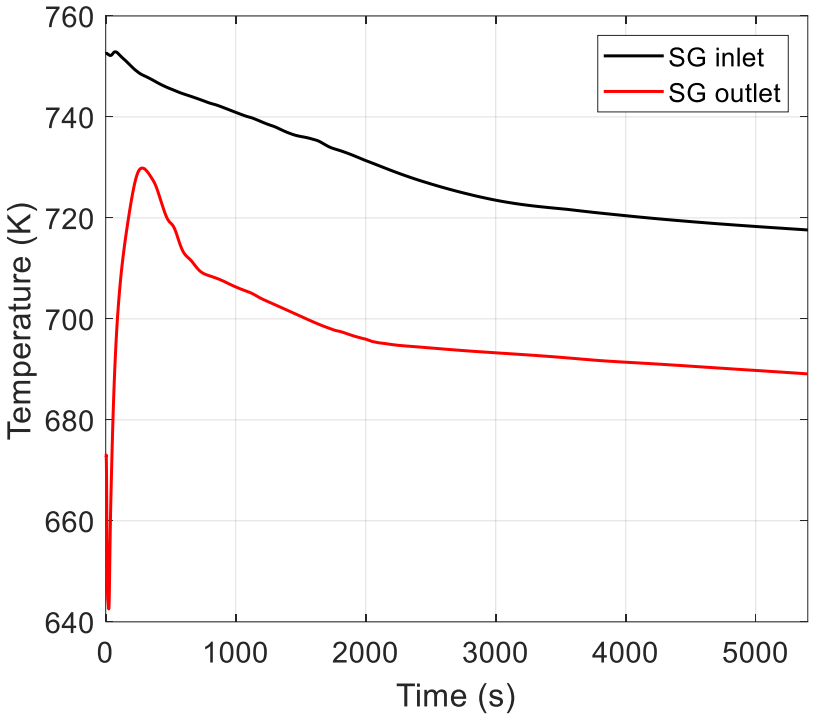

Figure 186. Pb temperature drop across the SG: zoom of the firsts 5400 s

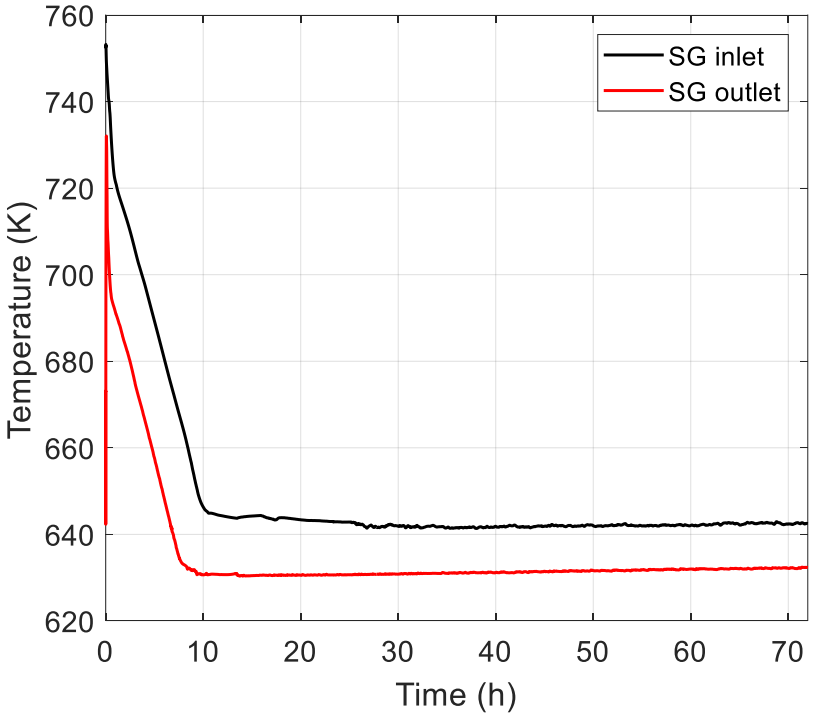

Figure 187. Pb temperature drop across the SG

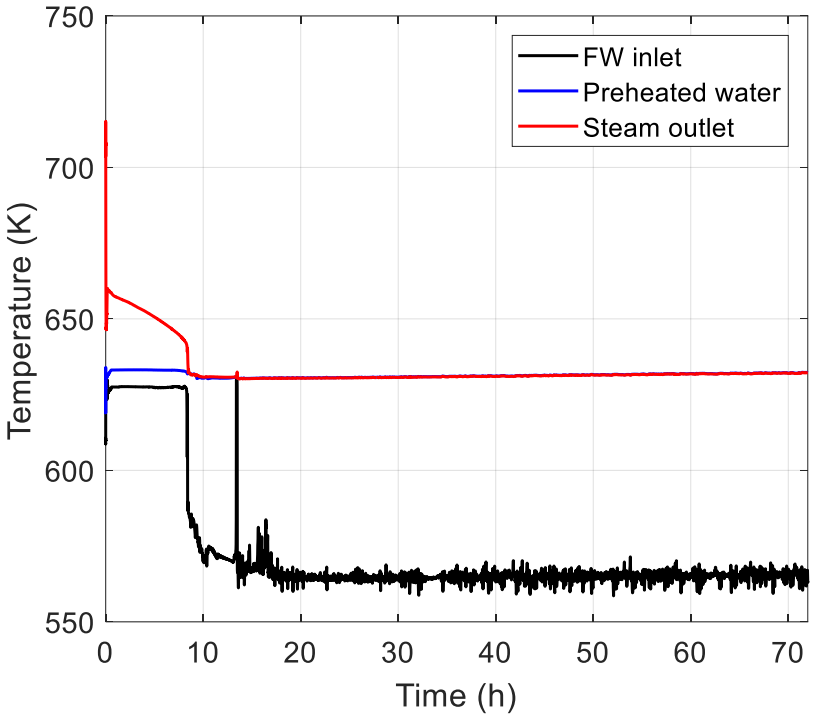

Figure 188. Water temperature through the bayonet elements

Figure 189 shows the coolant average temperature at the inlet and outlet sections of the inner core. Except for the firsts seconds of the transient, when outlet temperature increases as a result of the PPs trip and SCRAM delay, the trend is similar to the one observed at the SG. In the first phase, when the IC heat exchanged exceeds the decay power, the temperature decreases; after the depressurization of the secondary system, the temperature remains almost constant over the whole transient. A detailed analysis of the core outlet temperature is presented in Figure 190 and Figure 191, where the Pb average outlet temperature is compared with the coolant temperature at the hottest FA and pin and with the maximum cladding temperature. Figure 190 shows the first 250 s of the transient, focusing on the temperature increase that characterized the very beginning of the accident. The maximum temperatures obtained by the calculation must be compared with the reference limits, presented Ref. [98] and reported in Table 26, where the maximum temperature conditions and the corresponding holding times are summarized for three relevant regions of the reactor, under accidental conditions referred to the stage 2 operation. As observed in Figure 190, the maximum cladding temperature reaches 871 K (lower than 923 K, see Table 26), remaining only for few seconds. The holding time is a relevant parameter in the identification of the maximum allowed temperature. Indeed, due to the chemistry kinetics related to the corrosion phenomena, temperature characterized by short holding times can be neglected. In addition, the maximum cladding and Pb temperatures across the hottest pin are conservative, neglecting the mass transfer through adjacent subchannels.

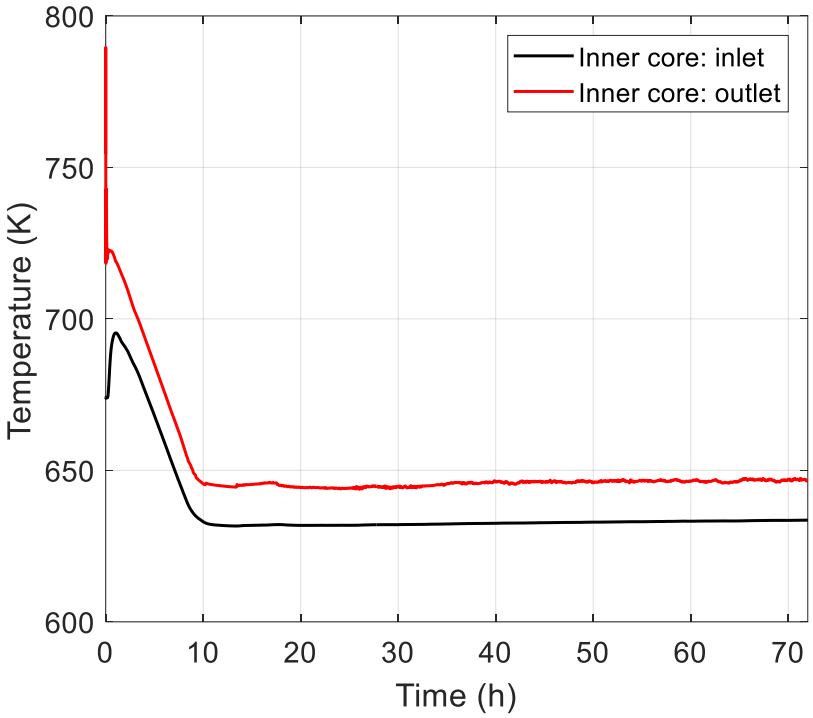

Figure 189. Pb temperature increase across the core

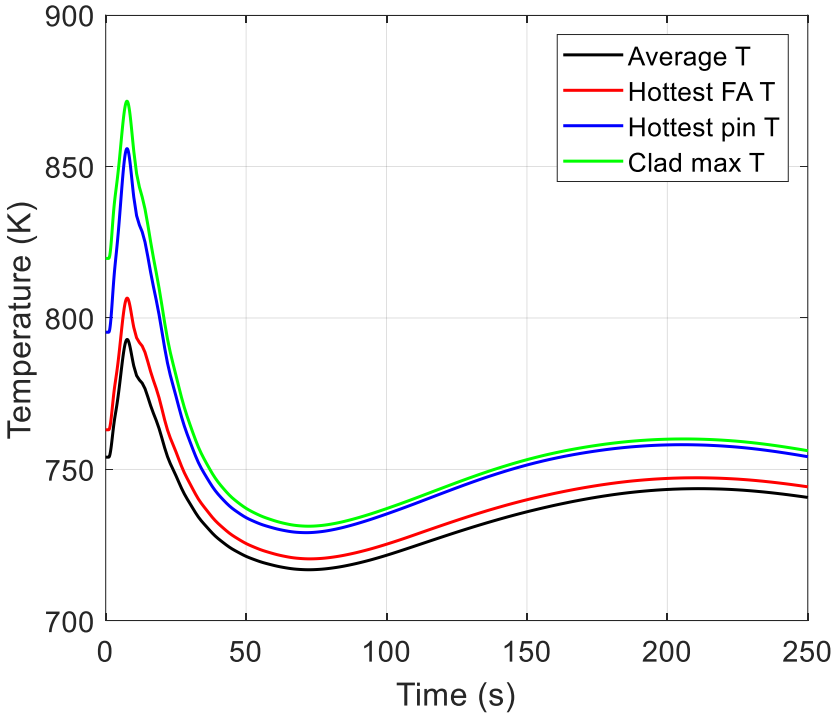

Figure 190. Core outlet temperatures: zoom of the firsts 250 s

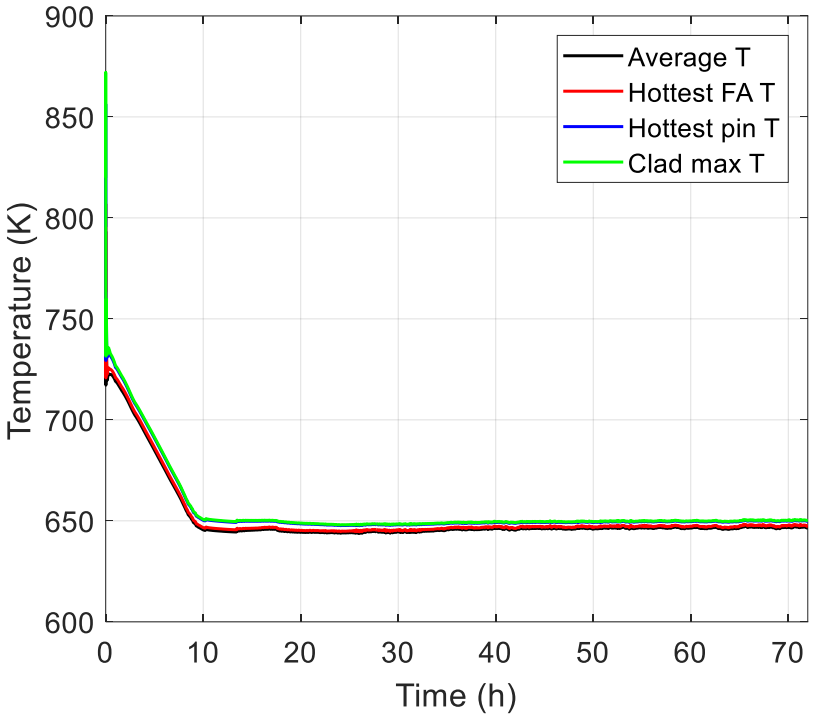

Figure 191. Core outlet temperatures

Table 26. Maximum temperature conditions and corresponding holding time in accident scenario (stage 2)

Region	Maximum temperature (K)	Holding time (h)
Hot spot	923	0.01
Hot pool	863	2.5
Cold pool	703	1000

Asymmetrical effects, related to the actuation of two of the three DHR systems, are analyzed in Figure 192 and Figure 193, where Pb temperatures calculated at the inlet and outlet sections of the three SGs are compared. In the first hour of the transient, asymmetrical effects are visible at the SGs outlets, where Pb temperature at the SG-3 outlet reaches a lower peak of 688 K (see green dotted line in Figure 192). In the long term, uniform conditions are restored (see Figure 193).

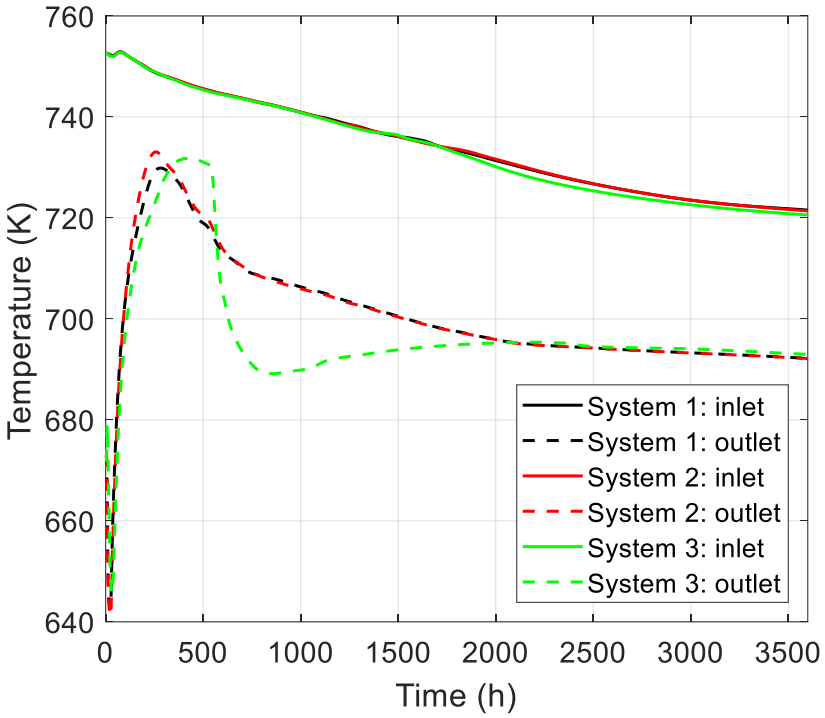

Figure 192. Asymmetric effects: zoom of the first hour

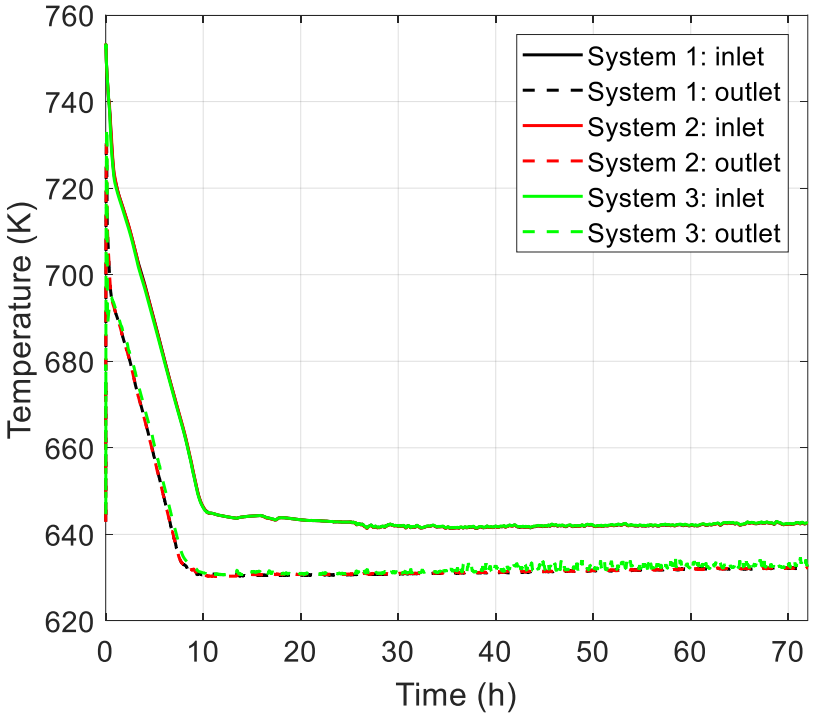

Figure 193. Asymmetric effects

Figure 194 shows the Pb temperature evolution within the RV. Immediately after the transition event, due to the primary MFR decrease, the level in the hot region above the core increases, and the intermediate cold pool is heated by the hot fluid exiting the SGs (see Figure 194 (a)). The hotter Pb, discharged within the intermediate cold pool, moves upward towards the holes obtained on the IS, and the bottom region of the pool remains cooler than the upper volumes. This is observed in Figure 194 (b), representing the condition after 1h. In this phase the hot pool starts to decrease its temperature following the cooling trend observed at the core outlet, and a slight thermal stratification phenomenon establishes in the lower plenum of the RV (about 15 K). After that, the whole system is progressively cooled reaching balance conditions (Pb temperature is constant between 10 and 50 hours, except for the region above the core, which is progressively cooled). Figure 194 demonstrates that the improved concept of the pool prevents the establishment of relevant thermal stratification also under natural circulation flow rate, following a postulated PLOOP.

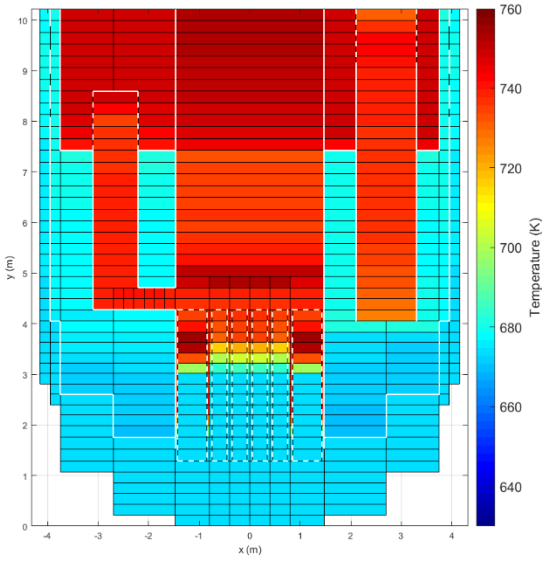

(a) 295 s

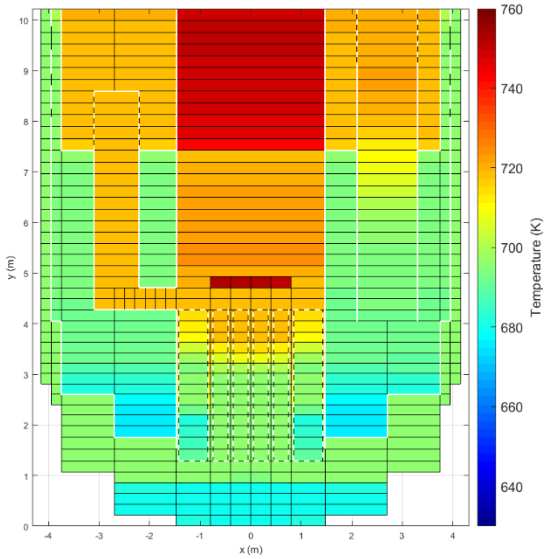

(b) 1 h

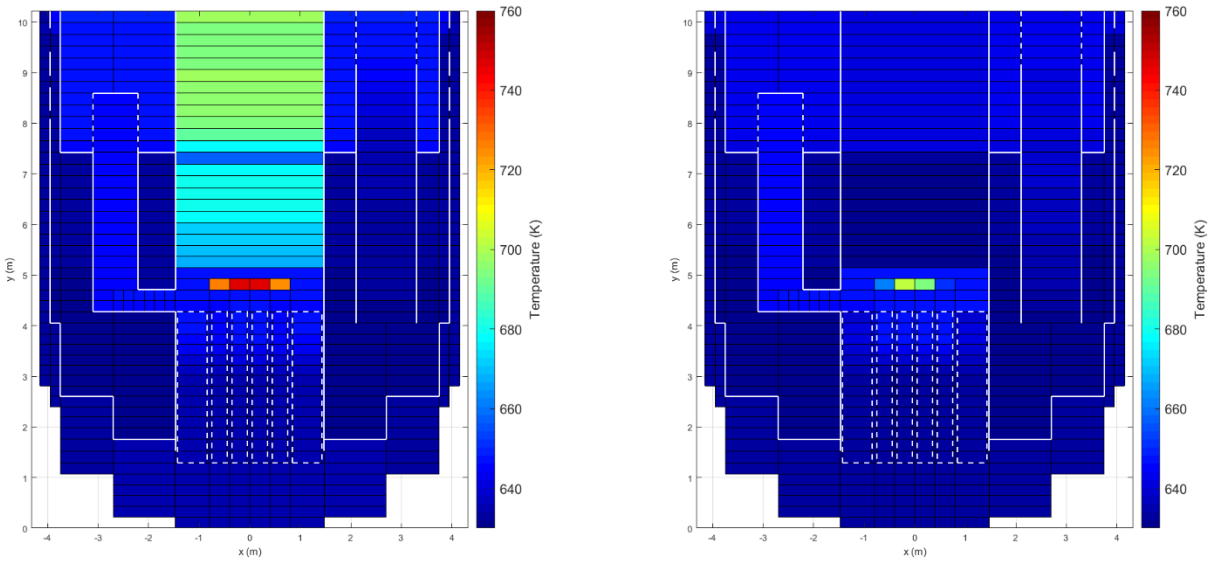

(c) 10 h (d) 50 h

Figure 194. Temperature evolution within the RV

In order to evaluate the effect of the heat and mass transfer between adjacent subchannels within the hottest FA, the transient calculation has been repeated with the improved model, presented in section 5.2.2. As expected, thermal-hydraulics of the whole system, during the postulated PLOOP accident, does not present considerable differences than the previous analysis presented above. The only discrepancies are observed in the evaluation of the maximum temperature calculated within the reactor core. The peculiarity of the FA, to includes a dummy pin in the center of the assembly, leads to the characteristic temperature distribution presented in Figure 195, determining a temperature difference between the inner subchannels and the adjacent ones of about 20 K. Figure 195 (a) shows the coolant outlet bulk temperature obtained at full power steady-state conditions. In this condition, the maximum coolant temperature is obtained equal to 785 K, 10 degrees lower than the one reported in Table 24. The peak cladding temperatures on the outer wall is calculated equal to 808 K (12 K lower than the one obtained with the simpler model). Immediately after the transition event, the core outlet temperature increases due to the PPs trip and the SCRAM delay. The maximum temperature conditions are shown in Figure 195 (b). At this time, the maximum bulk temperature and the peak cladding temperature on the outer wall are 839 K and 854 K, respectively 16 and 17 degrees lower the ones evaluated with the simpler model.

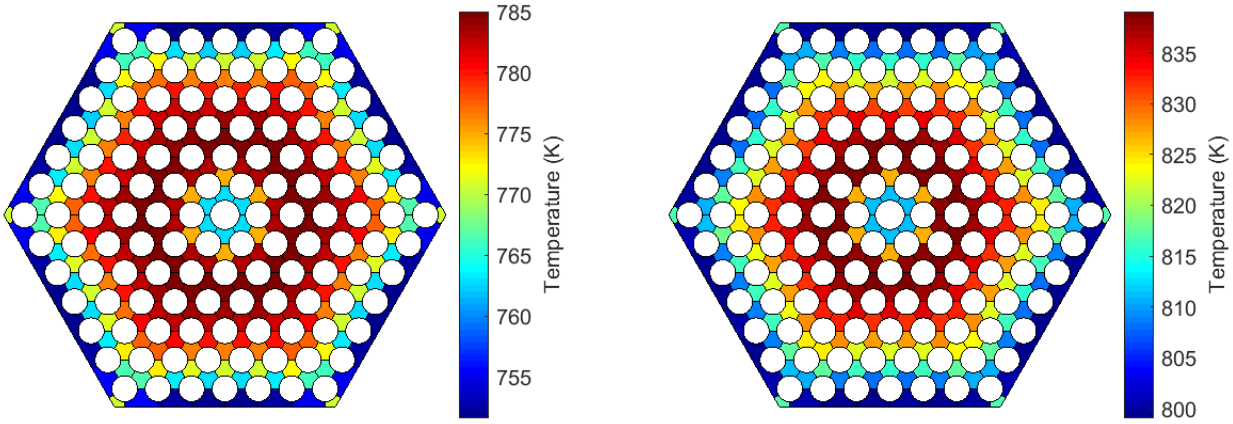

(a) Initial conditions (b) Maximum temperature

Figure 195. Pb temperature at the outlet of the hottest FA

5.2.4 Conclusive remarks

The computational activity has been aimed to investigate the thermal-hydraulics of the improved pool configuration proposed in the revision of ALFRED concept. The technical review of the reactor was based on the main outcomes obtained from LEADER project, which highlighted three main sources of concerns related to the ALFRED reference configuration:

- establishment of thermal stratification phenomenon within the cold pool;
- possibility to transport voids within the reactor core in case of SGTR accident;
- lead freezing in long term accident conditions.

The new configuration was improved by an internal structure which forces the cold Pb, exiting the SGs, to move upward, towards the coolant free level and, after that, passing through specific holes, to flow downward towards the core inlet. This simple scheme avoids the presence of Pb volumes that are not involved in the primary flow path, preventing thermal stratification formation. In addition, in the case of steam entrainment under SGTR scenario, the steam is transported upward by the primary FR and it is separated from the lead in the upper part of the RV, avoiding water ingress within the core. The third point conceives the capability of a passive safety system to modulate the power removed from the primary coolant, limiting the maximum temperatures in the first phases of a postulated SBO scenario and avoiding the lead freezing in the long term. A solution was proposed, introducing a non-condensable tank in the DHR system designed for the ALFRED reference configuration. It was based on the operation of an IC immersed in a water pool. The non-condensable tank allows to passively modulate the power removed by the DHR system, by injecting nitrogen within the IC bundle. The non-condensable flow rate in passively controlled by the pressure difference between the gas tank and the water system.

The improvements introduced in the revised concept must be verified by numerical activities. In this framework, UNIROMA1, in collaboration with ANSALDO NUCLEARE, has developed a detailed thermal-hydraulic model of the new configuration of ALFRED, mainly focused on the verification of the pool capability and on the safety operation in long term, after postulated PLOOP accident. The nodalization scheme presents a detailed

nodalization scheme of the pools and of the secondary systems, which are separately modelled including the safety systems.

The numerical activity demonstrates the improved pool thermal-hydraulics. In the revised configuration of the reactor, thermal stratification establishment has been avoided in both normal and accidental operations. Following the postulated accident, the new DHR system is able to restrict the maximum temperatures in the first phases of the transient within the technological limits. In the long term, as the depressurization of the secondary system occurs, nitrogen is injected within the IC bundle, degrading the heat exchange. This is enough to limit the power removed by the DHR system to the decay heat value, limiting the Pb minimum temperature to 630 K, about 30 K higher the Pb freezing point.

6 A METHOFOLOGY FOR THE UNCERTAINTY QUANTIFICATION BASED ON RELAP5-3D/RAVEN COUPLING

In the past, safety analysis was based on the application of conservative assumptions and models to evaluate safety margins in the NPP licensing process, especially in the phenomenological areas where the knowledge was not considered satisfactory. Application of such conservatisms determined large margins between the conservative evaluation of a safety parameter and the "real" value. This reflected on the NPP design, that had to consider too large safety margins, affecting the performances and the costs.

With the diffusion of the best estimate (BE) codes, an improved approach has been used in the licensing of the NPPs. The recent methodology is based on the application of the BE tools, combined with the identification of the uncertainties related to the computational results: the so-called Best Estimate Plus Uncertainty (BEPU) method [99][100][101].

This chapter aims to present a BEPU approach, based on the RELAP5-3D©/RAVEN coupling methodology, and the response using different validation metrics. For this purpose, the LBE-cooled loop-type facility, called NACIE (NAtural CIrculation Experiment), has been modelled at DIAEE of "Sapienza" University of Rome using RELAP5-3D© and a statistical analysis was performed with a RELAP5-3D/RAVEN coupled calculation. The results have been compared with the experimental data to evaluate the merit of the methodology.

6.1 Overview of the test facility and of the numerical model

NACIE is an LBE-cooled loop-type facility [102], designed and realized in the ENEA Brasimone RC for the characterization of components, procedures and systems related to the HLM nuclear technologies. The DIAEE of "Sapienza" University of Rome developed a mono-dimensional scheme to investigate the capabilities of R5-3D to reproduces relevant thermal-hydraulics of an HLM loop system. Figure 195 compares the schematic layout of the test facility (a) with the geometrical scheme developed with R5-3D.

The facility mainly consists of a primary LBE loop with a rectangular geometry, composed of two vertical pipes 7.5 m long, working as riser and downcomer respectively, connected by two horizontal pipes of 1 m, and a secondary water loop, acting as a heat sink. The main components are listed below:

- the fuel pin simulator, located at the bottom of the loop (see Figure 196 (a)); it consists of two electrical pins (total power of about 45 kW), supported by two additional dummy pins, as presented in Figure 197 (a);
- the tube-in-tube HX, located at the top of the downcomer; it consists of three coaxial pipes, as shown in Figure 197 (b), determining the LBE downcomer, the leaks monitoring system (pressurized helium plus stainless-steel powder) and the ascending water side. The HX is characterized by a thermal duty of 30 kW;
- the expansion tank, at the top of the riser; it allows the separation between LBE and Ar, injected downward the FPS to enhance primary circulation;
- the secondary pump, for the water circulation.

The thermal-hydraulic model reproduces the whole primary system and the HX secondary ascending side. It is composed of an overall number of 170 hydrodynamic volumes, 169 junctions, 174 heat structures and 3690 thermal nodes. A detailed description of the nodalization scheme is provided in Ref.

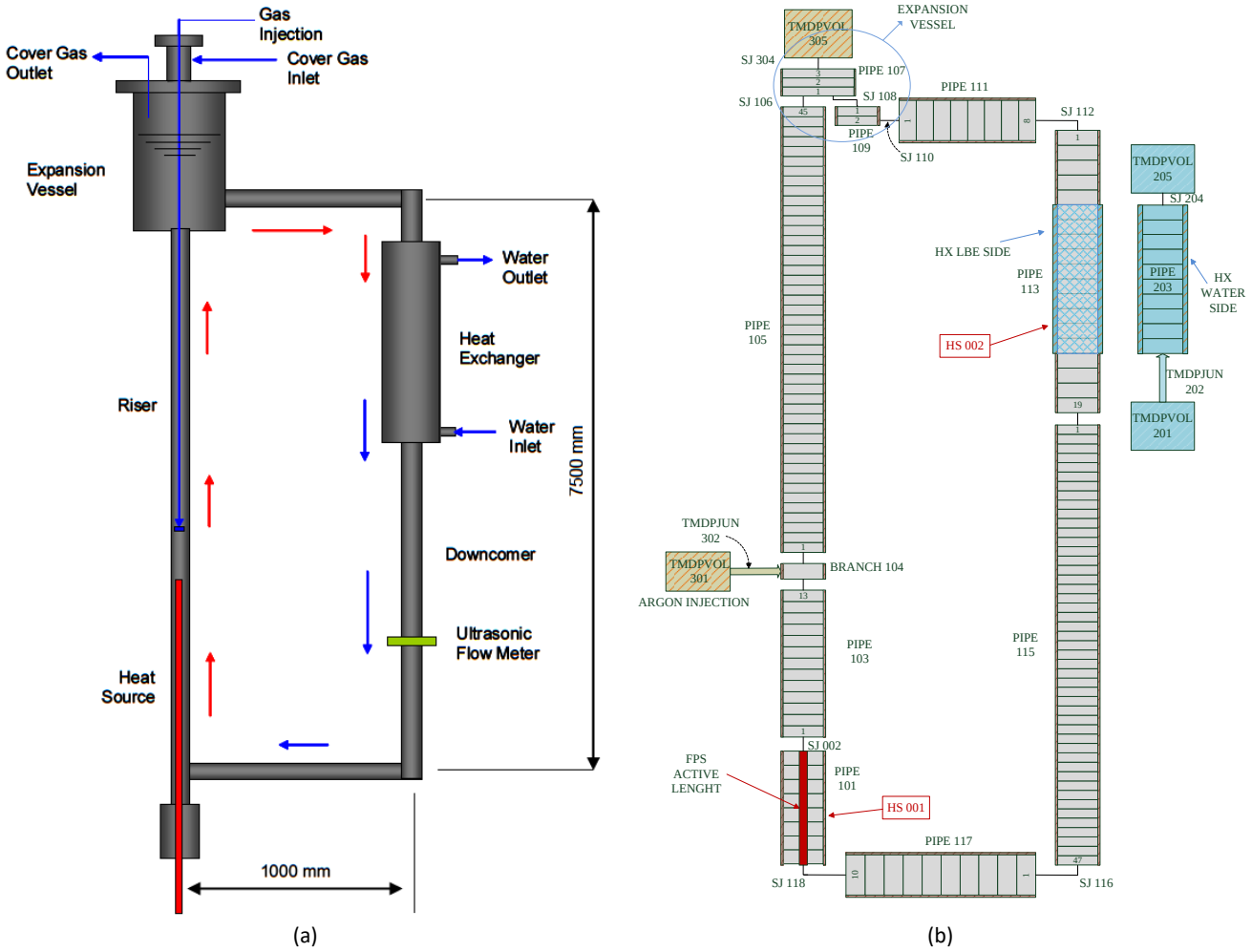

Figure 196. NACIE primary system: schematic layout (a) and nodalization scheme (b)

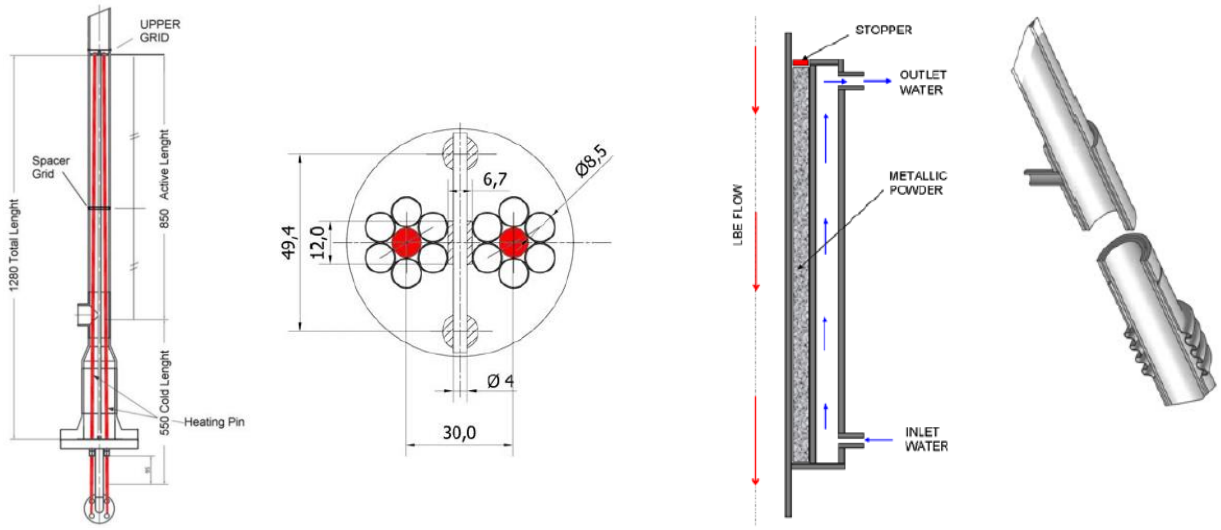

Figure 197. Schematic view of the FPS (a) and of the heat exchanger (b)

6.2 Experimental campaign

The experimental activity performed on the NACIE facility consisted in a series of tests aiming to investigate the system behavior in NC conditions, GEC operations and transition from GEC to NC (and vice-versa). Of the two electrical pins, only one has been activated on the tests with a maximum power supplied of 22.5 kW. In this work, two tests have been analyzed: Test 201 and Test 203, characterized by the boundary conditions reported in Table 27. Test 201 was aimed to characterize the LBE flow in case of pure natural circulation regime and Test 203 was aimed to investigate the system behavior under GEC regime and, afterwards, the transition from GEC to NC.

Table 27. NACIE test matrix

Parameter	Unit	Test 201	Test 203
Average LBE temperature	K	473-523	473-523
FPS Power	kW	9.5	9.5
Timing ramp	min	5	5
Gas lift	Nl/min	0	5
Heat sink	-	yes	yes
Transition from NC to GEC	-	no	no
Transition from GEC to NC	-	no	yes

6.3 Probabilistic comparison metrics

The validation of simulation codes (e.g. RELAP5-3D) is always a fundamental process in the development and assessment of the accuracy of the employed physical models. The state-of-art methodology is well described in Ref. [34]. Such an approach treats uncertainties individually (i.e. each uncertain parameter is considered distinctly from one another), while the RAVEN proposed methodology path performs the exploration of the input space considering the associated uncertainties altogether and analyzes the responses with several validation metrics. Uncertainties in the input space are taken into account separately from ones in the output space. Such distinction is performed employing sampling of the input space. Such capability, available in the RAVEN code, permits to compare a larger sample of data [35].

In order to assess the accuracy of the physical model under consideration, the inclusion of the experimental data uncertainties is fundamental. Those uncertainties are going to be directly mirrored in the input space of the experiment, being modeled with the system code under investigation. The uncertainties associated to the input space can be represented by Probability Density Functions (PDFs); when dealing with experiment uncertainties, it is common practice to use the following PDFs, sorted in ascending order of "knowledge" regarding the uncertainty sources:

- uniform PDF: used when no knowledge of the dispersion and mean of the data are available, but only the variation boundaries (i.e. lower and upper boundaries);
- triangular PDF: utilized when the variation boundaries and the most probable mean are known, but no information on the dispersion of the data are available;
- normal PDF: used when information about the mean and dispersion is available.

When the representative uncertainties have been selected, the physical model needs to be perturbed following a sampling strategy. Several sampling strategies are available in the RAVEN code. Traditionally, a Monte Carlo sampling is generally performed since completely independent (in terms of output figure of merit (FOM) convergence) on the number of the uncertainties to be propagated [104].

Once the uncertainties have been propagated employing a sampling strategy, the final goal of the validation assessment is the comparison of the results (output FOMs) with the experiment measured FOMs (including the associated uncertainties). In the RAVEN code, three main probabilistic comparison metrics are available: Cumulative Density Function (CDF) area metric, PDF area metric and the difference PDF metric [105]. In the following, a brief introduction of the three metrics is reported.

The CDF area metric, also called Minkowsky L1 metric, calculates the area difference between the code output CDF_c and the experimental CDF_e using the following equation:

$$d(CDF_c(x), CDF_e(x)) = \int_{-\infty}^{+\infty} \|CDF_c(x) - CDF_e(x)\| \, dx \tag{14}$$

This metric has the same units of the compared FOM *x* and it provides an estimation of the integrated distance between the simulated results and the experiment considering all the propagated uncertainties (see Figure 198).

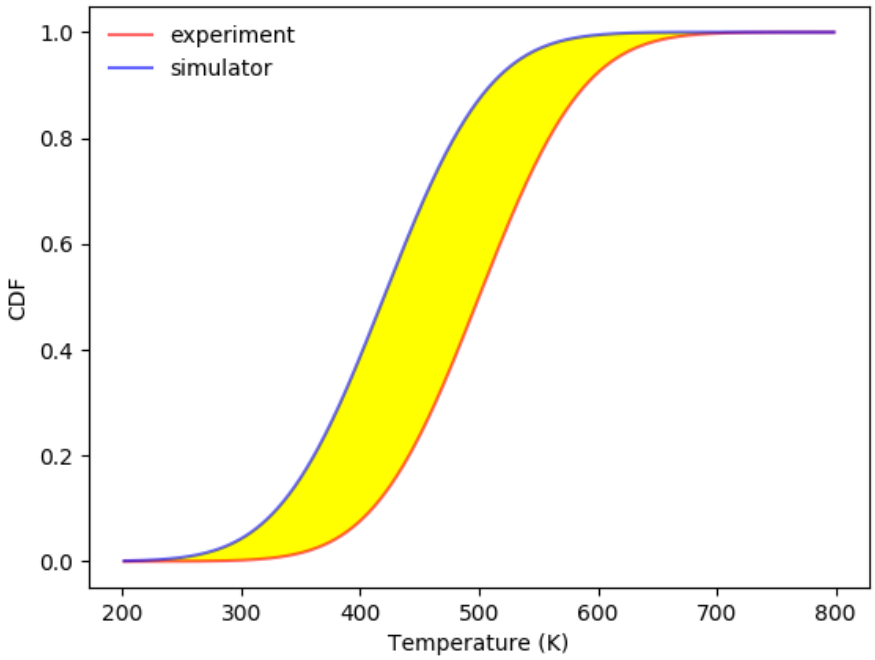

Figure 198. CDF area metric example

The PDF area metric is aimed to compute the degree of agreement between the PDFs constructed with the experimental and simulated data. It computes the common area between the two PDFs. The resulting computed metric varies between 0.0 (no agreement) to 1.0 (perfect agreement), following the following equation:

$$d_{p.u.}\left(PDF_c(x), PDF_e(x)\right) = \int_{-\infty}^{+\infty} min(PDF_c(x), PDF_e(x))\, dx \tag{15}$$

As graphically shown in Fig. 12, the PDF area is represented by the yellow region.

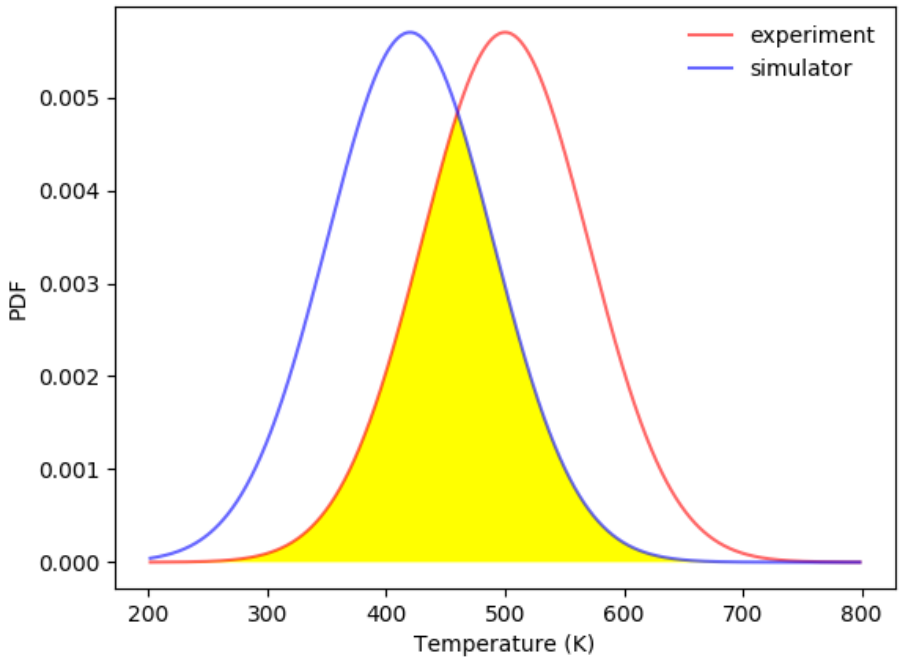

Figure 199. PDF area metric example

The difference PDF metric is a newly developed, by the RAVEN team, comparison metric. Being *z* a continuous random variable equal to the difference of two random variables (*z = x - y*), and being the two random variables statistically independent, the PDF of the difference is computed with the following equation:

$$f_Z(z) = \int_{-\infty}^{+\infty} f_X(x) f_Y(x - z)\ dx \tag{16}$$

This produces a PDF that contains information about the difference between the two PDFs, *fX(x)* and *fY(y)*. The mean can be calculated as:

$$\bar{z} = \int_{-\infty}^{+\infty} z f_Z(z)\ dz \tag{17}$$

This metric is quite useful for the engineer since it provides a way to define the probability of the signed difference between the experiment and the simulation. For example, Figure 200 shows the PDF of the distance between an experiment and a simulator response. The integral of the PDF distance metric provides a simple tool to assess the probability of the distance between the experiment and the simulator response. For example, Figure 201 (red line) shows that the difference between the temperature predicted by the simulator and the experiment has a probability of 25% to be less equal to 75 K.

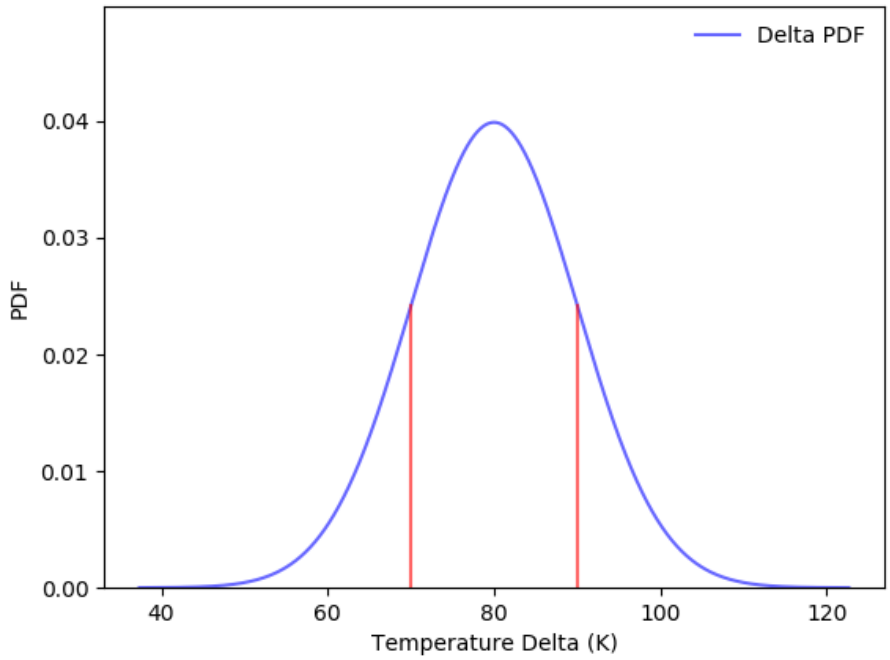

Figure 200. PDF difference metric example

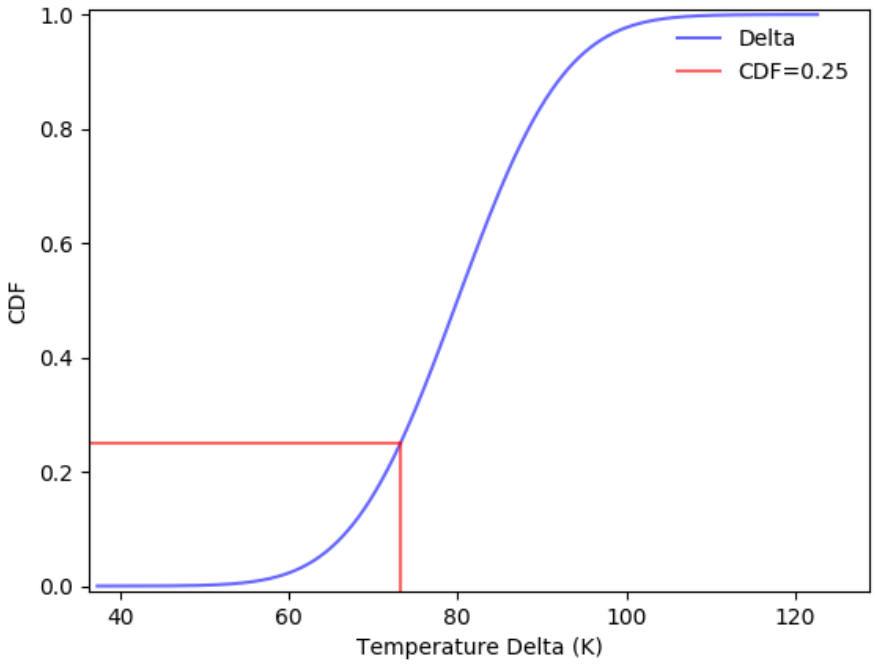

Figure 201. Integral function (CDF) of PDF difference metric example

6.4 RELAP5-3D/RAVEN calculations

Reference [103] provides a detailed analysis of the post-test activity performed with RELAP5-3D, highlighting the capability of the model to predicts the main experimental outcomes. The following stage has been to carry out the statistical analysis, using the RELAP5-3D/RAVEN coupling methodology.

The first step of a statistical strategy is the identification of the parameters which mainly influence the response of the system. The parameters are divided into two sets: independent and dependent parameters. The first ones are the quantity set up in the experiment and they represent the initial and boundary conditions of the simulation; the second ones are the FOMs that consist of the most representative variables monitored during the experiment which will be the objects of the comparison with the system code results. The studied cases consist of a NC and a transition from GEC to NC experiments; the main independent variables are the initial temperatures (primary and secondary side), the power supplied to the facility, the feedwater mass flow rate and the argon injection. In addition, the powder thermal conductivity, influenced by a multitude of factors, is a considerable source of uncertainties and it is added to the set of the independent variables. Except for the powder thermal conductivity, the uncertainties on the input parameters are related to the precision (3σ) of the measurement system. About the powder thermal conductivity, a variability of 10 % has been assumed. The selected uncertainty parameters are summarized in Table 28.

Table 28. Selected uncertainty parameters (3σ)

Parameter	Unit	Test 201	Test 203
LBE temperature	K	+/- 1.5	+/- 1.5
FPS Power	%	+/- 3	+/- 3
FW MFR	%	+/- 10	+/- 10
FW temperature	K	+/- 1.5	+/- 1.5
Ar injection	%	-	+/- 0.5
Powder conductivity	%	+/- 10	+/- 10

According to Ref. [106], considering the two-sided statistical tolerance interval, 93 samples are required to obtain a maximum response with a 95% confidence level and 95% probability. In order to improve the statistical outputs results and to account for the failure of some calculation, 3000 sample runs with random sampled input are carried out for each test and the selected data are collected to identify the uncertainty band of the most representative results.

Figure 202 and Figure 203show the main results of the calculations, comparing the experimental data with the simulated expected value (Expval) and the 95% and 5% percentile extrapolated from the RAVEN results database. The calculated expected value well reproduces the experimental trend in each test. The percentile offers an estimation of the uncertainty range of the results.

Concerning the primary mass flow rate, the simulation results have been compared with the mass flow rate obtained from the EB equation (EBMFR in the plots). As shown in Figure 202 (a) and in Figure 203 (a), the LBE mass flow uncertainty range is rather limited, especially in Test 201, where the primary MFR depends only on the buoyancy. In Test 203, transition from GEC to NC is well reproduced and the uncertainty range is larger during the first phase, due to the uncertainty on the gas injection system. Figure 202 (b) and (c), and Figure 203 (b) and (c) compare the FPS and HX inlet and outlet temperature; in each test the expected value well predicts the experimental trend, but the uncertainty range is much higher than the one observed in the MFR. It can be explained by the large uncertainties related to the powder thermal conductivity, representing the major source of uncertainty. It also affects the uncertainty on the feedwater outlet temperature, shown in Figure 202 (d) and Figure 203 (d).

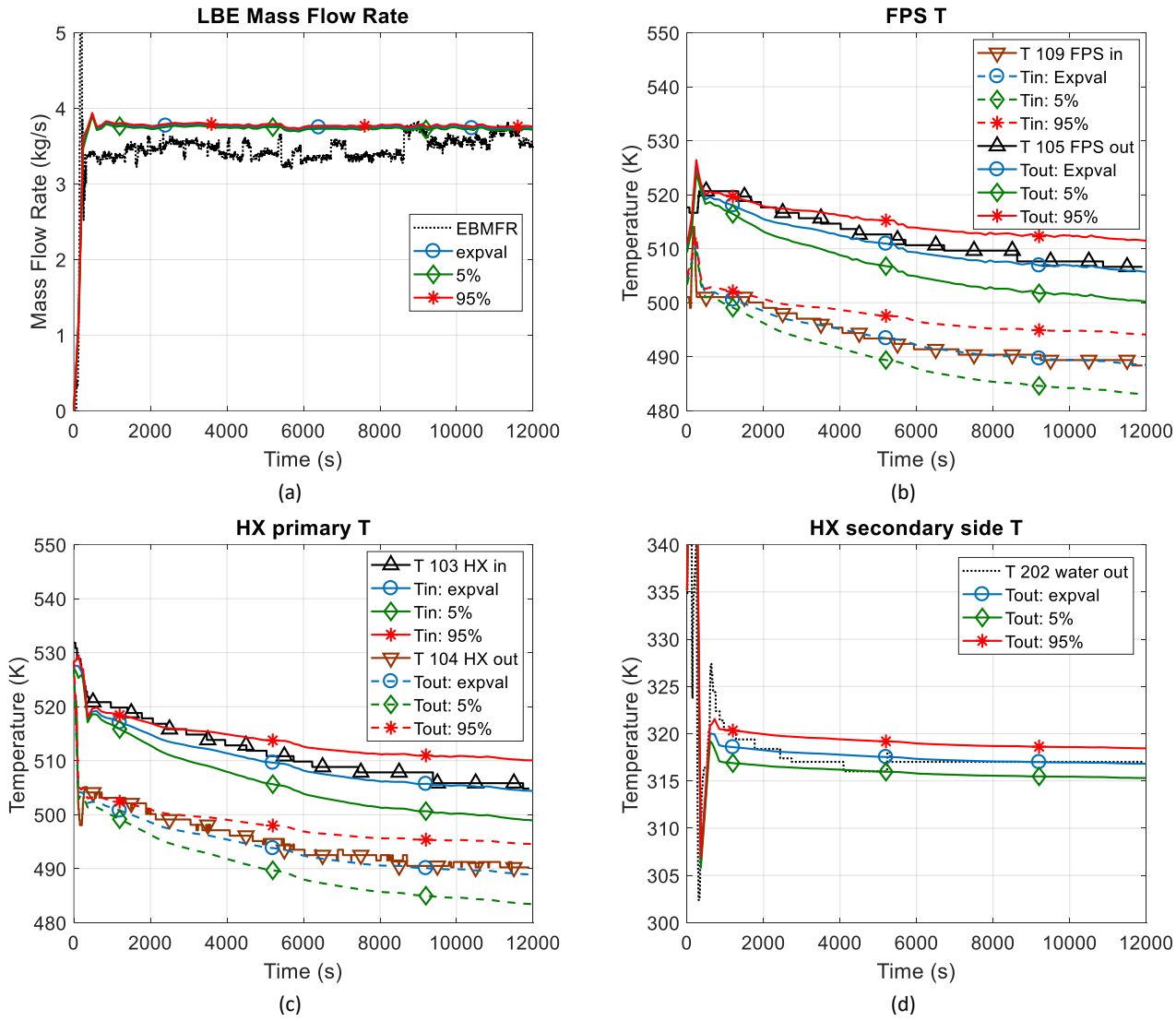

Figure 202. Test 201: main results

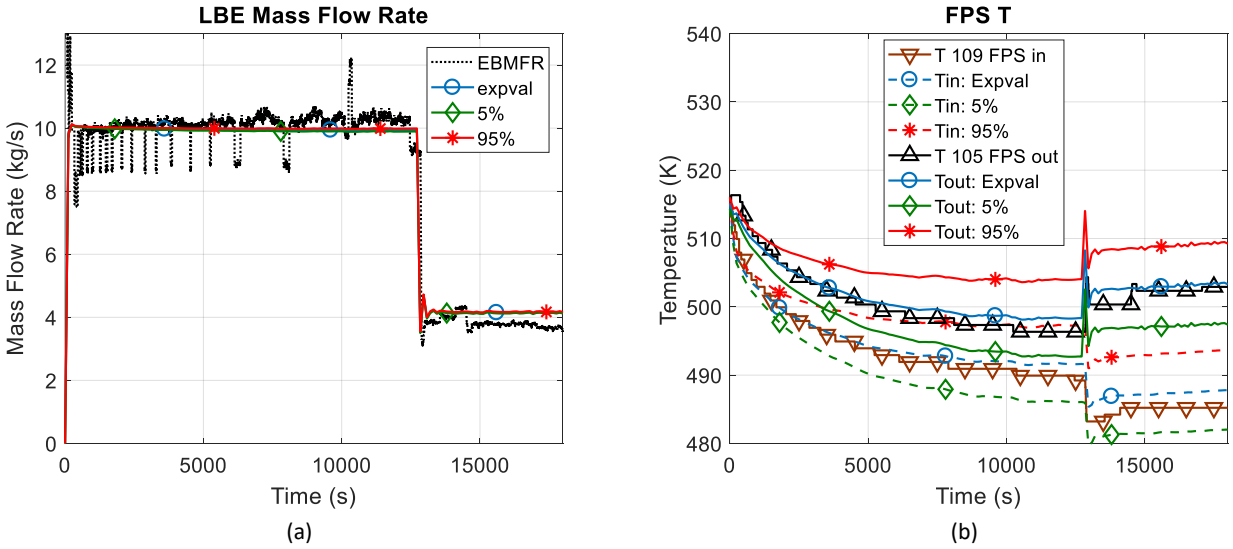

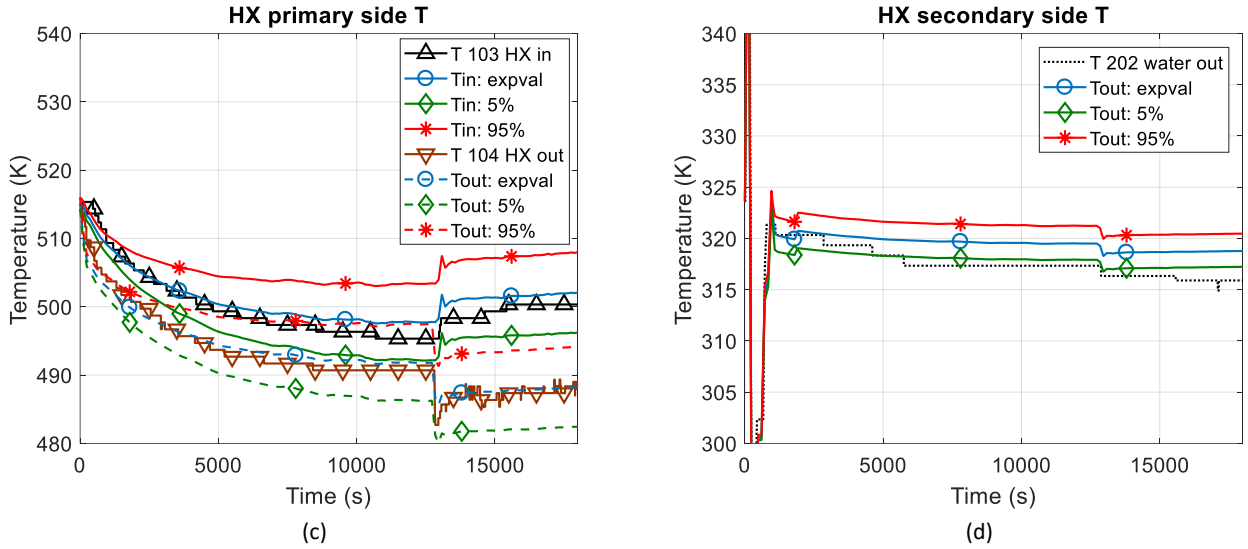

Figure 203. Test 203: main results

RAVEN uses an automatic binning algorithm to subdivide the output data and to minimize the noise caused by statistical sampling; when all the data collected are divided in the optimized number of bins, the probabilistic curves are constructed. The number of counts per each bin is normalized to one and summed up bin by bin; a quadratic interpolation is used to fit the data, and the CDF curve is obtained. Starting from the cumulative distribution function, the derivative is calculated in order to compute the PDF curve. The computed probabilistic curves are compared with the experimental data, assuming for these a normal distribution, using the measured value as the mean and the precision of the instrumentation as the 3σ (see Table 28). In this section, three examples are analyzed, showing the capability of the methodology.

Computed mean value and variance of each output FOM are summarized in Table 29, compared to the experimental data and the associated uncertainties. One relevant instant is chosen for the Test 201 (12000 s, representative of the NC conditions) and two for the Test 203 (12000 s and 18000 s, representative of the GEC and the NC conditions).

As shown in Figure 202 (a), the LBE mass flow rate computed by R5-3D, in Test 201, is characterized by a little uncertainty; the comparison between probabilistic curves of the experimental data and the computed value at the end of the test is shown in Figure 204. The main outcome is that the model predicts rather well the mean value of the mass flow rate, but it provides a lower value of the standard deviation. Two are the possible reasons: the model is not able to predict the experimental propagation of the uncertainty or some relevant uncertainties of the system have been omitted in the model. In this case, and also in the LBE MFR of Test 203 (see Table 29), the second thesis seems right. As reported in Ref. [103], the acquisition of the primary MFR by the flow meter is affected by error due to the calibration of the instrument and the mass flow obtained with the energy balance equation is used for the comparison. This value is characterized by uncertainties due to the measurements of the temperatures and by uncertainties related to the specific heat in the balance equation which is not included in the model.

Figure 205 shows the comparison of the LBE temperature at the inlet section of the FPS. The code well reproduces the mean value, but it predicts a larger standard deviation than the experimental data. In this case, or the model is not able to attenuate the propagation of the uncertainties or the uncertainties on the input data has been not well estimated. As presented in Ref. [103], thermal conductivity of the stainless-steel powder represents a high source of uncertainty, due to the lack of information. This causes the high value of the standard

deviation of all LBE temperatures, larger than the standard deviation associated with the precision of the thermocouples; so, the second thesis seems to be right.

Regarding Test 203, Figure 203 shows good agreement between the computed outcomes and the experimental data. LBE mass flow rate is well predicted by the code during the GEC phase but it is slightly overestimated after the transition to NC conditions. Figure 206 shows the comparison of the primary MFR in NC. An error on the mean value is added to the underestimation of the standard deviation already analyzed in Figure 204; the model could not predict very well the transition from the GEC to the NC conditions or a wrong measurement of the mass flow could be occurred. In this case, the analytical methodology for the measurement of the MFR could explain the inconsistency between the computed results and the experimental data.

Table 29. Probabilistic analysis: main results

Operation			**Experimental data**		**Simulation results**	
	FOM	**Unit**	**Mean**	**σ^2**	**Mean**	**σ^2**
Test 201	LBE Mass flow rate	kg/s	3.7	3.50E-03	3.7	1.70E-04
	FPS inlet T	K	488.6	0.25	488.5	11.43
	FPS outlet T	K	506.7	0.25	505.7	11.85
	HX inlet T	K	504.8	0.25	504.4	11.49
	HX outlet T	K	490.2	0.25	488.9	11.56
Test 203 GEC	LBE Mass flow rate	kg/s	10.2	2.66E-02	9.9	8.16E-04
	FPS inlet T	K	489.9	0.25	491.8	11.30
	FPS outlet T	K	496.3	0.25	498.4	11.39
	HX inlet T	K	495.3	0.25	497.8	11.26
	HX outlet T	K	490.7	0.25	491.9	11.34
Test 203 NC	LBE Mass flow rate	kg/s	3.65	3.50E-03	4.15	2.21E-04
	FPS inlet T	K	485.2	0.25	487.8	12.41
	FPS outlet T	K	502.9	0.25	503.3	12.80
	HX inlet T	K	500.3	0.25	502.1	12.55
	HX outlet T	K	488.4	0.25	488.2	12.49

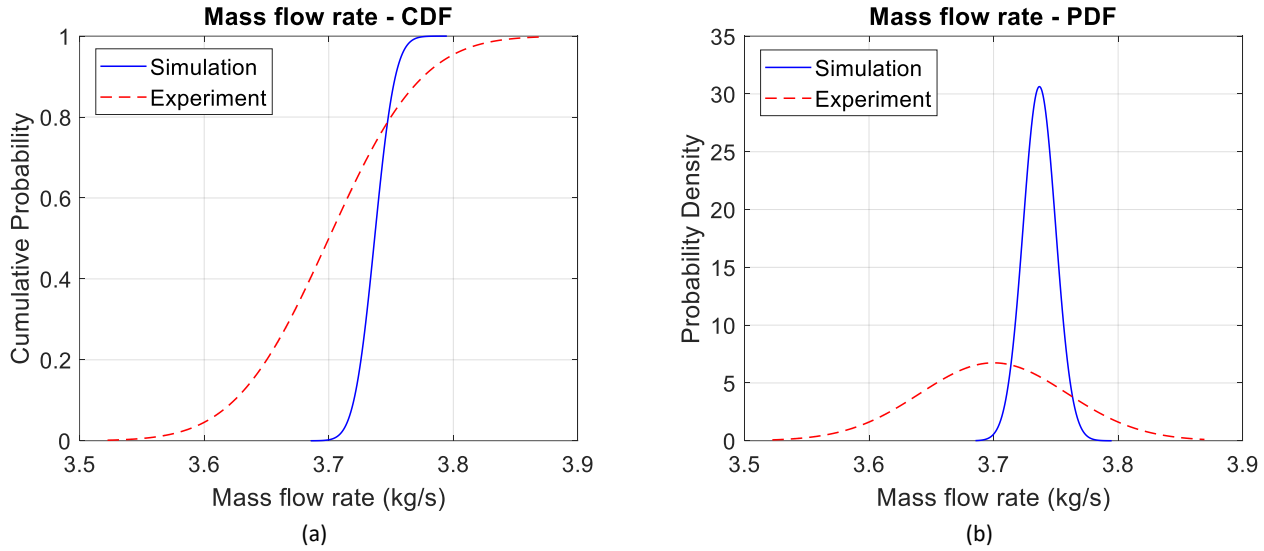

Figure 204. Test 201 (12000 s): LBE mass flow rate

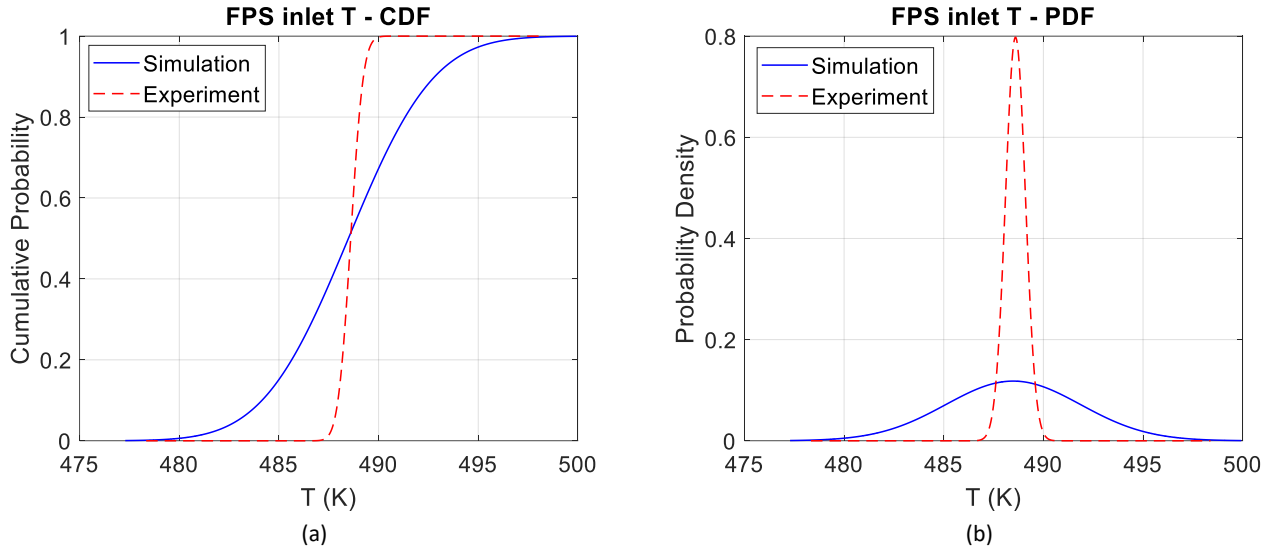

Figure 205. Test 201 (12000 s): FPS inlet temperature

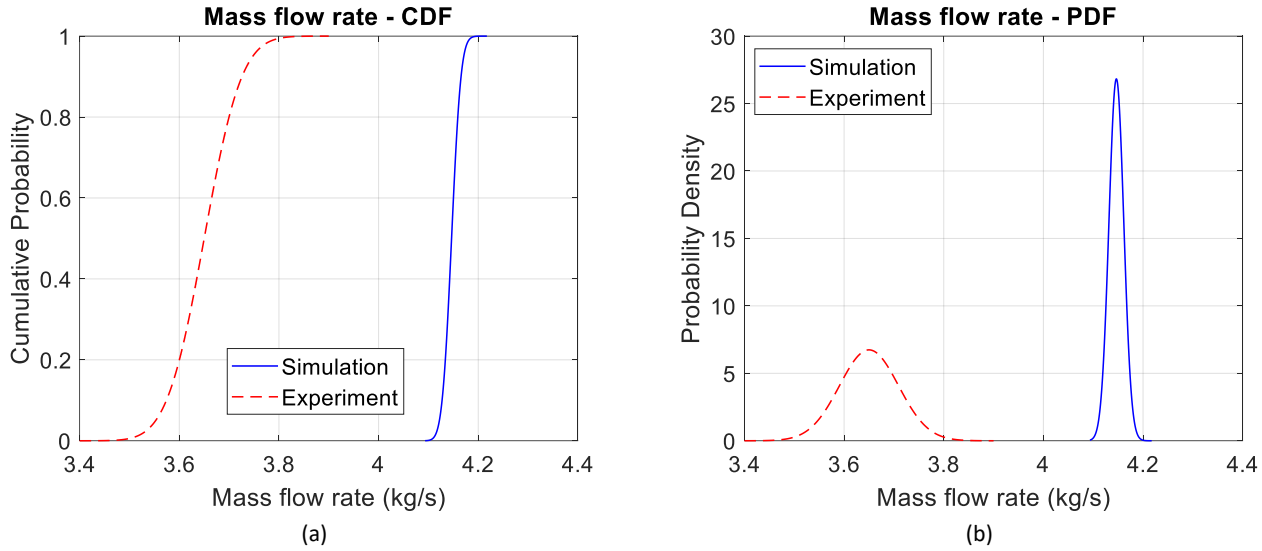

Figure 206. Test 203 (18000 s): LBE mass flow rate

Figure 205 (a) shows a good prediction of the mean value of the LBE temperature at the FPS inlet; if the analysis of the calculation outcomes was founded only on the mean value, the information concerning the discrepancy between simulated results and experimental data would not be complete. The CDF area metric provides this information in the same units of the compared FOM. Table 30 summarizes the outcomes of this metric; regarding the LBE temperature, the average difference between the CDF_c and the CDF_e is 2.5 K. The maximum value is obtained for the HX outlet temperature, where the difference is about 3 K. A good agreement is observed for the LBE mass flow rate, where the CDF area difference is lower than 0.5 kg/s in all the three cases. Even if, as shown in Figure 206 (a), the mean value of the primary mass flow under NC conditions (Test 203) is not well predicted, the difference between simulated outcomes and experimental data is always below 0.5 k/s.

The PDF area metric provides a bit different results than the previous metric. This analysis computes the degree of agreement between the PDF curves but it losses information about how far apart the two sets of data are. This is the case of the LBE mass flow rate in NC during Test 203; Figure 206 (b) shows that the common area between the PDFs is essentially zero (see also Table 31) but the previous metric highlights that discrepancy between calculated value and experimental data is lower than 0.5 kg/s, highlighting a good prediction of R5-3D.

The last one is the difference PDF metric. Figure 207 (b) shows the PDF of the difference between the two probability density functions depicted in Figure 204 (b). The mean of this PDF provides information about the mean value of the difference between experimental data and simulated outcomes; the more the mean values are close, the more the mean of this PDF is close to zero. Figure 207 (b) shows that the mean difference is -0.028 kg/s and the uncertainty is contained between -0.3 and 0.25 kg/s. The CDF of the difference is obtained integrating the PDF. This curve offers useful information to the engineers; it is able to provide the probability to obtain a difference below a certain value. For example, Figure 207 (a) shows the CDF of the difference for the LBE mass flow rate in Test 201. The probability to obtain a discrepancy between the computed value and the experimental data below 0.0 (i.e. between -0.3 and 0.0 kg/s) is 70 %. In the same way, the probability to obtain a difference between -0.3 and -0.1 is 10%. This metric provides useful outcomes on the definition of the safety margins for the NPP design.

Figure 209 shows the PDF and the CDF of the difference for the LBE mass flow rate in natural circulation conditions (Test 203). The PDF area metric highlights the no matches between calculated and experimental values; the difference PDF metric shows the same results (the difference is always negative both in PDF and CDF curve) but it provides additional information on the probability to obtain the specific difference between the simulation and the experiment.

Table 30. CDF area difference

Test (Condition)	LBE MFR (kg/s)	FPS inlet T (K)	FPS outlet T (K)	HX inlet T (K)	HX outlet T (K)
201 (NC)	0.045	2.49	2.86	2.59	2.99
203 (GEC)	0.274	2.44	2.51	2.64	2.36
203 (NC)	0.492	2.78	2.59	2.56	2.70

Table 31. PDF common area

Test (Condition)	LBE MFR	FPS inlet T	FPS outlet T	HX inlet T	HX outlet T
201 (NC)	35.85%	24.13%	20.65%	23.12%	19.51%
203 (GEC)	9.13%	26.85%	27.07%	27.31%	25.87%
203 (NC)	1.8E-12%	26.24%	22.81%	26.05%	21.56%

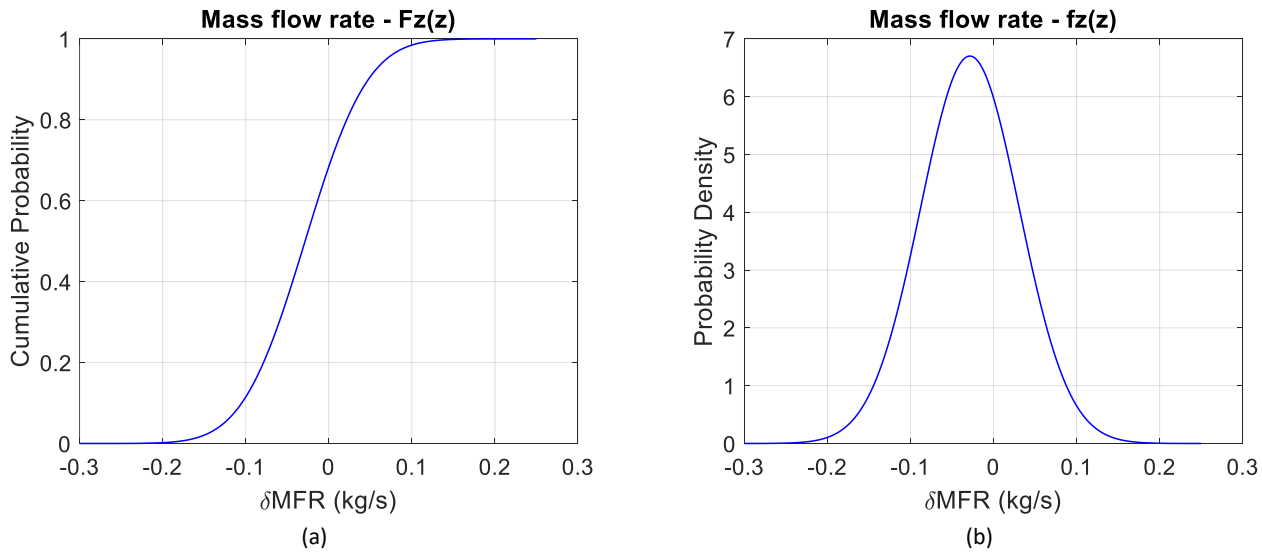

Figure 207. Difference PDF metric: Test 201 LBE mass flow rate (12000 s)

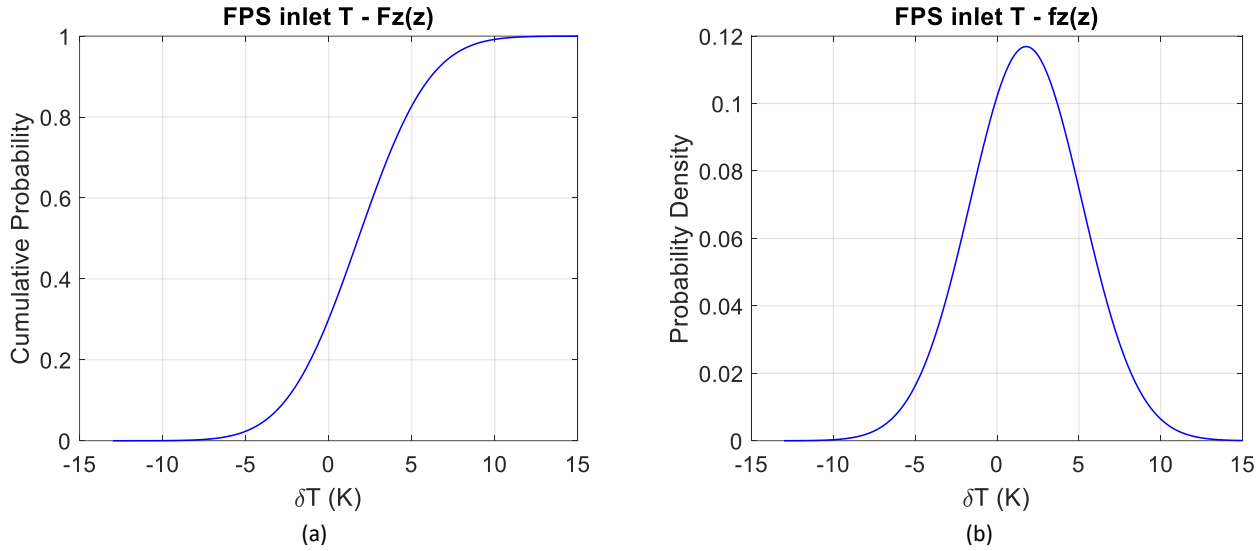

Figure 208. Difference PDF metric: Test 201 FPS inlet temperature (12000 s)

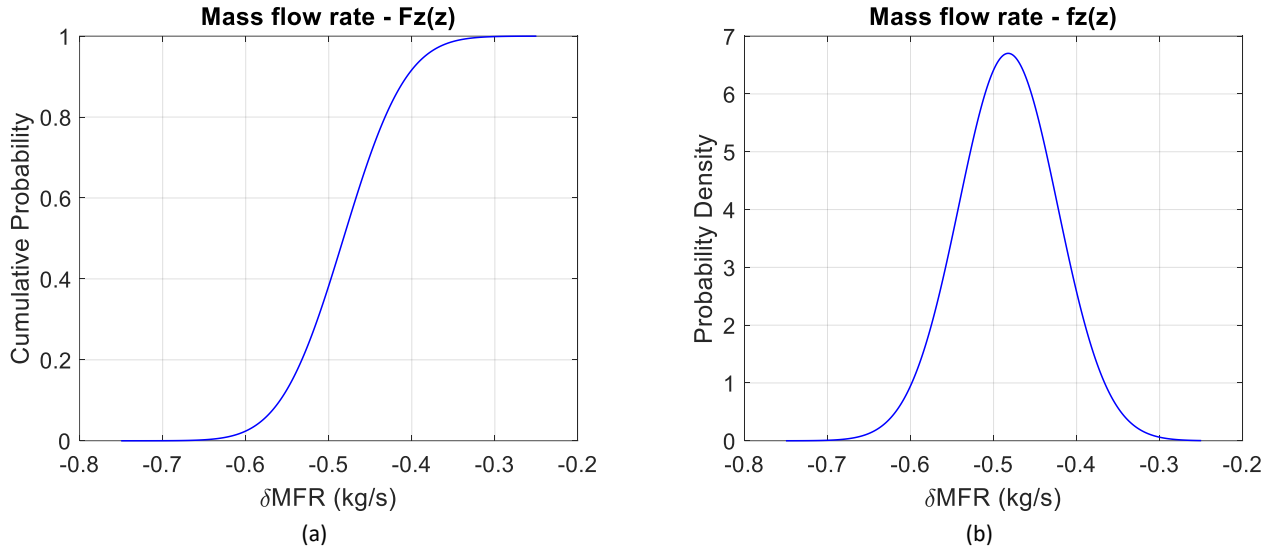

Figure 209. Difference PDF metric: Test 203 LBE mass flow rate (18000 s)

6.5 Conclusive remarks

The objective of the activity has been to verify a coupled RELAP5-3D/RAVEN methodology for the uncertainty quantification on HLM system. At this purpose, a mono-dimensional model for NACIE facility has been developed and the post-test calculations have been carried out using RELAP5-3D©. Two experimental tests have been selected for the activity: Test 201, aimed to investigate thermal-hydraulics on pure natural circulation conditions regime, and Test 203, aimed to analyze system behavior under the transition between GEC and NC regime. Post-test calculation has verified capability of the model to qualitatively predicts the main experimental outcomes, but this is not sufficient to perform a safety analysis. The evaluation of the quantitative code accuracy is needed. The BEPU method plays a key role in the development of innovative GEN-IV reactors. At this purpose, the activity aims to verify a BEPU methodology based on the RAVEN code, developed at Idaho National Laboratories.

Starting from the post-test results, the independent parameters space has been perturbed following a Monte Carlo sampling. The uncertainties have been propagated and the main results are collected in a database. The final step has been the comparison of the calculated FOMs and the experimentally measured results, including the associated uncertainties. Three comparison metrics, fully integrated into RAVEN, have been adopted and the main results have been analyzed. According to the post-test calculations, the comparison metrics have shown good results in terms of mean values, but they also have highlighted not perfect uncertainty prediction due to the lack of some input information, especially related to the stainless-steel powder thermal conductivity.

7 CONCLUSIONS

The present research activity has been focused on the thermal-hydraulics of innovative liquid metal-cooled fast reactors, belonging to the so-called Generation IV. It aims to contribute to the understanding of relevant thermal-hydraulic phenomena that characterize the operations of the LMFR, and to the fundamental validation process of the innovative numerical tools, adopted for safety analysis and licensing of new NPPs. The research activity has dealt with the validation of RELAP5-3D© for applications on liquid metal-cooled pool-type fast reactors.

In order to provide a useful summary of the main outcomes and of the future perspective coming out during the present research activity, this chapter has been divided in four sections, dealing with four relevant topics: the pool modelling, the liquid metal system operation, the passive safety system and the BEPU methodology.

7.1 Pool modelling

Pool-type configuration assumed a relevant role in the GEN IV reactors design, allowing to eliminate the issues related to the out-of vessel primary system and to provide a high self-shielding capacity [4]. However, pool thermal-hydraulics is characterized by several phenomena, such as thermal stratification, thermal striping or mixing convection, that determine some technological challenges and require to be further investigated. Thermal stratification can assume relevant role in both water and LM systems. This phenomenon occurs in quasi-stagnant volumes, where the movements of the fluid are restricted to the buoyancy effects. For example, in pool-type LMFR, the hotter walls of the primary components warm the primary fluids contained into the pool. The hot fluid moves upwards within the pool and a thermal front appears dividing cold and hot fluid. The interface between two layers is subjected to large temperature differences that can expose surrounding structures to low-cycle thermal fatigue. The same phenomenon can occur into water tanks of passive DHR systems, where the water contained within the pool is heated by the IC bundle.

Several experimental activities were designed to study pool thermal-hydraulics in LM systems. In this framework, the experimental campaigns performed in CIRCE facility represent a milestone of the HLM pool investigation. Two configurations have been analyzed in this research activity, focusing on the analysis of a primary flow path typical of a LMFR (ICE test section) and of a steam generator in a relevant configuration for ALFRED SG (HERO test section). Relevant efforts were dedicated to the investigation of pool thermal stratification.

Focusing on the pool modelling, several examples were found in literature, mainly concerning the simulation of large water tanks with RELAP5. For an accurate evaluation of the vertical temperature trend, RELAP5 includes a thermal stratification model that can be applied to vertically oriented components without cross junctions. Although this model provides relevant improvements in the thermal front prediction within tank characterized by a limited volume, such as the pressurizer, some limitations were observed on the application of this model to large pools. An improved modelling approach consists in the division of the pool in more parallel vertical pipes, connected with several junctions, trying to simulate buoyancy within large tanks.

The actual state of art on the pool modelling has been used in the CIRCE numerical activity. The modelling approaches, found in literature, have been assessed comparing the outcomes of the simulation with experimental data from the CIRCE-ICE campaign. In addition, an improved modelling approach, based on the application of the MULTID component to reproduce the pool, has been evaluated. The simplest mono-dimensional approach, based on a single vertical pipe component, has highlighted relevant discrepancies with the experiment, failing on the prediction of the axial temperature profile. In this case, the absence of natural flow within the pool, impeded by the modelling approach, causes a temperature peak in the middle of the tank, at the level where the higher amount of heat losses from the hottest primary flow path are expected. Discrepancies have been increased by the lack of a thermal conduction model within the coolant. To assess the

effect of this thermodynamic properties of the liquid metal, a thermal conduction model has been implemented in the nodalization, implementing several dedicated heat structures. Some improvements have been obtained in the outcomes of the simulations, even if the thermal conduction model is not enough to reproduce the qualitative temperature trend.

The pool modelling has been improved in order to simulate buoyancy within the tank. It has been divided in three parallel vertical pipes, connected with cross junctions. This approach allows improved capabilities on the evaluation of the thermal stratification, thanks to the simulation of the LBE natural circulation, promoted by the density difference between cold and hot fluid. Regarding the CIRCE-ICE campaign, the qualitative trend has been well reproduced, predicting two relevant stratification phenomena at the top and in the middle of the pool. Although the qualitative trend has been well reproduced, and the LBE temperature in the lower part of the pool has been in good agreement with experimental data, the plateau temperature at the middle of the pool has been underestimated of about 15 K and this discrepancy has been maintained up to the top head of the facility.

A more detailed nodalization scheme has been developed adopting the MULTID component, dividing CIRCE pool in several volumes, with a three-dimensional cylindrical grid. Although the MULTID component was implemented in RELAP5-3D to simulate volumes where the flow is preferably 1D, it introduces relevant improvements on the prediction of the pool thermal stratification. The two stratifications, observed under full power operation of the facility, have been well estimated, reducing the discrepancy in the middle height to 5 degrees, which could be attributed to the underprediction of the HTC in quasi-stagnant conditions within large volumes. Following the postulated transient test, the MULTID component has shown good capabilities in the prediction of the thermal front movements from the HX exit to the DHR outlet. Moreover, this modelling approach has shown good capabilities in predicting the upper stratification attenuation, following the deactivation of the HX. The capabilities of the MULTID components have been confirmed with the numerical activity performed on CIRCE-HERO experimental campaign. The modification of the test section led to a different temperature profile within the pool: the thermal insulation of the SG case avoided the thermal front establishment in the upper part of the pool, and the lower stratification moves downward, at the level of the SG outlet. The pool modelling, improved in accordance with the geometry of the new test section, has provided results in good agreement with experimental data, predicting both the quote of the stratification and the magnitude of the thermal front.

The main outcomes coming out from the numerical activity performed on CIRCE campaigns have been the capability of the MULTID component to reproduce pool thermal-hydraulics, that provides relevant improvement in the prediction of the thermal stratification phenomenon, even if the computational cost increases. For these reasons, the application of the multi-dimensional modelling approach is preferable if relevant thermal stratification phenomena are expected. On the other hand, the mono-dimensional modelling approach, consisting in parallel pipe components connected with cross junctions, provides satisfactory results, reducing the computational time.

Considering a more complex system, such as a nuclear reactor, asymmetrical effects could play a relevant role in the evolution of transition events. At this regard, the Phénix Dissymmetric End-of-Life test offered useful data for the knowledge increase and for the code validation. As a participant of the code validation benchmark, promoted within the H2020 SESAME project, UNIROMA1 developed a detailed model of the Phénix reactor, aiming on the assessment of R5-3D capabilities to reproduce thermal-hydraulics asymmetries in LM-cooled pool-type systems. For this purpose, the MULTID approach was selected for the pool modelling. In this case, a single MULTID components simulates the cold pool, the hot pool and the core bypass. The simulation results provide good agreement with experimental data and the comparison with the outcomes of the other benchmark participants, has highlighted improved capabilities of the MULTID component to reproduce asymmetrical

evolution of the system [67]. The movement of the hot sodium within the cold pool is well predicted by the code, that provides a good estimation of the local peak temperature at the PP1 inlet, in the first seconds of the transient test.

As mentioned above, thermal stratification phenomenon could affect water systems, where a large amount of water is contained and warmed within a tank. This is the case of a typical configuration of a DHR system, based on an isolation condenser immersed in a water tank, which operates as a final heat sink. Such a system was investigated in PERSEO facility, providing experimental data for the realization of a validation benchmark. In this case, it is expected that thermal stratification does not affect the operation of the whole system in a relevant way. For this reason, the mono-dimensional modelling approach, based on parallel pipes with cross junctions, was selected to simulate the two pools. Reasonably agreements have been observed between the simulation results and the experimental data, even if the main limitation has been the significant underestimation of the power exchanged between the HXP and the HX bundle, attributed to the underprediction of the HTC evaluation in pool boiling and in-tube condensation under NC condition. For this reason, a constant multiplicative factor, equal to 2.4, applied to the HTC, has been necessary to improve the simulation. As expected, the pool modelling approach adopted for the calculations, determines an underestimation of the thermal stratification, although this phenomenon does not affect the global goodness of the calculations.

The main target of the validation activity was to qualify the R5-3D pool modelling to support the design of the GEN IV nuclear power plants. The numerical activity was used to explore and validate different pool modelling approaches and the acquired know-how has been used to support the design of ALFRED reactor. At first, the support numerical activity has concerned the reference concept of the reactor, developed within the LEADER project. Based on the experience learned during the analysis of the experimental campaign performed in CIRCE and on the references found in literature, a thermal stratification phenomenon was expected into the main pool of the reactor. For this reason, a detailed three-dimensional model of the pool has been developed. The full power calculation has highlighted a relevant thermal stratification, of about 70 K, in the upper part of the pool, that is not been involved in the primary flow path.

Thermal stratification represents a significant technological issue. This was one of the reasons that encourages the designers to develop a revised concept of ALFRED reactor. In this frame, the solution was to include an internal structure, within the RV, that forces the cold lead, exiting the SG, to move upward and then, passing through specific holes in the upper part of the IS, to move downward towards the core inlet. In this way, zones not involved in the flow path are avoided. A thermal-hydraulic model of the new configuration was developed in order to verify, among other issues, the absence of relevant thermal stratifications in both normal and accidental operations. For this purpose, a detailed MULTID component was developed to reproduce the pools of the reactor. The numerical activity has demonstrated the improved pool thermal-hydraulics: significant thermal stratifications are avoided in both full-power operation and SBO scenario.

As demonstrated by the research activity, the pool modelling represents one of the main relevant issues in the frame of the STH validation process. This activity has shown satisfactory capabilities of the code to reproduce pool thermal-hydraulics, highlighting advantages and drawbacks of two modelling approach, basically concerning a three-dimensional and a mono-dimensional methodology. However, the calculations reveal some crucial aspects that required to be more investigated (buoyancy within large volumes) and to be implemented in future versions of the STH codes. Regarding the latest point, UNIROMA1 is actually working on a modified version of RELAP5 mod. 3.3, integrating improved thermal-hydraulic properties of fluids relevant for fission and fusion applications, dedicated correlations for the evaluation of the heat transfer and pressure drops of liquid metals

in relevant configurations (such as once though steam generators, helical coil steam generators, wire wrapped pin bundle…) and an improved model of the magneto-hydrodynamics.

7.2 Liquid metal system operation

One of the main improvements introduced in RELAP5-3D is the capability to simulate systems cooled by a wide variety of fluids, including liquid metals. These improvements consist in the thermophysical properties and thermal-hydraulics correlations related to the heat and mass transfer. It is an attractive feature for the LMFR development and licensing, even if these capabilities must be validated.

One of the objectives of this research activity was to verify the capability of RELAP5-3D to reproduce thermal-hydraulics of innovative LMFR, in safety relevant operation conditions. For this purpose, several examples have been included in this thesis, concerning both lead and sodium systems.

CIRCE facility offered useful experimental data for the code validation, reproducing, in both the configurations, the primary system of an HLM-cooled pool-type reactor. In addition, HERO test section is equipped by a DWBT steam generator in a relevant configuration for the ALFRED SG.

The experimental campaign performed on CIRCE-ICE test facility was aimed to the investigation of the thermal-hydraulics of an HLM-cooled primary system under two full power steady-state conditions and under a transition from GEC to NC, simulating a PLOHS plus LOF accident, with the activation of a DHR system. The purpose was to study the behavior of the whole system and the core cooling performance under critical conditions. The thermal-hydraulic model, developed with R5-3D, has exhibited excellent abilities to reproduce the experimental data. Several figures of merit have been considered to assess code capabilities: primary flow rate, heat exchange across the FPS, HX and DHR, LBE temperature in different sections of the flow path, pressure drops and heat losses. The code provides an excellent prediction of the GEC operations, proving the ability to reproduce gas enhanced primary circulation and the cooling performances of the FPS and of the heat exchanger at high flow rate operation. The good evaluation of the heat losses is assessed by the correct evaluation of the temperature difference in the monitored sections of the flow path and by the satisfactory thermal stratification prediction. Following a postulated accident, characterized by the deactivation of the Ar injection system, the code has been able to reproduce the transition from GEC to NC, matching the experimental trend of the primary flow rate, unless minor discrepancies contained within the experimental uncertainty bands. Cooling capabilities of the whole system have been well predicted, proving the merit of the simulations at low flow rate conditions.

Within CIRCE-HERO campaign, the efforts were mainly focused on the investigation of the DWBT SG performances, equipping the secondary loop with a detailed monitoring system, acquiring temperatures and flow rates through the bayonet elements. Two experimental tests have been considered in this work, investigating the transition from GEC to NC operation, following two PLOFA scenarios. The abilities of the code to reproduce the thermal-hydraulics of the primary system under safety-relevant operation conditions have been confirmed by this numerical activity. The main discrepancies have been related to the lack of some information by the experimental monitoring system, basically concerning the secondary loop. The simulation activity has provided useful information to the understanding of the experimental tests, highlighting some uncertainties that significantly affected the operation of the facility. Some assumptions have been adopted and the code has highlighted excellent capabilities on the prediction of the main FOMs related to the SG operation. This numerical campaign proved the importance of a detailed description of the boundary conditions.

In addition, a subchannel modelling methodology, using the R5-3D STH code, has been assessed, using experimental data provided by CIRCE campaigns. The FPS was equipped with a detailed monitoring system, acquiring bulk and clad temperatures in different subchannels and several levels of the active bundle. The

analysis has shown good capabilities of R5-3D as subchannel code, reproducing the expected temperature trend within a typical fuel bundle of a LMFR. In addition, the code has been able to simulate the transition from high to low primary circulation, highlighting a negligible effect of the radial thermal conduction between adjacent subchannels under high flow conditions, and rather significant effect in NC operations.

The Dissymmetric test performed on Phénix reactor provided useful data for the assessment of R5-3D to reproduce thermal-hydraulics of a complex sodium-cooled reactor. The asymmetrical boundary conditions suggested a detailed nodalziaiton of the reactor, separating each component. The asymmetric evolution of the system has been well reproduced by the code, which has shown excellent capabilities to reproduce the evolution of the primary system under accidental conditions. A detailed geometrical scheme of the core has been developed, in order to allow NK-TH calculations.

The knowledge acquired from the numerical activities has been applied for the simulations of ALFRED reactor, aiming to verify the performance of the reactor at full power steady-state conditions and under a postulated SBO accident. The modelling approach, validated in CIRCE and Phénix computational activities, has been applied to the reference configuration of ALFRED, to verify the nominal operation of the reactor. A detailed nodalization of the reactor core (FA per FA in the active region) has allowed the calculation of the power distribution in BOL conditions, through a NK-TH calculation. The code has confirmed the operability of the reactor at full power configuration, highlighting some critical points mainly related to the configuration of the pool.

The simulation activity performed in the framework of the revised ALFRED configuration, has highlighted the improved thermal-hydraulics of the new concept, showing excellent performance of the system under safety-relevant operating conditions. In particular, the activation of safety systems allows to limit the maximum temperature in the first instant of the accident below the technological edges and avoids lead freezing in the grace time period. In order to provide the best estimation of the maximum temperature reached in the hottest FA, following the primary pump trip and the delayed SCRAM command, a subchannel modelling of the hottest FA has been developed, based on the know-how acquired in CIRCE numerical activity. The simulation has confirmed the safety conditions predicted by the first calculation, reducing the maximum temperature of about 10 degrees.

Globally, the calculations have highlighted satisfactory capabilities of R5-3D to reproduce the primary system of LMFR under safety-relevant conditions. The calculations performed in the frame of ALFRED, have highlighted the importance of a STH code in the verification and licensing process of an innovative NPP. Further investigations concerning a wide range of accidental scenario and innovative configuration of the LM reactors are necessary to carry out a full validation of the code for these systems.

7.3 Passive safety system

Safety and reliability are relevant aspects of the development of GEN IV reactors. In this framework, LMFRs present peculiar characteristics related to the thermophysical properties of the coolant, basically regarding the possibility of coolant freezing, that can occur in long term DHR operation if the thermal power removed by the DHR system exceeds the decay residual power. For this reason, in LMFRs, the DHR system must ensure an efficient power removal, avoiding to overcome technological limits in terms of maximum temperatures, and must prevent coolant freezing in the grace time period. In addition, according to GIF guidelines, passive DHR systems are needed to prevent unexpected evolution of accidental scenarios following a total loss of the continuous electrical power supply.

The solution consisting of an isolation condenser immersed in a water tank, acting as a final heat sink, could meet the above-mentioned characteristics. The operation of such a system, is based on in-tube condensation under NC condition and pool boiling. For this reason, the validation process is required for STH codes, such as R5-3D.

In this framework, PERSEO facility offered useful experimental data. The numerical activity performed at DIAEE has shown good capabilities of the code to reproduce safety performance of the passive system. However, R5-3D, as much as the other codes used for the validation benchmark, has highlighted some limitations in the prediction of the power removed by the IC, requiring a corrective multiplicative factor of 2.4, applied to the HTC in both in-tube and pool sides. At this regard, the improving process of RELAP5 mod. 3.3, ongoing at DIAEE of "Sapienza" University of Rome, could overcome this limitation, implementing specific HTC correlations for In-tube condensation under NC and for pool boiling.

The modelling approach validated in PERSEO activity, has been applied for the safety analysis of the revised ALFRED concept, that includes an innovative DHR passive system, based on an IC equipped with a non-condensable tank to limit the power removed in the long term, preventing primary coolant freezing. In this preliminary phase, HTC multiplicative factor has not been considered. Such an approach is conservative, reducing the thermal power removed by the safety system in the first phase of the accident. The calculation has demonstrated the DHR capabilities, restricting the maximum temperatures within the technological limits, and preventing lead freezing in the grace time period.

7.4 BEPU methodology

The last chapter of the thesis has proposed a BEPU methodology, based on a statistical exploration of the input space considering the associated uncertainties altogether and the analyses of the responses with several validation metrics. The methodology consists in the RELAP5-3D/RAVEN coupled calculation.

The objective of this research activity has been to verify the coupled methodology for the uncertainty quantification of LM-cooled systems. For this purpose, the experimental campaign performed on NACIE facility and the thermal-hydraulic model developed by UNIROMA1 have been considered. The UQ has been based on the perturbation of the input space following a Monte Carlo sampling, propagating the input uncertainties. The analysis of the main outcomes related to selected FOMs, has been performed with three comparison metrics, fully integrated into RAVEN tool. The application of the comparison metrics has shown the capabilities of the methodology, highlighting the merits and the weaknesses of the thermal-hydraulic model. The future perspectives could be the application of the model to more complex models to increase the validation process of the methodology and to apply it to the verification process of the new NPP concepts.

NOMENCLATURE

Abbreviations and acronyms

1D	One-dimensional
2D	Two-dimensional
3D	Three-dimensional
AC	Alternating Current
ADS	Accelerator Driven System
ALFRED	Advanced Lead Fast Reactor European Demonstrator
ANL	Argonne National Laboratory
Ar	Argon
ARA	Axial Reflector Assemblies
ASTEC	Accident Source Term Evaluation Code
ASTRID	Advanced Sodium Technological Reactor for Industrial Demonstration
ATHLET	Analysis of THermal-hydraulics of LEaks and Transients
BAF	Bottom of Active Fuel
BE	Best Estimate
BEPU	Best Estimate Plus Uncertainty
BOL	Beginning Of Life
BT	Bayonet Tube
CATHARE	Code for Analysis of THermalhydraulics during an Accident of Reactor and safety Evaluation
CDF	Cumulative Density Function
CDF_c	Code output CDF
CDF_e	Experimental CDF
CEA	French Alternative Energies and Atomic Energy Commission
CFD	Computational Fluid Dynamics
CHF	Critical Heat Flux
CIRCE	CIRColazione Eutettico
CIRTEN	Interuniversity Consortium for Technological Nuclear Research
CR	Control Rod
CSNI	Committee on the Safety of Nuclear Installations
DHR	Decay Heat Removal
DIAEE	Department of Astronautical, Electrical and Energy Engineering
DOTE	Dispositif d'Obturation des Traverses d'Echangeurs (Exchangers plugging system)
DP	Differential Pressure
DWBT	Double-Wall Bayonet Tube
EB	Energy Balance
EBMFR	Energy Balance Mass Flow Rate
EC	External subChannel
ENEA	Italian National Agency for New Technologies, Energy and Sustainable Economic Development
EURATOM	European Atomic Energy Community
Expval	Expected value
FA	Fuel Assembly
FALCON	Fostering ALFRED Consortium
FBR	Fast Breeder Reactor
FM	Flow Meter
FOM	Figure Of Merit
FP	Framework Programme
FPS	Fuel Pin Simulator

FR	Flow Rate
FW	FeedWater
GEC	Gas-Enhanced Circulation
GEN III	Generation III
GEN III+	Generation III+
GEN IV	Generation IV
GEST	GEnerator Separator Tests
GFR	Gas-cooled Fast Reactor
GIF	Generation IV International Forum
H2020	Horizon 2020
HERO	Heavy liquid mEtal pRessurized water cOoled tubes
HLM	Heavy Liquid Metal
HS	Heat Source
HTC	Heat Transfer Correlation
HTGR	High-Temperature Gas-cooled Reactors
HX	Heat eXchanger
HXP	Heat eXchanger Pool
IAEA	International Atomic Energy Agency
IC	Isolation Condenser
ICE	Integral Circulation Experiment
ICN	Institute for Nuclear Research
IEA	International Energy Agency
IHX	Intermediate Heat eXchanger
INL	Idaho National Laboratory
IRSN	Institut de Radioprotection et de Sûreté Nucléaire
IS	Internal Structure
KIT	Karlsruhe Institute of Technology
L1	Loop 1
L3	Loop 3
LBE	Lead Bismuth Eutectic
LEADER	Lead-cooled European Advanced DEmonstration Reactor
LFR	Lead-cooled Fast Reactor
LM	Liquid Metal
LMFR	Liquid Metal-cooled Fast Reactor
LOF	Loss Of Flow
LWR	Light Water-cooled Reactor
MFLOW	Mass FLOW
MFR	Mass Flow Rate
MOX	Mixed OXide
MSR	Molten Salt Reactor
MULTID	MULTI-Dimensional
MYRRHA	Multi-purpose hYbrid Research Reactor for Hightech Applications
Na	Sodium
NACIE	NAtural CIrculation Experiment
NC	Natural Circulation
NEA	Nuclear Energy Agency
NK	Neutronic Kinetic
No	Number
NPP	Nuclear Power Plant

NRG	Nuclear Research and consultancy Group
OECD	Organization for Economic Co-operation and Development
OP	Overall Pool
PANTHERS	Performance ANalysis and Testing of HEat Removal System
Pb	Lead
PCC	Passive Containment Cooling
PCCS	Passive Containment Cooling System
PCS	Power Conversion System
PDF	Probability Density Function
PERSEO	in-Pool Energy Removal System for Emergency Operation
PHISICS	Parallel and Highly Innovative Simulation for INL Code System
PhW	Phenomenological Window
PLOFA	Protected Loss Of Flow Accident
PLOHS	Protected Loss Of Heat Sink
PLOOP	Protected Loss Of Offsite Power
PP	Primary Pump
R5-3D	RELAP5-3D©
RAVEN	Risk Analysis and Virtual ENviroment
RC	Research Center
R&D	Research and Development
RELAP	Reactor Excursion and Leak Analysis Program
RV	Reactor Vessel
SA	Sub-Assembly
SAC	Système d'Arrêt Complémentaire, complementary shutdown system
SBO	Station Black Out
SBWR	Small Boiling Water Reactor
SCK-CEN	Research Centre for the Applications of Nuclear Energy
SCWR	SuperCritical-Water-cooled Reactor
SESAME	thermal-hydraulic Simulations and Experiments for the Safety Assessment of MEtal-cooled reactors
SFR	Sodium-cooled Fast Reactor
SG	Steam Generator
SGBT	Steam Generator Bayonet Tube
SGTR	Steam Generator Tube Rupture
SIET	Società Informazioni Esperienze Termoidrauliche
SPECTRA	Sophisticated Plant Evaluation Code for Thermal-hydraulic Response Assessment
SR	Safety Rod
STH	System Thermal-Hydraulic
SV	Safety Vessel
TAF	Top of Active Fuel
TC	ThermoCouples
TDV	Time Dependent Volume
TDJ	Time Dependent Junction
TFM	mini Turbine Flow Meter
TH	Thermal-hydraulic
TRACE	TRAC/RELAP Advanced Computational Engine
TrT	Transient Test
TS	Test Section
ULOF	Unprotected Loss Of Flow

UNIROMA1	“Sapienza” University of Rome
UQ	Uncertainty Quantification
UTOP	Unprotected Transient of Over-Power
VCS	Vessel Cooling System
VHTR	Very-High-Temperature Reactor
VV	Verification & Validation
WGAMA	Working Group on Analysis and Management of Accidents

Roman letters

A_{flow}	Free flow area (m^2)
A_{grid}	Area occupied by the grid (m^2)
C_v	Modified drag coefficient
D_h	Equivalent hydraulic diameter (m)
h	Hour
K_{CF}	Local pressure drop coefficient in cross-flow
$K_{Venturi}$	Local pressure drop coefficient of the Venturi flow meter
L	Characteristics length (m)
MW_{th}	Thermal Mega Watt
MW_{el}	Electrical Mega Watt
N_2	Nitrogen
Nu	Nusselt number
p/d	Pitch to diameter ratio
Pe	Peclet number
Pr	Prandtl number
R	Radius
Re	Reynolds number
$\bar{s}$	Pitch ratio
T	Temperature (K)
v	Velocity (m/s)
z_p	Number of ranks

Greek letters

ε	Grid flow blockage factor
θ	Angle between the cross-flow direction and the inclination of the rods
ρ	Density (kg/m^3)
φ	Flow direction coefficient

BIBLIOGRAPHY

[1] OECD Nuclear Energy Agency, 2018. Preparing the Future through Innovative Nuclear Technology: Outlook for Generation IV Technologies.

[2] OECD Nuclear Energy Agency, 2014. Technology Roadmap Update for Generation IV Nuclear Energy Systems.

[3] International Atomic Energy Agency, 2002. Comparative assessment of thermophysical and thermohydraulic characteristics of lead, lead-bismuth and sodium coolants for fast reactors. Technical report, IAEA-TECDOC-1289, Vienna, Austria.

[4] Roelofs, F., 2019. Thermal-hydraulics Aspects of Liquid Metal Cooled Nuclear Reactors. Editor: Roelofs, F., Elsevier – Woodhead Publishing (WP), Duxford, UK, 464 pages.

[5] Aoto, K., Dufour, P., Hongyi, Y., Glatz, J.P., Kim, Y., Ashurko, Y., Hill, R. and Uto, N., 2014. A summary of sodium-cooled fast reactor development. Prog. Nucl. En., vol. 77, pp. 247-265. http://dx.doi.org/10.1016/j.pnucene.2014.05.008

[6] Alemberti, A., Smirnov, V., Smith, C.F. and Takahashi, M., 2014. Overview of lead-cooled fast reactor activities. Prog. Nucl. En., vol. 77, pp. 300-307. http://dx.doi.org/10.1016/j.pnucene.2013.11.011

[7] Kimura, N., Miyakoshi, H. and Kamide, H., 2012. Experimental Study on Thermal Stratification in a Reactor Vessel of Innovative Sodium-Cooled Fast Reactor – Mitigation Approach of Temperature Gradient across Strtification Interface – . Jou. Nucl. Sci. Tech., vol. 47, pp. 829-838. https://doi.org/10.1080/18811248.2010.9711659

[8] Planquart, P. and Van Tichelen, K., 2019. Experimental investigation of accidental scenarios using a scale water model of a HLM reactor. Nucl. Eng. Des., vol. 346, pp. 10-16. https://doi.org/10.1016/j.nucengdes.2019.02.016

[9] IAEA, 2009. Safety Assessment for Facilities and Activities. Safety Standars Series No GSR Part 4 – General Safety Requirements. Vienna, Austria.

[10] Kadambi, C.E.R.S.N.H.S.S.L.N.P., 1988. Bulletin 88-11: pressurizer surge line thermal stratification. Retrieved from https://www.nrc.gov/reading-rm/doc-collections/gen-comm/bulletins/1988/bl88011.html

[11] Thuy, N.T.T., Trung, T.V.and Dien, L.D., 2012. Investigation of temperature stratification in cold leg and downcomer in LSTF/ROSA experiment. Retrieved from https://inis.iaea.org/collection/NCLCollectionStore/_Public/45/058/45058897.pdf

[12] Schuler, X. and Herter, K.H., 2004. Thermal fatigue due to stratification and thermal shock loading of piping. In 30th MPA-Seminar in conjunction with the 9th German-Japanese Seminar. Retrieved from https://inis.iaea.org/collection/NCLCollectionStore/_Public/36/036/36036665.pdf

[13] D'Auria, F., 2017. Thermal-hydraulics of water cooled nuclear reactors (First edit). Duxford; Cambridge, MA: Woodhead Publishing. Retrieved from https://www.sciencedirect.com/book/9780081006627/thermal-hydraulics-of-water-cooled-nuclear-reactors#book-description

[14] Harten, A., 1989. ENO schemes with subcell resolution. Jour. Comp. Phy., vol. 83, pp. 148-184. https://doi.org/10.1016/0021-9991(89)90226-X

[15] The RELAP5-3D© Code Development Team, 2015. RELAP5-3D Code Manual Vol. I: Code Structure, System Models, and Solution Methods. INL/MIS-15-36723 Volume I, Revision 4.3

[16] Saedi, H.R., 1983. Insurge pressure response and heat transfer for PWR pressurizer. Massachusetts Institute of Technology. Retrieved from https://dspace.mit.edu/handle/1721.1/15523

[17] Kim, S.N., 1984. An experimental and analytical model of a PWR pressurizer during transients. Massachusetts Institute of Technology. Retrieved from https://dspace.mit.edu/handle/1721.1/15611

[18]Shumway, R., Bolander, M. and Aktas B., 2002. Prediction of MIT Pressurizer Data using RELAP5 and TRAC-M. Proc. 10th Int. Conf. Nucl. Eng., Arlington, VA, USA. doi: 10.1115/ICONE10-22580

[19]Bayless, P.D., et al., 2015. RELAP5-3D Code Manual Vol. III: Developmental Assessment. INL/MIS-15-36723 Volume I, Revision 4.3

[20]Ahn, J.S., Bluck, M., Eaton M. and Jackson, C., 2018. A validation of RELAP on predicting nuclear power plant phenomena. Proc. 26th Int. Conf. Nucl. Eng., London, England. doi: 10.1115/ICONE26-81424

[21]Verma, P.K., Nayak, A.K., Jain, V., Vijayan, P.K., Vaze, K.K., 2013. Suppression of thermal stratification in gravity driven water pool of an advanced reactor using shrouds. Ann. Nucl. En., vol. 58, pp. 221-227. http://dx.doi.org/10.1016/j.anucene.2013.03.012

[22]Kumar, S., Vijayan, P.K., Kannan, U., Sharma, M. and Pilkhwal, D.S., 2017. Experimental and computational simulation of thermal stratification in large pools with immersed condencer. App. Therm. Eng., vol. 113, pp. 345-361. http://dx.doi.org/10.1016/j.applthermaleng.2016.10.175

[23]Hou, X., Sun, Z. and Lei, W., 2017. Capability of RELAP5 code to simulate the thermal-hydraulic characteristics of open natural circulation. Ann. Nucl. En., vol. 109, pp. 612–625. https://doi.org/10.1016/j.anucene.2017.06.010

[24]Bandini, G., Polidori, M., Meloni, P., Tarantino, M. and Di Piazza, I., 2015. RELAP5 and SIMMER-III code assessment on CIRCE decay heat removal experiments. Nucl. Eng. Des., vol. 281, pp. 39-50. http://dx.doi.org/10.10167j.nucengdes.2014.11.005

[25]Del Nevo, A. and Martelli, E., 2016. Validation of a Three-Dimensional Model of EBR-II and Assessment of RELAP5-3D Based on SHRT-17 Test, Nuclear Technology, vol. 193, No. 1, pp. 1–14 https://doi.org/10.13182/NT14-152

[26]Grasso, G., Sarotto, M., Lodi, F. and Castelluccio, D.M., 2019. An improved design for the ALFRED core. Proc. Of International Congress on Advances in Nuclear Power Plants, ICAPP 2019. May, 12-15, Juan-les-pin, France.

[27]Memmott, M., Buongiorno and J., Hejzlar, P., 2010. On the use of RELAP5-3D as a subchannel analysis code. Nucl. Eng. Des., vol. 240, pp. 807-815. doi: 10.1016/j.nucengdes.2009.11.006

[28]Yoo Y.J., Sabharwall P., Reyes J.N., Wu Q. and Sienicki J.J., 2003. Effects of the fluid axial conduction on liquid metal natural circulation and linear stability. In: 2003 ANS/ENS International Winter Meeting, New Orleans, LA, pp. 1523-1530.

[29]Balestra, P., Parisi, C., Alfonsi, A. and Rabiti, C., 2016. Simulation of AER-DYN-002 and AER-DYN-003 control rod ejection benchmarks by RELAP5-3D/PHISICS coupled codes. Nucl. Tech., vol. 193, pp. 175-182. doi: 10.13182/NT14-138

[30]Balestra, P., Alfonsi, A., Strydom, G., Rabiti, C., Giannetti, F. and Caruso, G., 2017. Improvements to PHISICS/RELAP5-3D© capabilities for simulating HTGRs. Trans. Am. Nucl. Soc., vol. 116, pp. 1009-1012.

[31]Balestra, P., Alfonsi, A., Strydom, G., Sen, R.S., Rabiti, C., Giannetti, F. and Caruso, G., 2017. New phisics perturbation method module verification using the HTTR neutronic model. Trans. Am. Nucl. Soc., vol. 117, pp. 1412-1415.

[32]Narcisi, V., Giannetti, F., Martelli, E., Del Nevo, A., Tarantino, M. and Caruso, G., 2019. Steam Generator mock-up preliminary design suitable for Pb-Li technology demonstration and code assessment. Fus. Eng. Des., vol. 146, pp. 1126-1130. https://doi.org/10.1016/j.fusengdes.2019.02.022

[33]Martelli, E., Del Nevo, A., Lorusso, P., Giannetti, F., Narcisi, V. and Tarantino, M., 2019. Investigation of heat transfer in a steam generator bayonet tube for the development of PbLi technology for EU DEMO fusion reactor. Under review for publication in Fus. Eng. Des.

[34]Oberkampf, W.L. and Roy, C. J., 2010. Verification and Validation in Scientific Computing, Cambridge University Press., 2nd ed.

[35]Alfonsi, A., Rabiti, C., Mandelli, D., Cogliati, J., Wang, C., Talbot, P. W., Maljovec, D. P. and Smith, C., 2017. RAVEN Theory Manual and User Guide. INL/EXT-16-38178.

[36]SESAME Project, EURATOM H2020, Grant Agreement N. 654935, April 2015.

[37]Gauché,F., 2012. Generation IV reactors and the ASTRID prototype: Lessons from the Fukushima accident. Com. Ren. Phy., vol. 14, pp. 365-371. https://doi.org/10.1016/j.crhy.2012.03.004

[38]Frignani M., Grasso G., Tarantino M., Constantin M., Turcu I., Di Gabriele F., Romanello V. and Alemberti A., 2017. FALCON advancements towards the implementation of the ALFRED Project. In: Proc. Int. Con. Fast Reac. Rel. Fuel Cycl.: Next Gen. Nucl. Syst. Sust. Dev. Yekaterinburg, Russian Federation

[39]Engelen, J., Abderrahim, H.A., Baeten, P., De Bruyn, D. and Leysen, P., 2015. MYRRHA: Preliminary front-end engineering design. Int. Jou. Hyd. En., vol. 40, pp. 15137-15147. http://dx.doi.org/10.1016/j.ijhydene.2015.03.096

[40]ENEA, Accordo di Programma MISE-ENEA 2015-2017. Available online: http://www.enea.it/it/Ricerca_sviluppo/lenergia/ricerca-di-sistema-elettrico/accordo-di-programma-MiSE-ENEA-2015-2017/generazione-di-energia-elettrica-con-basse-emissioni-di-carbonio/nucleare-da-fissione

[41]The RELAP5-3D© Code Development Team, 2015. RELAP5-3D Code Manual Vol. IV: Models and correlations. INL/MIS-15-36723 Volume IV, Revision 4.3

[42]Narcisi, V., Giannetti, F. and Caruso, G., 2019. Investigation on RELAP5-3D© capability to predict thermal stratification in liquid metal pool-type system and comparison with experimental data. Nucl. Eng. Des., vol. 352, 110152, https://doi.org/10.1016/j.nucengdes.2019.110152

[43]Turroni, P., Cinotti, L., Corsini, G. and Mansani, L., 2001. The CIRCE test Facility, in: ANS Winter Meeting AccApp. Reno, Nevada, USA

[44]Tarantino, M., Agostini, P., Benamati, G., Coccoluto, G., Gaggini, P., Labanti, V., Venturi, G., Class, A., Liftin, K., Forgione, N. and Moreau, V., 2011. Integral Circulation Experiment: Thermal-hydraulic simulator of a heavy liquid metal reactor. Jou. Nucl. Mat., vol. 415, pp. 433-448. doi: 10.1016/j.jnucmat.2011.04.033

[45]Tarantino, M., Martelli, D., Barone, G., Di Piazza, I. and Forgione, N., 2015. Mixed convection and stratification phenomena in a heavy liquid metal pool. Nucl. Eng. Des., vol. 286, pp. 261-277. doi: 10.1016/j.nucengdes.2015.02.012

[46]Martelli, D., Forgione, N., Di Piazza, I. and Tarantino, M., 2015. HLM fuel pin bundle experiments in the CIRCE pool facility. Nucl. Eng. Des., vol. 292, pp. 76-86. http://dx.doi.org/10.1016/j.nucengdes.2015.06.004

[47]Ambrosini, W., Azzati, M., Benamati, G., Bertacci, G., Cinotti, L., Forgione, N., Oriolo, F., Scadozzo, G. and Tarantino, M., 2004. Testing and qualification of CIRCE instrumentation based on bubble tubes. Jou. Nuc. Mat., vol. 335, pp. 293-298. doi: 10.1016/j.jnucmat.2004.07.030

[48]Agostini, P., Alemberti, A., Ambrosini, W., Benamati, G., Bertacci, G., Cinotti, L., Elmi, N., Forgione, N., Oriolo, F., Scadozzo, G. and Tarantino, M., 2005. Testing and qualification of CIRCE Venturi-nozzle flow meter for large scale experiments. Proc. 13th Int. Conf. Nucl. Eng., Beijing, China. doi: 10.1115/ICONE13-50909

[49]Martelli, D., Tarantino, M. and Di Piazza, I., 2016. Experimental activity for the investigation of mixing and thermal stratification phenomena in the CIRCE pool facility. Proc. 24th Int. Conf. Nucl. Eng., Charlotte, North Carolina, USA. doi: 10.1115/ICONE24-60920

[50]Narcisi, V., Giannetti, F., Tarantino, M., Martelli, D. and Caruso, G., 2017. Pool temperature stratification analysis in CIRCE-ICE facility with RELAP5-3D© model and comparison with experimental tests. J. Phys. Conf. Ser., vol. 923 (012006). doi: 10.1088/1742-6596/923/1/012006

[51]Schikorr, M., Bubelis, E., Mansani, L. and Litfin, K., 2010. Proposal for pressure drop prediction for a fuel bundle with grid spacers using Rehme pressure drop correlations. Nucl. Eng. Des., vol. 240, pp. 1830-1842. doi: 10.1016/j.nucengdes.2010.03.039, 2010

[52]Kazimi, M.S. and Carelli, M.D., 1976. Clinch River Breeder Reactor Plant Heat Transfer Correlation for Analysis of CRBRP Assemblies, CRBRP-ARD-0034, Westinghouse.

[53]Ushakov, P.A, Zhukov, A.V. and Matyukhin, N.M., 1977. Heat transfer to liquid metals in regular arrays of fuel elements. High Temp., vol. 15, pp. 868-873 translated from Teplofizika Vysokikh Temperatur, vol. 15, pp. 1027-1033.

[54]Giannetti, F., Di Maio, D.V., Naviglio, A. and Caruso, G., 2016. Thermal-hydraulic analysis of an innovative decay heat removal system for lead-cooled fast reactors. Nucl. Eng. Des., vol. 305, pp. 168-178. http://dx.doi.org/10.1016/j.nucengdes.2016.05.005

[55]Idelchik, I.E., 1986. Handbook of Hydraulic Resistance. Second ed. Hemisphere Publishing Corporation.

[56]OECD/NEA Nuclear Science Committee, 2015. Handbook on Lead-bismuth Eutectic Alloy and Lead Properties, Materials Compatibility, Thermal-hydraulics and Technologies. https://www.oecd-nea.org/science/pubs/2015/7268-leadbismuth-2015.pdf

[57]Balestra, P., Giannetti, F., Caruso, G. and Alfonsi, A., 2016. New RELAP5-3D lead and LBE thermophysical properties implementation for safety analysis of Gen IV reactors. Sci. Technol. Nucl. Install., vol. 2016. doi: 10.1155/2016/1687946

[58]Press W.H. and Teukolsky S.A., 1990. Savitzky-Golay Smoothing Filters. Comp. Phy., vol. 4, pp. 669-672. doi: 10.1063/1.4822961

[59]Lorusso, P., Pesetti, A., Tarantino, M., Narcisi, V., Giannetti, F., Forgione, N. and Del Nevo, A., 2019. Experimental analysis of stationary and transient scenarios of ALFRED steam generator bayonet tube in CIRCE-HERO facility. Nucl. Eng. Des., vol. 352, 110169. https://doi.org/10.1016/j.nucengdes.2019.110169

[60]Narcisi, V., Giannetti, F., Del Nevo, A., Tarantino, M. and Caruso G., 2018. Pre-test analysis of accidental transients for ALFRED SGBT mock-up characterization. Nucl. Eng. Des., vol. 333, pp. 181-195. https://doi.org/10.1016/j.nucengdes.2018.04.015

[61]Lorusso, P., Pesetti, A., Tarantino, M. and Narcisi V., 2019. Protected loss of flow accident simulation in CIRCE-HERO facility: experimental test and system code assessment. Proceedings of the 2019 27th International Conference on Nuclear Engineering, May 19-24, 2019, Ibaraki, Japan.

[62]Narcisi, V., Giannetti, F., Del Nevo, A., Tarantino, M. and Caruso, G., 2019. Post-test simulation of a PLOFA transient test in the CIRCE-HERO facility. Nucl. Eng. Des., vol. 355, 110321. https://doi.org/10.1016/j.nucengdes.2019.110321

[63]Giannetti, F., Lorusso, P., Narcisi, V., Caruso, G., Naviglio, A., Pasquali, U., Frignani, M., Alemberti, A., Tarantino, M. and Martelli, D., 2019. ALFRED protected loss of flow accident experiment in CIRCE facility. TECDOC Proceedings of the Technical Meeting on the Benefits and Challenges of Fast Reactors of the SMR Type, September 24-27, 2019, Milan, Italy.

[64]Lorusso, P., Pesetti, A. and Tarantino, M., 2018. ALFRED Steam Generator Assessment: design and pre-test analysis of HERO experiment. Proceedings of the 2018 26th International Conference on Nuclear Engineering, July 22-26, 2018, London, England, ICONE26-81824, doi: 10.1115/ICONE26-81824.

[65]Narcisi, V., Giannetti, F., Del Nevo, A., Tarantino, M. and Caruso, G., 2017. Pre-test analysis of protected loss of primary pump transients in CIRCE-HERO facility. J. Phys. Conf. Ser., vol. 923 (012005). https://doi.org/10.1088/1742-6596/923/1/012005

[66]Breijder, P.A., Stempniewicz, M.M., Alcaro, F., Ferry, R., Narcisi, V., Lorusso, P., Giannetti, F., Caruso, G. and Tarantino, M., 2019. Analysis of argon-enhanced circulation in CIRCE-HERO with RELAP5-3D and SPECTRA codes. Under review for publication in Nucl. Eng. Des.

[67]Narcisi, V., Giannetti, F., Del Nevo, A., Alcaro, F., Wang, X., Kraus, A., Brunnett, A., Thomas, J., Girault, N., Grosjean, B., Caruso, G. and Gerschenfeld, A., 2019. System thermal-hydraulic modelling of the phénix dissymmetric test benchmark. Nucl. Eng. Des., vol. 353, 110272. https://doi.org/10.1016/j.nucengdes.2019.110272

[68]Sauvage, J.F., 2009. Phénix: 35 years of history: the heart of a reactor. CEA/Valrhô Edition, Bagnols-sur-Cèze, France.

[69]Vasile, A., 2011. PHÉNIX final tests. Proceedings of the 11th International Congress on Advances in Nuclear Power Plants (ICAPP-11), Nice, France, May 2-6, Paper #11298.

[70]IAEA-TECDOC-1703, 2013. Benchmark analyses on the natural circulation test performed during the PHÉNIX end-of-life experiments. 186 pages. Free download from: https://www-pub.iaea.org/MTCD/Publications/PDF/TE_1703_web.pdf.

[71]IAEA-TECDOC-1742, 2014. Benchmark analyses on the control rod withdrawal tests performed during the PHÉNIX end-of-life experiments. 262 pages. Free download form: https://www-pub.iaea.org/MTCD/Publications/PDF/TE-1742_web.pdf.

[72]Varaine, F., 2009. IAEA CRP on PHÉNIX end of life tests: Control rod withdrawal, Technical Report CEA/DEN/CAD/DER/SPRC/LEDC.

[73]Narcisi, V., Giannetti, G., Subioli, A., Del Nevo, A., Caruso, G., 2019. Assessment of a RELAP5-3D three-dimensional analysis based on PHÉNIX dissymmetric transient test. Jou. Nuc. Eng. Rad. Sci., NERS-19-1001. https://doi.org/10.1115/1.4044847

[74]Giannetti, F., Narcisi, V., Subioli, A. and Del Nevo, A., 2018. Phénix transient analysis for the assessment of RELAP5-3D based on dissymmetric test benchmark, Proceedings of the 26th International Conference on Nuclear Engineering (ICONE-26), London, England, July 22-26, Paper #82419. doi: 10.1115/ICONE26-82419

[75]Grosjean, B. and Li, S., 2016. PHENIX dissymmetric test description, Deliverable D4.1, H2020 SESAME project, 39 pages.

[76]Cheng, S.K. and Todreas, N.E., 1986. Hydrodynamic models and correlations for bare and wire-wrapped hexagonal rod bundles – Bundle friction factors, subchannel friction factors and mixing parameters, Nucl. Eng. Des., vol. 92, No. 2, pp. 227-251. https://doi.org/10.1016/0029-5493(86)90249-9

[77]Davis, C.B., 2006. Applicability of RELAP5-3D for Thermal-Hydraulic Analyses of a Sodium-Cooled Actinide Burner Test Reactor, INL/EXT-06-11518. Free download from: https://inldigitallibrary.inl.gov/sites/sti/sti/3374827.pdf

[78]Pfrang, W. and Sruwe, D., 2007. Assessment of Correlations for Heat Transfer to the Coolant for Heavy Liquid Metal Cooled Core Design, Forschungszentrum Karlsruhe GmbH, Karlsruhe FZKA 7352. Free download from: http://citeseerx.ist.psu.edu/viewdoc/download?doi=10.1.1.499.6021&rep=rep1&type=pdf

[79]IAEA, 2016. IAEA Safety Glossary, Terminology Used in Nuclear Safety and Radiation Protection. 2016 Rev., Vienna, June.

[80]Caramello, M., Gregorini, M., Bertani, C., De Slave, M., Alemberti, A. and Panella, B., 2017. Thermal-hydraulic analysis of a passively controlled DHR system. Prog. Nucl. En., vol. 99, pp. 127-139. http://dx.doi.org/10.1016/j.pnucene.2017.05.015

[81]Masoni, P., Botti, S. and Fitzsimmons, G.W., 1993. Confirmatory tests of full-scale condensers for the SBWR. Proceedings of the 2nd International Conference on Nuclear Engineering (ICONE-2), San Francisco, California, USA, March 21-24.

[82]Mascari, F., Bersano, A., Ferri, R., Lombardo, C. and Burgazzi, L., 2019. Description of PERSEO Test N 7. Tech. Rep. SICNUC-P000-029, 68 pages.

[83]SIET S.p.A., available online: https://www.siet.it/research-and-development/steam-separators.html

[84]Ferri, R., Achilli, A., Cattadori, G., Bianchi, F. and Meloni, P., 2005. Design, experiments and Relap5 code calculations for the perseo facility. Nucl. Eng. Des., vol. 235, pp. 1201-1214. Doi: 10.1016/j.nucengdes.2005.02.011

[85]Bandini, G., Meloni, P., Polidori, M. and Lombardo, C., 2011. Validation of CATHARE V2.5 thermal-hydraulic code against full-scale PERSEO tests for decay heat removal in LWRs. Nucl. Eng. Des., vol. 241, pp. 4662-4671. https://doi.org/10.1016/j.nucengdes.2011.02.034.

[86]Bianchi, F., Meloni, P., Ferri, R. and Achilli, A., 2004. Assessment of RELAP5 mod3.3 and CATHARE 2 v1.5A against a full scale test of PERSEO device. Proceedings of the 12th International Conference on Nuclear Engineering (ICONE-12), Arlington, Virginia, USA, April 25-29.

[87]Frogheri, M., Alemberti, A. and Mansani, L., 2013. The advanced lead fast reactor European demonstrator (ALFRED). Proceedings of the 15th International Topical Meeting on Nuclear Reactor Thermal – Hydraulics (NURETH-15), Pisa, Italy, May 12-17.

[88]Frignani, M., Alemberti, A. and Tarantino, M., 2019. ALFRED: A revised concept to improve pool related thermal-hydraulics. Nucl. Eng. Des., vol. 235, 110359. https://doi.org/10.1016/j.nucengdes.2019.110359

[89]Grasso, G., Petrovich, C., Mattioli, D., Artioli, C., Sciora, P., Gugiu, D., Bandini, G., Bubelis, E. and Mikityuk, K., 2014. The core design of ALFRED, a demonstrator for the European lead-cooled reactors. Nucl. Eng. Des., vol. 278, pp. 287-301. https://doi.org/10.1016/j.nucengdes.2014.07.032

[90]Petrovich, C., 2013. ALFRED core. Summary, synoptic tables, conclusions and recommendations. Tech. Rep. UTFISSM-P9SZ-006, 23 pages.

[91]Bubelis, K. and Mikityuk, K., 2012. Plant data for the safety analysis of the ETDR (ALFRED). Tech. Rep. TEC058-2012, LEADER project, 65 pages.

[92]Ciurluini, C., Narcisi, V., Giannetti, F., Cretara, L. and Caruso, G., 2019. Preliminary neutron kinetic – thermal-hydraulic coupled analysis of the ALFRED reactor using PHISICS/RELAP5-3D. Accepted for publication in J. Phys. Conf. Ser.

[93]Rimpault, G., Plisson D., Tommasi, J., Jacqmin, R., Rieunier, J.M., Verrier, D. and Biron, D., 2002. The ERANOS code and data system for fast reactor neutronic analyses. Proceedings of the International Conference on the New Frontiers of Nuclear Technology: Reactor Physics, Safety and High-Performance Computing (PHYSOR 2002), Seoul, Korea, October 7-10.

[94]Alfonsi, A., Rabiti, C., Epiney, A., Wang, Y. and Cogliati, J., 2012. PHISICS TOOLKIT: Multi-Reactor Transmutation Analysis Utility MRTAU. Proceedings of the International Conference on the New Frontiers of Nuclear Technology: Reactor Physics, Safety and High-Performance Computing (PHYSOR 2012), Knoxville, Tennessee, USA, April 15-20.

[95]Alfonsi, A., Epiney, A., Rabiti, C., Wang, Y., Cogliati, J. and Strydom, G., 2012. PHISICS multi-group transport neutronic capabilities for RELAP5. Proceedings of the 2012 International Congress on Advances in Nuclear Power Plants (ICAPP 12), Chicago, USA, June 24-28.

[96]Fabrizio, V., Dulla, S., Nervo, M., Ravetto, P., Bianchini, A.G. and Peluso, V., 2013. ALFRED Reactor: evaluation of multi temperature cross section sets by deterministic and stochastic methods. Tech. Rep. ADPFISS-LP2-001, 14 pages.

[97]Bandini, G. and Polidori, M., 2013. Report on the Results of Analysis of DEC Events for the ETDR (ALFRED). Tech Rep. UTFISSM-P9SZ-007, 402 PAGES.

[98]Frignani, M., Alemberti, A., Tarantino, M. and Grasso, G., 2019. ALFRED staged approach. Proceedings of the International Congress on Advances in Nuclear Power Plants (ICAPP 2019), Juan-les-pins, France, May 12-15.

[99]D'Auria, F., Camargo, C. and Mazzantini, O., 2012. The Best Estimate Plus Uncertainty (BEPU) approach in licensing of current nuclear reactors. Nucl. Eng. Des., vol. 248, PP. 317-328. https://doi.org/10.1016/j.nucengdes.2012.04.002

[100] Queral, C., Montero-Mayorga, J., Gonzalez-Cadelo, J. and Jimenez G., 2015. AP1000® Large-Break LOCA BEPU analysis with TRACE code. Ann. Nucl. En., vol. 85, pp. 576-589, https://doi.org/10.1016/j.anucene.2015.06.011

[101] Wilsom, E.G., 2013. Historical insights in the development of best estimate plus uncertainty safety analysis. Ann. Nucl. En., vol 52, pp. 2-9. https://doi.org/10.1016/j.anucene.2012.03.002

[102] Tarantino, M., Bernardi, D., Coccoluto, G., Gaggini, P., Labanti, V., Forgione, N. and Napoli, A., 2010. Natural and Gas Enhanced Circulation Tests in the NACIE Heavy Liquid Metal Loop. Proceedings of the 18th International Conference on Nuclear Engineering (ICONE-18), Xi'an, China, May 17-21. https://doi.org/10.1115/ICONE18-29968

[103] Narcisi, V., Lorusso, P., Giannetti, F., Alfonsi, A. and Caruso, G., 2019. Uncertainty Quantification method for RELAP5-3D© using RAVEN and application on NACIE experiments. Ann. Nucl. En., vol 127, pp. 419-432. doi: 10.1016/j.anucene.2018.12.034

[104] Alfonsi, A., Rabiti, C., Mandelli, D., Cogliati, J., Kinoshita, R. and Naviglio, A., 2014. RAVEN and Dynamic Probabilistic Risk Assessment: Software Overview. Eu. Saf. and Rel. Conf., Wroclaw, Poland.

[105] Rabiti, C., Alfonsi, A., Cogliati, J., Mandelli, D., Kinoshita, R., Sen, S., Wang, C. and Chen, J., 2017. RAVEN User Manual. INL/EXT-15-34123

[106] Wilks, S.S., 1941. Determination of Sample Sizes for Setting Tolerance Limits. Ann. Math. Stat., vol. 12, pp. 91–96. https://doi.org/10.1214/aoms/1177731788